Mechanical Properties of Alginate Anisotropic Capillary Hydrogels for Directed Regeneration in Spinal Cord Injury

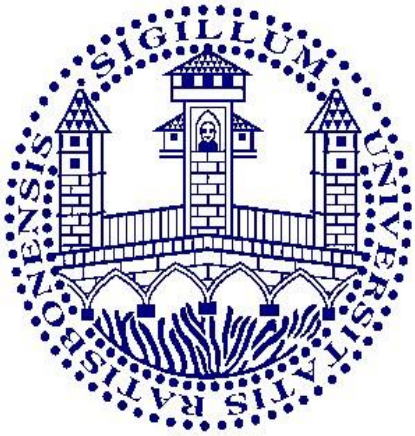

DISSERTATION

zur Erlangung des Doktorgrades der Naturwissenschaften
(Dr. rer. nat.)
der Fakultät für Chemie und Pharmazie
der Universität Regensburg

vorgelegt von

Maximilian Nützl

aus **Ampfing**

Mai 2023

Die vorgelegte Dissertation entstand im Zeitraum von November 2018 bis Mai 2022 am Institut für Physikalische Chemie der naturwissenschaftlichen Fakultät IV der Universität Regensburg in Kooperation mit der Klinik für Paraplegiologie des Universitätsklinikum Heidelberg.

Die Arbeit wurde angeleitet von Apl. Prof. Dr. Rainer Müller.

Promotionsgesuch eingereicht am:

Datum der mündlichen Prüfung:

Prüfungsausschuss: Prof. Dr. Oliver Tepner (Vorsitzender)

Apl. Prof. Dr. Rainer Müller (Erstgutachter)

Prof. Dr. Werner Kunz (Zweitgutachter)

Prof. Dr. Frank-Michael Matysik (Drittprüfer)

Abstract

Injury to the adult spinal cord and its ascending and descending axonal pathways can arise the debilitating condition known as spinal cord injury. In order to restore the connectivity between the brain and the periphery of the human body, a large effort has been put into understanding and solving the multifaceted complications, that this injury entails. Besides cell-based approaches, biomaterials as a standalone solution, or in combination with cells, offer a wide array of benefits in aiding the repair process of such conditions. Strategies deploying these materials harbor many advantages compared to the common treatment of spinal cord injury, as the structures are able to mimic the properties of natural tissues, such as the extracellular matrix of the spinal cord. To improve the biocompatibility of biomaterials as an implant, lots of efforts have addressed their functionalization with cells and biological factors, but less so their mechanical conformity to the properties of the targeted tissue. With that in mind, a physical guidance structure was provided by fabricating alginate-based capillary hydrogels, whose mechanical properties were adjusted to occupy a wide range of mechanical properties in microindentation and shearing experiments. The implants were designed to match the mechanical properties, that were identified for human and animal spinal cord tissue, by altering the gelation and chemical-crosslinking procedure of the fabrication methodology. Besides the mechanical properties, the overall morphology of the capillary scaffold was adjusted to enhance its capabilities regarding the infiltration of host tissue, while still providing guidance cues for a directed axonal regrowth in the anisotropic material.

Table of Contents

1. Fundamentals

1.1 Spinal Cord Injury

The spinal cord (SC) is a longitudinal vertebrae-surrounded nervous structure, that, in connection with the brain, poses the central nervous system (CNS) of vertebrates. It poses a pathway for sensory- and motor-related information from the brain to the peripheral nervous system (PNS), which is interconnected to the CNS via dorsal and ventral roots. Besides transmitting information, the SC also partakes in signal processing, as its motoneurons and interneurons receive and process inputs, e.g. for movement execution. Besides the bony vertebral column, the SC and parts of the adjacent PNS are also surrounded by three different meningeal layers (pia, arachnoid, and dura matter). The SC extends from the base of the skull to the conus medullaris above the coccyx, which spans about 45 cm of distance in humans. The vertebral structure can be segmented into cervical (C), thoracic (T), lumbar, and sacrococcygeal regions. Caudally (coccyx-oriented) of every one of the 31 vertebrae, a pair of dorsal and ventral roots transitions from the SC into the spinal nerves of the PNS over the ganglion, which is shown in Figure 1. Inside the SC, the butterfly-shaped gray matter houses moto- and interneurons, that pass transversally and are arranged in horns, each representing a different class of functional neurons. Besides glial cells, the surrounding white matter also contains neurons, which are primarily myelinated, longitudinally oriented, and arranged in posterior, anterior, and lateral columns, to which different neuron classes of specific functionality are assigned. Originating from motor neurons of the gray matter, a variety of filaments emerge, which unite in the form of the aforementioned ventral roots, posing the link between CNS and PNS [1]–[3].

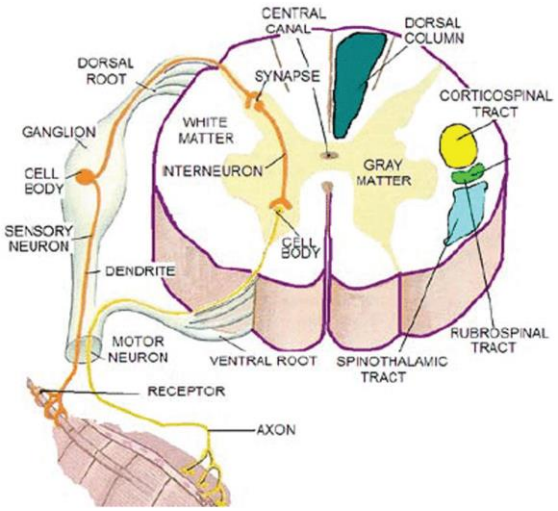

Figure 1: Schematic drawing of a transverse transection of the SC, taken from [4].

Since spinal cord injury (SCI) was first described by ancient Egyptians in 1500 BC as a hardly treatable medical condition, not much progress beyond palliative measures was made for a long time [5], [6]. This acceptance of the irreversibility and permanence of SCI has been persistent until the latter part of the 20th century, as the neurobiological understanding of SCI was slowly improving. 8000 to 10000 individuals, primarily male, get affected by SCI annually in the US alone, of which most traumatic events originate from vehicular accidents, followed by various forms of violence and sports accidents. As the average SCI occurs in 33-year-old individuals, survival rates are generally above 90%, and life expectancy is hardly affected by it, 2.5 million people are currently affected worldwide and associated direct lifetime cost can be up to a staggering 4.7 million dollars per patient [7]–[13]. Different clinical malfunction deficits, ranging from loss of motor, sensory, urologic, or sexual function, to common secondary disorders, which include various respiratory, cardiovascular, gastrointestinal, and musculoskeletal disorders, can be attributed to the interruption of axonal pathways [14]. During traumatic events to the SC, such as penetrating wounds (gunshots, knife wounds, blasts), blunt traumas (falls, crush injuries, collisions), and also oncological surgeries, mechanical torsional and tearing forces are acting on the SC, in which four different mechanisms of resulting primary injury are distinguished. Besides impact alone with transient compression, distraction, and laceration/transection, impact plus persistent compression is the most common mechanism behind SCI [15], [16]. During the primary injury, axonal tear and demyelination are prevalent and damage to smaller blood vessels in the area entails hypovolemia and hemodynamic shock, which disrupts blood flow to the SC. In the upcoming minutes, hours, and days, the secondary injury arises acute hemorrhage and ongoing ischemia, which is more significant in the gray matter of the SC, due to a higher degree of vascularization [17]. Ionic calcium fluxes, lipid peroxidation from free radicals, loss of vascular autoregulation, and the neurotoxicity from neurotransmitters, like glutamate, entail excitotoxic or ischemic apoptosis or necrosis in this secondary injury stage of SCI [8], [10], [18]–[21]. In the subacute stage of SCI, the spinal shock phase, a loss of cutaneous and deep-tendon reflexes below the level of injury occurs, of which, in this 24-hour time window post-SCI, only cutaneous reflexes may show signs of recovery [18]. The current management of SCI involves the immediate stabilization of the spine via a rigid cervical collar and a backboard and the transport to a specialized SCI center, where imaging (CT, MRI, X-ray) and further assessment of the SCI are deployed. Surgical decompression of the SC is performed to improve the vascular supply of the affected SC and thus dampen the secondary injury, ideally within 24 hours after SCI [22]–[24]. The administration of a systemic steroid therapy, like methylprednisolone, preferably within eight

hours of SCI and control of blood pressure, to circumvent ischemia, may further improve the outlook on motor recovery [18], [23], [25], [26]. The majority of motor skill recovery occurs within three months after SCI, however, additional functional improvement may occur up to 18 months after an event [27]. Ultimately, the resulting pathology is determined by the location of the SCI. Whilst paraplegia (impairment of the lower extremities) is common with lower thoracic SCI, quadriplegic impairment (affecting all four limbs) is associated with cervical spine injury [10], [28]. Furthermore, it was found, that over a ten-year period, patients who suffer from paraplegia generally have higher survival rates than those with tetraplegia, of which again those with higher cervical injury have a higher risk of mortality compared to those with lower cervical injury. In addition, it appears to be evident, that individuals with complete SC transection during SCI have a mortality risk three times higher and generally worse recovery prospects than those who suffer from incomplete injuries, as in the former cases generally no spared motor or sensory function remains below the level of injury [13], [28]. To objectively gauge locomotor behavioral characteristics in different stages of SCI, Basso, Beattie, and Bresnahan (BBB) established a benchmark score, with a score of 0 indicating complete paralysis and a maximum score of 21, which signals normal gait mechanics [29], [30]. On top of primary and secondary injury processes, SCI regeneration barriers are arising in the form of loss of parenchymal volume, further demyelination and dieback of surviving axons, formation of micro-cystic compartments, and the accumulation of scar-forming astrocytes and extracellular matrix (ECM)-molecules, such as chondroitin sulfate proteoglycans (CSPGs). These factors ultimately constitute the formation of a glial scar, which poses an impediment to SCI recovery [10], [18], [31]. The glial scar arises within hours after SCI and is sustained into the chronic phase of SCI, as even after 42 years post-injury its presence could be determined [32], [33]. Although the glial scar is thought to initially stabilize the SC after SCI, its role in SCI recovery was thought to be rather inhibitory, as reactive astrocytes and their upregulated expression of molecular inhibitors, mainly CSPGs, would inhibit axonal regeneration, sprouting, conduction, and remyelination [10], [34], [35]. This point of view has been challenged lately, as axon regrowth across a lesion site may even be improved in the presence of a supposedly inhibitory astrocytic glial scar. Rather, independent of the presence of these astrocyte-associated inhibitory processes, a lack of sustained axon-growth-specific factors supply in SCI lesions was identified as the major detriment in the stimulation of axonal regrowth [36], [37]. According to these studies, the formation of the glial scar is ultimately an endogenous repair mechanism, which intriguingly allows for axonal sprouting, albeit only few regenerating axons can span an entire lesion site without intervention [38], [39].

1.2 Combinatorial Approaches to Spinal Cord Injury

To overcome the limitations of endogenous repair mechanisms in SCI, transplantation of a variety of biomaterial and cell types has been researched in recent history. At the center of interest are multifaceted therapeutical approaches, in which cells and bioactive molecules like neurotrophins provide a suitable biochemical environment to recover the axonal pathways in the gray and white matter and promote functional recovery after SCI [39]. However, the direct injection or transplantation of cells into a lesion cavity has shown to be disadvantageous compared to a biomaterial-assisted application. Thus, to augment a cell-based approach to SCI, the deployment of a physical support and transport vehicle is desired alongside it [40], [41].

1.2.1 Cell-based Approaches to Spinal Cord Injury

Stem cells pose a promising approach to stimulate axonal regeneration in SCI. Mesenchymal stem cells (MSCs) have been reported to show anti-inflammatory, trophic, anti-apoptotic, and immunomodulatory properties in different CNS-related pathologies, like Alzheimer's or Parkinson's disease [42], [43]. In particular, bone marrow MSCs demonstrate immunosuppressive, anti-inflammatory, neuroprotective properties, and trophic support through the expression of a variety of CNS-specific growth and trophic factors, such as brain-derived neurotrophic factor (BDNF) in rat SCI models [44]. These factors are known to facilitate the outgrowth of injured axons in nerve injuries and aid in axonal entry into the distal SC parenchyma in SCI [45], [46]. Rodents, that were treated with bone marrow MSCs, have shown various degrees of functional improvements, however, in clinical tests, individuals only have shown signs of slightly improved motor and sensory function after a combinatorial bone marrow MSC transplantation [47], [48]. Intravenous injection of MSCs derived from umbilical cords has shown similar advantages as bone marrow MSCs, furthermore, they demonstrated very little immunogenic responses in clinical trials and also partial recovery of nerve functionality, possibly due to differentiation of the implanted cells into recovery-supporting glial cells [49], [50]. Treatment of SCI with amniotic fetal MSCs poses a similar prospect, as their isolation is not invasive and they are especially low in tumorigenicity and immunogenicity and they harbor many of the same advantages as the prior MSC approaches [51]. Additionally, transplantation of MSCs from adipose tissue into the parenchyma of injured rat SC has shown its axonal regrowth and locomotion recovery potential, which was encompassed by a reduction of the glial scar through the expression of trophic factors and immunosuppression [52], [53]. An ethically more troubled approach is the introduction of embryonic stem cells (ESCs) into SCI therapeutics. These pluripotent stem cells have

been shown to promote functional recovery, preservation of axons, and remyelination of demyelinated axons, as well as differentiation into neural cells and oligodendrocytes in different approaches in rodent SCI. However, clinical trials have been deferred due to ethical concerns and a reported uncontrollable stem cell proliferation. Ethically less problematic than ESCs, but quite similar, due to their equally pluripotent nature, are induced pluripotent stem cells. Although these reprogrammed somatic cells have shown their safety and proficiency in the form of regained motor functionality in the rodent SCI model, clinical data is outstanding, as the therapy protocols still need to be refined, due to the potential risk of tumor formation [54]–[57]. A less promising approach involves the transplantation of neural stem cells (NSCs), despite the cell's ability to differentiate into neurons, astrocytes, and oligodendrocytes and their viability in Parkinson's and Huntington's disease applications. A proficiency in rodent SCI models could, however, could not be replicated in clinical trials [58]. The same ethical rationale as with ESCs applies to adult endogenous stem cells, which have to be isolated from the adult spinal canal. They are capable of differentiation into glial cell subtypes and even support functional recovery in rat SCI [59]. A different cell-based approach to combat the multifaceted problems that arise with SCI is the deployment of olfactory ensheathing cells. These types of glial cells can be isolated from the olfactory nasal mucosa and their transplantation to SCI might create permissive microenvironments for axonal recovery, remyelinate spared axons, express fitting neurotrophic agents, and reduce the formation of inhibitory microenvironmental factors, which manifested in functional and structural recovery in the rat SCI [60], [61]. Pilot studies in human SCI have been done and although some participants had a modest functional recovery, the methodology needs to be revised and modified to reproduce the results, which were obtained in animal research [62]. Another prominent glial-cell subtype in SCI treatment is represented by Schwann cells. They are able to support sustained growth of axons, remyelination, expression of trophic factors, reduced formation of cystic cavities, and white matter sparing in the rat SCI [63]. Upon the therapeutical combination of Schwann cells with separate trophic factors, stem cells, or a variety of drugs, an improved number of remyelinated axons and recovered functionality could be observed [64]. Clinical trials have demonstrated the effectiveness of standalone Schwann cells or in combination with bone marrow MSCs or different types of glial cells, whilst displaying minor adverse effects and partially even functional recovery [65]–[67]. Despite these advantages, bone marrow MSCs and Schwann cells do not integrate well into the surrounding glial scar tissue, which mainly consists of reactive astrocytes, that on the one hand initially confine inflammation and infection of surrounding tissues in SCI but also can guide axonal

regrowth on themselves [68], [69]. Thus, astrocytes, that had been adhered to anisotropic poly-L-lactic acid fibers, have been demonstrated to provide a suitable cellular guidance cue for sensory axons and also altered the spatial orientation of expressed ECM molecules, such as fibronectin or CSPGs [70], [71].

1.2.2 Hydrogels as Biomaterials

In general, a crucial obstacle in regenerative medicine is the need for scaffolds, which mimic the ECM of the targeted host tissue. To live up to this proposition, the desired biomaterials should provide appropriate structural stability, biocompatibility, and tunable morphological and mechanical cues like stiffness, porosity, swellability, and general structure [72]. Hydrogels, which are water-swollen and cross-linked three-dimensional networks of synthetic or natural polymeric structures can satisfy all these preconditions. Furthermore, they are very permeable for smaller molecules, viscoelastic in nature, and show low interfacial tension with biological fluids. During hydrogel gelation, a colloidal species, which is dispersed in water, is cross-linked by radiation or changes in pH, ionic strength, or temperature. Hydrogels can be of natural or synthetic origin or a mix of these two, whereas the natural ones usually trump in medical applications due to their biocompatible, biodegradable, and non-toxic nature. On the flip side, the reproducibility of natural hydrogel research is limited, their (bio-)degradability can also be a detriment, and their generally poor mechanical properties and degradability require the use of further cross-linking. Synthetic hydrogels, on the other hand, prevail in very sterile applications and their architecture, stiffness, and degradation behavior can be better tailored to task-specific demands. Their aforementioned poor biocompatibility can be circumvented through functionalization with bioactive agents, like adhesion-, growth-, or differentiation-facilitating compounds [73]–[78]. In general, natural hydrogels can be categorized into protein- and polysaccharide-based subtypes. The polymeric structure of all hydrogels can be categorized into three different classes, in which homo-polymeric hydrogels exhibit one single type of monomeric subunit, co-polymeric hydrogels are made of two or more different monomers and multi-polymeric hydrogels describe two independently formed polymers within the same three-dimensional network. During gel formation, polymers can form chemical hydrogels by forming covalent cross-links (Michael addition, Schiff-base reaction, click chemistry, aldol reactions, disulfide linkages, irradiation crosslinking, radical polymerization) or physical hydrogels through association via van-der-Waals forces or hydrogen bonds, ionic interaction, protein interactions, antigen-antibody interaction, chain entanglement, and crystallite polymer aggregation. In some instances, the cross-linking procedure can entail potentially cytotoxic effects from coupling agents, catalysts, or photo-initiators, which may affect the biomaterial's biocompatibility.

The same holds true for all the macromolecular breakdown products, which necessitates knowledge about the entire erosion evolution up until bio-elimination of the water-soluble remainders of the polymer constituents. Hydrogels can be derived from a variety of different gelation methodologies (electrospinning, bioprinting, self-assembly, freeze-drying, salt-leaching, and lithography) and can be further classified based on their overall charge and their physical structure, which categorizes as amorphous, semi-crystalline, hydrogen-bonded, supermolecular or hydrocolloidal [72], [79]–[88]. In general, the elastic response of hydrogel samples can be altered by variations in polymer and cross-linker concentration, polymer hydrophobicity, or changes in pH or temperature [89], [90]. The degradation kinetics of a hydrogel biomaterial should accommodate for the rate of tissue regeneration at the defect site, which can be achieved by altering their liquid diffusivity, cross-linker concentration, or enzymatic degradation characteristics [72]. Furthermore, the degradation behavior can be addressed by the type of chemical bonding, pH, (co-)polymer composition, and water uptake, all of which drive either passive hydrolysis or more specifically, enzymatic decomposition processes. Thereby, the velocity of the degradation as a decay in molecular weight is traceable by a reduction in mechanical integrity [87], [91]. The first application of hydrogels as a potential biomaterial was reported in 1960, as conventional plastics were known to show unfavorable host-biomaterial interactions due to mechanical irritation, which eventually could lead to inflammation and tumors. Thus, a material, which is water and metabolite permissive, but exerts inertness to biological processes for prolonged timeframes, was of need [92]. In general, hydrogels find application in the medical and pharmaceutical sector, as contact lenses, membranes, biosensor membranes, artificial skin, and drug delivery systems are prevalent use cases for hydrogels as biomaterials. Besides that, hydrogels can be also applied in the food industry and environmental control [90], [93].

1.2.3 Biomaterials in Spinal Cord Injury

While small gaps in SC connectivity may only require simple surgical intervention, larger gaps were commonly treated by deploying nerve auto-, allo-, or xenografts, as those harbor Schwann cells, a variety of adhesion molecules, and provide trophic support. As autografts stem from the same individual, loss of donor site functionality and a complicated surgical procedure is weighing on this approach to SCI. Allo- and xenografts may furthermore require immunosuppressive treatment, thus, a natural or synthetic material, which harbors similar advantages as nerve grafts, is desired. Biomaterials can act as three-dimensional substrates, that permit tissue replacement, axon regrowth, and prevention of scar formation [76]. This is achieved by providing directional axonal guidance, while also providing an

appropriate cellular and extracellular microenvironment, similar to the milieu of the SC ECM, with the aid of the aforementioned cells, neurotrophic factors, and ECM molecules [94], [95]. This is of importance, as the natural SC is not homogenous, but shows a highly ordered occurrence of cells [40]. Besides these micro-environmental features, the biomaterial ought to show mechanical integrity in the timeframe of the experiment, therefore, degradation and denaturation characteristics need to be well-adjusted. For this reason, Marchand et al. concluded, that introducing a secondary matrix in the form of chemical cross-links into a polymer biomaterial is also of utmost importance in the timeframe of an SCI. This especially applies to physically cross-linked hydrogel scaffolds, as their mechanical strength is rather low. However, there is a trade-off between mechanical stability and bio-degradability, as with an increasing amount of chemical cross-links, the potential cytotoxicity of the material tends to increase and its viability for cells hence may decrease [72], [96]. Furthermore, the material is supposed to be permeable for nutrients, small proteins, and smaller molecules like glucose, whilst preventing the undirected movement of larger structures, such as larger proteins and cells [40], [97]. According to *in-vitro* studies performed by Kokai et al., a porosity of 80% (v/v) vastly improves the diffusion of such smaller molecules compared to a porosity of 50% (v/v) in porous polycaprolactone biomaterials [98]. Besides the influence of matrix stiffness on cell behavior, which will be elaborated on in the following section, the cells are also affected by the pore size distribution of the matrix, as for example, MSCs tend to migrate further and show higher maximum cell displacement inside pore structures, which are of medium size (12 µm), compared to larger (17 µm) or smaller ones (7 µm) [99]. Smaller conduits (< 1 µm) of a scaffold structure enable nutrient diffusion and larger ones (> 10 µm) accommodate for axon ingrowth, cell dispersion, and ingrowth of other host tissue [100]. In studies performed by Rutkowski et al., a volume porosity of about 70 to 75% (v/v) was identified as a sweet spot in synthetic nerve conduit scaffolds, as this effectively improved the axonal growth into Schwann-cell loaded scaffolds, when compared to higher or lower respective porosities [101]. Common treatments to obtain porous features inside hydrogel structures are porogen leaching, gas formation, freeze-drying, electrospinning, bio-printing, or microfluidics [72]. More specifically, as the native neuroarchitecture of the SC exhibits a parallel arrangement of axons, an ideal biomaterial is not only porous but also ought to provide anisotropic features in the micron range to allow for tissue ingrowth and organization and ultimately support the directed regeneration of axons [19], [87]. Smeal et al. found, that dorsal root ganglia, which were cultured on an extruded filamentous polypropylene matrix, showed more directional growth on matrices with smaller parallel-oriented filaments. Hence, as the diameter of the longitudinal filaments

decreased to 200 µm and below, the growth path of the nerve cells was aligned more parallel to the filament itself, which has to be taken into consideration if a strict caudal-rostral reinnervation process is the objective [102]. The pore size distribution still has to be spacious enough to allow the infiltration of axons and biological constituents into the biomaterial [76]. On the other hand, an increased surface area for a highly porous scaffold material may elicit a stronger immune response in the CNS [87], [103]. Scaffolds, that consist of a single-lumen or only a few compartments in the millimeter range were also researched in the past, some of which are also outlined in section 1.2.5. In these instances, the alignment of ingrowing tissue mainly occurs in the proximity of the border of the respective compartments, therefore, the amount of available guidance cues is limited [19]. Besides the physical guidance, a biomaterial can also confine the infiltration of astrocytes, cysts, and fibroblasts in the lesion site, which may have positive implications on the outcome of SCI [104]. The focus of this work will be hydrogels as biomaterials in SCI. They pose promising contenders in the biomaterial approach to SCI, as they in many cases accomplish all the prerequisites of a suitable biomaterial. Due to their high water content, they exhibit low interfacial tension to surrounding body fluids. On top of that, this class of biomaterials is also an attractive environment for the migration and proliferation of different cell types, due to its high surface-to-volume ratio and therefore high specific surface area [16], [76], [78], [105].

1.2.4 Mechanical Properties of Biomaterials in the Context of Spinal Cord Injury

Besides some of the factors outlined in the section above, the stiffness of biomaterials in SCI is of utmost importance, as this not only dictates the host-biomaterial interaction but also establishes biomaterial-cell interactions. As outlined in section 1.2.1, a regenerating SC is strongly dependent on cell and trophic support, which simulates the effects of the ECM in the SC. For that matter, one has to take into account, that mechanical cues from cell-surrounding matter influence cell survival, differentiation, migration, integration, and orientation. Mechanotransduction describes a cell's ability to adapt its morphology and lineage to the elasticity of the matrix around it [106]. For instance, Leipzig et al. found, that NSCs tend to differentiate into neural cells on methacrylamide chitosan hydrogels of elasticity below 1 kPa, but rather evolve into oligodendrocytes on hydrogels above 7 kPa in stiffness [107]. On the other hand, human embryonic stem cells have shown improved actin polymerization and therefore improved cell attachment, spreading, and propagation on polyacrylamide hydrogels of higher stiffness [108]. Microglial cells also showed distinct elasticity dependency, as they adhered to spherical morphologies on 100 Pa matrices, when compared to much stiffer 30 kPa surfaces, on which these cells obeyed a rather spread-out

conformation [109]. Furthermore, human umbilical vein endothelial cells, have shown a viability of 89% in calcium cross-linked alginate hydrogels with a shearing modulus G' of 30 Pa, whereas the mere immersion in phosphate-buffered saline (PBS) solution reduced the viability of the cells to 59%. Stiffer alginate hydrogels also lead to worse cell viability outcomes in this instance [110]. Apart from biomechanical cueing, hydrogels, whose mechanical properties are in-line with those of SC tissue, facilitate low inflammation of the surrounding tissue, axonal organization, and regeneration in CNS applications and specifically also in SCI [16], [76], [78], [111]. In *in-vivo* experiments, 100 Pa and 30 kPa hydrogels elicited vastly different levels of gliosis, as around the stiffer specimens an upregulation of microglia, reactive astrocytes, and interleukin-1β indicated a more pronounced glial scar formation [109]. Adjusting the mechanical properties of porous biomaterials poses a big challenge as if one advances the porosity of a biomaterial for the sake of permeability and mechanical softness, the mechanical integrity tends to deteriorate, and the structure might collapse under the pressure of surrounding tissues, which may prevent infiltration of the native SC and facilitate the formation of a fibrous capsule around the then non-permeable structure [76], [98], [112]. The mechanical stiffness and volume porosity are strongly correlated, as Shahriari et al. found, that the elastic moduli of polycaprolactone biomaterials for SCI are strongly inversely correlated to the volume porosity [113]. A minimally invasive approach to improve the outcome in non-complete injuries of the SC is the injection of an isotropic biomaterial, which preserves the axons below the site of injury and promotes the regeneration of damaged SC tissue. As stated in section 1.2.5.1, by a targeted application, these biomaterials alongside drugs and bioactive molecules can be directly delivered to the SC, which circumvents blood-brain-barrier permeability constraints but only requires injection through a non-invasive insertion to the SC. The mechanical properties of these systems ought to be tuned precisely, not only regarding the elastic properties but also regarding time-dependent shearing behavior [85]. Due to the viscoelastic nature of the SC, strain speed, maximum strain, and preconditioning steps are to be monitored as one establishes a measurement protocol for a biomaterial implant in SCI. In the case of compression and tensile experiments, the often not explicitly stated region of the stress-strain curve, that was used to calculate elastic moduli, poses an unknown quantity, as many examination protocols lack such information. Measurement setup variables, such as specimen thickness and apparatus surface condition (hatched plate-plate geometries or adhesives in shearing measurements, surface roughness in unconfined compression experiments, and adhesives in tensile testing) ultimately also have a major impact on the obtained results [114]–[117]. Data on the mechanical properties of the native SC and even more so on the injured

SC is sparse and contradictory, as variances in species, number of specimens, tissue type, tissue preparation, measurement temperature, and post-mortem time are not trivial to account for [117], [118]. Cheng et al. released an extensive review on different mechanical testing protocols for CNS tissue. Briefly, *in-vitro*/*ex-vivo* measurements involve oscillatory shearing rheometry, which can be utilized to obtain storage and loss moduli of tissue samples *in-vitro* under varying stress and strain regimes in the linear viscoelastic region of CNS samples. Furthermore, elasticity values for cylindrical *in-vitro* samples can be obtained from confined and unconfined compression and also tensile testing in constant strain-rate procedures, while relaxation and creep experiments gauge the viscoelasticity. Indentation measurements also apply compressive forces, however, not to an entire sample surface area, but only to a smaller subsection of it. Here, due to fewer apparatus constraints, *in-vivo* determinations in the CNS are feasible, which allows measurement in the native SC canal with physiological blood flow, hydration with cerebrospinal fluid, and temperature with no onset of tissue degradation. Other *in-vivo* measurement setups are pressure-volume studies, ultrasound, and magnetic resonance elastography [117], [119]. Native human tissues occupy a wide range of elastic moduli from 167 Pa for breast tissue and up to 54 GPa for cortical bones, whereby SC tissue sits towards to lower end of this range, as elaborated in the following [120], [121]. Due to the whole SC's neuroarchitectural inhomogeneity, one would generally also assume an anisotropy in mechanical properties. To examine that, Ozawa et al. utilized a pipette aspiration method to determine the mechanical properties of the gray and white matter of Japanese white rabbit SC tissue. They monitored the suction of the tissue into the pipette with a video microscope and derived the elastic moduli from it. Roughly equal moduli for the white and gray SC matter were recorded in different planes, which are given below in Table 1. Contradicting results were obtained by Ichihara et al., as they compared the gray and white matter stiffness of bovine SC in tensile testing (0.05 s^{-1} straining until rupture) and the obtained moduli indicated distinct differences in mechanical stiffness between gray and white matter, which is also shown in Table 1 [122], [123].

Table 1: Elasticity of SC gray and white matter determined by pipette aspiration in the transverse, frontal, and sagittal plane, research by Ozawa et al. [123]*; tensile testing by Ichihara et al. in the transverse plane* [122]*; other tensile tests in the transverse plane of the whole SC; *apparent elasticity (given the constraints of force-distance contact models) of SC gray and white matter determined by AFM microindentation in the transverse, frontal, and sagittal plane, research by Franze et al.* [118]*; elastic moduli from ultrasound elastography measurements of canine cadaver and intraoperative SC in the frontal plane of whole SCs by Prager et al.* [114].

methodology	plane of measurement	elasticity white matter / kPa	elasticity gray matter / kPa	source
pipette aspiration – rabbit SC	transverse	3.4 ± 0.9	3.4 ± 1.4	Ozawa et al. [123]
pipette aspiration – rabbit SC	frontal	3.5 ± 0.5	3.0 ± 0.3	Ozawa et al. [123]
pipette aspiration – rabbit SC	sagittal	2.8 ± 0.4	3.5 ± 0.9	Ozawa et al. [123]
tensile testing – bovine SC	transverse	61.3 ± 4.2	43.4 ± 3.2	Ichihara et al. [122]
tensile testing – canine SC	transverse	11.9 – 16.6 (complete SC)	-	Tunturi [124]
tensile testing – human SC	transverse	1230 (complete SC)	-	Bilston et al. [125]
tensile testing – cat SC	transverse	26 (complete SC)	-	Hung et al. [126]
tensile testing – cat SC	transverse	229 – 240 (complete SC)	-	Chang et al. [127]
tensile testing – cat SC (1.5 h post mortem)	transverse	560 (complete SC)	-	Chang et al. [127]
AFM indentation – rodent SC	transverse	*0.048	*0.125	Franze et al. [118]
AFM indentation – rodent SC	frontal	*0.075	*0.128	Franze et al. [118]
AFM indentation – rodent SC	sagittal	*0.077	*0.127	Franze et al. [118]
ultrasound elastography – canine cadaver SC	frontal	11.6 ± 4.7 (complete SC)	-	Prager et al. [114]
ultrasound elastography – canine intraoperative SC	frontal	18.3 (lesion site); 47.9 (surrounding tissue)	-	Prager et al. [114]

Concerning the work done by Ozawa et al., within the respective recorded standard deviations, no significant difference in elasticity between the different sample planes was present, therefore, the mechanical stiffness of SC in this macroscopic examination of mechanical properties was not subject to anisotropy. Furthermore, the gray and white matter appeared identical in mechanical stiffness. However, this was not apparent in SC tensile testing by Ichihara et al., as they found a distinct difference between white and gray SC matter. Other examinations of SC stiffness stated elastic moduli of 11.9 – 16.6 kPa (tensile testing of canine (dog) SC at different stresses), 1.23 MPa (tensile testing of human SC), 26, 229 – 240, and 566 kPa (tensile testing of cat SC) [124]–[127]. In the process of determining the elastic properties of canine SC tissue, Tunturi et al. also found, that the tissue relaxes about 40% of the initial stress in a 20-second stress relaxation experiment. More profound results were obtained by Chang et al., who examined the stress relaxation of cat SC in living animals at strains from 0.05 to as low as 0.007. The stress relaxation in the lowest and the highest strain environments merely ranged between 25 and 30% of the initial stress after 122 seconds. Besides a higher elastic modulus at 1.5 hours post-mortem, the SC of deceased animals appeared to take longer to reach an equilibrium state, therefore it was less viscoelastic than in its native state. Similar stress relaxations were obtained by Bilston and Thibault, who identified a stress decay of 20 – 30% over a 30-second timeframe in *in-vitro* tensile stress relaxation experiments with human C2 – C7 SC segments [124], [125], [127]. As one has to take into account, that cells occupy the space realm of up to 100 µm, the mechanical properties in the microscopic dimension of a biomaterial also need to be monitored and eventually tuned to accommodate cell-specific needs in *in-vivo* applications. Further, based on the SC's neuroarchitecture, one would likely ascribe an inhomogeneity in its mechanical properties on a microscopic scale to it. To examine that, Franze et al. conducted spherical microindentation experiments. They investigated the direction-dependent elastic properties of mice's SCs, in which the specimens were sacrificed, the ventral and dorsal roots were cut, the cord was removed from the animal, and 500 µm slices of SC tissue were prepared in a microtome. The samples were fixed to a Petri dish and incubated in artificial cerebrospinal fluid. To measure the apparent elasticity of gray and white SC matter, atomic force microscope (AFM) measurements were performed. To do so, polystyrene bead-equipped (Ø 37 µm) cantilevers were deployed in a JPK AFM and indented the samples in a two-dimensional grid pattern with up to 7 nN and 10 µm/s, which prevented excessive deflection during the cantilever approach and excessive sample indentation. The apparent elastic moduli of the SC white matter and the two horns of the gray matter are given in Table 1. As also found by Ichihara et al., the microindentation experiments performed

by Franze et al. also described a discrepancy between white and gray matter stiffness, however, in this instance the gray matter elastic moduli surpassed those of the white matter. Remarkably, only the transverse plane of the white matter showed any inhomogeneity when compared to the other tested planes of the same matter, the remaining planes of white and all three planes in the gray SC matter appeared isotropic in their mechanical properties. The same homogeneity was also found among different horn regions inside the gray matter [118]. Later on, Franze et al. examined the development of the SC's mechanical properties post-SCI. They inflicted crush injuries on the mouse SC. 1.5 or three weeks post-injury, the animals were sacrificed and 1 cm pieces of SC tissue were taken and transversally cut in the microtome. They deployed the same AFM procedure as outlined before, however, this time utilizing ~90 µm polystyrene cantilever spheres and higher indentation forces of 20 or 30 nN. The transverse sections, that underwent elastic moduli mapping in the AFM, showed, that healthy SC tissue (no crush injury, just removal of SC lamina 1.5 or three weeks prior) is softer in the area of the white matter, with an apparent elastic modulus of 177 Pa compared to the gray matter's 420 Pa, both of which significantly trump the elasticity values found in their prior studies (48/125 Pa). Post-crush SC tissue proved to be less stiff, yielding elasticities in the 100 to 200 Pa range on average, where the outer tissue maintained a higher degree of stiffness compared to the inner tissue region of the crush injury [128]. Thus, the assumption, that the glial scar tissue would be posing a mechanical barrier in SCI recovery, has to be questioned, as according to this research, the injured SC is softer in nature compared to the intact one, which implies other factors play a major role in this multifaceted issue. The importance of monitoring and adjusting of a biomaterial's mechanical properties to meet the requirements of a potential CNS application, however, cannot be understated [38], [129]. Despite this fact, that biomaterials are ought to be developed with regard to the target tissue's mechanical properties, clear cut standards in examining the tissues and biomaterials are lacking [87]. This will be apparent, as section 1.2.5 showcases a whole array of biomaterial interventions, in which the influence of mechanical properties of biomaterials on the outcome of different *in-vivo* SCI-related applications was evaluated.

1.2.5 Mechanical Properties of Biomaterials in Spinal Cord Injury Application

1.2.5.1 Injectable Hydrogels

Although not the focus of this work, an alternative to pre-assembled scaffold structures are in-situ gelled materials, which can aid in facilitating a favorable environment and mechanical stability in the host tissue. However, due to the lack of a directional cueing structure, the application of injectable hydrogels seems to be more appropriate in crushing injuries, rather than in larger SCI lesion sites [19]. Führmann et al.

developed an injectable furan-modified hyaluronic acid hydrogel, that was Diels-Alder coupled with bismaleimide-poly(ethylene glycol). The deployed biomaterials were furthermore equipped with poly(D, L-lactic-co-glycolic acid) (PLGA)-encapsulated BDNF and injected into the SC canal of compression-injured rats at the T2 level. Before that, the viscoelastic properties of the gels during gelation were recorded in a parallel plate geometry of an oscillatory shearing rheometer in a stress- and frequency sweep. Histological and BBB locomotor assessments were utilized to gauge the recovery potential of the biomaterial *in-vivo*. By altering the ratio of cross-linker and hyaluronic acid, the mechanical properties could be altered. A mixture, that was still injectable after eight hours, had its viscoelastic properties measured over time. After roughly three hours, the mixtures G' outpaced the G" values and the former ultimately reached 48 Pa. During PBS immersion the same mixture exhibited a rather low swelling ratio of ~1.6 after 96 hours, which was an advantage *in-vivo*, as this avoided excessive swelling in the confined SC canal after injection. Non-injured control animals, that also received the non-invasive hyaluronic acid hydrogel injection, continued to perform optimally in BBB locomotion testing at all times (BBB 21). Between an injured group, that merely received cerebrospinal fluid and another group, which was treated with the BDNF-loaded hydrogels, no distinct difference in BBB scoring, as well as axon density, was observable. The injury arose major neurological deficits in both instances, which persisted for four weeks (BBB 10). The biomaterial group further demonstrated a continuous release of BDNF over four weeks. Compared to the cerebrospinal control group, the soft injectable hydrogel tended to reduce the inflammatory response in immuno-histological assessment [85]. Pupkaite et al. proposed, that a thiol-Michael addition cross-linked collagen biomaterial would be suitable to be deployed in such a non-invasive injection-based approach. Their system was tuned to provide an injectable hydrogel with a cross-link chemistry, that was cell-compatible and exhibited shear-thinning behavior. The thiol functionalized and subsequently PEG-maleimide oligomer click-cross-linked collagen hydrogels were analyzed in a parallel plate rheometry setup at 25 °C in frequency sweeps (0.1 – 25 Hz, maximum strain 0.267%). The Young's moduli were extracted from the linear viscoelastic region at 1 Hz. Despite varying the ratio between thiolated collagen and the cross-linker from 1:1 to 1:40, Young's moduli of the mixture showed no distinct trend, with elastic moduli in the 4 to 6 kPa range. The gels furthermore demonstrated shear thinning properties in viscosity measurements, reaching approximately 6 Pas at 5 s^{-1}, which rendered the gels injectable through a 27-gauge needle. The decay of viscosity with an increase in shearing rate was also proven to be temporary, as the mixture was able to restore its initial viscosity in cycles of low and high-strain environments. As the mixture of this non-invasive

biomaterial intervention showed very little swelling and successfully carried bone marrow stem cells (viability > 80%) and human umbilical vein endothelial cells (viability > 70%) for up to four days *in-vivo*, the thiol-Michael click-reaction-linked collagen hydrogel appeared desirable for this kind of tissue engineering application [130]. An injectable suspension of a biomaterial was fabricated by Hsieh et al. 3D-bioprinted hydrogels were printed from polyurethane (PU) nanoparticles, which were synthesized from poly(ϵ-caprolactone) diol and poly(L-lactic acid) diol (PU1) or poly(ϵ-caprolactone) diol and poly(D, L-lactic acid) diol (PU2) and a diisocyanate compound, respectively. NSCs from mouse brains were incorporated into the water dispersion of PU at a concentration of 4×10^6 cells/mL. The mixture was printed on a Petri dish at 37 ° at a pressure of 55 kPa and stored inside a culture medium. The mechanical properties of the resulting bio-printed scaffold structures were easily adjustable by varying the solid content of the monomer dispersion. Four different water dispersions of PU1 and PU2 with 25% or 30% (w/w) nanoparticle content were examined with regard to their mechanical properties. After phase-transitioning to a hydrogel after 200 and 600 seconds, the L-lactic acid-based mixture yielded 4 kPa (30% (w/w) PU1) or 1.1 kPa (25% (w/w) PU1), while the D, L-lactic acid-based compound obtained lower storage moduli at 2.4 kPa (30% (w/w) PU2) or 0.68 kPa (25% (w/w) PU2). The NSC-loaded hydrogels showed almost no swelling. In culture medium, the cells demonstrated less viability on the PU1-based hydrogels (viability < 50% on both concentrations after 72 h), than those on the PU2-based hydrogels (viability > 100% on both concentrations after 72 h). Therefore, the PU gels of lower stiffness (dependent on PU type) not only preserved NSCs but also aided in the proliferation of such. Further, in polymerase chain reaction testing of seeded NSCs, the levels of nestin, β-tubulin, and microtubule-associated gene 2 expression were strongly correlated with the overall storage moduli given above, with the 0.68 kPa matrix demonstrating the highest expression of these proteins and genes, which is indicative for cell self-renewal and differentiation of NSCs into neurons. The same correlation could be determined for the expression of growth factors, like BDNF, with a clear-cut outperformance for the softest hydrogel class, yielding the highest level of respective gene expression. On the flip side, the level of glial fibrillary acidic protein (GFAP) expression, which is signaling the presence of glial cells, such as Schwann cells, was more pronounced on the hydrogel matrices of higher stiffness. Animal studies with the injectable PU hydrogels were performed with zebrafish embryos. Besides a control group, that remained in embryo medium, the other groups were exposed to 2% (v/v) ethanol in embryo medium for four hours, which caused CNS damage. The ethanol groups were either not treated at all, or injected into the CNS with PBS, an NSC suspension, or one of the four NSC PU suspensions, which

then sol-gelled *in-vivo*. To test embryo locomotor recovery, a side-to-side contraction check was performed. While in the unharmed embryos roughly 85% of specimens demonstrated these contractions, all other injured groups performed worse in that regard, with the softer 0.68 kPa and 1.1 kPa hydrogels performing the second best, as these provided ~71%, respectively ~66% percent contracting activity, while the stiffer PU1 specimens and the solely PBS injected ones all demonstrated no contraction response. Further, with regard to the coiling rate, a measure for the activity of the embryos, the softest hydrogel-treated specimens (~0.065 Hz coiling rate) also performed not much worse than the unharmed fish embryos (~0.075 Hz coiling rate), with worse coiling rates in ever stiffer biomaterial groups, while all of those still did better than purely NSC- or PBS-treated specimens (~0.03 Hz coiling rate). And lastly, the researchers compared the hatching rates of the embryos. The native, unharmed ones had a hatching rate of ~90%, which again was closely followed by the softest hydrogel-treated embryos, which still had a hatching rate of ~60%, while only PBS-injected ones hatched merely in ~23 – 25% of all cases. Although the 0.68 kPa gels demonstrated their viability to combat ethanol-induced SCI, they were rather fragile [131].

1.2.5.2 Biomaterials derived from Natural Polymers

Collagen is a natural polymer of animal origin, which inherently exhibits a low antigenic and immunogenic response in biomaterial applications. However, due to purification and variability of natural origin constraints, collagen-based materials ought to be individually examined in the light of any novel application. In biomaterial applications, collagen typically possesses weak mechanical properties and might damage surrounding tissues due to excessive swelling in aqueous environments. But one can address these issues by altering the composition of the collagen backbone by introducing chemical cross-links. However, as a major constituent of the natural ECM, collagen has been shown to provide a suitable environment for the adhesion, migration, and differentiation of cells and support the myelination and axonal growth without prior functionalization in damaged nerve tissue [84], [130], [132]–[134]. Thus, Chen et al. UV used a collagen and heparin sulfate mixture in a freeze-drying process to obtain cylindrical porous scaffold bodies (Ø 3 mm). Alternatively, an identical mixture or a pure collagen compound was extruded in a 3D bio-printing process. To monitor biocompatibility, the structures were seeded with NSCs. In *in-vivo* experiments, rats were completely transected at the T10 level (1.5 mm lesion) and locomotor recovery was monitored. Prior to that, the mechanical responses of the scaffolds were examined in tensile testing with an Instron 5865, which applied a compressive tensile stress (maximum force 0.1 kN), which resulted in strains lower than 10%. Compared to scaffolds, that were bio-printed without heparin sulfate (2.31 MPa), the

compressive elastic moduli were elevated for the samples that included it (3.46 MPa). The modulus for the freeze-dried collagen/heparin sulfate mixture was lower (2.43 MPa), than for its bio-printed counterpart (3.46 MPa), hence a variability in elastic response could be attributed to the addition of heparin sulfate, as well as the to the fabrication methodology. Scanning electron microscope (SEM) analysis showed, that NSCs would proliferate in the porous material, in which all three different matrices performed equally. The best recovery in hindlimb functionality was recorded for the 3D-bioprinted collagen scaffolds with heparin sulfate (the stiffest scaffolds) in BBB scoring and incline plane climbing after two weeks and four weeks. The rodents treated with these scaffolds also demonstrated the most neurofilaments across the lesion site in immunofluorescence staining [135]. Due to limitations of most mechanical properties measurement setups, biomaterials, that were designed for SCI, can not be easily measured after implantation, as they are usually analyzed *ex-vivo* and require prior dissection. An innovative approach to analyze the mechanical properties of SC tissue *in-vivo* is ultrasound elastography, which measures the rate of displacement of a sample through ultrasound stimulation [136]. Prager et al. deployed the method to determine the stiffness of injured canine SC tissue and compared the results to collagen-made biomaterials. To do so, an acidic collagen solution in a culture medium with 1.25×10^6 encapsulated olfactory ensheathing cells per 100 µL was gelled by neutralization with NaOH. To allow for comparison with a conventional mechanical testing setup, results of the ultrasound elastography were compared with an indentation approach (Instron Universal Testing Machine 3367) on polyacrylamide hydrogels of known stiffness (8 – 80 kPa). The ultrasound method was performed using a Siemens Acuson S2000 and in a sample area of 5 × 5 mm the recorded shear wave velocities were transformed to respective Young's moduli. Dogs underwent decompression surgeries post-SCI and the disk material was partially removed and the ultrasound probe positioned above the site of SCI. The shear wave velocity of the ultrasound in the frontal plane from cranial to caudal was determined and the elasticity moduli were derived for Poisson's ratio $\nu = 0.5$. The biomaterial underwent the same examination after being immersed in PBS at 37 °C. The reference samples of known stiffness were about 40% stiffer in ultrasound elastography compared to their reference stiffness. However, when compared to elastic moduli, which were obtained from indentation experiments, no significant deviation was present. As it was also shown in Table 1, a canine cadaver control group obtained elastic moduli of 11.9 – 16.6 kPa, whilst intraoperative data from ultrasound elastography, that was recorded in the T2 – 3 SC section, revealed, that the stiffness of lesion site was significantly depressed compared to the surrounding SC. Hence, a median of 18.3 kPa in the lesion site, respectively 47.9 kPa in the surrounding

tissue demonstrated the variance in SC tissue elasticity in intraoperative dogs. Collagen hydrogels with the lowest pre-gelled concentration of collagen obtained elasticities of roughly 2 kPa, while the higher concentrated ones came in at 8 kPa. These values are generally in line with the results that the group found for the canine SC tissue and findings from other groups and other methods for different animal species. Cell viability of the olfactory ensheathing cells held up well inside the collagen biomaterial at 91% after 1 and 76% after three days. The encapsulation process itself increased the stiffness of the gels, as two hours after the cells were immersed into the gelling collagen sol, the elastic moduli were increased between 1.25 fold (lowest collagen concentration) and 1.73 fold (highest collagen concentration) [114]. Chitosan is a natural polysaccharide, that can be found in the exoskeleton of crustaceans and is a cationic copolymer, that consists of β(1-4)-connected D-glucosamine units and is obtained by deacetylation of chitin, which consists of β(1-4)-linked N-acetyl-D-glucosamine monomeric units. Chitosan and chitin can be utilized to develop different scaffold materials with different geometries and porous features. Although these kinds of biomaterials possess biocompatible and biodegradable features, their applicability in tissue engineering on their own is often limited due to their poor mechanical properties, which often necessitates the deployment of a cross-linking procedure or a utilization alongside other polymer types [137]–[139]. By adding chitosan to a collagen-based biomaterial, Sun et al. attempted to enhance the mechanical proficiency of collagen-based scaffolds. They derived collagen from bovine tendons, which they matched with an equal amount of chitosan. This mixture was subsequently bio-printed at 25 °C to form a scaffold, which was then freeze-dried. The structure obtained interconnected porous features in the 60 to 200 µm range and a volume porosity of 83.5% (v/v). The mechanical rigidity of the biomaterial was determined in a compression modulus test in an Instron 5865 device (0.1 kN load, sinusoidal loading at 5 Hz, 10% maximum strain). A reference chitosan/collagen biomaterial, which was merely freeze-dried, obtained a lower average compressive modulus of 2.67 MPa compared to the structured 3D bio-printed scaffold, which yielded 3.82 MPa. *In-vitro*, embryonic brain-derived NSCs showed a high degree of viability, as they spread well in the porous structures. In the adult rat SC, a T8 complete injury was inflicted and a freeze-dried or 3D bio-printed collagen/chitosan scaffold was inserted into the 2 mm void. Both biomaterial animal groups, besides two non-biomaterial-treated control groups, initially demonstrated the worst possible locomotion behavior (BBB 0). Between the groups, animals that obtained a 3D bio-printed scaffold not only obtained the highest degree of locomotion recovery after eight weeks (BBB ~7), compared to the freeze-dried scaffold group (BBB ~4) and the non-treated group (BBB- ~3), but also the most prolonged recovery, as the recovery in

the two latter groups already stagnated from week six to eight. Further, the 3D bio-printed chitosan/collagen matrix enabled a lesser degree of cavity formation inside the lesion site than the freeze-dried biomaterial class and even more so than the untreated group. In this instance, the stiffer 3D bio-printed performed better *in-vivo* than the softer freeze-dried analogs, but as the overall structures between those two were hardly comparable, the mechanical properties had unclear implications on the outlined SCI model in this case [140].

Fibrin is a protein, that is derived from fibrinogen, a natural blood-coagulation facilitating protein. In the presence of calcium ions and thrombin, fibrinogen is polymerizing into fibrin, which in itself can be broadly applied to medical applications, due to its biocompatibility, biodegradability, and bioactivity. Hence, Yao et al. fabricated fibrin biomaterials with an ordered hierarchical or a random fiber structuring in an electrospinning process. The mechanical properties of the spun matrices, which had performed well in prior *in-vitro* and PNS studies, were determined in AFM force-distance measurements with an approach speed of 3.0 µm/s and the elastic moduli were determined via the Hertz model. In the case of the hierarchically structured fibrin scaffolds, the biomaterial fibers were aligned with the caudal rostral orientation of the SC, while the randomly spun version was implanted in a random orientation in an incomplete rat SCI at the T9 level, which had been inflicted in the form of a 4 mm lesion. The randomly spun fibrin scaffolds obtained compression moduli of 0.36 kPa in AFM force-distance testing, while their hierarchically structured counterparts were significantly stiffer at 1.57 kPa. Two weeks post-surgery, the biomaterials were well integrated into the host's tissue, which infiltrated both types of biomaterials and replaced degrading fibrin structures, but a higher degree of host cell infiltration was present in the structured and mechanically stiffer scaffolds. In contrast to both biomaterial groups, non-biomaterial receiving animals demonstrated a severe degeneration of SC tissue and no signs of tissue regeneration, which persisted up until the 16-week mark. Further, after two and four weeks, the density of blood vessels within the respective scaffolds was significantly increased in aligned fibrin biomaterials compared to randomly structured and softer ones. A large number of neurons infiltrated the structured biomaterial in the orientation of the fibers, whereas infiltration occurred rather randomly in unstructured fibrin scaffolds. Four weeks post-implantation, an overall higher density of axons and a higher degree of anisotropic axon formation as well as myelination were present inside the structured, stiffer scaffolds. With regard to locomotion recovery in the animal specimens, the BBB scoring topped out at ~18 for specimens with the aligned scaffolds, at ~15 for animals with random fibrin biomaterials, and merely at ~13 in the untreated group after eight weeks. The designed

biomaterial of overall low elasticity performed well *in-vivo* and facilitated recovery in the SCI scenario, especially as anisotropic features were introduced [141]–[144].

A polyphenol-based scaffold biomaterial was proposed by Zhou et al., who gelled 0.15%, 0.6%, or 2.5% (w/w) tannic acid units with pyrrole in the presence of $FeCl_3$ as a catalyst, which promoted oxidative pyrrole polymerization, as well as ionic cross-linking of tannic acid units. The resulting porous structure obtained a large surface area and high swelling ratios of 2875 to 1960 (0.15 – 2.5% (w/w) tannic acid). Mechanical properties of the scaffolds were examined in a Physica MCR-301 rheometer in a 10 mm parallel plate setup with varying oscillation frequencies (0.1 – 10 Hz) and a maximum strain of 1%. The hydrogels with the lowest concentration (0.15% (w/w)) of tannic acid obtained the lowest storage modulus of 394 Pa, while samples of the highest tested concentration (2.5% (w/w)) yielded a modulus of 2260 Pa on average. NSCs, that had been seeded on all three tested hydrogels, exceeded 80% viability after seven days *in-vitro*. To examine the suitability of the material in an animal model, adult mice had an incomplete SCI inflicted at the T9 – 10 level. The partial 2 mm injury was patched with a 2.5 mm semi-tubular section of the biomaterial or not treated in a control group. Two weeks post-implantation, a reference pure polypyrrole biomaterial demonstrated poor compatibility as fibrous tissue amassed, which was not observable in the hydrogel-receiving instances. On top of that, the designed hydrogel allowed for longitudinal growth of nerve tissue and six weeks post-operation a reduced infiltration of macrophages into the lesion was present compared to the untreated control group, a sign, that the mechanically compatible biomaterial enabled a low inflammatory environment. The 0.6% (w/w) gels of medium stiffness (~800 Pa) provided the most favorable, least distinct fibrous cavity formation, however, this was explained due to an enhanced electrical conductivity of this biomaterial class, which ought to mimic the electrical conductivity of the SC and is known to facilitate NSC differentiation *in-vitro*. Further, endogenous NSCs successfully migrated into the hydrogel implants. The control group also demonstrated a much more pronounced glial scar formation. Initially, all animals demonstrated no right-hindlimb functionality (BBB 0), however, after six weeks, the hydrogel-treated specimens demonstrated a much better regeneration of motor skills (BBB ~15), compared to the control group (BBB ~6.5), due to an improved forepaw and hind paw coordination [145].

1.2.5.3 Biomaterials derived from Synthetic Polymers

Poly(ε-caprolactone) is a synthetic polymer, that is slowly biodegradable and is very easily malleable. Further, the polymer's mechanical properties can be altered to support a wide range of tissue engineering demands [146], [147]. Shahriari et al. fabricated porous scaffolds from a poly(ϵ-caprolactone) non-aqueous

solution with up to 70% (v/v) NaCl content. The NaCl particle size was adjusted by different degrees of ball-milling. The solvent of the solution was evaporated inside a copper wire (inner diameter Ø 200 µm) and the resulting smaller cylinders (Ø 260 µm) were assembled inside larger tubes (Ø 1800 µm), which had been formed around steel rods (Ø 1.6 mm). After immersing the structures in water, which removed the porogen NaCl, porous tubes with a variety of smaller porous microtubes inside of them remained. The introduction of varying amounts of NaCl resulted in varying porosity, which was directly correlated to the elasticity of the material. The elastic response of the biomaterials was determined by uniaxial tensile testing. The material was cut into rectangular pieces of 30 by 8 mm and the stress response was recorded while applying 0.2 mm/min of strain. The biomaterial with no added NaCl particles (0% (v/v) porosity) demonstrated an elastic modulus of 182 MPa, while the biomaterial with 70% (v/v) NaCl (particles of the smallest examined kind (17 µm)) (70% (v/v) porosity) was much softer, yielding an elastic modulus of 2.09 MPa. Scaffolds with porosities between 0 and 70% (v/v) showed a continuous decay of elastic modulus with rising NaCl content, in which the 70% (v/v) NaCl sample offered the lowest elastic modulus, whilst still providing mechanical integrity. Thus, these samples were also implanted in the transected rat SC at the T3 level. Compared to a control group, they facilitated the growth of axons much further into the lesion. No functional recovery experiments were performed [113]. Chen et al. proposed three different polymer scaffolds to approach rat SCI. A lactone-based scaffold was constructed by radically polymerizing poly(ϵ-caprolactone fumarate). Further, oligo (poly(ethylene glycol) fumarate) was radically polymerized under UV light, with an optional addition of a positively charged ammonium chloride compound, which ought to aid in neural cell attachment, SC migration, and axon remyelination [148]. Finally, a PLGA-based material was synthesized following the procedure described by Moore et al., as denoted below [149], [150]. All scaffolds were formed around seven parallel channels (Ø 660 µm), that introduced a capillary structure into the matrices. The scaffolds and a rat SC segment reference sample were cut into rods of roughly 8.5 mm in length and 2.5 mm in diameter and analyzed in a three-point bending dynamic analyzer (DMA 2980, TA Instruments). Disks, 2 mm in thickness, were prepared for stress-controlled (4 N/min) compression tests. For *in-vivo* tests, the scaffolds were consecutively loaded with cultured Schwann cells from rat sciatic nerves. Complete transection of the rodent SC at the T9 – 10 level arose 2 mm gaps, which were then patched with the respective biomaterial class, which remained in place until the animals were sacrificed one-month post-surgery. In flexing tests, the highest moduli by far were obtained for the PLGA sample with 66 MPa, followed by around 42 MPa for the caprolactone-based biomaterial, 8 MPa for the unmodified PEG-based

biomaterial, 2 MPa for the ammonium chloride-modified PEG-based biomaterial, and lastly about 0.7 MPa for the reference SC sample. Much lower moduli were measured in compressive mechanical testing, in which the caprolactone-based scaffold obtained 8.5 MPa, while the compressive moduli of the remaining four samples ranged between 0.1 and 0.3 MPa, with no significant differences between them. According to the authors, due to the high water content of the PEG-based biomaterial, its flexural and compressive modulus tended to be more in line with the native SC tissue. However, in this case, the measured flexural and compressive moduli of the SC reference samples clearly deviate from the aforementioned data, as showcased in Table 1. *In-vivo*, all scaffolds were seamlessly integrated into the caudal–rostral gap with no major cavity formation, except in the case of the PLGA scaffolds. In this case, a worse integration into the lesion site, potentially due to the higher flexing modulus of the PLGA biomaterial, was apparent. While all scaffolds supported axonal regeneration, the highest axonal counts by far were encountered in the ammonium chloride-modified PEG-based biomaterial, followed by its unmodified counterpart and the caprolactone scaffold. By far the lowest number of regenerating axons were present in the stiffer PLGA biomaterial. No significant difference in inflammation markers and BBB scoring after four weeks (BBB 4 – 5) was present among all scaffold types, despite the aforementioned axonal count difference and variance in mechanical properties [149].

Methacrylate-based polymers, like poly(2-hydroxyethyl methacrylate) (PHEMA), are very suitable for biomaterial applications due to their inertness in tissue engineering applications, which makes them a suitable constituent for contact lenses, hemoperfusion columns, wound dressings, and many more. To improve biocompatibility, tissue engineering with methacrylate-based materials often involves functionalization. For that cause, the functionalization with peptide structures, which mimic the structure of ECM molecules, like integrin, has shown to be suitable to aid the growth and proliferation of bone marrow-derived MSCs [30], [77]. Dalton et al. proposed one of the first methacrylate-based biomaterials for the use in nerve conduit applications. The group manufactured poly(2-hydroxyethyl methacrylate-co-methyl methacrylate) (PHEMA-MMA) hydrogel tubes in a liquid-liquid centrifugal casting process. In the process, different ratios of 2-hydroxyethyl methacrylate (HEMA), methyl methacrylate (MMA), and ethylene dimethacrylate (EDMA) were mixed with different amounts of water with an added redox- and thermal polymerization initiator and molded into tubes with an inner diameter of 2.4 mm. The polymerized tubes underwent mechanical properties determination after being immersed in water for one day. The elastic moduli of 20 mm long tubes were examined in a tensile test (Dynatek Dalta micro-mechanical tester)

at a strain rate of 0.5% per second. The transparent microporous hydrogels showed elastic moduli in the 25 – 400 kPa range, which the researchers deemed to be in the range of their SC target elasticity of 230 kPa. Surprisingly, the gels obtained higher elastic moduli, as the initial amount of monomers in the water-formulated monomer mixture was lower, as 25% (w/w) monomer content gels were stiffer than 30% (w/w) monomer ones. Further, the mechanical stiffness increased as the initial monomer mixture of HEMA and MMA was enriched in MMA, which yielded gels in the ~25 kPa (for both water/monomer ratios) realm for 1% (w/w) of MMA (99% (w/w) of HEMA) mixtures and on the other hand much stiffer scaffolds with ~270 kPa (30% (w/w) monomer/70% (w/w) water) and ~400 kPa (25% (w/w) monomer/75% (w/w) water) for 10% (w/w) MMA (90% (w/w) HEMA) formulations [151]. Belkas et al. utilized the approach of Dalton et al. to prepare PHEMA-MMA scaffolds for *in-vivo* experiments in the rat PNS. They cross-linked a mixture of 84% (w/w) HEMA and 16% (w/w) MMA with added EDMA by utilizing a redox initiator system. In the process, they molded the mixture inside cylindrical glass forms and obtained 12 mm long scaffolds with a porous inner surface and a more gel-like outer layer with an inner and outer diameter of 1.3 and 1.8 mm. Before *in-vivo* experiments, the sample's mechanical properties were measured in compressive straining tests (Dynatek Dalta micro-mechanical tester; incremental loads of 0.5, 1.0, 2.0, 3.0, 4.0, and 5.0 g). Unlike Dalton et al., who manufactured almost identical hydrogel samples, in this instance no clear mechanical properties were described, as the strain response of the material was only recorded in dependency of the applied weight (0.8 mm strain at the maximum load of 5 g). The scaffolds were equipped with type I collagen and implanted into an 8 mm lesion of the sciatic nerve in the rat PNS. It was found, over a 16-week timeframe, explanted tubes would show signs of collapse and their wall thickness would decrease, potentially indicating a mechanical weakening of the tube structure. Based on the biomaterial deformation *in-vivo*, the researchers concluded, that the amount of stress on the surrounding tissue would have increased from initially 0.6 g to 4.22 g in week 16 or that the biomaterial had weakened significantly, which was reasonable as the wall thickness had shrunk in the meantime [152]. Another PNS injury application was researched by Katayama et al., who also utilized Daltons PHEMA scaffold biomaterial [153]. A CNS application of the PHEMA-MMA biomaterial of Dalton and Belkas et al. was performed by Tsai et al., in which the biomaterial was deployed in a rat T8 SCI model. After radical polymerization of the monomers (HEMA, MMA) with an added peroxide compound, a tubular material of 3.6 mm in inner diameter was obtained, which was implanted in 4 mm lesions of completely transected rat SC for eight weeks. The tubes were produced with 11, 177, and 311 kPa in elasticity, which was examined

in tensile testing (1% strain/minute). The 11 kPa versions collapsed easily, which posed a significant challenge in handling and implantation, hence, no such hydrogels were implanted. The 177 kPa samples were spongy in nature, while the stiffest ones were more gel-like. In the 177 kPa hydrogel setups, CNS tissue bridging occurred in two out of two animals after eight weeks, while the same could be demonstrated for six out of seven rodents in the 311 kPa category. Despite lacking statistical significance in this instance, one could furthermore conclude, that more tissue regenerated through the 311 kPa biomaterial. In these stiffer samples, axons of different types bridged the entire lesion in higher numbers even without the deployment of any cell or trophic support, while predominantly running close to the hydrogel wall. Unfortunately, when compared to a transected control group of rodents with no biomaterial intervention, no statistically significant improvements could be recorded in locomotion testing. Although the materials were very high in stiffness, no signs of inflammation processes, due to a constant level of macrophages between the biomaterial and host tissue, could be detected [154]. In further studies, Tsai et al. combined the PHEMA-MMA tubes with different matrices and growth factors. PHEMA-MMA channels (Ø 3.4 mm) of 263 kPa elasticity were filled with collagen, fibrin, Matrigel™ (mixture of ECM proteins and growth factors), methylcellulose, or smaller PHEMA-MMA (Ø 1.2 mm) tubes. Optionally, collagen and fibrin matrices were provided with fibroblast growth factors and neurotrophin-3 trophic support. All inner matrices were injected in the biomaterial tube space post-implantation in a T8 rat SCI or before implantation in the case of the hierarchical biomaterial, that carried smaller PHEMA-MMA tubes inside. Axons formed inside the regenerating tissue in all added matrices, where the most rostral-caudal orientation of axons was found in the Matrigel™ supplemented hydrogel tubes, followed by methylcellulose-assisted, the hierarchical biomaterial, and the fibrin-equipped ones, while the collagen matrix-filled one came in last in this regard. However, the addition of the aforementioned growth factors to the collagen matrix yielded a higher number of rostral-caudal regenerating axons, elevating its recovering rostral-caudal axon density to that of the methylcellulose setup. Remarkably, locomotion testing for the fibrin and the hierarchical PHEMA-MMA biomaterial-treated specimens showed significant improvements compared to the matrix un-supplemented biomaterial and non-biomaterial-receiving control group after eight weeks [155]. In a similar approach, Hejcl et al. prepared porous hydrogels by radically polymerizing HEMA and EDMA around NaCl particles (Ø 50 – 90 µm), which acted as a porogen. The hydrogel scaffolds were implanted into a T9 rat SCI model immediately after SC transection or one week later. Histological evaluation of the explanted hydrogel biomaterial three months post-operation revealed an ingrowth of host SC tissue, with blood vessels,

neurofilaments, and Schwann cells being present. A significant increase in cyst volume formation was observable in the rodent group that was just treated with the biomaterial one week post-operation and especially in an untreated control group [156]. Later on, further research from the same group examined the histological incorporation of similar hydrogels, but with ammonium oxalate as a porogen and with prior peptide functionalization and cell seeding of the hydrogel. In a partially dissected rodent SC at the T9 level, the modified PHEMA scaffolds were introduced into the lesion site one week after transection. The amount of ethylene dimethacrylate was adjusted to obtain mechanically suitable hydrogels, which was not further specified, but due to the fact, that no cystic cavities could be observed over time *in-vivo*, the biomaterial had appeared adequate in that regard. Besides decent blood vessel infiltration of the biomaterial, no difference in axonal ingrowth could be determined between MSC-seeded and non-seeded hydrogels. In both cases, peripheral axonal growth was present, but hardly any axons crossed the biomaterial to its caudal side [157]. In another work, Cai et al. constructed functionalized hydrogel biomaterials by free-radical cryo-polymerization of PHEMA and methacrylated heparin with phenyl azide. To investigate the photo-immobilization of proteins, collagen was attached to the hydrogel scaffold under UV radiation in a photomask. Mechanical testing of the macroporous scaffolds was performed in compressive (100 N, 10 mm/min strain) and tensile (100 N, 0.5 mm/min strain) testing. The sponge-like scaffold network with pores in the 50 to 80 µm realm, exhibited elasticity values in line with results obtained for various SC tissue, as compressive moduli ranged between 2 and 3 kPa, irrespective of the amount of methacrylated heparin in the pre-gelled mixture. However, as the amount of the latter was increased from 0 to 10 mg/L, tensile moduli increased from 5 to 35 kPa. Scaffolds with an $E_{tensile}$ of 20 kPa and an $E_{compressive}$ of 2 kPa were transferred to 2 mm lesion gaps of a T9 – 11 rat SCI. The combination of the protein-functionalized scaffolds with fibroblast growth factors proved to a be suitable environment for the proliferation of NSCs. The combinatorial approach also showed the best outcome in BBB score testing in the rat SCI model after twelve weeks (BBB 10), followed by a solely collagen-functionalized biomaterial class (BBB 9). A non-treated SCI control group and a biomaterial group, that only received a non-functionalized and NSC-free biomaterial scaffold, performed much worse (BBB 3 – 4). Histological analysis revealed, that the two better-performing biomaterial groups in the BBB testing also demonstrated consistent neuron development throughout the whole scaffold dimension, where the developing neurons maintained an orientation similar to the native SC [30]. Kubinová et al. developed highly porous PHEMA hydrogels with pores in the 60 µm range by polymerizing HEMA and other methacrylates with a radical polymerization initiator. In a salt-

leaching process, the porous features were set up by ammonium oxalate fibers, which were later on removed by water washing. To fetch the mechanical properties of the methacrylate scaffolds, compressive testing was performed at 0.5 mm/min in PBS. The direction-dependent elastic moduli were obtained from the recorded stress-strain data in the 5 to 10% strain region. The structures obtained porosities of up to 76.5% (v/v) and specific surface areas of 49 to 82 m^2/g. The material exhibited higher elastic moduli parallel to the ammonium oxalate imprinted capillary structures, with a modulus of 11 kPa, compared to 45 kPa perpendicular to them, for the stiffest class of biomaterial samples. 27 and 4 kPa were found for a biomaterial class of medium stiffness and finally 6.7 and 2.9 kPa for even softer biomaterial specimens, respectively. To enhance the biomaterials viability for cell adhesion, oligopeptides were covalently attached to the polymer network and MSCs were seeded throughout the scaffolds in advance. Three different biomaterials of varying composition and mechanical properties within the ranges outlined above were transplanted into an incomplete transection of the rat SCI at the T8 level. Consecutively, the animals were sacrificed two weeks post-operation and a 3 cm long section of the rodent SC, including the biomaterial, was explanted and underwent histological assessment. In those, no fibrotic tissue could be identified in the proximity of the biomaterial. The two softer hydrogel classes trumped with regard to the integration to the host tissue, as in these cases, seamless host-biomaterial interfaces were present. Tissue debris and macrophage-filled cavities around the stiffest hydrogel class prevented a proper immersion in the host tissue. Tissue ingrowth into the hydrogels of lower elasticity was also improved compared to the stiffest one. However, the latter had shown the highest degree of axonal ingrowth, while the second stiffest followed closely in this regard, and the softest hydrogels performed the worst by a big margin. Going forward, the hydrogel of medium stiffness (27/4 kPa) was also incorporated in a complete transection model of the rodent SC. After two months, axons spanned the entire lesion, although they were few and far between at this point. No astrocyte infiltration could be recorded in both transection models after two months, but a sparse occurrence of these glial cells was present after six months in the complete SCI model [100]. Bakshi et al. developed a non-biodegradable hydrogel, as they polymerized PHEMA units by thermally induced radical polymerization, which they deployed as a biomaterial in combination with BDNF in an incomplete rat SCI cervical model. After preparing cylindrical sample bodies, which were immersed in PBS prior to measurement, the scaffold's compressive moduli were determined in compression tests in an Instron model 4422 at a change of strain of 50%/min. By tuning the water content of the cross-linking mixture between 60 and 90% (v/v), the moduli of the resulting scaffold structures could be controlled, as for the lowest water

content over 100 kPa and for 85 – 90% (v/v) of water 3 – 5 kPa were recorded. As this falls in line with SC elasticity data, gels with 85% (v/v) initial water content were deployed in *in-vivo* experiments. The biomaterials could be easily transferred to the lesion cavity and after four weeks only a very small degree of inflammation and scarring, in the form of astrocyte penetration into the biomaterial, was present. Further, at two weeks and especially four weeks post operation, blood vessels penetrated the entire PHEMA scaffold. A control group, which only provided a PHEMA biomaterial without any BDNF performed equally in preventing a pronounced inflammation response and scarring, while also supporting blood vessel integration. However, the control group without BDNF did not support axon growth, which was observable in the growth factor-treated group after one and two weeks [158]. Woerly et al. incorporated a poly(N-(2-hydroxypropyl) methacrylamide) (PHMPA) hydrogel, which was fabricated by radical polymerization, with porous features, which were facilitated by a solvent in the process, in a 2 mm T9 level lesion SCI in rats for up to 20 weeks. After di-vinyl cross-linking, the gels were examined for the diffusion of tetramethylammonium, swelling behavior, porosity, and specific surface area, as well as for mechanical properties. The latter were determined by dynamic small-amplitude rheological testing. The samples were cut into disks (Ø 1.5 mm, 1.3 mm thickness) and measured in a Bohlin-CVO rheometer with a gap of 1.1 mm at 37 °C. Initially, stress sweep tests were performed to gauge the viscoelastic stress limit of the samples and subsequently, in a constant stress amplitude frequency sweep, the viscoelastic response to frequencies ranging from 0.0016 – 16 Hz was examined. The gels demonstrated a predominant elastic behavior in rheometry measurements, as the elastic moduli of about 2.6 kPa exceeded the loss moduli by far ($G' \gg G''$). The complex moduli of rat brain tissue, which was recorded alongside, obtained similar results as the hydrogel. Upon a gap reduction in the rheometry instrument and therefore higher normal forces, the complex modulus increased, possibly due to a loss of network water. The rodents of this study suffered tetraplegia upon incomplete transection of the SC. The hydrogel biomaterials were well integrated into the host SC after five weeks *in-vivo* with no cyst formation in the adjacent tissue. In contrast to that, animals with SCI and no biomaterial intervention demonstrated cyst and scar tissue infiltration into the lesion site. After twelve weeks, axons, glial cells, and blood vessels penetrated the porous hydrogel from both sides. Remarkably, as soon as five weeks post-implantation, rodents treated with a biomaterial showed improved hind limb functionality compared to the control group with no intervention. The authors also concluded, that the implanted hydrogel induced minimal inflammation, as its stiffness roughly matched that of a reference rat brain sample [16], [76]. A similar *in-vivo* study was done by Pertici et al., which

deployed the Woerly et al. PHMPA hydrogel in an incomplete rat T10 injury. Although initially after one week, the biomaterial-treated group showed worse locomotion recovery (BBB 0.71) compared to an untreated group (BBB 3.3), the biomaterial-treated group improved its score substantially over the course of 14 weeks, as the respective rodent group on average obtained a significantly higher locomotion scoring (BBB 14.29), than the untreated group (BBB 8.66). Further, the biomaterial-assisted animal groups demonstrated an improved conservation of myelin rostral and caudal of the lesion site axons, which highlighted the neuroprotective capabilities of this kind of mechanically fine-tuned methacrylate biomaterial, as proposed by Woerly et al. [159].

Dumont et al. provided a PEG-based hydrogel scaffold, that exhibited aligned porous features. In a two-step polymerization process, PEG maleimide was first cross-linked with a peptide cross-linker to form microspheres (Ø 15 – 105 µm), which were subsequently photo-chemically cross-linked inside silicone or acrylate molds with tube features to obtain chemically cross-linked PEG-based tube and bridge structures. The tube structures underwent an additional third cross-linked step, as five tubes were interconnected by gelling them inside a fibrin solution. Besides imaging via SEM, the sample's compressive moduli were determined in a microsquisher (Cell Scale), that was equipped with a ~60 mm cantilever and a ~0.6 mm bearing as an indenter. 2 mm sections of tubes or bridges were implanted into a 2.25 mm incomplete injury in the mouse T9 – 10 SC. A control group received no biomaterial and the lesion site was merely covered with a gel patch. After one, two, and eight weeks animals of both groups were sacrificed. Both, bridges and tube structures demonstrated about 65% (v/v) of porosity and 80 to 85% (w/w) of water content (swelling ratios 5 – 7), but the bridge scaffolds yielded slightly smaller (Ø 150 µm) capillaries compared to the tube structures (Ø 250 µm). The compressive moduli of slabs of the PEG tubes and bridges, which were prepared as noted above, were 12.5 kPa. In a two-step cross-linking procedure the tube structures were assembled into a larger structure by a peptide- and photo-initiated cross-linking procedure, which yielded a tube scaffold structure of a much higher stiffness (129 kPa). The glial scar formation was much less pronounced in both biomaterial-treated specimens, as merely 124/127 µm of glial scar formation in bridges/tubes-treated animals compared to 337 µm in the untreated group was observed. Further, the axon ingrowth into the rostral and caudal border regions was more distinct in the case of the tube biomaterial groups, compared to the bridge ones. In turn, both biomaterials proved to be more viable in this regard and also with regard to the remyelination of axons than the control group setup. However, no significant difference in axon density in the center was present over all groups. Locomotion testing revealed, that animals with PEG

biomaterials showed better hindlimb functionality than the control group. To conclude, the two-step polymerization process of the biomaterial enabled the fine-tuning of spatial and porous features of a biomaterial, that demonstrated mechanical properties only partially in line with the SC (raw bridge structures). However, all biomaterials appeared to be well integrated and also demonstrated *in-vivo* prowess in the recovery from SCI [19].

PLGA is a copolymer and a synthetic polymer, whose degradation kinetics *in-vivo* can be fine-tuned by varying the ratio of its monomers, poly(lactic acid) and poly(glycolic acid). As it is approved by the U.S. Food and Drug Administration in PNS disease applications, rapid deployment of respective biomaterials in clinical trials is attainable. The group around Moore et al. demonstrated the proficiency of this biomaterial class in the context of SCI. A PLGA solution was injection molded and dried around 500 – 600 µm steel wires, yielding an anisotropic capillary structure with highly porous walls in-between. Upon varying the polymer concentration in the molding solution, the overall porosity (porosity of the capillary walls and capillary lumen combined) of the hydrogel was negatively correlated to it, ranging between 88% (v/v) for 30% (w/w) PLGA hydrogels and 78% (v/v) for 70% (w/w) gels, respectively. The scaffolds showed strong degradation, as a 70% (w/w) loss of biomaterial mass occurred between 20 and 32 weeks *in-vivo*. Chen et al. found a modulus of 66 MPa in dynamic three-point bending tests for a PLGA hydrogel, that was identical in composition, as it has been outlined above. A model drug, which was introduced in the polymer mixture before injection molding, showed a high degree of drug release in the first eight weeks of implantation, which then subsided in the remainder of the 32-week timeframe. Seeded Schwann cells densely populated the ~500 µm capillaries, which led to improved axon regeneration in the rat SCI compared to a non-cell-seeded biomaterial and another no-intervention control group, both of which showed very little regenerating axonal structures [160], [161]. An overview of all mentioned biomaterials, whose mechanical properties had been determined prior to deployment in an SCI model, is given below in Table 2.

Table 2: Biomaterial scaffolds, which were utilized in an SCI model and whose mechanical properties had been determined in the process.

category	scaffold type (fabrication; cross-linking; cells)	SCI model	elastic modulus	method of mechanical properties quantification	outcome of the *in-vivo* experiment	references
collagen	collagen + heparin sulfate scaffolds (Ø 3 mm); freeze-drying/bio-printing)	rat SCI T10; complete transection (~1.5 mm gap)	2.31 – 3.46 MPa	tensile testing (up to 0.1 kN and 10% strain)	• 3D-bioprinting of collagen with heparin sulfate yielded more rigid scaffolds (3.46 MPa), the best result in locomotor recovery, and axonal growth, compared to softer scaffolds without heparin sulfate (2.43 MPa) and freeze-dried collagen with heparin sulfate scaffolds (2.31 MPa) • best NSC proliferation in- and *ex-vivo* in 3-D bioprinted collagen with heparin scaffolds	Chen et al. [135]
collagen	collagen scaffold; olfactory ensheathing cells	canine SCI T2 – 3	2 – 8 kPa	ultrasound elastography	• olfactory ensheathing cells-equipped collagen gels showed elastic moduli in line with findings for SC tissue of other groups, but lower ones than for canine injured tissue and surrounding uninjured tissue of the same work	Prager et al. [114]
collagen	chitosan blended with collagen; bio-printing or freeze-drying (Ø 60 – 200 µm)	rat SCI T8	2.67 MPa (freeze-dried), 3.82 MPa (bio-printed)	compressive tensile testing	• NSCs spread evenly in the porous biomaterial (BM) • locomotor recovery in all BM-treated animals is superior to those without but even better inside stiffer bio-printed BMs	Sun et al. [140]

fibrin	fibrin fibers with hierarchical or unordered fiber structure	rat SCI T9	0.36 kPa (random fibers), 1.57 kPa (hierarchical fibers)	AFM micro-indentation	• both BMs integrated well into the host tissue but with better cell and blood vessel integration into the stiffer hierarchical BM • infiltration of neurons and myelination inside hierarchical BMs was more pronounced than in random ones and also a better locomotor recovery in hierarchical BMs	Yao et al. [141]
methacrylate	PHEMA-MMA tubes (Ø 3.6 mm); radical polymerization	rat SCI T8; complete transection (~4 mm gap)	11, 177, 311 kPa	tensile testing (strain 1%/minute)	• collapse of the softest hydrogel class • most regenerating tissue in the stiffest hydrogel class • no locomotor recovery in any BM	Tsai et al. [154]
methacrylate	PHEMA-MMA tubes (Ø 3.4 mm); radical polymerization; different matrices	rat SCI T8; complete transection (~4 mm gap)	263 kPa	tensile testing (strain 1%/minute)	• improved axonal regeneration and locomotion recovery compared to the non-matrix-assisted BMs • no implication of mechanical properties on the outcome	Tsai et al. [155]
methacrylate	PHMPA; di-vinyl cross-linker	rat SCI T9; incomplete transection (~2 mm lesion)	2.6 kPa	oscillatory shearing rheometry (frequency sweep 0.0016 – 16 Hz)	• the deployed hydrogel demonstrated viability in axon regrowth and locomotion improvements and a low inflammation response *in-vivo* • no direct impact of the BM's mechanical properties was implied	Woerly et al. [16]

methacrylate	PHMPA; di-vinyl cross-linker	rat SCI T10	2.6 kPa	oscillatory shearing rheometry (frequency sweep 0.0016 – 16 Hz)	• better locomotion recovery after 14 weeks *in-vivo* and improved preservation of myelination rostral and caudal to the BM compared to an untreated SCI group	Pertici et al. [159]
methacrylate	PHEMA; cryo-polymerization; methacrylated collagen, phenyl azide; optionally added collagen and NSCs	rat SCI T9 – 11; complete transection (~2 mm lesion)	20 kPa (tensile testing), 2 kPa (compressive testing)	tensile testing (100 N, strain 10 mm/min) of rectangular scaffold samples; compression, and cyclic compression tests (100 N, 0.5 mm/min) with cylindrical samples	• a combination of the scaffold and NSCs showed the best outcome in locomotion testing in rodents after twelve weeks (BBB 10), followed by a non-NSC and only collagen-equipped scaffold (BBB 9), and lastly, a pure BM receiving group, which scored equal to a non-treated control group (BBB 3-4) • best neuron development inside the first two groups	Cai et al. [30]

methacrylate	HEMA and other methacrylates; radical polymerization; salt leaching of NaCl; oligopeptides + MSCs	rat SCI T8; incomplete transection (~2 mm lesion); complete transection	45/11 kPa, 27/4 kPa, 7/3 kPa (parallel/perpendicular to pore structure)	compressive testing (strain 0.5 mm/min)	• incomplete transection: better host integration for the two softer BM classes as fewer cavities at the host-BM interface were present; best tissue ingrowth into the softest BM class, however, the best axonal ingrowth was observed for the stiffest class • complete transection: the 27/4 kPa hydrogel had few axons spanning the entire BM after 2 months and also glial cell infiltration after six months	Kubinová et al. [100]
methacrylate	PHEMA; radical polymerization; BDNF support	cervical rat SCI; incomplete transection	3 – 5 kPa	compressive testing (strain 50%/min)	• BM caused a muted inflammation response and proper blood vessel formation and axonal regeneration occurred inside it after four weeks	Bakshi et al. [158]
lactone	porous polycaprolactone tubes (Ø 260/1800 µm)	rat SCI T3; complete transection	2.09 – 182 MPa	tensile testing (strain 0.2 mm/min)	• no distinction between different mechanical classes • 0.5 mm ingrowth in T3 lesion inside the softest 2.09 MPa BM	Shariari et al. [113]

lactone	poly(ϵ-caprolactone fumarate) scaffold with seven channels (Ø 660 µm); radical polymerization	rat SCI T9 – 10; complete transection (~2 mm lesion)	42 MPa (bending modulus), 8.5 MPa (compression testing)	three-point mechanical bending; stress-controlled compression testing (4 N/min)	• the bending and compressive moduli obtained for the PEG-based BMs were more in line with the results obtained for the SC tissue than the other two • PLGA-based BMs got integrated worse into the host tissue • the highest density of regenerating axons was determined in the ammonium chloride-modified PEG-based scaffold, while the worst performing BM in that regard was PLGA • no difference in BBB scoring between all BM classes was present after four weeks of BM intervention	Chen et al. [149]
PEG	oligo(poly(ethylene glycol) fumarate) scaffold with seven channels (Ø 660 µm); radical polymerization	rat SCI T9 – 10; complete transection (~2 mm lesion)	unmodified: 8 MPa (bending modulus), < 1 MPa (compression testing); ammonium chloride modified: 2 MPa (bending modulus), < 1 MPa (compression testing)			
PLGA	PLGA scaffold with seven channels (Ø 660 µm); injection molding	rat SCI T9 – 10; complete transection (~2 mm lesion)	0.7 MPa (bending modulus); < 1 MPa (compression testing)			

PEG	PEG tube and bridge structures; peptide cross-linker + photo-initiated cross-linking	rat SCI T9 – 10	12.5 – 1588 kPa	microsquisher	• both BM classes (bridges/assembled tubes) lead to less glial scar formation than was present in an untreated control group • better axon ingrowth into the assembled tubular structures than into the softer bridge structure • all BM treated animals demonstrated less glial scar formation and better locomotion recovery than untreated ones	Dumont et al. [19]
polyphenol	tannic acid gel; oxidative pyrrole polymerization	mouse T9 SCI	394 – 2260 Pa	rheometer	• seeded NSC exceeded 80% viability after seven days *in-vitro* • compared to a reference BM, the hydrogel caused less formation of fibrous tissue and glial scar *in-vivo*; • the gel allowed for longitudinal growth of nerve tissue and facilitated less infiltration of macrophages into the lesion void • gels of medium stiffness (~800 Pa) provided the most favorable environment • locomotion recovery more pronounced in hydrogel-receiving mice	Zhou et al. [145]

1.3 Viscoelasticity of Hydrogel Samples

When a material is subject to an outer force, the material itself can translate or rotate, therefore, all the smaller constituents move in unison. If they are not, the material is forced to undergo deformation, in which a variety of different models can be deployed to understand the response of any material to deformation-arising effects.

1.3.1 Ideal Solids and Liquids

In an ideal elastic material, a uniaxial tensile force F is acting on a uniform surface area A and stretches the material of length L over the distance ΔL, which is depicted in Figure 2.

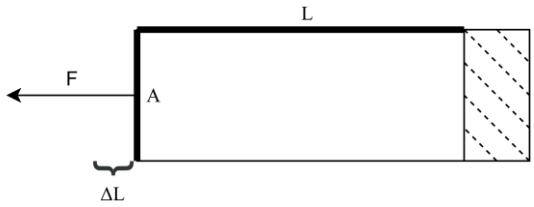

Figure 2: Tensile stressing of an ideal elastic material with force F, which is acting on the surface area A and strains the material in the dimension L by ΔL; the dashed lines symbolize the fixation point of the sample.

In this instance, the degree of deformation ε is given as a ratio of the change in length ΔL and the total length L, as outlined by Eq. 1.

$$\varepsilon = \frac{\Delta L}{L} \tag{1}$$

Consequently, given ideal solid behavior, the applied force F on the surface area A directly correlates with the degree of deformation ε through the elastic modulus or Young's Modulus E, which is a measure of a material's ability to build up a resisting stress in for a given amount of relative deformation and is a material- and temperature-dependent factor, all of which is incorporated in Eq. 2.

$$F = E\, A\, \varepsilon \tag{2}$$

Young's modulus E can also gauge a material's build-up in compression stress for various compression strains, as the force F is oriented oppositely as portrayed in Figure 2. In any case, if the force F is uniformly applied to the surface area A, the stress σ can replace the force F, which yields Hooke's law according to Eq. 3.

$$\sigma = E\, \epsilon \tag{3}$$

As a stress is enacted on a cuboid body, not only does the material's dimension change in the same direction as the stressor's but also in directions perpendicular to it. The Poisson's ratio ν defines the ratio of strain, which occurs perpendicular to the direction of stress, to the strain in the stress direction.

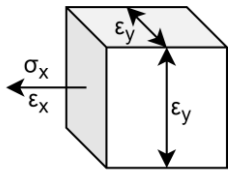

Figure 3: Stress σ_x enacted on a cubic solid material yields not only deformation in the stressor's direction but also perpendicular to it, which results in the strain ε_y.

In the example from Figure 3, where a uniform stress acts uniformly on a surface of a solid tube, the Poisson's ratio can be calculated according to Eq. 4.

$$\nu = -\frac{\varepsilon_y}{\varepsilon_x} \tag{4}$$

Hereby, the strain ε_x is oriented parallel to the stress σ_x, whilst ε_y represents the relative strain in perpendicular orientations. Incompressible materials exhibit a Poisson's ratio of ~0.5 and their overall volume remains constant as they experience stretching or compression. If a material undergoes shearing instead of tensile stress, like in Figure 4, a shearing deformation is occurring.

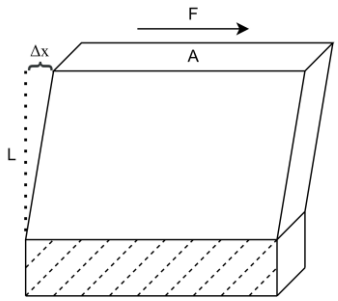

Figure 4: Shear deformation of an ideal elastic material with force F, which is acting on the surface area A and strains the material perpendicular to the dimension L by Δx; the dashed lines symbolize the fixation point of the sample.

The shearing modulus G of a material can be determined as a function of the acting force F, the area A and the deformation Δx and the material dimension L and relates to the modulus of elasticity or Young's modulus E and the Poisson's ratio ν according to Eq. 5.

$$G = \frac{\frac{F}{A}}{\frac{\Delta x}{L}} = \frac{E}{2(1+\nu)} \tag{5}$$

The Equation can be narrowed down to Eq. 6 if one assumes ν = 0.5 for an incompressible material.

$$G = \frac{E}{3} \tag{6}$$

Such an incompressible material would demonstrate an infinitely high bulk modulus K. Ordinary deformation experiments involve a change of material shape and size. On the other hand, the bulk modulus describes the material's response to isotropic stress. The material would then change in size, however, the shape itself would be unaltered. By leveraging Poisson's ratio ν, the elastic or Young's modulus E compares to the bulk modulus K according to Eq. 7.

$$K = \frac{E}{3(1-2v)} \tag{7}$$

Experimental data on ideal liquids, which can be approximated by low molecular weight liquid compounds, can be obtained from shearing experiments. To do so, the liquid can be sheared between a variety of plate–plate geometries. For instance, as an ideal liquid is exposed to a laminar shear between a stationary lower plate and a moving upper plate with area A, the outer force F is equal to the frictional forces between adjacent parallel layers of fluid. With regard to the acting stress σ, one obtains Eq. 8.

$$\sigma = \frac{F}{A} = \eta\,\dot{\varepsilon} = \eta\frac{\mathrm{v}_{upper\ plate}}{d} \tag{8}$$

Here, the deformation variable is the shear rate $\dot{\varepsilon}$, which is defined as the gradient in velocity between the moving upper plate with mean velocity v and the stationary lower plate over the distance d in-between plate geometries, which is schematically depicted in Figure 5.

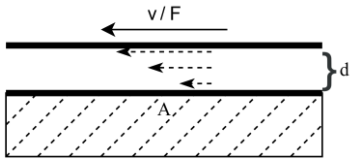

Figure 5: Liquid, which is sheared between two parallel plates, with the gap d in-between; the upper plate is sheared by the force F with the velocity v over the stationary plate of area A and a gradient in fluid velocity gets established between the moving and the stationary plate.

The variable η is the dynamic viscosity of the liquid medium, which, for ideal liquids, is temperature dependent, but indifferent to the rate of shearing. Viscosity is a size to measure the amount of energy, that is dissipated between the moving and the stationary plate, as a higher degree of energy dissipation is present for more viscous compounds. The mechanical responses of homogeneous and isotropic ideal elastic solids

and ideal liquids, respectively their mechanical parameters are indifferent to varying measurement setups, strain rate or strain velocity, or shape or form of the material itself [162]–[164].

1.3.2 Elasticity of Polymer Networks

Hydrogels can be classified as viscoelastic materials, hence, fluid-like or viscous properties due to the bound water, as well as purely elastic properties due to the polymer framework around it, can be attributed to them. Mechanical properties of polymer systems are usually determined via uniaxial tensile or shearing experiments. In doing so, the polymer in the hydrogel resists applied outer stresses while being deflected or strained accordingly. However, different patterns of strain response are distinguished, as materials can demonstrate affine or non-affine/phantom nature. In the case of affine deformation, the material is uniformly deformed on a network strand level by the applied force. On the other hand, non-uniform deformation on a lower scale is occurring in non-affine/phantom three-dimensional hydrogel structures. The principle is depicted in Figure 6. In this instance, only in affine deformation, the deformation on the microscale level is directed in the same direction as the macroscopic deformation and scales according to the vertical position in the sample z [90], [164, p. 66], [165].

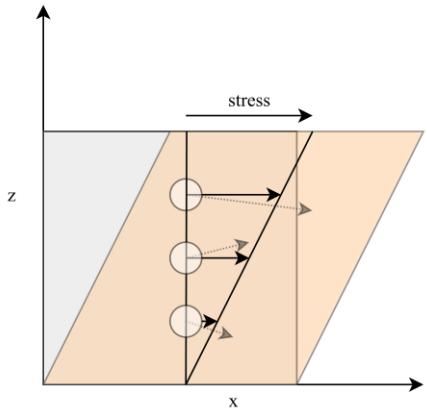

Figure 6: Schematic sketch of an unstrained elastic square sample (gray square) and the resulting strained sample (orange square) after a uniform shear stress was applied parallel to the upper sample surface; the affine microscale deformation of the sample spot (circle) is portrayed as non-dashed arrows, the non-affine/phantom deformations are demonstrated by the dashed arrows [90].

In practice, the distinction between affine and phantom networks is difficult, as sample heterogeneities, that stem from non-uniform cross-linking and chain entanglement, hinder the validation of the respective models [90], [165]. The mechanical response of hydrogels can be approximated by the ideal rubber elasticity model. In low-strain paradigms, perfect rubber-elastic materials are capable of instantaneous extension, even under low mechanical stresses. Furthermore, they are always able to return to their original-pre strain state after small deformations. In other words, elastic stretching from the unstrained to the low-strained

state solely relies on configurational entropy changes – never on changes in the total internal energy. Therefore, the work, that is applied by an outer force, is equal to the emission of heat from the perfect rubber-elastic material or the change of conformational entropy, as polymer chain entropy is diminished, due to the straightening of the individual polymer chains. Therefore, the deformation work dW between the stretched and un-stretched rubber material at a constant temperature T is given by Eq. 9 [162], [166].

$$dW_{deformation} = -dQ_{straining} = -\frac{dS_{polymer\ conformation}}{T} \tag{9}$$

To ensure this reversible and instantaneous deformation process, the polymer chains ought to be mobile, whilst exhibiting small and constant intermolecular interactions during deformation. In the molecular kink paradigm, a model to predict stress-strain behavior in rubber elasticity, one assumes, that stressed rubber polymer chains with kinks are arranged in tubes, which confine the overall polymer conformation and pose an energetic threshold to complete chain straightening. Then, as a stress is applied, the material's initial strain response is rather Hookean, therefore, the extension of the material scales with the applied stress. In this part of the deformation, the elastic limit of the model has not been exceeded and upon relief of the outer force, the material ought to return to its pre-strained state like an ideal solid, which is indicated by the blue arrow in Figure 7. In the molecular kink model, a simultaneous entropic extension of all polymer kinks within their confined tubular arrangement in this section (I) of Figure 7 is assumed. However, during further deformation, approximately in the region of 1 to 600% deformation, the stress-strain relationship becomes non-linear. In the molecular kink paradigm model, this is explained by a distortion of the tube around the polymer chain, which in essence symbolizes, that the polymer conformation is permanently changing distinctly to a straighter one, which is depicted as region II in Figure 7. Hereby, the elastic limit of the rubber material is exceeded and permanent deformation or hysteresis even after the outer force subsides is the consequence, which is schematically indicated by the red arrow. Lastly, in section III of the stress-strain curve, the polymer chain reaches its taut state or contour length, in which the chain is completely straightened. Through an extension of bond angles or molecular bond lengthening, further extension of up to 40% beyond the contour length is possible, but ultimately covalent bond failure of the polymer is looming [162], [167], [168].

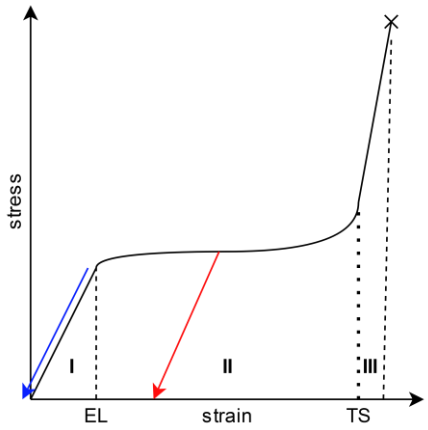

Figure 7: Stress-strain response of an elastic rubber with an initial Hookean behavior (I) until the elastic limit (EL), followed by non-linear elastic deformation (II), and lastly the fastest rise of stress in relation to strain (III) after the polymer chains exceed their taut state (TS) and break down (×); complete reversion of strain after the stressor is removed (blue arrow) and hysteresis after relaxation from the non-elastic realm (red arrow).

Less ductile, more brittle polymer networks, like polystyrene, often exhibit more metal-like stress-strain behavior, as they exhibit a steeper stress build-up, with an abrupt material failure around the elastic limit. Less brittle materials, like semi-ductile poly(methyl methacrylate) and ductile polycarbonates, demonstrate stress failure in the non-linear section of their stress-strain response curve as outlined in Figure 8. Just like rubber materials, ductile materials may exhibit permanent deformation, if the stress is relieved after a certain point, which is not necessarily the elastic limit, but after exceeding the yield point, which can be closer to the elastic limit, but also further out in the non-elastic section of the stress-strain curve. [164, pp. 25, 66].

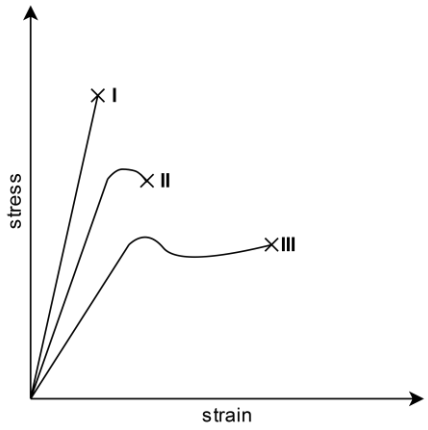

Figure 8: Stress-strain response for brittle (I), semi-ductile (II), and ductile materials (III) up until their failure point (×) [164, p. 67].

As apparent in the rubber elasticity model, basic ideal solid and ideal liquid models do not suffice to accurately track the stress-strain response of real elastomer materials. Especially, when assessing polymer

plastics, such as biomaterials, that display viscoelastic behavior, one has to apply more sophisticated models to accurately track differences in mechanical properties.

1.3.3 Linear Viscoelasticity

Ideal elastic solids and liquids are merely models, which can only be approximated by metals, respectively, low molecular weight liquids. Polymers on the other hand, always demonstrate characteristics of fluids and solids, therefore, exhibit viscoelastic behavior under different temperature regimes. They show partial structural memory, thus exhibiting time-dependent behavior. In other words, materials that obey linear viscoelasticity, show a proportionate strain response to an array of superpositioned stresses, which can be regarded as consecutive intervals of varying stress degrees, where the effects of the following stressor only partially add to the effects of the prior stressor. Ideal liquids show no structural memory of prior deformation processes, as those effects immediately dissipate after the stress subsides due to molecular rearrangement, which happens irrespective of the rate of prior deformation. On the other hand, ideal solids maintain the effects of strains or stresses of the past, therefore, they are high in structural memory and future stresses/strains add to the effects of prior stresses/strains at any time in the future. Stress relaxation experiments can gauge the viscoelasticity of a system by applying a quasi-static tensile or compression strain and subsequently monitor the stress response of said material. Figure 9 shows the stress relaxation response of an ideal solid (II) and an ideal liquid (III) after an initial strain ε_0 (I), which was kept constant during the time t of the experiment, was applied. The ideal solid shows no stress relaxation, the ideal liquid system, however, dissipates all stress immediately after an initial stress σ_0 [162], [164, p. 75].

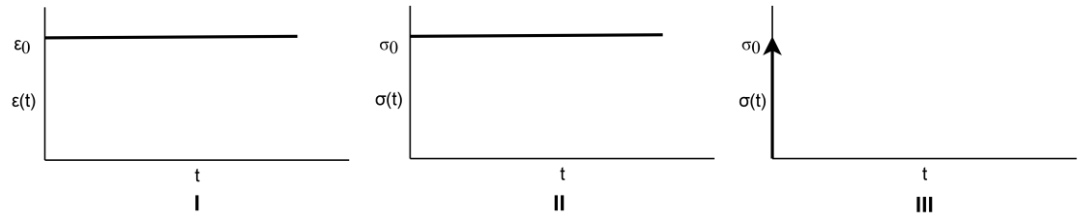

Figure 9: Stress relaxation after an initial strain ε_0 (I) was applied and maintained on an ideal elastic solid (II) or an ideal liquid (III) [162].

In reality, no such distinct discrepancies between ideal elastic solid and ideal liquid properties can be identified for any material. This is due to the fact, that every material shows stress relaxation of prior deformations, where the distinction between any non-ideal solid and non-ideal liquid behavior is vague, as the timeframe of observation is of importance in this regard. Thus, almost ideal solids can appear to be viscous under really extended observation periods, while almost ideal liquids may showcase partially elastic

behavior for much shorter observation frames. Hence, one can gauge the Deborah number N_D, which is defined according to Eq. 10.

$$N_D = \frac{\tau}{\tau_{exp}} \tag{10}$$

Here, τ is the time, that an applied stress takes to relax to a certain level, for instance, to reach the level of $\frac{1}{e}$ of the initial stress σ_0. τ_{exp} represents the duration of the experiment. For materials, that are viscoelastic in the timeframe of the experiment, one assumes the Deborah number to be in the realm of $N_D = 1$. $N_D \approx 0$ can be estimated for ordinary liquids and $N_D \rightarrow \infty$ for real solids. Figure 10, shows the stress σ(t) decay for a real solid (II), which takes a long time to relax an initial stress σ_0 to $\frac{1}{e}\sigma_0$ and until an equilibrium state σ_∞ is obtained. A corresponding stress decay after an initial strain ε_0 (I), which raises the stress σ_0 on an ordinary liquid (III), occurs within a much shorter period, thus, yielding a much lower relaxation time τ and eventually dissipating all the present stress [162].

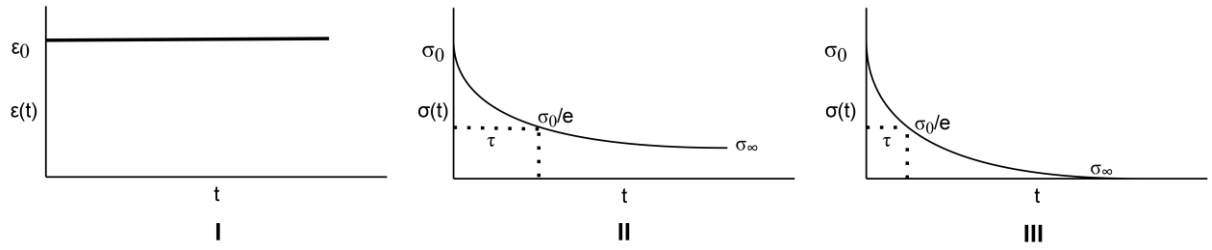

Figure 10: Stress relaxation after an initial strain ε_0 (I) was applied and maintained on an ordinary elastic solid (II) or an ordinary liquid (III); the dashed lines point out τ at 1/e levels of the initial stress values σ_0 [162], [164].

Polymeric systems can respond to mechanical perturbations by a fast rearrangement of more flexible polymer strands or the much slower disentanglement of polymer chains. Due to the inhomogeneity of real polymer networks, their relaxation response is also inhomogeneous on the molecular level. Besides stress relaxation, one can also monitor the strain development, as a constant shear stress σ(t) is applied and maintained on a material. As showcased in Figure 11, one can also strictly distinguish ideal solid (II) or viscous (III) tendencies in a creep experiment.

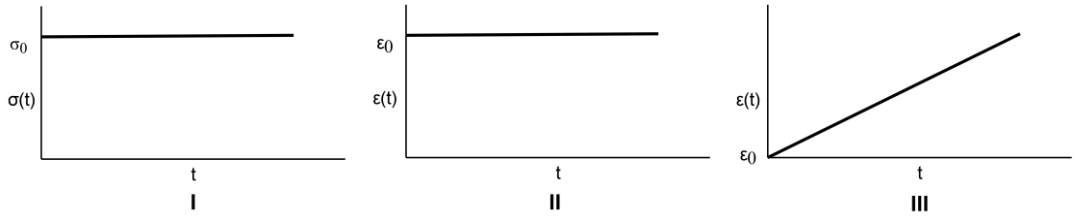

Figure 11: Creep experiment with a maintained stress σ_0 (I) and the strain response of an ideal elastic solid (II) or an ideal liquid (III) [162].

A perfect elastic solid reacts to a constant stress σ_0 with an instant and constant deformation or strain ε_0, which scales according to Hooke's law in Eq. 3. Contrarily, an ideal liquid slowly creeps, thus permanently builds up creep-strain during a constantly applied stress.

$$\varepsilon(t) = \frac{\sigma}{\eta} t \tag{11}$$

According to Eq. 11, ideal liquids exhibit time-dependent creep, which scales with the ratio of the applied stress σ and the inherent dynamic viscosity η of the compound. In the realm of rather solid or rather viscous ordinary materials, which is represented by viscoelastic materials, deviation from this ideal behavior is once again observable.

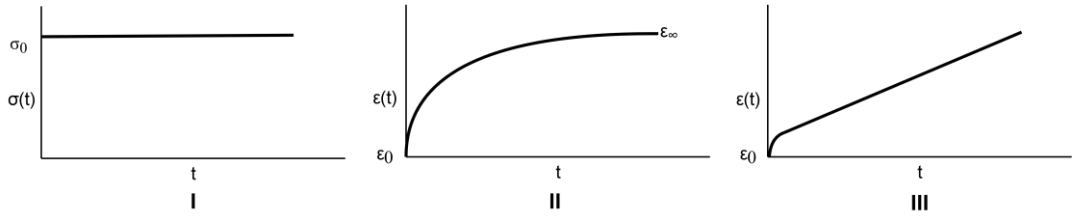

Figure 12: Creep experiment with a maintained stress σ_0 (I) and the strain response of a real elastic solid (II) and a real liquid (III) [162], [164].

As noticeable in Figure 12, the line between real solids and real liquids in creep experiments can be drawn, as the strain in real or ordinary solids converges to a strain-value ε_∞ (II), while after an initial non-linear relationship, the strain nearly linearly increases with time for real liquids (III) [162]. In both systems, as the stress is suddenly disrupted, an initially elastic recovery, followed by a non-elastic recovery sequence, recovers only parts of the built-up strain, which is depicted in Figure 13. If the viscoelastic material has more solid characteristics, the initial elastic recovery is more distinct than the non-elastic part and vice versa for rather liquid viscoelastic materials.

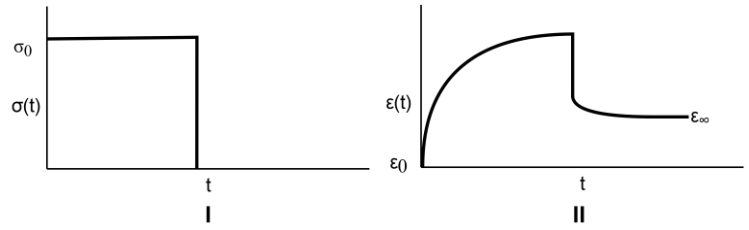

Figure 13: Creep experiment with a stress σ, which is eventually relieved (I); the strain initially recovers elastically, followed by a non-elastic section until a permanent strain ε_∞ materializes (II) [162], [164].

The permanent deformation from a creep experiment also becomes apparent in cyclic stress relaxation experiments. As demonstrated in Figure 14, after each strain build-up and subsequent release, the material maintains more strain and also does not build up as much stress in the following straining cycles, as the material permanently adjusts to the constraints of the applied strain [162], [169]–[171].

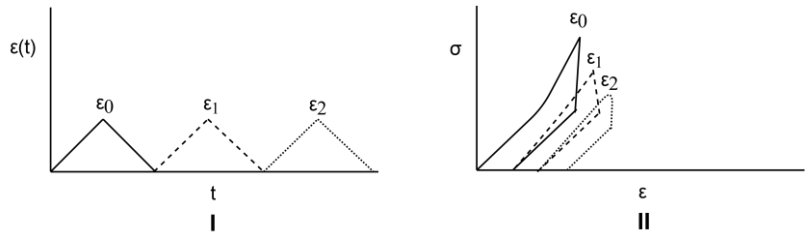

Figure 14: Cyclic stress relaxation experiment; after each strain cycle (ε_1, ε_2, ε_3,…) the sample does not return to its pre-strained state and the total accumulated stress in each subsequent cycle becomes less [162], [164].

1.3.4 Linear Viscoelastic Models

The complex viscoelastic response of polymers in stress relaxation and creep experiments can be modeled by combining the stress-strain responses of Hookean springs with those of linear viscous dampers in a variety of virtual rheological models. The schematic setup of such a linear elastic spring and a viscous dashpot is outlined in Figure 15.

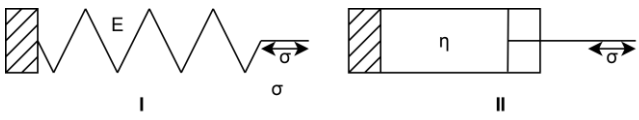

Figure 15: Schematic setup of an elastic spring (I) and a linear viscous damper (II), where a stress σ causes deformation in the elastic spring of elasticity E or flow in the medium of viscosity η [164, p. 84], [169].

The elastic deformation of the Hookean spring yields a strain ε at a given stress σ, like in an ideal solid of elasticity E, according to Eq. 3. The fluid of viscosity η in the linear viscous damper also exhibits ideal linear behavior, as its stress-strain response follows that of an ideal liquid in the context of Eq. 8. In order to

describe a real viscoelastic system with these two idealized models, one can combine them in the simplest linear viscoelastic model, the Maxwell model, which is delineated in Figure 16.

Figure 16: Maxwell model with an ideal Hookean spring with elastic modulus E in series with an ideal viscous damper with a fluid of viscosity η [169], [172].

The stress-relaxation response of this serial setup of an ideal viscous damper and a Hookean spring is similar to that of a real liquid, which was depicted in Figure 10 (III). Initially, as the strain is enacted, the entire strain is immediately built up in the spring component of the setup. This causes an immediate stress σ_0 in the Maxwell element. The stress relaxes, as the initially unaffected viscous damper gradually builds up strain, which in turn relieves strain from the spring component and stress of the whole series setup as shown in Figure 17 (I). As shown in Figure 17 (II), in a creep experiment, the applied stress initially only strains the spring component of the Maxwell element to ε_0, however, no relaxation of the spring occurs and the continuing stressor results in a creep of the whole element, as the viscous damper starts to creep like an ideal fluid. The Maxwell element vaguely describes the stress relaxation response of real viscoelastic materials, however, it completely fails to account for the real creep response. This is due to the fact, that, whilst being exposed to a certain stress level, the strain does not reach a steady state, as the sample creeps to infinity. This may only be accurate for materials like Silly Putty or warm tar, but not for polymer systems that exhibit chain entanglements and other forms of junctions [173]. Furthermore, the model lacks a course of non-elastic recovery upon stress cancellation, as only the remaining strain in the spring element is recovered, but the viscous damper has no way to undo its past deformation, similar to the creep response outlined in Figure 13, where the non-linear section before the steady-state strain state would not be recoverable in this model at all [164, p. 85], [169, p. 295], [172]–[174].

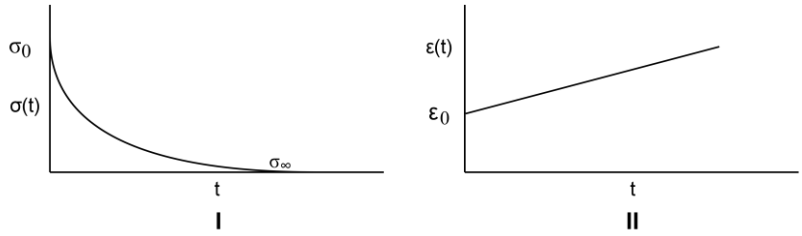

Figure 17: Stress relaxation (I) and creep experiment (II) of a Maxwell element after a strain ε_0 (I) or a stress σ_0 (II) was applied infinitely [164, p. 89].

In a stress relaxation experiment, based on Appendix A, the rate of force decay of the Maxwell element can be tuned by varying the model parameters η and E, which can demonstrate a variety of exponential stress decay responses, within the boundaries outlined above. To circumvent those, more proficient linear viscoelastic models are desired. Better models to reproduce stress relaxation and creep behavior in real viscoelastic samples are the Linear Kelvin-Voigt model, the standard linear solid (SLS) model, and the Wiechert model, which are outlined in Figure 18.

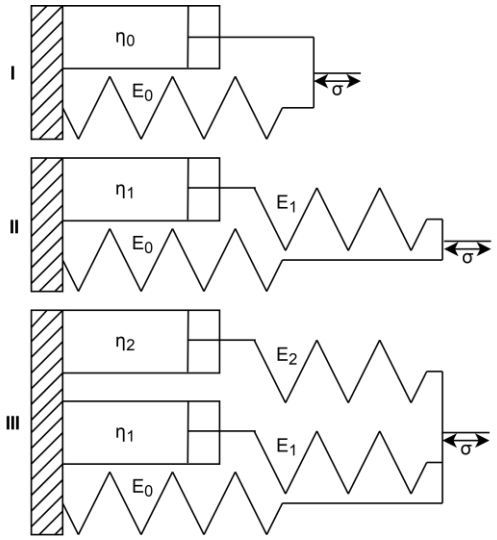

Figure 18: Kelvin-Voigt model (I), SLS model (II), and Wiechert model with two Maxwell elements (III), which are constituted of one or more linear elastic springs of elasticity E_x and linear viscous dampers with the liquid of viscosity η_x [169], [173], [174].

Contrary to the Maxwell element, the viscoelastic material in the Kelvin-Voight model can completely recover from prior strains due to the parallel spring and damper setup. However, the model fails to accurately track stress-relaxation behavior, as it has no way to rapidly build up strain through the viscous damper element, due to its laggard manner and it always diminishes all of the present stress or force, which is not typical for ordinary viscoelastic materials, which tend to show hysteresis, as outlined prior in Figure 14. On the other hand, the SLS model, which is also depicted in Figure 18, can account for abrupt initial deformation and does not relax all the present stress, as the viscous damper itself is interconnected with a separate elastic spring in a Maxwell series, that is in parallel with a second elastic spring. Therefore, it can recreate the stress-strain response during creep and stress relaxation experiments in real viscoelastic materials more accurately. The sole downfall in the case of the SLS model is the single combination of a viscous damper with an elastic spring, that interact with each other in the framework of a single Maxwell element, where the ratio of the imaginary damper viscosity and the elasticity of the spring stipulate the relaxation time of the whole system, according to Appendix A. To accommodate for less ideal exponential

force decay behavior, which is present in polymer networks of non-uniform size distribution, where smaller molecular arrangements tend to relax quicker than larger ones, one can introduce two or more total Maxwell elements in the SLS model, which is then called Wiechert model [169], [174].

1.3.5 Dynamic Viscoelasticity

When studying viscoelastic behavior, linear viscoelastic models tend to be more precise for longer experiment timeframes. On the other hand, dynamic examination of the stress-strain response allows for very high rates of loading, thus, keeping the material loading intervals in the μs to ms range. In a dynamic sinusoidal stressing setup, for example in a parallel plate rheometer setup, with a circular frequency ω, the strain follows in a similar oscillation manner, but usually with a shift in phase δ, as outlined in Figure 19.

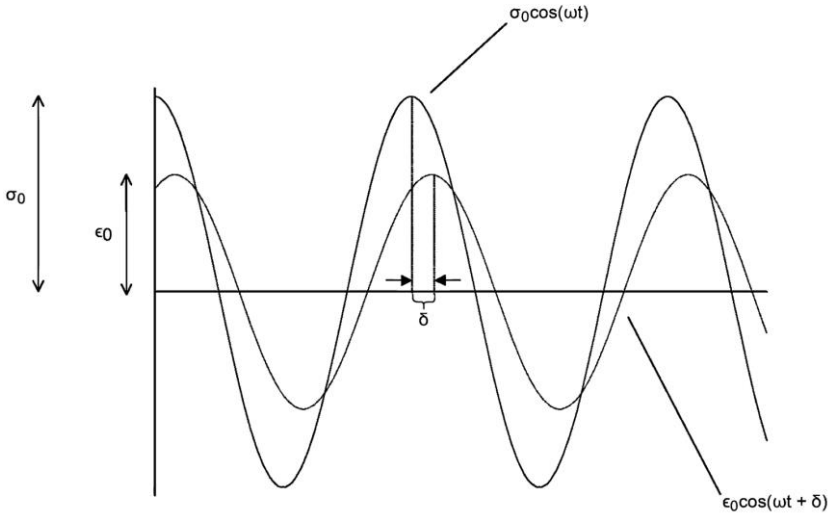

Figure 19: Development of stress and strain of a viscoelastic material in an oscillatory shearing experiment, in which the strain lags behind the imposed stress by the phase shift δ.

The experiment can either take place in a sinusoidal strain- or stress-controlled environment. Respectively, the time-dependent stress σ(t) or strain ε(t) can be expressed as a function of the circular frequency ω and a maximum of stress σ_0 or strain ε_0, according to Eq. 12.

$$\varepsilon(t) = \varepsilon_0 * \cos(\omega t)$$
$$\sigma(t) = \sigma_0 * \cos(\omega t + \delta) \tag{12}$$

The time-dependent stress function can be rewritten as a complex stress function, where one component is in phase with the strain ϵ(t) and one is 90° out of phase, which is represented by the imaginary section of Eq. 13 [169], [173].

$$\sigma^*(t) = \sigma_0' \cos(\omega t) + i\sigma_0'' \sin(\omega t) \tag{13}$$

The imaginary stress component σ′′ can be portrayed in the imaginary dimension of the polar form, while on the other hand the real harmonic part σ′, as well as the strain component, are a part of the real dimension. The complex stress component can be found between those extremes, where the angle of this complex stress entity to the real components is equal to the stress-strain phase shift δ. Utilizing the Pythagorean theorem and trigonometry functions one obtains Eq. 14 and 15.

$$|\sigma^*| = \sqrt{(\sigma_0')^2 + (\sigma_0'')^2} \tag{14}$$

$$\tan\delta = \frac{\sigma_0''}{\sigma_0'} \tag{15}$$

The two stress components can be expressed in dependence on the real maximum stress σ_0 as in Eq. 16 and 17.

$$\sigma_0' = \sigma_0 \cos(\delta) \tag{16}$$

$$\sigma_0'' = \sigma_0 \sin(\delta) \tag{17}$$

Consequently, a real or storage modulus G' can be defined as the ratio of the real stress component σ_0' and the maximum strain ε_0, according to Eq. 18. On the flip side, the ratio of the imaginary stress component σ_0'' and the maximum strain yields the imaginary or loss shearing modulus G", as in Eq. 19.

$$G' = \frac{\sigma_0'}{\varepsilon_0} \tag{18}$$

$$G'' = \frac{\sigma_0''}{\varepsilon_0} \tag{19}$$

As outlined for the stress above, the elastic contribution of the storage modulus and the viscous portion of the loss modulus can be joined to the complex shearing modulus G^*, which is defined as follows in Eq. 20 [169], [173].

$$G^* = G' + i\,G'' \tag{20}$$

1.3.6 Viscosity of Polyelectrolyte Sols

Polyelectrolytes are synthetic or natural macromolecules, whose repeating or constitutional units are ionic, ionizable, or both in nature. Prominent natural examples thereof are nucleic acids, proteins, or certain polysaccharides, such as alginate. The shearing behavior of polyelectrolyte sols is more complex than that of an ordinary polymer solution, as the expansion of the polyelectrolyte molecule coil is not only dictated

by its molar mass, solvent quality, and temperature but also by the structuring of its ionic groups and their respective degree of dissociation in solution. To account for the viscosity of the solvent of a general polymer sol, the measured dynamic viscosity η can be cleared of the dynamic viscosity of its solvent η_s to obtain the relative viscosity η_{rel} and specific viscosity η_{spec}, as shown in Eq. 21 and 22.

$$\eta_{rel} = \frac{\eta}{\eta_s} \tag{21}$$

$$\eta_{spec} = \eta_{rel} - 1 \tag{22}$$

The specific viscosity η_{spec} is dependent on the concentration of the polymer, which can be accounted for by deploying the reduced viscosity η_{red}, as in Eq. 23, instead.

$$\eta_{red} = \frac{\eta_{spec}}{c} \tag{23}$$

The reduced viscosity η_{red} is solely influenced by polymer-specific properties, however, this only is valid for concentrations c → 0, in the ideal-dilute state of the solution, in which the polymer chains are in their statistically most likely conformation and only interact with the solvent, but not with each other. The true inherent shearing behavior of a polymer solution can therefore be measured by extrapolating its reduced viscosity at different dilute concentrations to c →0 at very low shearing rates $\dot{\varepsilon}$→0, which yields the intrinsic viscosity [η], according to Eq. 24.

$$[\eta] = \lim_{\substack{c\to 0 \\ \dot{\varepsilon}\to 0}} \eta_{red} \tag{24}$$

The reduced viscosity of a concentrated polyelectrolyte solution decreases as it goes from a concentrated to a semi-diluted state. During that process, the dilution further enhances the dissociation of the polyelectrolyte counterions, which reduces the osmotic pressure into the polymer coil, leading to a contraction of the polymer coil and a lower reduced viscosity. The so-called "polyelectrolyte effect" describes a rising reduced viscosity as one goes from this semi-diluted concentration state to a diluted concentration regime, in which the counterion dissociation is so advanced, that intrachain charge repulsion entails a re-expansion of the polymer. At further dilution, the reduced viscosity recedes again due to subsiding intermolecular interactions. By adding a low molecular weight salt to any polyelectrolyte sol, the aforementioned osmotic pressure and charge repulsion effects are commonly suppressed, which allows for a clearer interpretation of any reduced viscosity data. This enables a more consistent evaluation of a polyelectrolyte's intrinsic viscosity, which can be utilized to gauge the respective average viscosity molecular

mass M, by deploying the Kuhn-Houwink-Sakurada relationship. The relationship can be summed up in Eq. 25, with $K_{[\eta]}$ and α being empirical solvent- and temperature-dependent polymer-specific parameters [175], [176].

$$[\eta] = K_{[\eta]}\, M^{\alpha} \tag{25}$$

1.3.7 Atomic Force Microscope Force-Distance Measurements

Conventional ways to examine the mechanical properties of polymeric materials can only access information on the mechanical properties of the bulk material, but especially as materials demonstrate spatial and temporal heterogeneous features, nano- or microscale mapping of such properties is of interest. An AFM provides the necessary toolkit to access this information. A sharp tip, ranging in the nano- to microscale, is attached to a force-sensing cantilever, which measures a spatial variation of the tip upon changes in the tip-sample surface interaction. Besides the mechanical properties, topographic, electrical, or magnetic properties can be determined in gaseous as well as in liquid medium. Tip-surface interatomic and electromagnetic interactions as low as 10^{-18} N are sufficient to cause a deflection of a soft cantilever beam. On the flip side, a stiffer cantilever, with a higher resonance frequency, may be of benefit to minimize vibrational noise from the surroundings. The cantilever itself is attached to a piezo element, which positions the cantilever-tip construct in the z-direction. The sample is attached to a different piezoelectric element setup, which adjusts it in an x-y orientation. An optical deflection of the beam of a laser diode on the upper section of the cantilever toward a quadrant photodiode detects a displacement of the cantilever-tip composite [177]–[179]. Hansma et al. were the first group to use an AFM to determine the mechanical properties of soft materials (100 Pa – 10 GPa). Besides force-volume and AFM phase-imaging, force-distance measurements with extend and retract cycles far below the resonance frequency of the cantilever were established as a prominent way of classifying the mechanical properties of a sample surface in different sections. The piezo approaches the tip to the surface of a sample and the resulting deflection of the cantilever, with a known spring constant, is utilized to assign tip-surface interaction forces to various z-positions of the tip relative to the surface. To determine the indentation depth, the displacement of the piezo element z is corrected for the deflection of the cantilever x, which yields the raw indentation depth I, which is demonstrated in Figure 20.

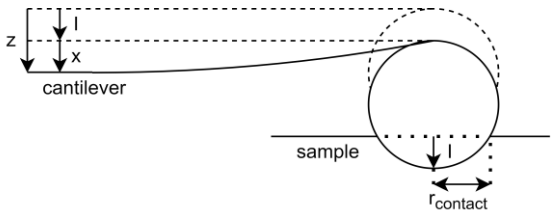

Figure 20: Indentation of a sample, while a piezo approaches the cantilever with a spherical probe in z-direction, which deflects the cantilever by the distance x and results in the raw indentation depth I.

In this off-resonance method of the cantilever, the resulting force-distance curve can be fitted to a contact mechanics model [180]–[183]. As the tip makes contact with a rather solid sample surface, only a fraction of the deformation energy is dissipated over time, while the majority is stored as elastic energy. To establish contact models, one has to assume a linear, homogenous, and isotropic elastic material, which can be described by a set of two independent mechanical parameters among those outlined in section 1.3.1, namely the elastic modulus E, the shearing modulus G, the bulk modulus K, and the Poisson's ratio ν. To account for the deformation of the tip material, whose elastic modulus is not infinite, in an indentation experiment, the reduced elastic modulus E_{eff} of the sample material can be expressed as in Eq. 26, with the Poisson's ratio ν_t and the elastic modulus E_t of the tip material. The equation simplifies, as the tip material is assumed to be much stiffer than the sample with modulus E ($E_t \gg E$) and one obtains an apparent elastic modulus E_{app} [163], [184].

$$\frac{1}{E_{eff}} = \frac{1-\nu^2}{E} + \frac{1-\nu_t^2}{E_t} \approx \frac{1-\nu^2}{E_{app}} \tag{26}$$

As the indenting tip deforms the sample, an integral, which expresses the indentation force as a function of indentation depth, the radius of the indenter r_{tip}, the radius of the circular indenter-sample contact area $r_{contact}$, and a shape-function of the indenter, can be deployed to approximate the apparent elastic modulus of the sample material. Different indentation contact functions for various axisymmetric indenter shapes, such as conical, cylindrical, and spherical indenters, have been established. Sneddon's general solution for the indentation of a material in its elastic regime with a variety of axisymmetric indenter geometries can be utilized to establish Eq. 27, which expresses the force F, that is present at various indentation depths I. The model further requires, that the indentation depth does not exceed the radius of the contact sample-indenter contact area $r_{contact}$, that the force is applied perpendicular to the sample surface, and that the sample is much thicker than the indentation depth I.

$$F(I) = \alpha\, E_{app}\, I^{\beta} \tag{27}$$

The parameters α and β represent indenter geometry-specific terms. To simplify the approach, an indentation with a half-sphere can be approximated as an indentation with a paraboloid of revolution with the tip curvature r_{tip} (radius of a sphere, that approximates the apex of the paraboloid of revolution). In this case, α amounts to $\frac{4\sqrt{r_{tip}}}{3(1-\nu^2)}$ and β is 1.5, which approximates the force between a sphere and an elastic half-space in the Hertzian contact model. Other α and β are known for cylindrical or conical indenters [181], [183], [185].

1.4 Anisotropic Alginate Hydrogels

Alginate hydrocolloids are salts of alginic acid, which is a linear polyuronic polysaccharide, a heteropolymeric polyelectrolyte, consisting of guluronic and mannuronic acid units. Alginates can be derived from natural sources, as it occurs as a structural component in marine brown seaweeds as well as in certain soil bacteria species. For instance, the dry matter of the marine brown algae *Phaeophyceae* consists of up to 40% (w/w) alginic structures. Most prominent, alginates obtained from the seaweed species *Macrocystis pyrifera* (Pacific Coast of America), *Ascophylllum nodosum* (Europe), *Laminara* (Europe and Japan), and *Ecklonia* (South Africa) are of commercial interest, based on their common occurrence. Although alginate polymers could be obtained from microbial fermentation and subsequent post-polymerization modification, commercially available alginate products, to this day, still originate from seaweed species, such as those listed above. The alginic structures can be found primarily in the intercellular space of algal organisms, in which the alginic acid polymers are in an equilibrium state with their ionic counterparts, which is determined by basic exchange reactions with the surrounding salt solution and the overall polymer composition. As seawater contains a relatively high amount of bivalent cations, the alginic polymers are found in a partially gelled state [186]–[189]. Alginate was first described by the British chemist Stanford (1881), as he patented the preparation of "Algic acid" from brown algae [190]. Later on, Atsuki and Tamoda (1926) and Schmidt and Vocke (1926) proposed, that alginate structures contain uronic acid units. Subsequently, Nelson and Cretcher (1929, 1930, 1932), Bird and Haas (1931), and Miawa (1930) further specified the uronic acid units, as they found D-mannuronic acid in alginate hydrolysates. Fischer and Dörfel (1955) finally discovered the complete structure of alginate, as they found the second monomeric unit of alginate, L-guluronic acid. The two monomers of alginic polymers are epimers. As shown in Figure 21, they differ in the stereogenic conformation of the C-5 atom [191]–[197].

Figure 21: β-D-mannuronic acid and α-L-guluronic acid in their $^4C_1$ conformation; the black dot marks the stereogenic center, which differs in the two epimers; guluronic acid is not in its more stable $^1C_4$ conformation, as the carboxylic acid group is in an unfavorable axial position.

In 1959, Haug, et al. partially hydrolyzed alginate structures and identified three fractions of characteristic polymeric structures, as two showed a homopolymeric and another one a heteropolymeric composition. A homopolymeric fraction of (1→4) linked mannuronic acid units, which is commonly described as an "MM"-block was identified. In this case, the monomers are linked with β-1,4-glycosidic bonds in a diequatorial plane, as demonstrated in Figure 22.

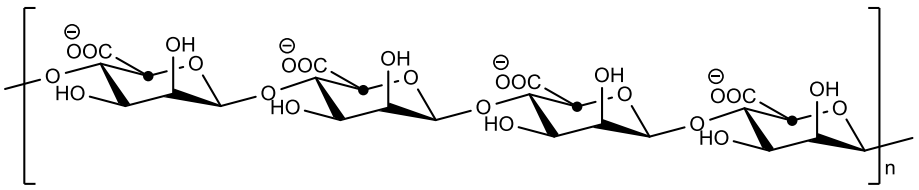

Figure 22: Homopolymeric region of alginate, consisting of poly β-D-mannopyranosyl uronate units in their $^4C_1$ conformation.

Another homopolymeric polymer subsection of (1→4) linked guluronic acid units was also identified, as showcased in Figure 23 [198].

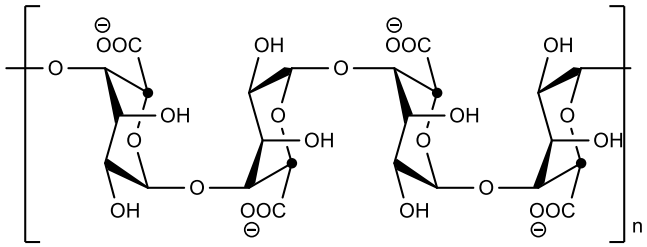

Figure 23: Homopolymeric region of alginate, consisting of poly α-L-gulopyranosyl uronate units in their $^1C_4$ conformation.

X-ray diffraction experiments performed by Atkins, Mackie, and Smolko (1970) showed that monomers in "MM" regions are present in a $^4C_1$-conformation, however, in "GG" blocks they obey a $^1C_4$ orientation. This forces the guluronic monomers into a diaxial position, connecting them with α-1,4-glycosidic bonds. As this conformation is sterically hindered, this prevents a rotation of the glycosidic bonds. Therefore, "GG" blocks are high in polymer stiffness, causing the overall extended nature of the alginate polymer [187], [199], [200]. The composition and the distribution of these polymer blocks are dependent on the seaweed

source, however, seasonal as well as local conditions also contribute [187]. According to the required features of an alginate product, the source has to be properly evaluated, as different alginate seaweed sources show significant deviation in overall monomer and sequence composition, which significantly impacts different polymeric properties such as stiffness, swelling, and rheological behavior. The gelling strength of alginate polymers strongly depends on the relative amount of guluronic acid monomers and "GG" sequences. The alginate backbone is chelating ionic species predominantly with its poly-guluronate units, due to the high negative charge density in the "pits" of the diaxial-diaxial linked monomeric units. "MM" blocks can only partially participate in ionic cross-linking, however, higher concentrations of cross-linking ions are required to do so. As several monomeric units are intermolecularly cross-linked, a whole "GG" block acts as a junction zone, which is demonstrated in Figure 24, allowing for an energetically favorable conformation of two or more cross-linked alginate chains, forming a so-called "egg-box" [201].

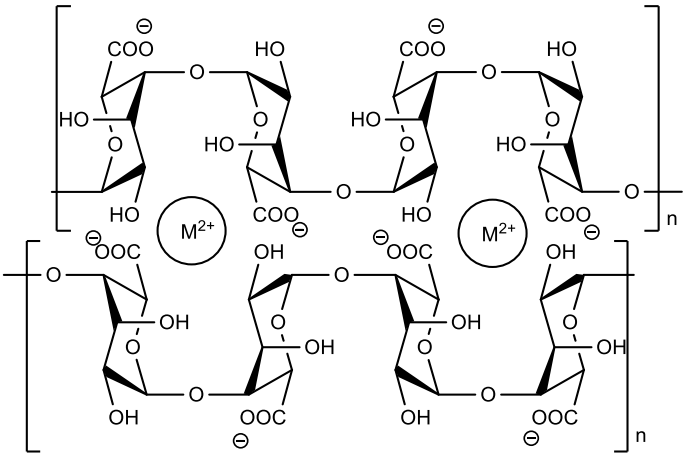

Figure 24: Sketch of a "GG" block forming an "egg-box" of chelated bivalent cations.

As bivalent cations uniformly diffuse through an alginate sol, a birefringent alginate gel is formed. The "MM" and "GM" sequences, which are copolymeric blocks of alternating mannuronic and guluronic acid units, act as spacing units inside the newly dissipated structure. The gelling strength of alginate polymers is mainly dependent on their guluronic acid unit content, as well as on the distribution of the individual homopolymeric "GG" regions. As alginate gels with a higher amount of mannuronic acid units are less likely to possess a great amount of cross-linking junctions, gels of this type usually are softer and less rigid, than ones with a high amount of guluronic acid units [186]. In the 1950s, H. Thiele found, that the formation of ionotropic gels by the anisotropic diffusion of a bivalent metal species through a polyelectrolyte sol not only obtains birefringent features but also exhibits symmetrical capillary structures,

that are aligned parallel to the direction of the diffusing ions. He specifically investigated this phenomenon by experiments with alginate, although similar kinds of polyelectrolytes showed an identical behavior. Thiele stated, that during the process of ionotropic gelation with a bivalent salt compound, an insoluble alginate salt would precipitate. The formation of the highly ordered capillary systems was explained by Thiele as a process of "droplet-shaped separation". He stated, that water is segregated during the gel formation process as droplets through dehydration of the polyelectrolyte. These local water units would then move with the gel formation front, thereby creating the capillary structure of an anisotropic capillary hydrogel (ACH) [202]. Later on, Thumbs and Kohler proposed a hydrodynamic model instead, as they observed a flow pattern of convective motion in the sol near the gelation front. They assumed, that alginate polymer chains get contracted by the cross-linking of the bivalent metal species. This yields a frictional force with alginate chains in proximity to the contracted chains, resulting in a hydrodynamic flow pattern, which is similar to Rayleigh-Bénard convection cells, but with friction instead of buoyancy as the driving force. According to the model, inter- and intramolecular cross-linking of the alginate chains is occurring in the gelation front, which causes the contraction of alginate chains from the sol. Alginate chains would then accumulate and get cross-linked in regions, where the streamlines approach the alginate gel body [203], [204]. Alginate products find use in food, industrial, as well as in pharmaceutical sectors. In food and industrial production, alginate is mainly deployed as a water holding, a gelling, an emulsifying, or a stabilizing agent. Alginates found in pharmaceutical applications also have a diverse field of use. From cell microencapsulation techniques to tissue engineering and drug delivery systems, there are many ways of utilizing this naturally occurring polysaccharide. In general, alginate-based biomaterials have to maintain their physical integrity until they completed their task. Furthermore, an alginate biomaterial has to meet mechanical demands, thus the rigidness and swelling behavior have to be controlled by manipulating parameters such as cross-linker concentration, cross-linking type, or molecular weight and composition of the alginate polymer. A three-dimensional scaffold of cross-linked alginate hydrocolloids with a capillary structure is applicable for biomedical purposes, as it can help in guided nerve regeneration in SCI. The aforementioned factors of SCI, such as microenvironmental inhibition, cavitation, unavailable permissive extracellular matrix, fibroglial scarring, and unavailable growth-stimulating factors, prevent a proper axonal regeneration of the adult CNS [186], [205]–[209]. Besides our own work, a variety of alginate biomaterials have been researched in SCI-related applications. Of those, only a small fraction take into account the material's mechanical properties and those typically are *in-vitro*-based approaches. For

instance, different alginate matrices of varying mechanical properties have been researched by Joung et al., who bioprinted varying mixtures of alginate and methylcellulose to form scaffolds, which also incorporated induced pluripotent stem cell-derived neural progenitor cells, which were able to survive, attach and differentiate successfully inside the bioprint. Ideally, the mixture contained ¾ methylcellulose, as this composition enhanced the 3D printing ability of the pure alginate, as it lowered the viscosity of the mixture. The scaffold exhibited 150 µm channel structures and was cross-linked with Ca^{2+} or Ba^{2+} ions. The neural progenitor cells were printed into the structure simultaneously and were shown to survive for three days after printing. Furthermore, the cells proliferated and differentiated into axons, which extended throughout the hollow structure. Oligodendrocyte progenitor cells showed similar differentiation and proliferation viability on the examined anisotropic scaffold, emphasizing the biomaterial's neuro-compatibility. To determine the mechanical properties of the alginate/methylcellulose structures and also of rat SC explants, dynamic longitudinal tensile testing was performed. The stress-strain response of the samples was utilized to derive the respective Young's Moduli. All samples were stored in PBS at 37 °C prior to compression tests in a dynamic mechanical analyzer. Reference samples of the transected SC yielded 2 – 8 kPa in elasticity, which falls in line with results obtained from tensile testing of SC tissue, as outlined in section 1.2.4. The alginate/methylcellulose bio-printed biomaterials had moduli of 35 to 95 kPa, which depended on the viscosity of the deployed alginate compound and the type of cross-linking ion, where more viscous biomaterial precursors and Ba^{2+} instead of Ca^{2+} yielded stiffer scaffolds. The biomaterials in the lower elastic modulus range were not self-supporting in their overall structure [40]. Further, a 1:1 blend of alginate and chitosan was used to form a biomaterial in a freeze-casting process by Francis et al. After the mixture was adjusted to pH 7.4, it had been cooled to -150 °C in a Teflon mold. Subsequent lyophilization and cross-linking with Ca^{2+} were performed and optionally the polycations poly-L-lysine, poly-L-ornithine (PLO), and the ECM-constituent laminin were adsorbed to the scaffold to enhance the *in-vitro* biocompatibility of the network. Besides swelling behavior and SEM analysis, the samples also underwent mechanical testing. To do so, the samples were first cut into 5 mm cubes and hydrated in PBS prior to measurement. Unconfined axial compression (Instron Model 4442) was performed at a constant strain of 0.01 s^{-1} and 5 N to obtain compressive moduli from the linear stress-strain response of the material. The freeze-casting process yielded a highly porous scaffold with linear and parallel capillary structures (Ø 68 µm). As the scaffolds and a non-Ca^{2+}-cross-linked control group were exposed to PBS for 24 hours, it became apparent, that the former demonstrated much less swelling, as their average increase in capillary wall diameter was

only 4.4%, while the latter scaffold walls gained 11.7%. PBS-immersed scaffolds showed elastic moduli of ~5 kPa, which put it right in the range of native SC. *In-vitro* testing of dorsal root ganglia, that had been seeded alongside its longitudinal channel structure, remained viable at a rate of greater than 91% on an uncoated biomaterial, a PLO-, a poly-L-lysine-, a laminin-, or a PLO/poly-L-lysine and laminin-coated biomaterial, with no significant difference between them. However, as dorsal root ganglia were merely seeded on the biomaterial surface and neurite ingrowth into the biomaterial was monitored, the PLO/poly-L-lysine and laminin-coated biomaterials (ingrowth 793/769 µm) trumped the only laminin coated ones (ingrowth 483 µm) by a small margin, while the three completely laminin-free biomaterials performed much worse in this regard (ingrowth < 100 µm). Inside the PLO and laminin coated alignate-based biomaterial, which had shown the furthest ingrowth, 62% of neurites had an orientation, which deviated no further than 20 ° from the parallel capillary structure [139].

1.5 Rationale and Hypothesis

ACHs, which had been developed in the group of Prof. Dr. Müller in cooperation with first and foremost the Spinal Cord Injury Center of the University of Heidelberg, have undergone a variety of *in-vitro* and *in-vivo* testing to provide a permissive substrate in mammal SC injury sites and conceptually serve as the basis of any hydrogel biomaterial in this thesis. Initially, the groups designed the novel alginate biomaterial with capillaries throughout the entire length of hydrogel with a smaller pore size (Ø 27.4 µm), which were formed during a physical cross-linking procedure of a 2.0% (w/w) alginate sol with a 1 M $Cu(NO_3)_2$ solution. The hydrogel had been chemically cross-linked with hexamethylene diisocyanate (HDI) to form polyurea and urethane linkages to enhance the gel's stability in physiological fluids, which would otherwise destabilize the gel structure in ion exchange processes. This also gets apparent, as calcium alginate hydrogels have been shown to decrease their dynamic shearing modulus by 90% over a period of 15 hours, as they were immersed in 0.15 M NaCl solutions [210]. After chemical cross-linking, the redundant bivalent cationic species were removed from the gel bodies by immersing them in an acidic solution, which would circumvent a potential detrimental effect of these ionic species on tissues and cells. Four individual washing steps with 0.1 M HCl would later on be found to be sufficient to lower the cationic species concentration in the gel below $1/100^{th}$ of the initial concentration. In an *ex-vivo* rat hippocampus model, the chemically-stabilized biomaterial was resilient for up to 14 days and lesioned axons grew longitudinally through the entire ACH, in which the orientation of the capillaries matched their orientation. In the next step, the group introduced the ECM-native compounds laminin, collagen, PLO, or fibronectin. This process was thought

to enable a biomaterial colonization with growth-supportive cells or facilitate general axon regeneration processes. However, only a negligible influence on axon ingrowth distance or axon density of these factors was observable in the same *ex-vivo* model. In another approach, ACHs of this kind, which had been implanted into a cervical rodent SCI, remained stable for six weeks and arose no significant inflammatory response by way of cyst formation or macrophage, microglia, or GFAP expression. The axons regenerated into the permissive hydrogel biomaterial but only crossed about 100 µm of the entire 500 µm scaffold length. However, the proliferation of neural progenitor cells on the capillary walls *in-vitro* provided a clear indication of the biomaterial's ability to be permissive for nerve repair-aiding cell types. Further studies would need to provide information on how growth beyond the entire implant dimension, rostral reinnervation, and functional recovery would be obtainable [211] (Prang et al., 2006). In a subsequent study, the cross-linking ion species was changed to tune the capillary diameter of the ACH. Besides that new parameter, gelatin was introduced during ACH assembly as an alternative to the prior utilized ECM compounds to improve cell adhesion to the alginate biomaterial. It was found, that the cross-linking of a 2.0% (w/w) alginate sol would yield 10 µm capillaries in a Cu^{2+}-, 18 µm in a Sr^{2+}-, and 55 µm in a Zn^{2+}-ion (1 M)-based physical cross-linking procedure. High concentrations of utilized gelatin entailed an improper capillary formation, while lower ones still permitted a capillary formation, however, the addition altered the capillary structure by increasing all ion-specific capillary diameter dimensions (10 → 18 µm (Cu^{2+}), 18 → 28 µm (Sr^{2+}), 55 → 77 µm (Zn^{2+})). PNS axons, that sprouted from dorsal root ganglia, grew into the longitudinal capillary structure of the ACH alongside Schwann cells and fibroblasts. The capillary diameter of the respective ACH influenced the axonal growth and SC migration, as only single axon formations populated the smaller diameter ACHs, while those with a higher capillary diameter allowed more SC migration and housed larger bundles of axons, thereby increasing the overall density of axons. The addition of gelatin to the alginate sol prior to gelation yielded a biomaterial, which would ultimately contain longer axons as longer ingrowth distances were recorded inside the larger capillaries (28/77 µm). This correlation was not observed for non-gelatin-containing gels specimens [212] (Pawar et al., 2011). An attempt to replicate these results in a CNS application necessitated the utilization of medical-grade alginate as the biomaterial precursor. Besides the three ionic species, that had been utilized prior, Ba^{2+} was now also deployed, which in combination with the 2.0% (w/w) medical-grade alginate sol-based approach yielded the smallest capillaries of all tested instances (11 µm), while the Cu^{2+}-, Sr^{2+}-, and Zn^{2+}-based medical-grade gels obtained slightly larger capillaries than the respective non-medical-grade ACHs from prior studies.

Gelatin-containing medical-grade hydrogel specimens varied only slightly in diameter from their non-gelatin-containing counterparts this time around, as shown in Table 3. The mechanical properties of the different ACHs were determined by measuring 4 mm thick disk samples in oscillatory shearing rheometry utilizing an AR 2000 rheometer (TA Instruments, Germany). The respective storage moduli G´ of alginate gels with and without added gelatin, which were cross-linked with Ba, Sr, or Zn, were obtained at 100 µNm shearing torque in a stress sweep experiment and are given below in Table 3. The respective G`` values came in lower by a factor of 10.

Table 3: Storage moduli from an oscillatory stress sweep at 100 µNm and median capillary diameter of 2.0% (w/w) medical-grade alginate samples with and without added gelatin; gelation with 1 M Ba, Sr, or Zn [213].

	Ba	Sr	Zn
median capillary diameter / µm	11	29	89
G' / kPa	41.4 ± 10.3	39.0 ± 5.7	20.3 ± 2.2
median capillary diameter / µm (+ gelatin)	15	23	86
G' / kPa (+gelatin)	48.3 ± 3.9	51.3 ± 4.8	42.7 ± 5.4

Rat entorhinal cortex and SC tissue were placed on the medical-grade ACHs to assay the axonal ingrowth from both tissue classes into the biomaterial. In doing so, a smaller-scale scaffold structure also entailed a more longitudinally directed axon growth pattern and also a more pronounced longitudinal orientation of infiltrating astrocyte cells, as also found by Smeal et al. [102]. There was no stark difference between the two tested tissues with regard to biomaterial ingrowth, however, the entorhinal cortex slice culture axons would populate the 29 µm compared to the 11 µm capillary ACHs more densely, but no improvement in that regard would occur upon a further enlargement of the tube structures. On the flip side, axons sprouting from the SC slice culture would populate the most porous and larger 89 µm (Zn) capillary-equipped ACHs in significantly higher numbers. The addition of gelatin did not provide a clear picture in this instance, as an elevated density of axons originating from the brain slice culture was observable in gelatin containing ACHs compared to those without gelatin, while there was no significant difference for axons sprouting from the SC tissue. An increase in capillary diameter from 11 to 29 µm did not enhance astrocyte migration or axon density in the biomaterial in the brain tissue model, but such an increase in capillary diameter was shown to be of benefit in the SC

slice model. However, no distinct correlation between astrocyte migration and gelatin addition could be identified (Pawar et al., 2015). The group's next efforts involved combining the established medical-grade biomaterial with BDNF-secreting bone marrow MSCs in the rat SC. A 2 mm incomplete injury at the C5 level was treated with Sr^{2+}- or Zn^{2+}-based ACHs, in which the former case yielded smaller capillary structures of higher density, while the latter demonstrated larger capillary features in a less densely structured manner, which is in accordance with prior findings. Only minor cavitation of the biomaterial, which stayed properly aligned with the rostrocaudal orientation of the SC, was observable post-implantation. Sr^{2+}-based ACHs, which had been supplemented with bone marrow MSCs, housed nearly four to five times as many axons as a control hydrogel, that was merely equipped with green fluorescent protein. The stem cell-containing ACHs promoted axon extension deep into the material, but even then the caudal SC parenchyma wasn't reached. A slight, non-significant reduction of axon density in the ACHs was present in the larger capillary-containing Zn^{2+} hydrogel samples. The axon regeneration inside the larger capillaries also occurred in a less oriented manner, as the angular orientation of more axons deviated further from the rostral-caudal orientation, which is represented in Table 4 [207] (Guenther et al., 2015).

Table 4: Relative portion of axons of the natural white matter, of axons in a cell-only SCI intervention, and of axons in SCI in different ACHs with differently sized capillaries, that were oriented 10 or 20 ° within the rostral-caudal orientation [207].

axons within angle	± 10°	± 20°
intact SC white matter / %	46	73
SCI, only cell intervention / %	9	19
SCI, Sr^{2+} hydrogel + cells / %	46	70
SCI, Zn^{2+} hydrogel + cells / %	36	61

The authors concluded, that the seeded BDNF caused a growth factor oversaturation of the lumen in the ACHs compared to the host tissue, which would inhibit axon extension beyond the biomaterial and consecutively integration into the caudal parenchyma. Besides that, bone marrow MSCs were found to not be well integrated into the regrown SC tissue and the biomaterial implant, which might eventually had caused the fibroglial scarring around it. In exchange for bone marrow MSCs, Schwann cells alongside a distal delivery of BDNF were probed. To avoid complications, such as spasticity or potential impairment of functional recovery due to BDNF overexpression, a tetracycline-regulated viral expression of BDNF caudal to an ACH was utilized [214], [215]. In this new approach, ACHs arose

only mild cavitation in the same rodent C5 SCI model as used before, while remaining intact for eight weeks. The seeded Schwann cells integrated well, both into the ACH and also the biomaterial-tissue interface. The axons entered the ACH in a linear parallel pattern in the proximity of seeded Schwann cells. The viral expression of BDNF within 4 mm of the caudal ACH border led to an increase in axons per capillary area, but growth factors, that were expressed farther from the biomaterial, were deemed to express an insufficient gradient of BDNF to reach the material. A significant axon extension beyond the ACH was not achieved after four weeks. An additional four weeks of *in-vivo* expression of BDNF enhanced the growth of certain axon types, however, once again extension beyond the ACH was still not observed. The authors concluded, that the glial scar would impede the extension into the host parenchyma. To circumvent this problem, additional Schwann cells were seeded 1 mm caudal to the biomaterial. Not only did this improve the overall axon density inside the ACH, but certain axons also penetrated the host-biomaterial interface and extended into the caudal parenchyma as far as 2 mm and beyond the caudal Schwann cell injection [209] (Liu et al., 2017). As already mentioned in section 1.2.1, astrocytes might provide a permissive environment for axonal growth and re-entry into the host parenchyma, due to their homeostatic and also axon-guiding capabilities. Besides that, the modification of alginate ACHs with poly (amino acid)s can mask the negative surface charge of the polyelectrolytic alginate network, which might also create a more permissive environment for axonal regrowth. To examine these propositions, our alginate biomaterial was once again deployed in a C5 rat injury model. While only a minor amount of acidic amino acids was bound, due to their negative charge in neutral environments, higher amounts amount of the basic amino acid PLO could be immobilized in the alginate hydrogel scaffold. Even higher amounts of the also positively charged poly-D-lysine were fixable, however, PLO had previously demonstrated a lower degree of immunogenicity [216]. Neonatal astrocytes survived in numbers ten times higher on PLO-coated ACH samples than on uncoated ones. Further, the addition of the ECM molecule altered the astrocyte cell shape, resulting in larger somata and longer cytoplasmic processes. A similar outcome in favor of the PLO-coated ACHs was found in *in-vitro* experiments with dorsal root ganglia cells, which demonstrated extension, survival, and attachment on PLO- and laminin-coated alginate materials, which was not possible on uncoated biomaterials. The same held true in *in-vivo* experiments with rodents, that had suffered a partial C5 SCI. Neurites and host cells infiltrated the rostral entry zone of the ACHs in higher numbers in PLO/laminin-coated samples, however, the coating effect alone was not sufficient to induce prolonged

axonal growth inside the biomaterial, as no host astrocytes would be able to penetrate the ACH-host border. Although the integration of astrocytes into the biomaterial facilitated its integration into the lesion site, it did not meaningfully improve the axonal entry into the biomaterial. (Schackel et al., 2018) [71]. In the scope of this thesis, the aforementioned biological factors will not be further investigated. As already outlined in section 1.2.4, the mechanical properties have big implications in biomaterial application in general and also have been paid attention to in SCI use cases. To gauge the influence of the viscoelastic properties of our alginate ACH biomaterial on the outcome of *in-vitro* and *in-vivo* SCI applications, three medical-grade biomaterial classes with elastic moduli in the 1 to 10 kPa ought to be established. This parameter range was chosen due to the assumption, that the mechanical properties of the biomaterial should fall in line with the respective properties of the surrounding tissue in different testing setups and conditions, as postulated in section 1.2.4. Besides the mechanical properties, the morphology of the ACH capillary lumens was also identified as a critical parameter in the design of physical guidance scaffolds and poses another important pillar of this work. Generally, a capillary diameter of 80 to 100 µm was targeted to counterbalance the axon-aligning proficiencies of smaller capillaries but to also allow for infiltration of sprouting axons and host tissue. By first establishing a parameter framework with lower-cost food-grade alginate products, the costs associated with the project were minimized and only later efforts involved the replication of prior findings with selected experiments, which then also involved medical-grade alginate products.

2. Experimental

2.1 Materials

Within this thesis, two different sodium alginate products were examined. FMC Biopolymer (Philadelphia, USA) provided the food-grade PROTANAL® LF 200 FTS alginic acid sodium salt (η (1% (w/w) H_2O) = 135 – 258 mPas (shear rate: 9.9 s^{-1} – 167 s^{-1})), a dental alginate product with a guluronic acid content of ≥ 60% (w/w), which will be also referred to as Protanal or food-grade alginate in this thesis. Further, the medical-grade alginate product PRONOVA® UP MVG of batch numbers 1003-03 or 1106-03 from NovaMatrix (Sandvika, Norway) was deployed. Both batch versions represent a medium viscosity (η > 200 mPas, M_w = 75 – 200 kDa) sodium alginate product with a guluronic acid content of ≥ 60% (w/w) and a protein content of ≤ 0.3% (w/w) and will be also referred to according to their batch number. The bivalent inorganic salts $Sr(NO_3)_2$, $Zn(NO_3)_2{\cdot}6H_2O$, and $Ca(NO_3)_2{\cdot}4H_2O$ were obtained in analytical quality (purity ≥ 99.0% (w/w)) from Sigma-Aldrich® (St. Louis, USA). Hexamethylene diisocyanate (HDI) (purity ≥ 99% (w/w)), octamethylene diisocyanate (ODI) (purity = 98% (w/w)), and decamethylene diisocyanate (DDI) (purity = 97% (w/w)) were also purchased from Sigma Aldrich® (St. Louis, USA). Hydrochloric acid solution (1 M) was purchased from VWR international® S.A.S. (Fontenay-sous-Bois, France). Ethanol *pro analysi* (p.a.) (purity ≥ 99.8% (v/v)) and acetone p.a. (purity ≥ 99.5% (v/v)) were provided by Sigma Aldrich® (St. Louis, USA). Dimethyl sulfoxide (DMSO) (purity ≥ 99.9% (v/v) and nitric acid (65% (v/v)) were obtained from Fisher Scientific UK (Loughborough, UK). Tablets to prepare 7.4 pH PBS solutions (1 tablet / 200 mL: 0.137 M sodium chloride, 0.0027 M potassium chloride, 0.01 M phosphate ($H_2PO_4^-$/HPO_4^{2-})), sodium *meta*periodate (purity ≥ 99.8% (w/w)), and Purpald® reagent (purity ≥ 99% (w/w)) were also obtained from Sigma Aldrich® (St. Louis, USA). Sodium borohydride (purity ≥ 96% (w/w)) and sodium acetate trihydrate (purity ≥ 99.5% (w/w)) were delivered by Merck KgaA (Darmstadt, Germany). Sodium chloride p.a. was provided by neofroxx GmbH (Einhausen, Germany). Ruthenium red (purity ≥ 85% (w/w)) was provided by Fluka (St. Gallen, Switzerland). Instant adhesive glue based on cyanoacrylate was provided by Uhu (Bühl, Germany) and 125 mL Nalgene® plastic cups with a screw cap were obtained from VWR international® LLC (Randnor, USA). Aluminum caps were fabricated by schuett-biotec (Göttingen, Germany) and treated in an anodic oxidation process at the University of Regensburg. All aqueous solutions used within this thesis were prepared with purified water (ρ ≥ 18 MΩcm) from a Millipore® water purification system. The AFM cantilever CP-CONT-BSG-B (borosilicate glass, diameter: 10.0 ± 1 µm, width: 50 µm, length: 450 µm, force

constant: 0.02 - 0.77 N/m) was purchased from NanoAndMore GmbH (Wetzlar, Germany). Petri dishes (Ø 34 mm) were obtained from Techno Plastic Products GmbH (Trasadingen, Switzerland).

2.2 Preparation of Alginate Hydrogels

2.2.1 Physical Cross-linking Procedure

Alginate ACHs were prepared in aluminum caps, which were 5.5 cm in diameter and 4.0 cm in height. Beforehand, these containers were oxidized to obtain a hydrophilic surface. To do so, they were treated with a nitric acid solution (32.5% (w/w)) in an ultrasonic bath at 70 °C for three minutes. Subsequently, the caps were rinsed with purified water and dried under a fan. Medical or food-grade alginate product was dissolved in purified water in Erlenmeyer flasks with an ST joint overnight while stirring. In doing so, sodium alginate sols of 0.5 to 2.0% (w/w) were obtained as duplicates (2 × 65 g) for every individual parameter setup. Sodium alginate sols in quantities of 65 g were poured into the oxidized aluminum caps and were covered with Petri dish covers. The sols rested in the containers overnight to remove any air bubbles. In order to initiate the physical cross-linking process, the surfaces of the alginate solutions were sprayed with a $Sr(NO_3)_2$, $Zn(NO_3)_2$, or $Ca(NO_3)_2$ solution of varying concentration (0.025 – 1.0 M) by utilizing a pressure nebulizer. By carefully spraying at a 40 – 50 cm distance to the prepared containers, a thin layer (~2 mm) of the respective divalent cationic solution was created on top of each sodium alginate solution to start the gelation process. After ten minutes, the remaining volume of the respective container was then topped off with the same solution. The experiments were covered with Petri dish covers and stood still for 48 hours. After that point in time, the formed gel bodies were removed from their gelation containers using a spatula. To remove excessive metal salt solution, that had not been required in the crosslinking process, the gels were washed with 500 mL purified water for two hours (4 × 2 h), as listed in Table 5. Before chemical cross-linking, the gel specimens had to be dehydrated gradually in advance. For this purpose, the gel bodies were immersed in an aqueous 25% (v/v) technical-grade acetone solution. Subsequently, cutting of the gel bodies on a custom-made band saw was performed. The duplicate gel samples, that had been prepared for each specific experimental setup, were cut differently, as from one gel only a disposable 5 mm slice was cut from the top. From the second specimen, the top 5 mm slice was also disposed of, while the remaining gel body was cut into 3 mm slices, which would serve for rheometry measurements later on. The remainder of the two cut gel bodies was transferred to a single 125 mL screw-cap plastic cup and underwent a sequence of further steps.

2.2.2 Chemical Cross-linking Procedure

To tune the mechanical properties and increase the alginate gel's resilience in the presence of monovalent ionic solutions, such as PBS solution or physiological fluids, two different chemical cross-linking procedures were established. On the one hand, urethane linkages in a water-free surrounding were established by cross-linking the carbohydrate structure of the alginate polymer with diisocyanate compounds, namely HDI, ODI, and DDI. The reaction in DMSO is outlined in Figure 25.

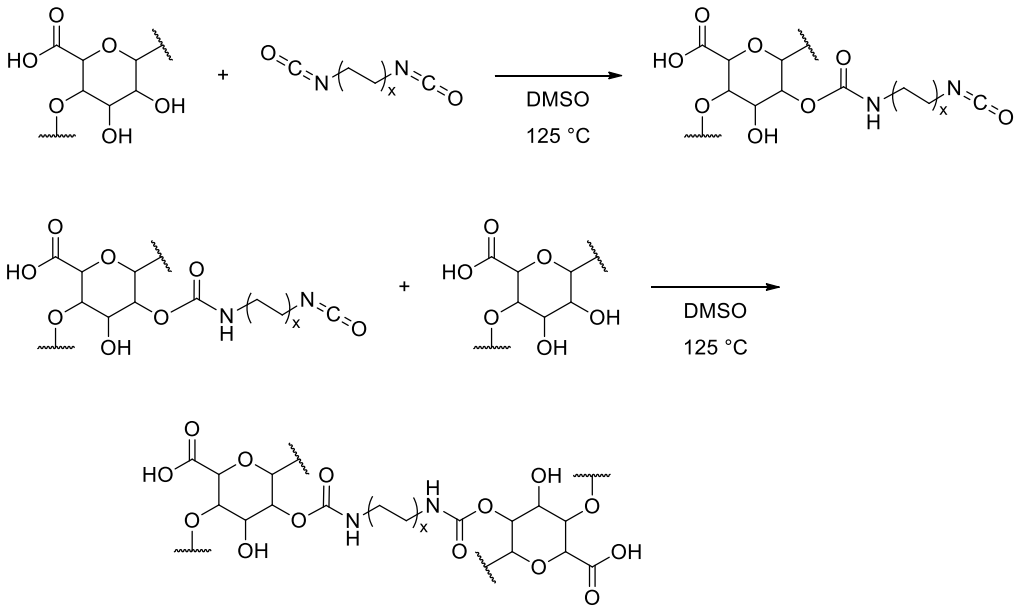

Figure 25: Formation of a urethane linkage between two hydroxyl groups of two alginate monomers with the diisocyanates HDI (x=3), ODI (x=4), or DDI (x=5).

Alternatively, a polyurea interpenetrating network inside the gel body was established. An interpenetrating polymer network is generally obtained by interlacing two or more polymer networks into each other without forming any covalent bonding between those [217, p. 18]. Initially, by decarboxylating the diisocyanate compounds in the presence of water, the respective diamine was formed, which in turn formed a urea polymer with the diisocyanate compound itself, as depicted in Figure 26.

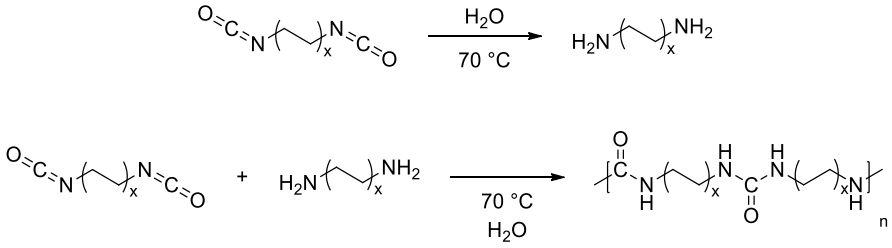

Figure 26: Formation of a polyurea polymer from the diisocyanates HDI (x=3), ODI (x=4), or DDI (x=5) in aqueous medium.

Irrespective of which way of chemical stabilization was desired, at first, the gels were immersed in a sequence of aqueous solutions with ascending acetone concentrations, as displayed in Table 5. Once complete dehydration was established, gel samples, which would further be stabilized via urethane linkages were also washed with DMSO. The water-deprived gel bodies were also left in the respective diisocyanate DMSO solution in a sealed beaker for three hours under constant stirring before the solution was then heated to 125 °C for 90 minutes. After cooling off, the gels were immersed in acetone p.a. to remove any DMSO and excess diisocyanate.

Gel specimens, which were cross-linked in H_2O, were immersed in 10 – 100 mM diisocyanate in acetone solution for three hours while shaking after being dried in acetone p.a. To flush out the residual crosslinking solution from the capillaries, the gels were immersed in acetone p.a. for five minutes while shaking and pressed between filter papers, which reinforced this process via capillary action. The cross-linking process was finished by polymerizing the diisocyanate units in the soaked gels in purified water at 70 °C for 45 minutes.

Samples of any cross-linking origin were then washed with purified water (4 × 10 min) to remove residual acetone. The alginate gel still contained the cross-linking cationic species at this point. Therefore, by immersing the gel bodies in 0.1 M HCl (4 × 2 h), the ions were exchanged. Afterward, the gel specimens were washed with purified water (5-6 × 2 h+), until pH neutrality was obtained. The gel bodies were stored in 70 – 80% (v/v) ethanol p.a.

Table 5: Two chemical cross-linking procedures of alginate ACHs after they had been physically cross-linked with bivalent cationic species.

washing in purified water (4 × 500 mL / 4 × 2 h)	
dehydration in acetone solution 25% (v/v) (1 × 500 mL / 1 × 2 h)	
cutting of the gel bodies in a custom-made band saw	
dehydration in acetone solution 50% (v/v) (1 × 100 mL / 1 × 2 h)	
dehydration in acetone solution 75% (v/v) (1 × 100 mL / 1 × 2 h)	
dehydration in technical-grade acetone (2 × 100 mL / 2 × 2 h)	
dehydration in acetone p.a. (2 × 100 mL / 2 × 2 h)	
cross-linking in DMSO at 125 °C	**cross-linking in H_2O at 70 °C**
dehydration in DMSO (4 × 100 mL / 4 × 2 h)	dehydration in acetone p.a. (2 x 100 mL / 2 × 2 h)
immersion in diisocyanate DMSO solution (1 × 250 mL / 1 × 3 h (stirring))	immersion in diisocyanate acetone solution (1 × 100 mL / 1 × 3 h (shaking))
cross-linking in diisocyanate DMSO solution at 125 °C (1 × 250 mL / 1 × 90 min (stirring))	washing in acetone p.a. (1 × 100 mL / 1 × 5 min (shaking))
washing in acetone p.a. (4 × 100 mL / 4 × 60 min)	pressing between filter papers
	cross-linking in 70 °C H_2O (1 × 2 L / 1 × 45 min)
washing in purified water (4 × 100 mL / 4 × 10 min)	
ion exchange in 0.1 M HCl (4 × 500 mL / 4 × 2 h)	
neutralization in purified water (5-6 × 500 mL / 5-6 × 2 h+)	
storage in 70 % (v/v) ethanol p.a. (1 × 50 mL)	

2.3 Mechanical Properties Examination

2.3.1 Microindentation with the Atomic Force Microscope

A Bruker Nanowizard® SENSE-AFM was deployed to perform force spectroscopy measurements on ACHs. A JPK NanoWizard® III SENSE AFM head with a piezo-driven x-y scan range of 100x100 µm and a piezo-driven z range of 15 µm was connected to a high-performance digital scanning-probe microscopy controller, which itself was connected via ethernet to a desktop computer. The controlling unit was also connected to a JPK motorized precision stage, which allowed for x-y positioning of the sample container in a 20 mm range. The stage was equipped with a JPK Petri dish heater with a temperature stability of 0.1 K. The AFM stage was seated on a base plate with a mounting post, which was isolated from building vibrations by an Accurion Halcyonics i4 benchtop active vibration isolation system on top of a granite table. JPK TopviewOptics, which comprised of a 12x manual zoom optical system, a 1/3" CCD fire wire color camera, an off-axis LED ring illumination, and a coaxial Köhler LED light source, was mounted onto the mounting post. The camera was directly connected to the computer via FireWire and provided imaging

with a resolution of < 4 µm. To perform force-spectroscopy measurements, NANOANDMORE CP-CONT-BSG, 450 µm long rectangular silicon cantilevers, which featured 10 µm (± 1 µm) borosilicate glass spherical tips, were attached to an extra-long glass prism as the cantilever holder. This rather small spherical probe was selected to enhance the resolution of force-distance curve measurement around the wall borders of the anisotropic gel samples. The hydrogel samples were cut into small slices (for indentation in the capillary direction) and stripes (for indentation perpendicular to the capillary direction) and stored in 50 mL of PBS solution at 37 °C for three hours. The 3-hour sample also served as the "0 day" sample in 12-week stability testing. For this purpose, the samples were measured again after 1, 2, 4, 8, and 12 weeks while they were immersed in a single PBS solution at 37 °C. Hence, at least six individual slices and strips of any individual sample were prepared in a Leica VT 1000 M microtome. To perform measurements, the gel samples were glued onto Petri dishes in two different orientations (gel capillaries perpendicular to the sample stage and parallel to it) and covered with PBS solution. The Petri dish heater heated the dishes to 37 °C and the AFM head was positioned with the cantilever aside the sample, over a clear area of the Petri dish. With the tip of the cantilever holder unit immersed in PBS, the detection laser was positioned onto the end of the cantilever backside, as shown in Figure 27.

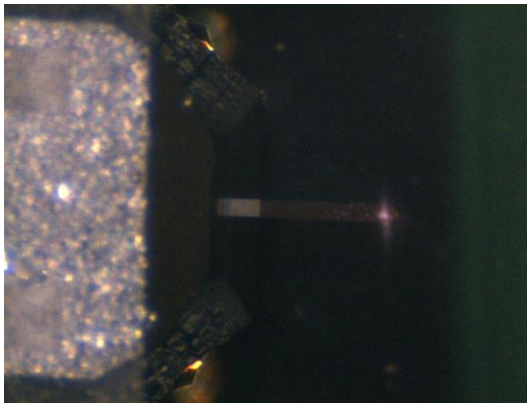

Figure 27: Cantilever chip and the attached rectangular cantilever, on which the detection laser is focused.

Consecutively, the mirror screw on the side of the AFM head was adjusted until a maximum voltage sum value in the laser alignment window inside the JPK SPM software was determined by the four-segment photo-diode detector system and the positioning of the detector was adjusted until the laser focus was positioned in the center of all four quadrants of the detector, as schematically shown in Figure 28.

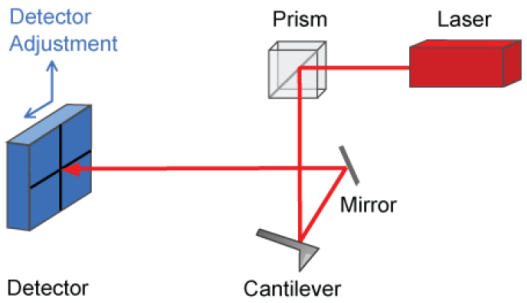

Figure 28: Schematic pathway of the detection laser beam, taken from [218].

To calibrate the AFM, an approach of the hard Petri dish surface, first manually up until 1000 µm off the surface and then via automatic successive approaches in 15 µm increments of the z-piezo range of the AFM head was performed. As the cantilever tip made contact with the hard calibration surface, the sensitivity of the cantilever-detector setup was determined to correlate the change in detector voltage to the deflection of the cantilever by performing a force-distance measurement with the standard method. To finish the calibration process, the cantilever was retracted from the surface and the thermal noise was utilized to determine the spring constant of the cantilever. In the process, thermal fluctuations in the cantilever deflection were measured and the measured resonance frequencies were fitted to a Lorentz curve. As the calibration was performed in a fluid, the resonance frequency of the cantilever was dampened to lower frequencies and amplitude. Therefore, the first higher overtone was used instead, which necessitated a correction factor in the SPM software of 0.251. The whole calibration procedure was repeated upon every cantilever change or adjustment of the glass prism or in general at the beginning of every day. Commencing with the force-distance measurements, the cantilever tip was positioned above the gel samples by moving the motorized stage. The tip geometry was then approached to the sample surface, ideally over a capillary wall section, as demonstrated in Figure 29. The approach was stopped at 1 nN indentation force, which ensured a proper positioning of the z-piezo for the upcoming measurement process.

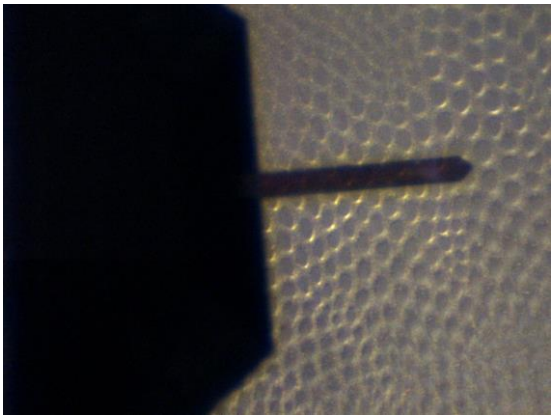

Figure 29: Cantilever approached to the capillary wall of a 1 M Sr^{2+} 1.0% (w/w) Protanal hydrogel.

For every sample, a 16 × 16 force map in an area of 100 × 100 µm area was recorded. At every measured point, two approaches were performed, initially with 1 µm/s and then again with 5 µm/s. The indentation force was altered between 5 and 20 nN. The lower end of the force range was small enough to not indent the sample surface of softer samples further than the radius of the contact area ($I < r_{contact}$), a constraint, that was outlined in section 1.3.7. On the flip side, the stiffer hydrogel required indentation forces of up to 20 nN, to obtain sufficiently detailed force-distance relationships. The general aim was an indentation depth of 1 to 4 µm. After every approach, a 4-second pause was initiated at a constant z-piezo height, during which the deflecting cantilever force was recorded. Up to 256 force-distance measurements per force map were processed in the JPK Data Processing Software. The approach force-distance curves, as showcased in Figure 30, were first corrected with regard to the force baseline prior to contact at every measurement point. The force level at 80 to 100% of maximal retraction served as the origin to derive a force baseline level. Further, the software gauged the contact point of each force-distance curve and offset the x-axis accordingly. Additionally, the bending of the cantilever (section 1.3.7), which would otherwise offset the vertical tip position during the indentation, was taken into consideration and the force-distance curve was corrected accordingly. Finally, the apparent elastic modulus E_{app} was determined utilizing the Hertzian contact model with a Poisson's ratio of 0.5. In many cases, the baseline was too tilted or the force curve was very unsteady, which resulted in the rejection of the force curve fit in question.

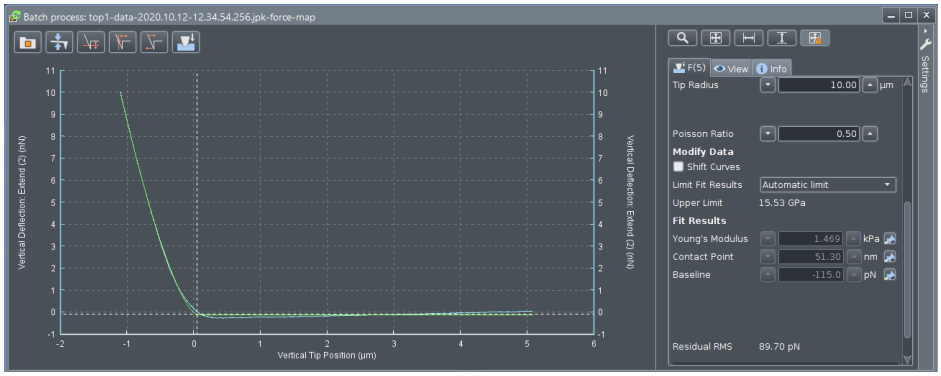

Figure 30: Determination of the apparent elastic modulus in the JPK Data Processing software with the baseline force adjustment, contact point offset, and correction of the cantilever bending; the light-blue line indicates the measured force-distance curve and the green overlay shows the best fit of the JPK software.

Given a sufficiently high number of adequate force-distance measurements, the recorded force maps could be also transformed into maps of apparent elastic moduli, as showcased in Figure 31.

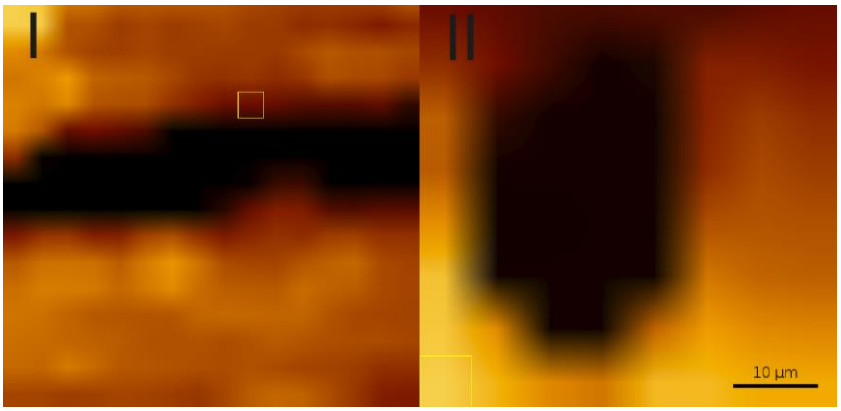

Figure 31: Apparent elastic moduli of alginate ACHs with areas of higher elastic modulus appearing brighter; examination of a hydrogel sample, that was indented perpendicular (90 °) to the capillary direction (I) or parallel (0 °) to it (II).

The 1 and 5 µm/s force-indentation curves were pooled and a minimum number of 20 individual force-distance curves for each sample were evaluated with regard to the median, first and third quartile, and the 5th and 95th percentile of the apparent elastic modulus.

In order to examine the viscoelastic behavior of ACH samples in microindentation experiments, a pause of four seconds was performed after each “extend” step of the measurement routine. The resulting force relaxation curve was recorded at 2048 Hz. The two pause sections of every force-distance curve, which had been successfully evaluated in the contact model evaluation, were analyzed by a Python script, which is shown in Appendix B. The scipy library was deployed to fit the recorded 4-second stress relaxation curves to a bi-exponential decay function, which is approximated by the Wiechert model, according to Eq. 28. The

arbitrary relaxation times 1.0 and 0.1 seconds were chosen as the two relaxation times of the two Maxwell elements.

$$F(t) = A_0 + A_1 e^{\frac{-t}{1\,s}} + A_2 e^{\frac{-t}{0.1\,s}} \tag{28}$$

A_0, A_1, and A_2 were approximated by the method of least squares for all valid force curves. To ensure a proper fitting of the relaxation curve, the variance and standard deviation of the individual parameters were derived from the diagonal of the respective covariance matrix of the fit parameters. A lower variance or standard deviation of a parameter value indicates a better fitting result, as in this case, even a small deviation in one of the parameters would significantly worsen the fitting outcome, which is generally not the case for bad-fit approximations. Thus, if one of the standard deviations of one of the parameters A_1 and A_2 relative to the parameter value itself would exceed 0.1 or 10%, it was determined, that the relaxation curve would be rejected due to poor fitting. Given that boundary condition, the ratio of $\frac{A_2}{A_1}$ was then calculated for each force curve and the median, first, and third quartile ratio values of all valid relaxation functions of a sample were determined. At least 20 force relaxation curves were evaluated per sample.

2.3.1 Oscillatory Shearing Rheometry

In order to determine the bulk mechanical properties of alginate ACHs, three to five ethanol-stored band-saw cut slices of one whole gel specimen were immersed in 50 mL of PBS solution for three hours. The viscoelastic behavior was determined with a TA Instruments AR 2000 Rheometer. Generally, a combination of stress- and strain rate-controlled experiments were performed in a frequency and a stress sweep test. A 40 mm stainless steel, cross-hatched plate with a solvent trap served as the top geometry. On the bottom, a Peltier element was covered by a stainless steel cover plate with a 40 mm cross-hatched surface. The parameters of both measurement modes are given in Table 6. After calibrating the measurement gap and the geometry inertia, the samples were measured. After the whole cross-linking procedure, the sample disks were much thinner than they had been after the band-saw cutting procedure, now ranging between 800 to 1100 µm, so the measurement gap range was adjusted accordingly. As the tested sample disks exhibited a wide range of mechanical rigidity, the normal force had to be varied between 0.2 and 2 N to avoid excessive syneresis and compression of softer gel bodies.

Table 6: Measurement modes and parameters for viscoelastic examination in the TA Instrument AR 2000 rheometer.

mode	frequency sweep	stress sweep
measurement system	PP40, cross-hatched (40 mm)	PP40, cross-hatched (40 mm)
bottom	40 mm cross-hatched	40 mm cross-hatched
temperature / °C	37	37
normal force / N	0.2 - 2.0 ± 0.1	0.2 - 2.0 ± 0.1
frequency / Hz	0.1 – 10 (5 steps)	1
oscillatory force / µNm	100	10-1000 (11 steps)

A minimum of three, but in most cases five individual disks of the alginate ACHs were utilized to determine the mean storage moduli and phase shift δ values (± standard deviation) for each sample. Samples, that were only measured once, were analyzed with regard to their G' and δ values, which were recorded in the stress sweep at 100 µNm oscillation torque and 1 Hz oscillation frequency. As no stress sweeps were performed in long-term PBS immersion experiments to preserve the integrity of the sample, the mean G' and δ values were obtained from the frequency sweep at the same torque and frequency as from above. For stability testing purposes, the PBS solution was renewed after the same gel disks had been re-measured after 1, 2, 4, 8, and 12 weeks of PBS immersion at 37 °C. The supernatant of the gel disks was also utilized to determine the release of alginate, which is outlined in section 2.5.

2.3.2 Determination of Average Viscosity Molar Masses of Alginate Products

To examine the average viscosity molar mass, the intrinsic viscosities of two of the utilized alginate products were determined in capillary and shearing viscometry. The Ubbelohde viscometer Schott AVS 360 with a capillary I type 537 was tempered at 25 °C and the flow time was measured at least four times for each sample. In combination with the density of the respective alginate solution, which was measured with an Anton Paar DMA 5000 M density meter, the Hagen-Poiseuille equation was utilized to determine the dynamic viscosity of the alginate sol samples. Alternatively, the double gap geometry DG 40/50 was deployed in a Bohlin CVO 120 rheometer. The instrument was filled with 30 mL of sample volume and tempered to 25 °C. After a 120-second temperature equilibration period, the dynamic viscosity was determined in 60-second integration periods for eleven shear rate increments, starting with 2 s^{-1} and ending with 22 s^{-1}. Higher shear rate ranges were neglected, as only in this selected shear rate interval, the apparatus recorded a Newtonian behavior for water. The final dynamic viscosity values were determined by linearly extrapolating the shear rate to 0. Alginate sols in 0.1 M NaCl were prepared in

mass concentrations of β = 0.0005, 0.00075, 0.001, 0.00125, and 0.0015 g/cm³ and measured in capillary and shearing viscometry. The measured dynamic viscosities were used to calculate the relative, specific, and reduced viscosities of each alginate product at the specific concentration. Intrinsic viscosities were obtained by linear extrapolation of the reduced viscosity values to a mass concentration of 0.

2.4 Morphological Examination

2.4.1 Light-Microscopic Investigation

In order to examine the capillary structure of anisotropic alginate hydrogels, a light-microscopic investigation was performed. By using a scalpel, an eighth of the ethanol-stored gel body was cut off. Utilizing an instant adhesive glue, this portion of the gel was fixed onto a Leica VT 1000 M microtome. Thin 300 µm cross-sections of the gel slice were cut off as a top cut ("5 mm" position, as the first 5 mm of the gel body already had been cut off in the band saw during the gel preparation). After removing one millimeter of the gel body twice, three slices of a middle cut ("6.9 mm" position) and a lower cut ("8.8 mm" position) were also obtained, as portrayed in Figure 32.

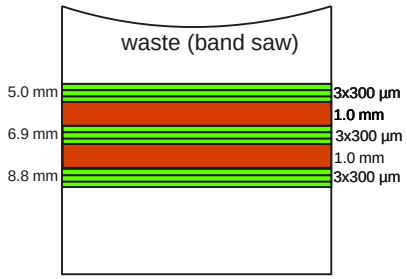

Figure 32: Scheme of the cutting procedure in the microtome for light-microscopic investigation of different positions of the gel bodies, which are represented in green.

For rehydration, the cross-sections were immersed in purified water for at least 30 minutes. The thin slices were applied on microscope slides and stained with fresh ruthenium red solution (200 mg/L). Imaging of the samples was performed with a Nikon Eclipse 400 microscope with an attached Canon EOS 650 D Camera. Three representative pictures of every cross-section level (5.0, 6.9, and 8.8 mm) were recorded with an ISO value of 100, which provided proper, sufficiently bright images. The images were cropped, re-sized, and evaluated with the custom software "Kapi Algi", which exported the diameter and area of every individual capillary. The median, first, and third quartile diameter of all, but of at least 20 different capillaries from the pooled data of all three layers were determined. The capillary density and volume porosity were determined as means (± standard deviation) from the nine individual images in the three

layers. In one instance, to showcase the anisotropy of the capillary features, the capillary diameter, capillary density, and volume porosity were calculated individually for each layer.

2.4.2 Scanning Electron Microscopy

To examine the sample's structure at a lower micron level, the samples underwent SEM imaging. In doing so, small wedges of about 3 – 5 mm were cut from the 70% (v/v) ethanol-immersed samples and rehydrated in 50 mL of purified water overnight. The microscope apparatus was an FEI Quanta 400 FEG environmental SEM (FEI Company, FEI Europe B.V. 5600 KA Eindhoven, the Netherlands, distributed by ThermoFisher Scientific, FEI Deutschland GmbH, 60322 Frankfurt/Main, Germany). The gel samples were fixed to 12.5 mm BP 2152 SEM specimen stubs (BALTIC-Präparation e.K., 58300 Wetter, Germany) by utilizing 12 mm G3347 carbon adhesive tabs (BALTIC-Präparation e.K., 58300 Wetter, Germany). The imaging was performed under a water vapor atmosphere in the low vacuum mode at 1.5 torr to curb sample shrinkage. The electron acceleration voltage amounted to 4 kV, the electron beam spot size to 4 nm, and the working distance ranged from 10.1 to 10.4 mm. For each sample, two different spots were examined, while obtaining a x800 SEM image (340 µm horizontal field width), a x3000 image (90 µm horizontal field width), and a x6000 depiction (45 µm horizontal field width) in each spot. The SEM secondary electrons were detected by a large field detector (FEI) with a pressure-limiting aperture.

2.5 Release of Sodium Alginate in Buffer Medium

To examine the degree of alginate release from the finished gel specimens, Purpald® assays were performed. After oscillatory shearing rheometry measurements at 1, 2, 4, 8, and 12 weeks of PBS immersion at 37 °C, roughly 5 mL of the PBS supernatant of each sample (3 – 5 sample disks) was decanted to a centrifugation tube before renewing the 50 mL of PBS solution. 1.5 mL of each supernatant and respective alginate solutions of known concentration for calibration purposes were transferred to a culture screw-cap tube and 0.5 mL 37% (v/v) (~12 M) HCl solution was added, respectively. Hydrolysis of alginate units was performed at 70 °C for seven days. The acidic solution was neutralized with roughly 650 to 700 µL of 8 M NaOH solution, which was slowly added in 2 to 10 µL increments under pH monitoring. The solution volume was raised to 5 mL by adding the respective amount of acetate buffer (17.99% (v/v) 0.1 M HAc; 82.01% (v/v) 0.1 M NaAc), which adjusted the pH to 5.2 - 5.4. 0.5 mL of the resulting solution was subsequently transferred to a 24-well plate and 0.5 mL of freshly prepared 30 mM sodium *meta*periodate in the same acetate buffer was added. Oxidation of alginate subunits was performed for one hour in the dark. 200 µL of the oxidizing solution was consecutively transferred to a new well plate and 300 µL 1% (w/w) Purpald®

reagent in 1 M NaOH was added. The reaction was performed while shaking and stopped after one hour by adding 0.5 mL 0.4% (w/w) $NaBH_4$ in 1 M NaOH. Eventually, the absorption of the formed purple colorant was measured in triplicates at 546 nm in a UV/VIS spectrometer. The initial dry weight of the samples was determined based on the total volume of 3 mm sample disks, that were prepared for rheometry stability tests in relation to the volume of the alginate hydrogel before the cutting procedure (65 mL) and the respective alginate sol concentration. The incremental amounts of alginate in solution were deducted from this initial amount of alginate to determine the retained alginate at any given point in time.

2.6 Swelling Experiments

Determination of swelling ratios was conducted after gel specimens, that were previously stored in 70% (v/v) ethanol p.a., were swollen in PBS solution overnight. In doing so, the samples ranged from 1 to 2 g in their swollen state after they were immersed in 50 mL of PBS. Subsequently, the samples were gently wiped with a paper towel to remove excess liquid from their surface. The samples were transferred to centrifugation tubes, which had been weighed before and then again after sample loading. Freeze-drying of the sample tubes was performed with un-tightened screw caps overnight at 4 to 8 mbar. Now only containing the solid remains of the alginate samples, the tubes were re-weighed and the swelling ratios were determined according to Eq. 29, with w_s as the weight of the gel specimen in its swollen state and w_d as its weight after freeze-drying.

$$swelling\ ratio = \frac{w_s - w_d}{w_d} \tag{29}$$

Three sample pieces were swollen in separate tubes to determine mean swelling ratios (± standard deviation).

2.7 Reporting and Statistical Analysis

In addition to depicting the first, second, and third quartiles, boxplots also include the representation of the average value (depicted as a small square) and the whiskers extend to the 5^{th} and 95^{th} percentiles. In case it is present, numbering indicates median values. Column diagrams illustrate mean values along with their respective standard deviations and numerical values represent the means. Statistical analysis was performed utilizing Origin(Pro) software (Version 2021 (9.8.0.200), OriginLab Corporation, Northampton, MA, USA) with the pair comparison tool. Statistical analysis was conducted by one- or two-way analysis of variance

(ANOVA) with Bonferroni post-hoc testing. The significance levels of $p \leq 0.05$, $p \leq 0.01$, and $p \leq 0.001$ are indicated in the charts.

3. Results

3.1 Capillary Structure of the Anisotropic Hydrogel

3.1.1 Light-Microscopy

The influence of the concentration of the bivalent cationic species in the initial ionotropic gelation process on the morphology of the final ACH structure was researched by examining 1.0% (w/w) food-grade alginate gels, that had undergone an identical gel preparation process. The physically cross-linked gels had been dehydrated in acetone and were subsequently immersed in 100 mM HDI and cross-linked in and with water to form polyurea-networks. The cations had also been exchanged in an acidic washing process. Four different concentrations of Sr^{2+} had been tested in combination with the food-grade alginate source. As the cation concentration was increased, the respective average capillary diameters demonstrated a statistically significant decrease for every concentration change. Although not significant, a similar trend was observable for the capillary density, as the ion concentration increase entailed a rise in average capillary density, except in the ACHs, which had been physically cross-linked with the highest amount of strontium. Despite a strong trend in the average values, a significant variation in overall volume porosity could only be determined between the highest and lowest concentration of Sr^{2+}-cross-linked ACHs.

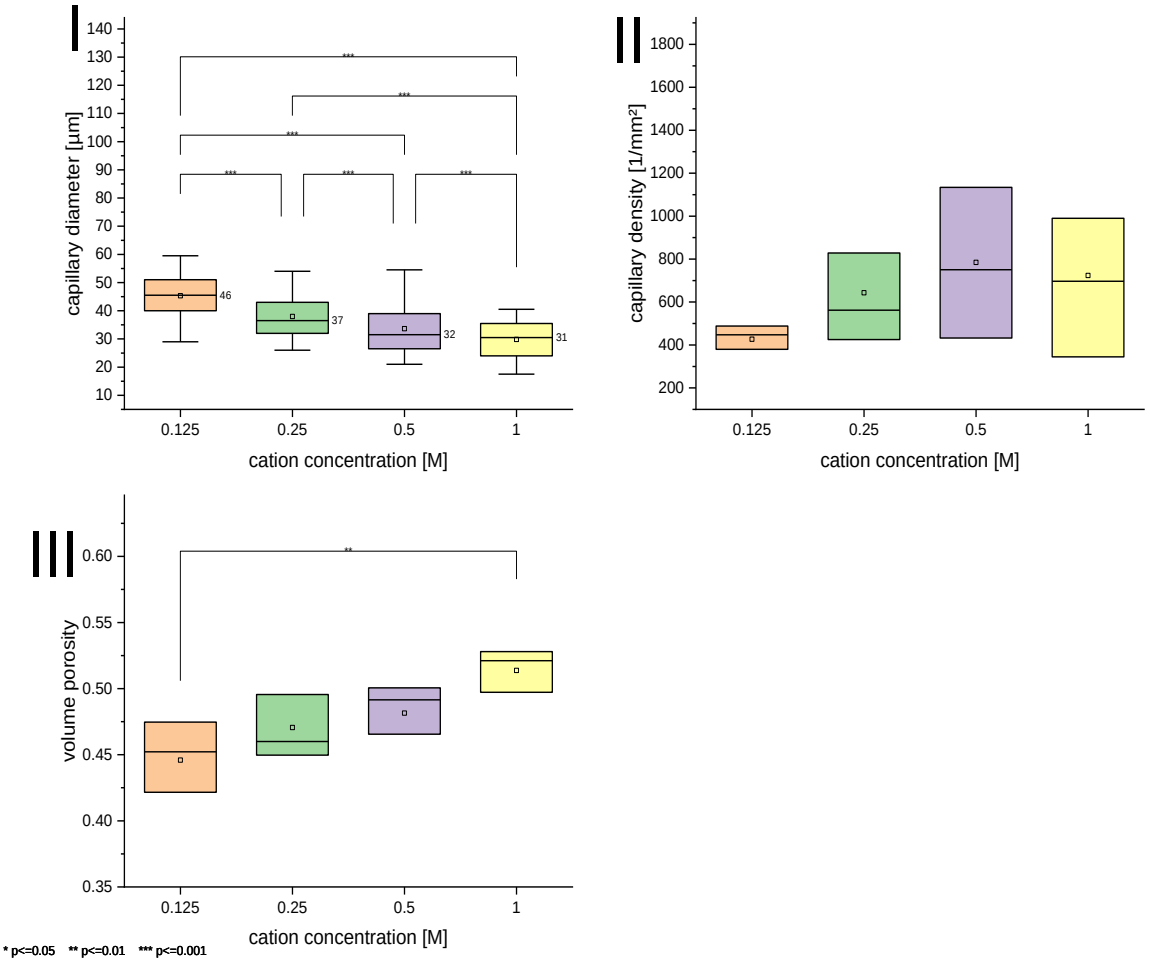

Figure 33: One-way ANOVA with Bonferroni post-hoc testing (ion cross-linker concentration as the parameter) of the capillary diameter (I), capillary density (II), and overall volume porosity (III) of 1.0% (w/w) food-grade ACHs, which were cross-linked with 0.125 – 1.0 M Sr^{2+} and 100 mM HDI in water.

Further, the position-dependent composition of the capillary tubes was determined for 1.0% (w/w) ACHs, that had been cross-linked with 0.125 – 1.0 M Sr^{2+} and 100 mM HDI in water. Gels, that were physically cross-linked with 0.125 M Sr^{2+} demonstrated only slightly increasing capillary diameters and slightly decreasing densities and porosities from the upper to the lower sections, as shown in Figure 34. Higher initial ionic cross-linker concentrations, especially the two highest ones (0.5 M, 1.0 M), entailed hydrogels with distinctly larger capillary diameters in lower positions of the gel body compared to the upper sections of the same specimen. An increase in capillary diameter went along with a decrease in capillary density and a slight decrease in volume porosity in the lower portions of the ACHs in all tested instances.

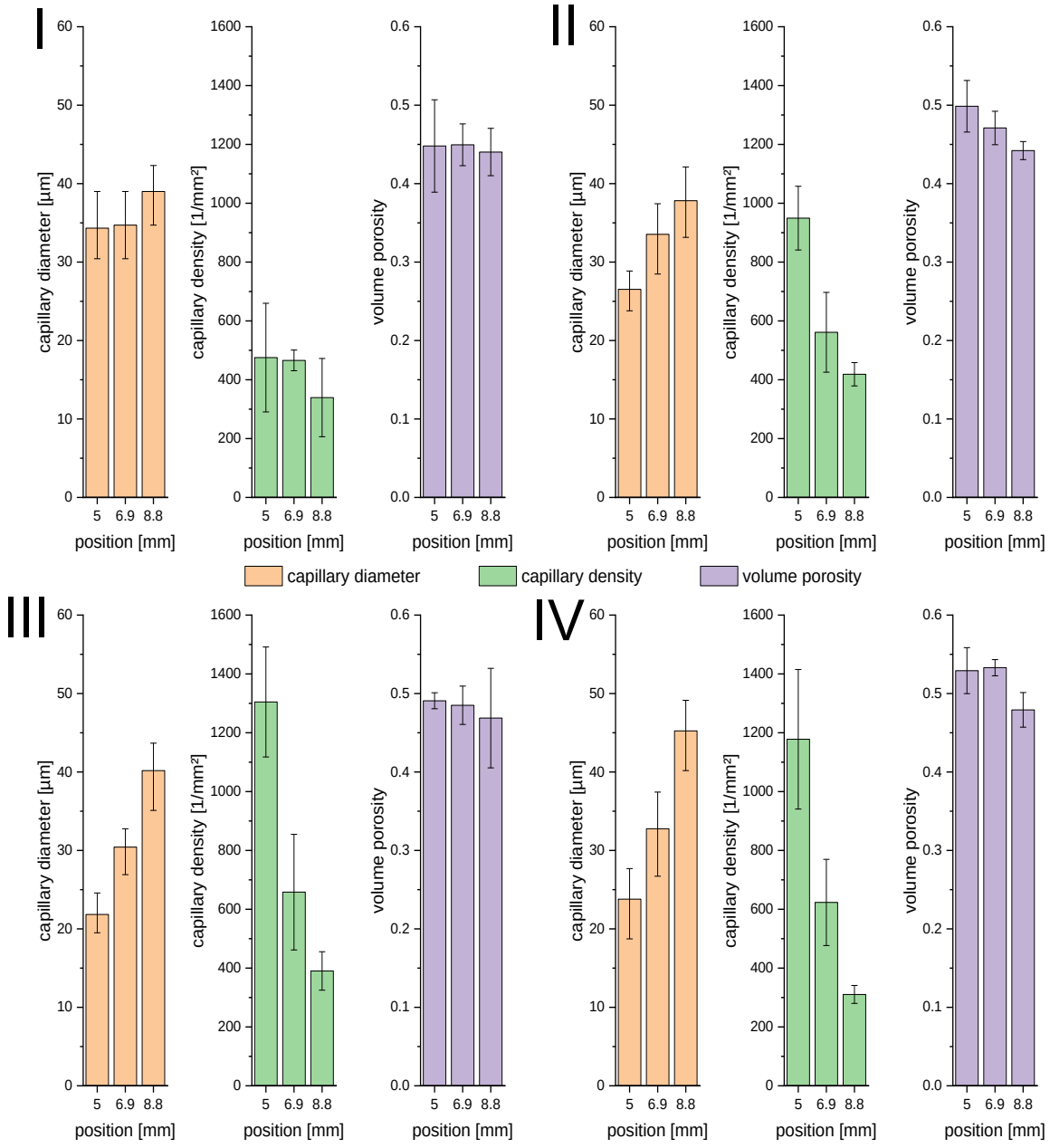

Figure 34: Median capillary diameter, average capillary density, and average volume porosity of 0.125 M Sr^{2+} (I) cross-linked ACHs, of 0.25 M Sr^{2+} (II) cross-linked ACHs, of 0.5 M Sr^{2+} (III) cross-linked food-grade ACHs, and of 1 M Sr^{2+} (IV) cross-linked ACHs (1.0% (w/w) food-grade alginate, 100 mM HDI in-water cross-linking in all cases).

Larger capillaries, as desired, were thought to be obtained by utilizing a $Zn(NO_3)$-based physical cross-linking procedure. However, only very unstructured alginate ACHs could be obtained this way and further food-grade alginate experiments were discontinued. For comparison, Figure 35 shows scaffolds, that were fabricated by different ionotropic cross-linking procedures.

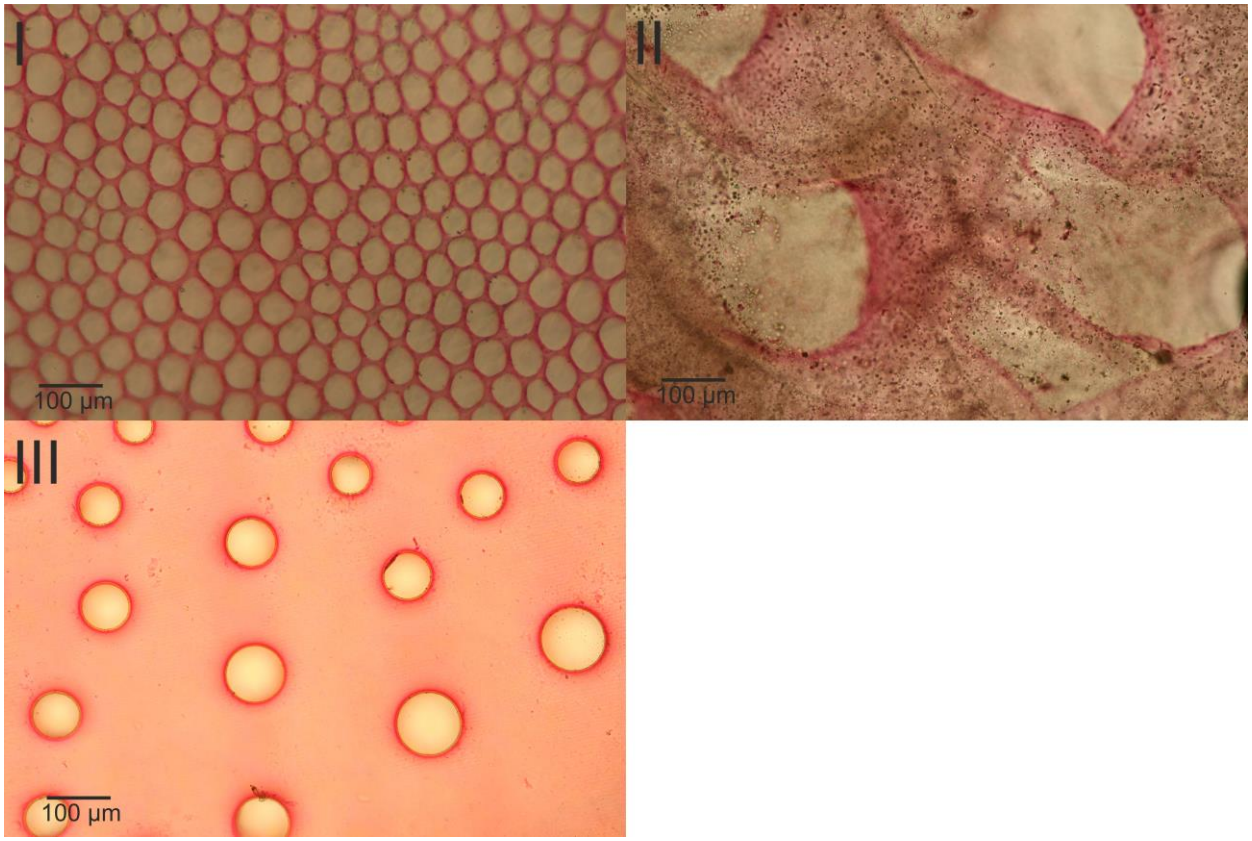

Figure 35: Light-microscopy images (x100) of cross-sections from 1 M Sr^{2+}(I), Zn^{2+} (II), or Ca^{2+} (III) cross-linked food-grade 1.0% (w/w) ACH hydrogel specimens (100 mM HDI in-water cross-linking in all cases).

Also, 1.0 M Ca^{2+}-based hydrogels showed larger capillary structures than Sr^{2+}-based ACHs, while still providing a high degree of structuring, despite significantly lower capillary densities. Unfortunately, no development of any anisotropic structure was present in food-grade alginate gels, as the $Ca(NO_3)_2$ concentration was lowered to 0.125 M in the sprayed solution. Very large and not very dense capillary structures were recorded with 0.25 M or 0.5 M Ca^{2+}-based analogs. As shown in Figure 36, the capillary densities and porosities merely came in at or below 10/mm², respectively 6% (v/v). A better prospect for permissive scaffold structures was obtained by cross-linking the food-grade alginate sol with 1.0 M Ca^{2+}. A significant decrease in median capillary diameter compared to the other Ca^{2+}-ACH to 80 µm was found and the porosity and capillary density rose significantly.

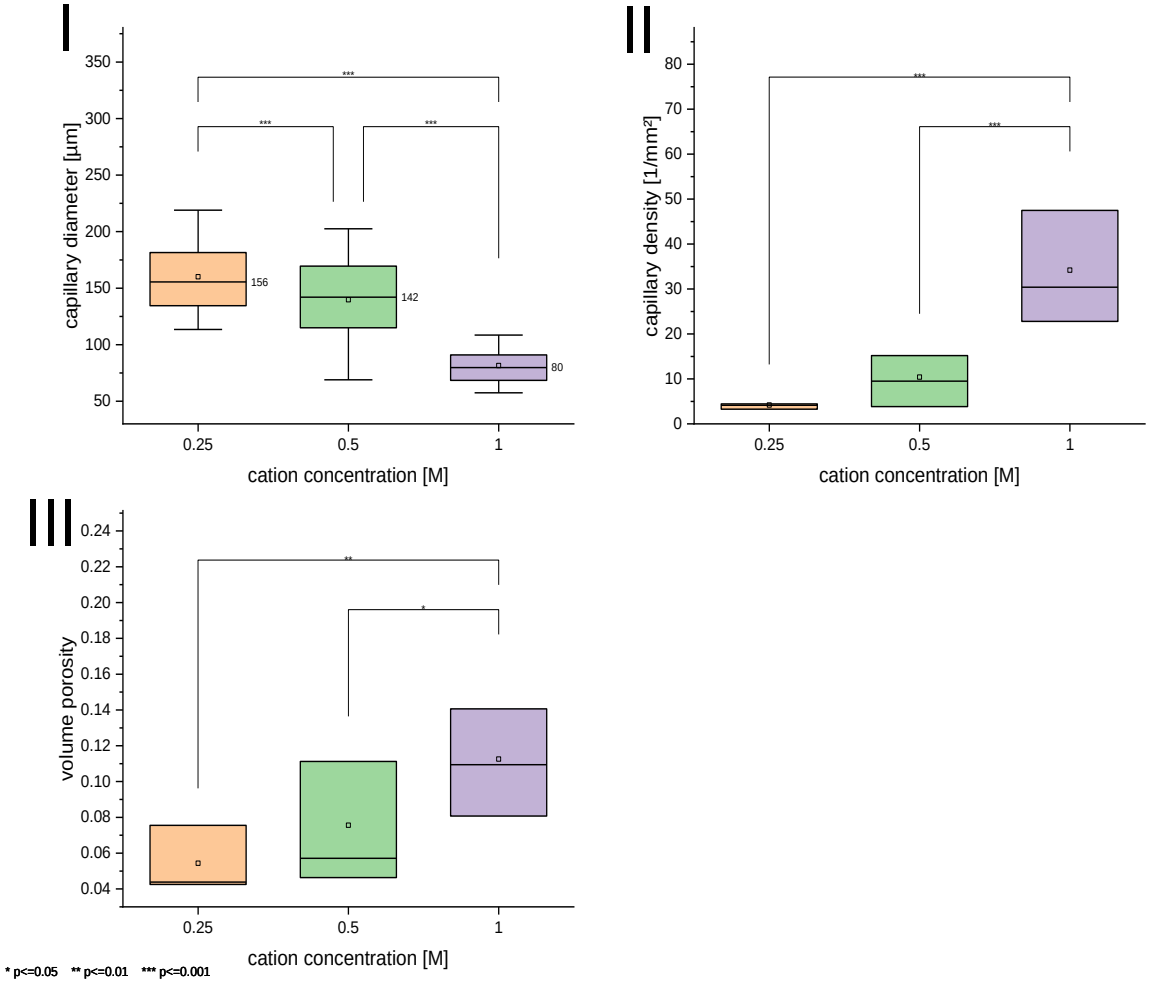

Figure 36: One-way ANOVA with Bonferroni post-hoc testing (ion cross-linker concentration as the parameter) of the capillary diameter (I), capillary density (II), and overall volume porosity (III) of food-grade ACHs, which were cross-linked with 0.25 – 1.0 M Ca^{2+} and 100 mM HDI in water.

As the overall gel morphology of the ACHs is set in the initial physical cross-linking procedure, the concentration of the alginate sol, which is gelled in the process, could also contribute. Food-grade alginate scaffolds of various alginate concentrations, that were cross-linked with 1.0 M Sr^{2+} and 100 mM HDI in water, did not demonstrate any distinct trend in median capillary diameters, which continually resided in the 31 to 49 µm range, as outlined in Figure 37. In contrast, the average capillary density and the overall volume porosity distinctly trended lower with an increase in alginate concentration.

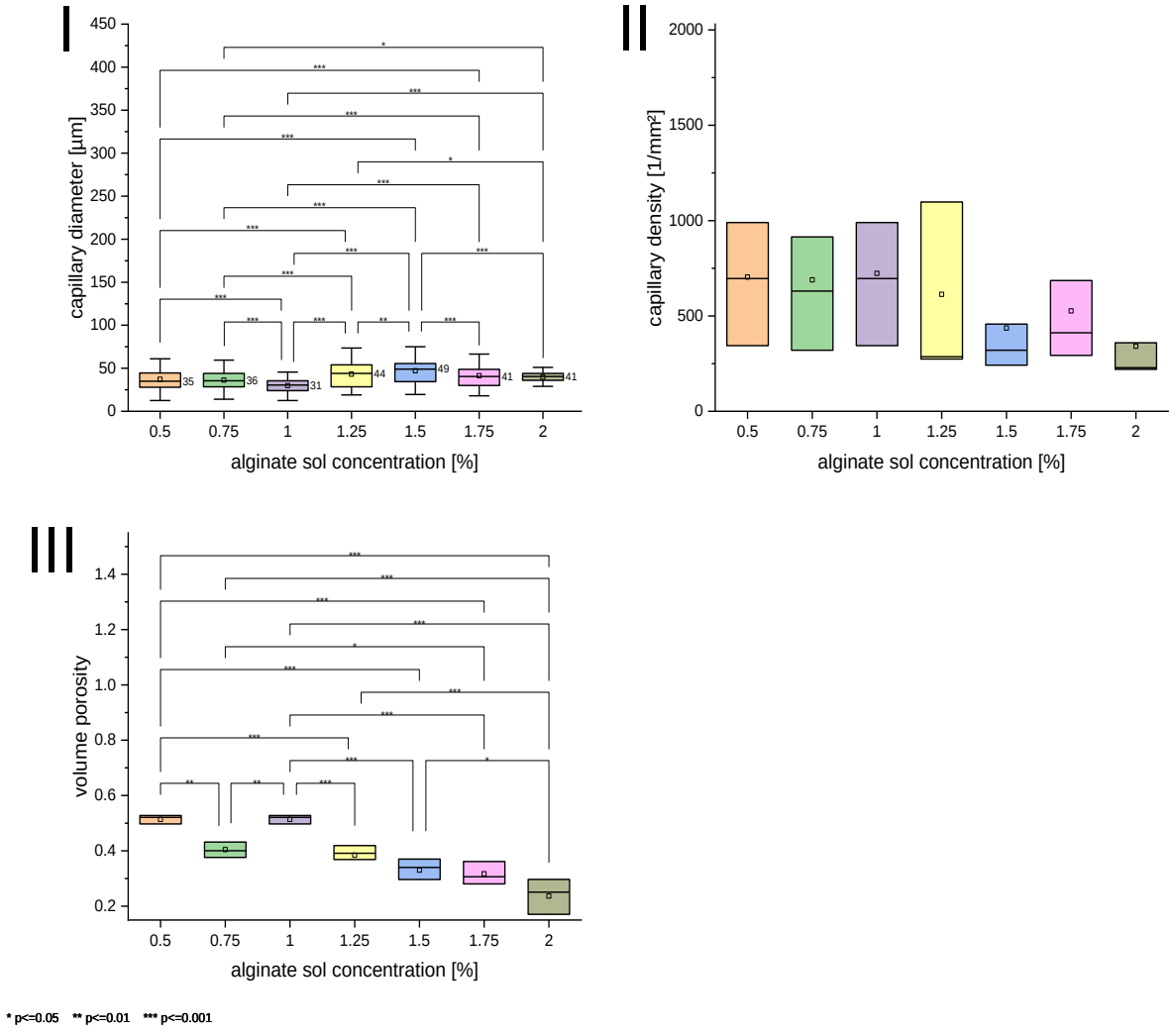

Figure 37: One-way ANOVA with Bonferroni post-hoc testing (alginate concentration as the parameter) of the capillary diameter (I), capillary density (II), and overall volume porosity (III) of 0.5 – 2.0% (w/w) food-grade ACHs, that were cross-linked with 1 M Sr^{2+} and 100 mM HDI in water.

The application of the alginate ACHs in an *in-vivo* scenario necessitated the replication of these results with a medical-grade alginate product. For this purpose, two different medical-grade alginate product batches were deployed, namely PRONOVA UP MVG 1003-03 and 1106-03, which were cross-linked with Sr^{2+}, Zn^{2+}, or Ca^{2+} solutions. As Sr^{2+}-based gelling procedures yielded capillaries much smaller than 80 – 100 µm, very low cation concentrations had to be deployed, while Ca^{2+}-formed hydrogels of lower concentration yielded capillaries too large in size and in an insufficiently dense manner. Therefore, in the latter case, higher initial ion concentrations were targeted. Despite exhibiting hardly any anisotropic structures in the case of the food-grade alginate specimens, zinc-gelled medical-grade ACHs were also examined. As depicted in Figure 38, the Zn^{2+}-based medical-grade hydrogel scaffolds also exhibited very large and unordered

capillary structures. The overall morphology of both Sr^{2+}-gelled medical-grade specimens was quite similar to their food-grade counterparts. Although of a lesser capillary density than Sr^{2+} ones, the Ca^{2+}-based scaffolds offered a very ordered gel structure in line with the results, that were obtained in food-grade experiments.

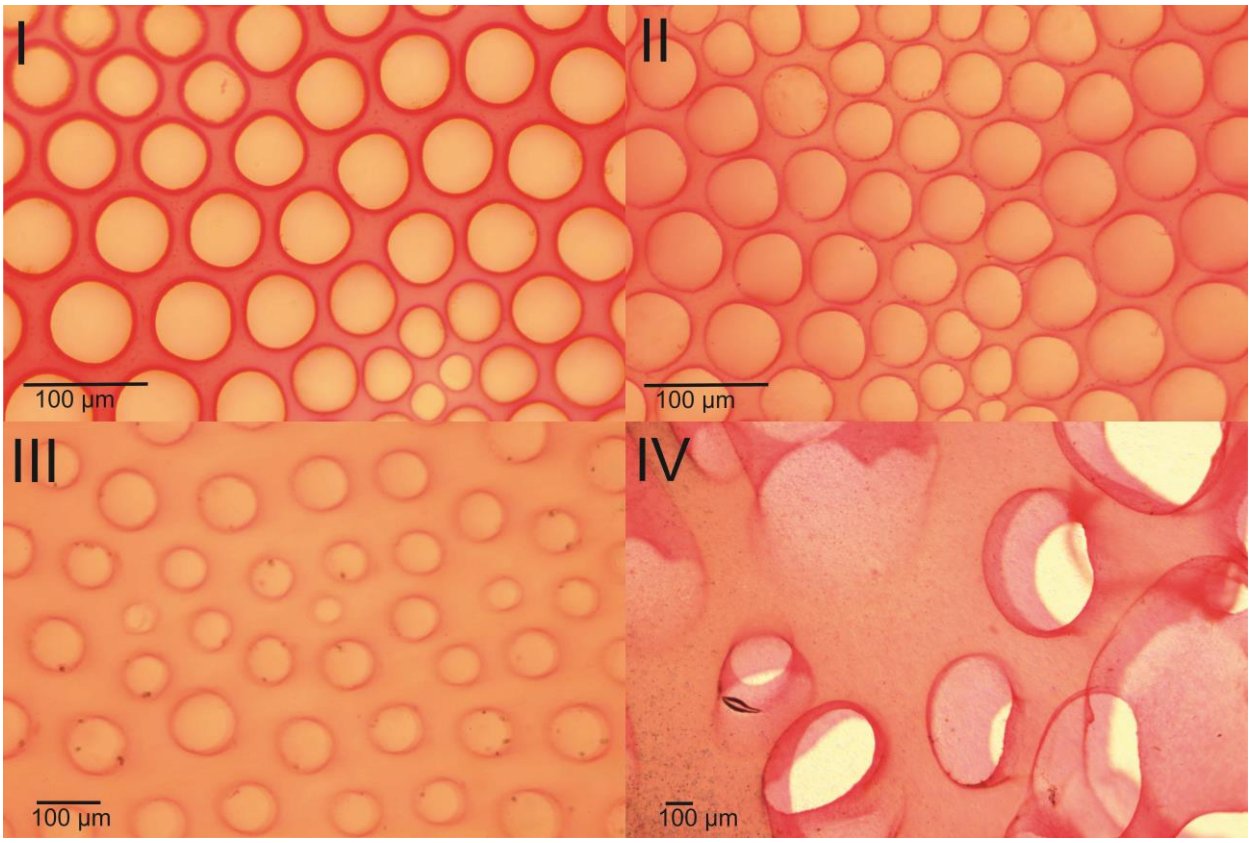

Figure 38: Light-microscopy images of cross-sections from a 0.125 M $Sr^{2+}$and 1.0% (w/w) PRONOVA UP MVG 1003-03 (I (x200)) hydrogel, a 0.125 M Sr^{2+} and 1.0% (w/w) PRONOVA UP MVG 1106-03 (II (x200)) hydrogel, a 1.0 M Ca^{2+} and 1.0% (w/w) PRONOVA UP MVG 1003-03 (III (x100)) hydrogel, and a 1.0 M Zn^{2+} and 1.0% (w/w) PRONOVA UP MVG 1003-03 (IV (x40)) hydrogel (100 mM HDI in-water cross-linking in all cases).

Unlike in food-grade alginate experiments, the significant rise in capillary diameter with a decreasing ion concentration in the ionic cross-linking process could not be replicated in the case of the UP MVG 1003-03 and only to a small extent in the UP MVG 1106-03 Sr^{2+}-hydrogel. As shown in Figure 39, this latter batch yielded UP alginate gels, which also demonstrated a significant increase in capillary density and volume porosity with an increase in cation cross-linker concentration, which was partially also observable, but not of significance in the 1003-03 version of the medical-grade hydrogel.

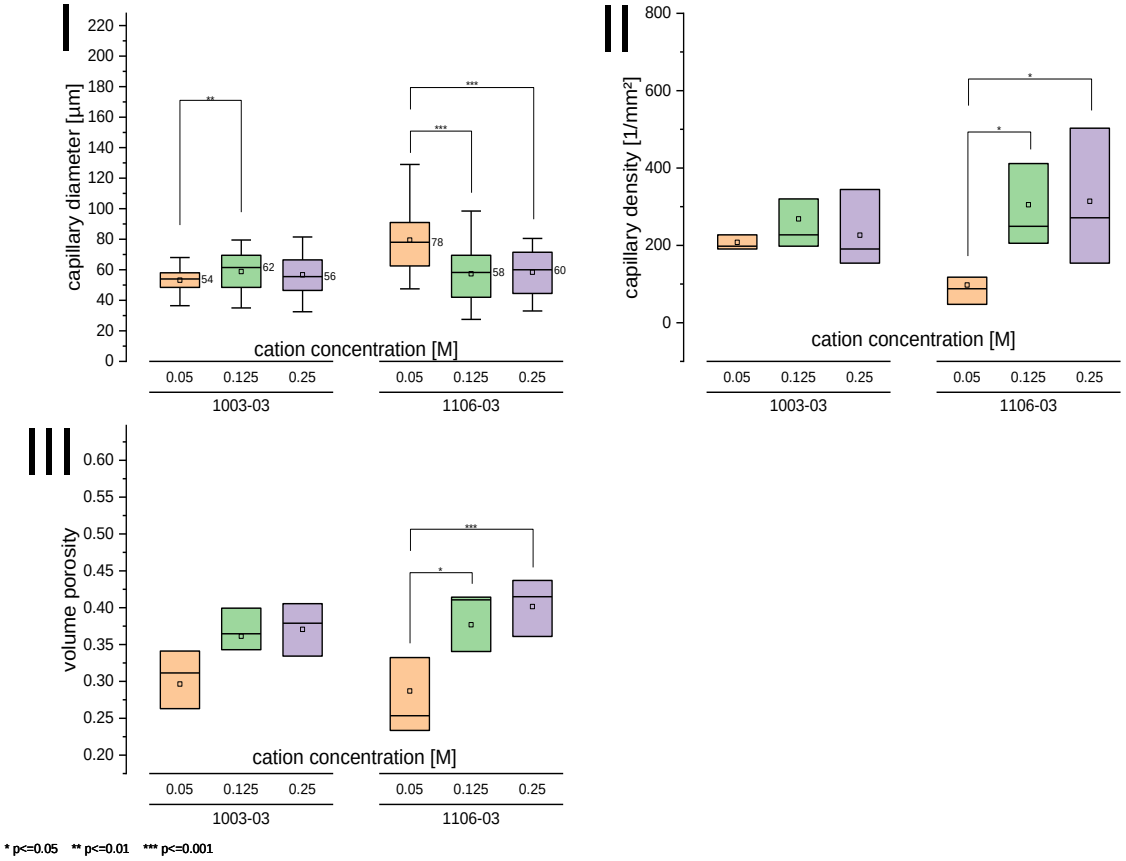

Figure 39: Two-way ANOVA with Bonferroni post-hoc testing (ion cross-linker concentration as the parameter) of the capillary diameter (I), capillary density (II), and overall volume porosity (III) of 1.0% (w/w) UP-MVG 1003-03 or 1106-03 hydrogels, that were cross-linked with 0.05 – 0.25 M Sr^{2+} and 100 mM HDI in water.

With the exception of the capillary diameter in 0.05 M Sr^{2+}-linked alginate scaffolds, the difference in batch origin of the medical-grade UP MVG product did not significantly affect the average capillary diameter, capillary density, or volume porosity in ACHs, that had been cross-linked with 0.05 – 0.25 M Sr^{2+}, like shown below in Figure 40.

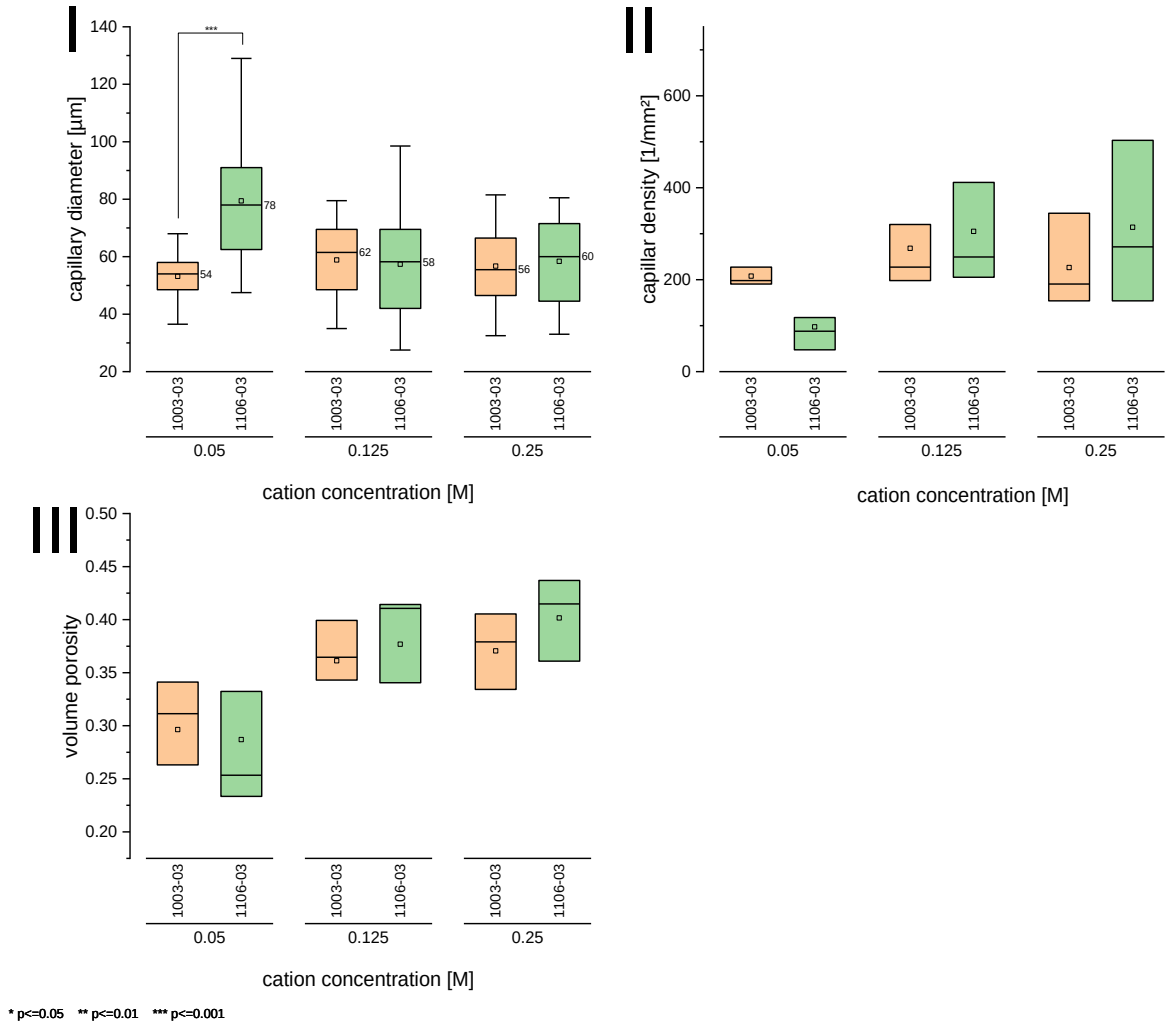

Figure 40: Two-way ANOVA with Bonferroni post-hoc testing (alginate product as the parameter) of the capillary diameter (I), capillary density (II), and overall volume porosity (III) of 1.0% (w/w) UP-MVG 1003-03 or 1106-03 ACHs, that were cross-linked with 0.05 – 0.25 M Sr^{2+} and 100 mM HDI in water.

To account for mechanical requirements, a DMSO-based cross-linking procedure turned out to be favorable as will be outlined in the following sections. In that, the reduction of the ionic cross-linker Sr^{2+} from 0.05 M to 0.025 M significantly increased the capillary diameter in 0.5% (w/w) medical-grade (UP-MVG 1003-03) alginate hydrogels, while decreasing the capillary density and volume porosity as shown in Figure 41. As at this point, strontium-derived ACHs still exhibited median diameters distinctly under 80 – 100 µm and Sr^{2+} concentrations even lower than 0.025 M Sr^{2+} resulted in partially unstructured hydrogels, the fabrication of Ca^{2+}-based medical-grade was honed in on instead. As expected, the HDI cross-linker only marginally affected the diameter of Ca^{2+} or Sr^{2+} medical-grade hydrogels in 0.5 and 1.0% (w/w) samples. The samples 1.0 M Ca 5 mM HDI 0.5% UP-MVG 1003-03, 1.0 M Ca 10 mM HDI 1.0% UP-MVG 1003-03, and 1.0 M Ca 20 mM HDI 1.0% UP-MVG 1003-03 (syntax: ion crosslinker concentration_HDI

concentration_alginate concentration (w/w)_alginate product type), all demonstrated capillary features, which aligned with the aim of this work and underwent further *in-vitro* and *in-vivo* testing at the Spinal Cord Injury Center of the Heidelberg University Hospital.

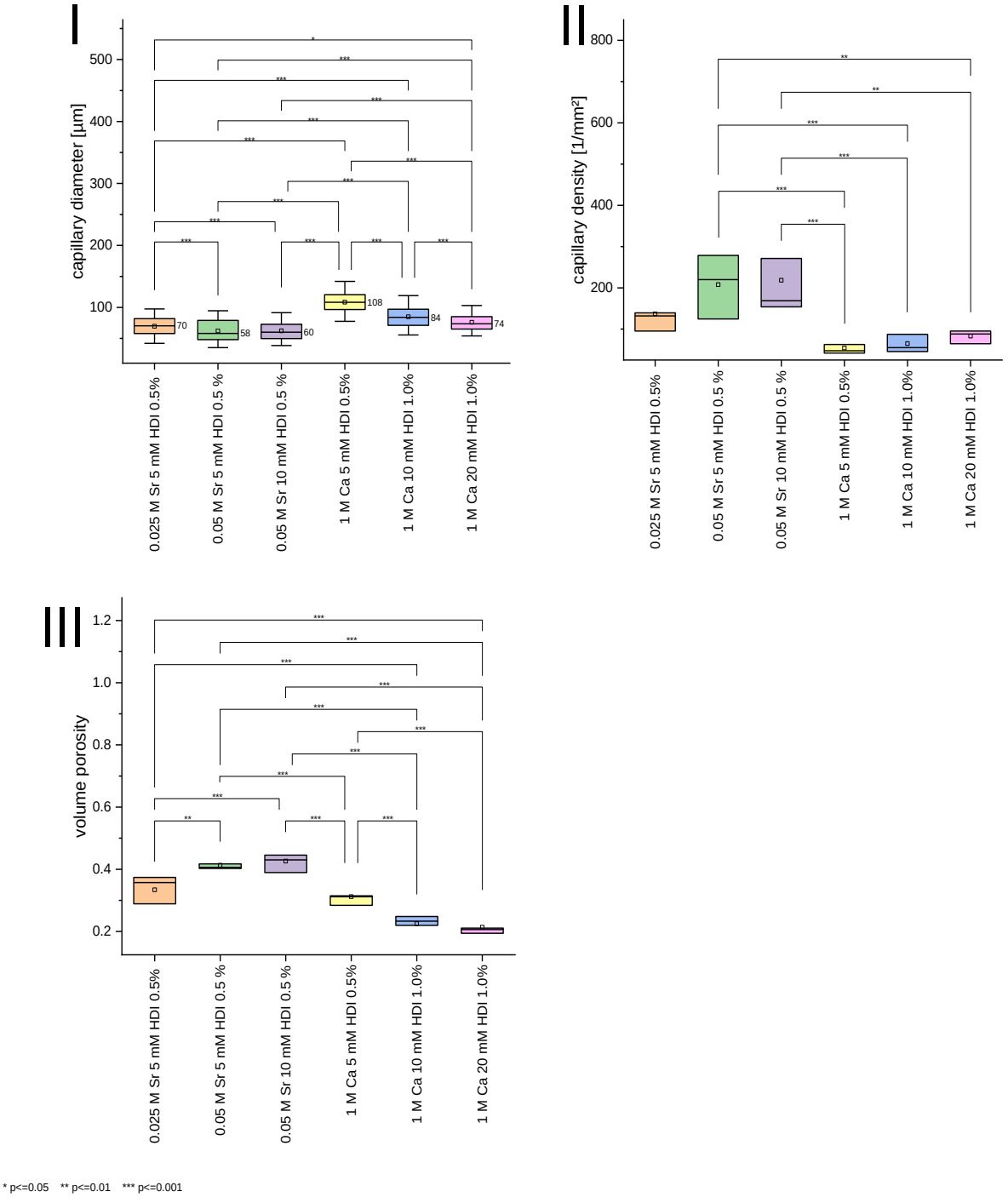

Figure 41: One-way ANOVA with Bonferroni post-hoc testing (sample specimen as the parameter) of the capillary diameter (I), capillary density (II), and overall volume porosity (III) of different Sr^{2+} or Ca^{2+} in-DMSO cross-linked 0.5 or 1.0% (w/w) medical-grade Pronova UP MVG 1003-03 ACHs.

3.1.2 Scanning Electron Microscopy

Scanning electron microscopy was utilized to highlight microscopic differences in the morphology of the capillary walls in detail. A reduction in alginate concentration of in-water cross-linked (100 mM HDI) food-grade ACHs entailed thinner capillary walls and an appearance of an overall weaker structure, as depicted in Figure 42.

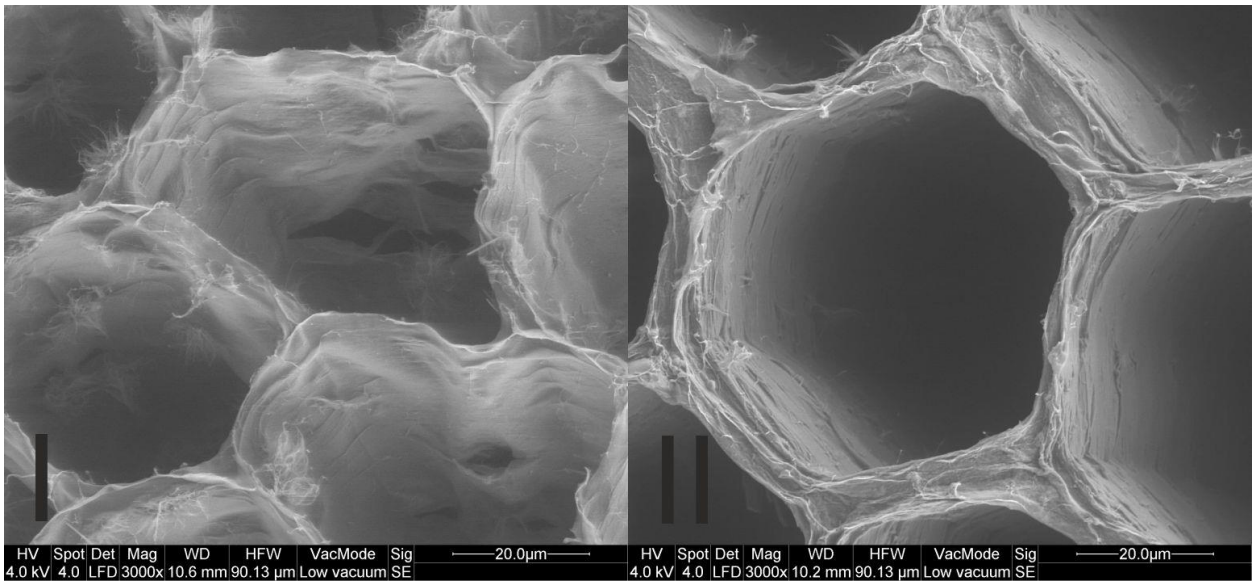

Figure 42: Scanning electron microscopy image (x3000) of 0.5% (w/w) (I) or 1.0% (w/w) (II) food-grade alginate ACHs, that were cross-linked with 1 M Sr^{2+} and 100 mM HDI in water.

Upon changing the cross-linking regimen to a water-free one, the capillary structure appeared to be more uniform and less debris was visible as shown in Figure 43. However, no clear difference in morphology could be established between gels, which were cross-linked with different concentrations of HDI in DMSO in this instance.

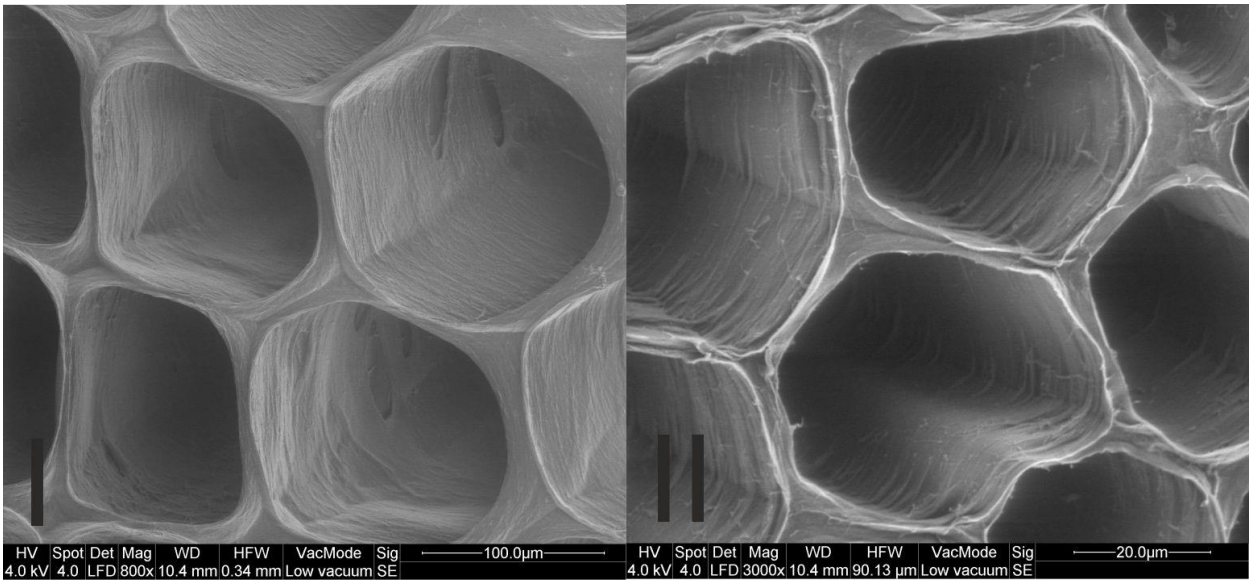

Figure 43: Scanning electron microscopy image (x800 (I) / x3000 (II)) of 1.0% (w/w) food-grade alginate ACHs, that were cross-linked with 1 M Sr^{2+} and 10 mM HDI (I) or 20 mM HDI (II) in DMSO.

Among each other, medical-grade hydrogels of different alginate concentrations demonstrated the same differences in morphology as their food-grade counterparts. Thus, the medical-grade ACH of lesser alginate content demonstrated a less uniform structure, while also exhibiting significantly less pronounced capillary walls than the medical-grade gel of a higher concentration. Overall, no distinct difference in morphology between food- and medical-grade hydrogels was observable.

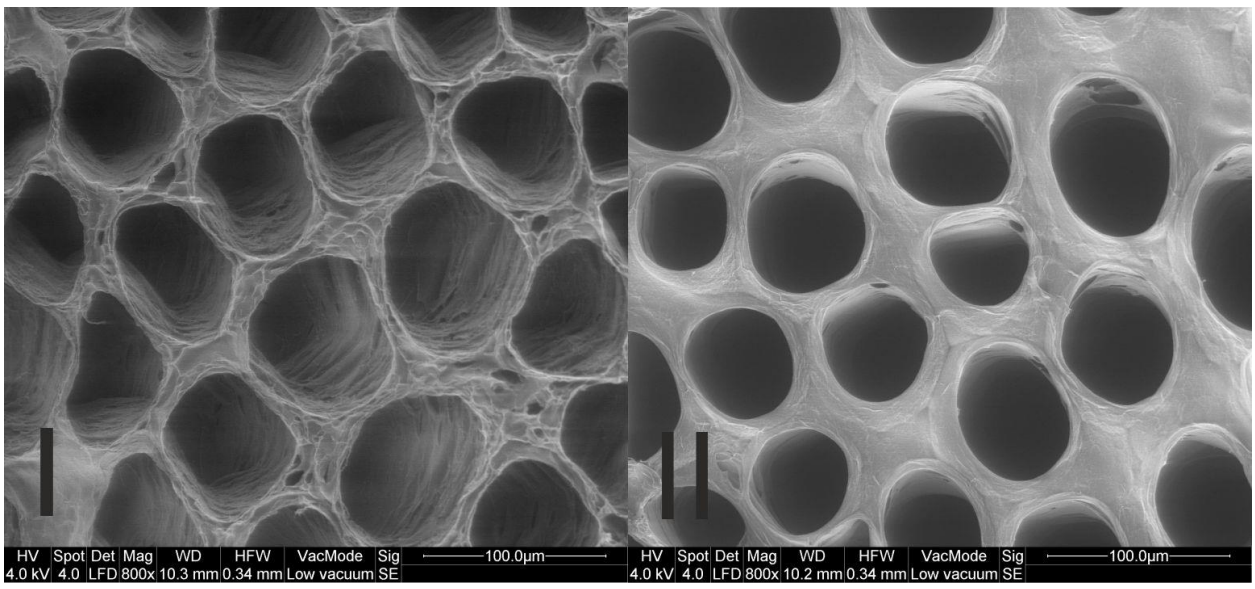

Figure 44: Scanning electron microscopy image (x800) of a 0.5% (w/w) medical-grade alginate ACH (Pronova UP MVG 1003-03), that was cross-linked with 1 M Ca^{2+} and 5 mM HDI in DMSO (I) and of a 1.0% (w/w) medical-grade alginate ACH (Pronova UP MVG 1003-03), that was cross-linked with1 M Ca^{2+} and 10 mM HDI in DMSO (II).

3.2 Mechanical Properties of the Anisotropic Hydrogel

3.2.1 Oscillatory Shearing Rheometry of Food-Grade Alginate Anisotropic Capillary Hydrogels

In order to examine the influence of the capillary structure on the macroscopic mechanical properties of the ACH, oscillatory shearing rheometry was performed on sample slices in a 40 mm parallel plate setup. Samples, that had been obtained from 1.0% (w/w) alginate and various Sr^{2+} concentrations, were chemically cross-linked with 100 mM HDI in water to predominantly form an interpenetrating network of polyurea, underwent oscillatory shearing rheometry, in which the storage moduli and δ values were determined. While the overall morphology of the hydrogel with regard to the capillary diameter, density, and scaffold volume porosity was varying greatly with the concentration of Sr^{2+} in the formation process of the scaffold, the storage moduli G' did not show a significant change, as the cation concentration was varied between 0.125 and 1.0 M. The storage moduli ranged between 8 and 12 kPa, as shown in Figure 45. Further, the variance in δ angles between the stress and responding strain curve was rather small, with mean values fluctuating between 3 to 4 °.

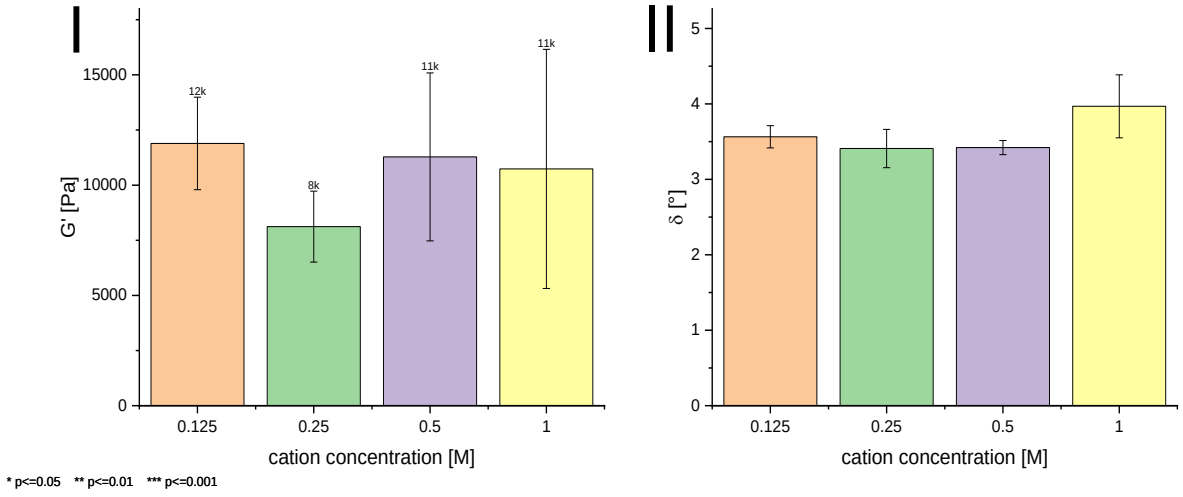

Figure 45: One-way ANOVA with Bonferroni post-hoc testing (ion concentration as the compared parameter) of the storage modulus G' (I) and phase shift δ (II) of 1.0% (w/w) food-grade alginate ACHs, which were cross-linked with 0.125 – 1 M Sr^{2+} and 100 mM HDI in water.

The next tangible parameter to alter our biomaterial's mechanical properties was the concentration of the initial alginate sol. The concentration was increased in 0.25% (w/w) increments, while the physical (1 M Sr^{2+}) and chemical cross-linking (100 mM HDI in water) conditions remained unchanged. As expected, a higher initial concentration of the carbohydrate polymer entailed hydrogel structures of higher stiffness, which would show in significantly higher respective storage moduli G', as can be seen in Figure 46. With

regard to the phase shift δ values, the picture was less clear, as from 0.75 to 2.0% (w/w) a slight increase in angles was present, while between 0.5% and 0.75% (w/w) a decrease occurred.

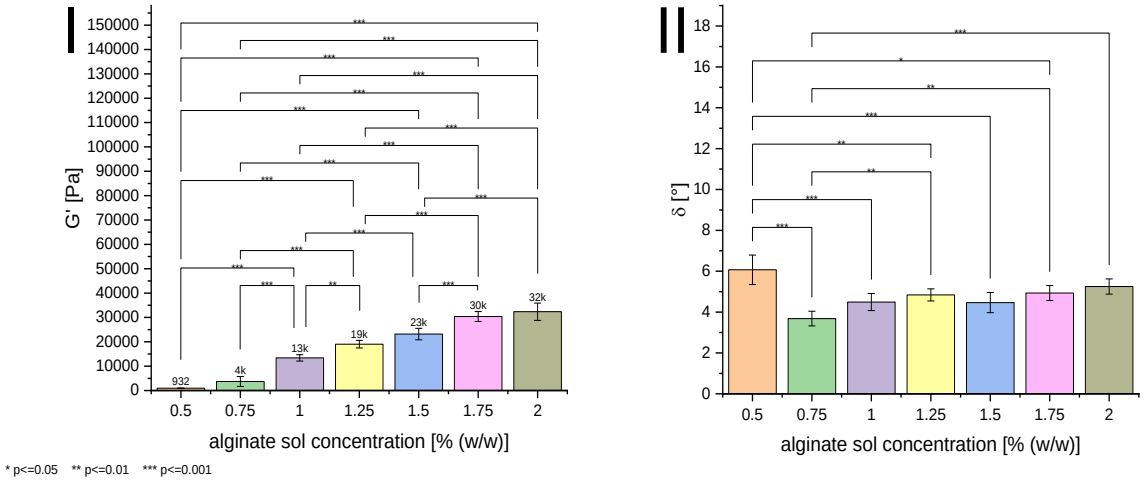

Figure 46: One-way ANOVA with Bonferroni post-hoc testing (alginate sol concentration as the compared parameter) of the storage modulus G' (I), phase shift δ (II) of 0.5 – 2.0% (w/w) food-grade alginate ACHs, which were cross-linked with 1.0 M Sr^{2+} and 100 mM HDI in water.

Not only was a distinct dependency between the alginate concentration and the storage moduli of ACHs observable when the samples had been chemically cross-linked with 100 mM HDI in water but also when the cross-linker concentration was lower. Like shown in Figure 47, an increase from 0.5 to 1.0 and finally to 2.0% (w/w) alginate concentration also entailed an increase in storage modulus, when the samples had been chemically cross-linked with 10, 20, or 50 mM HDI in water. Remarkably, the concentration of the cross-linker itself had no significant influence on the respective shearing moduli.

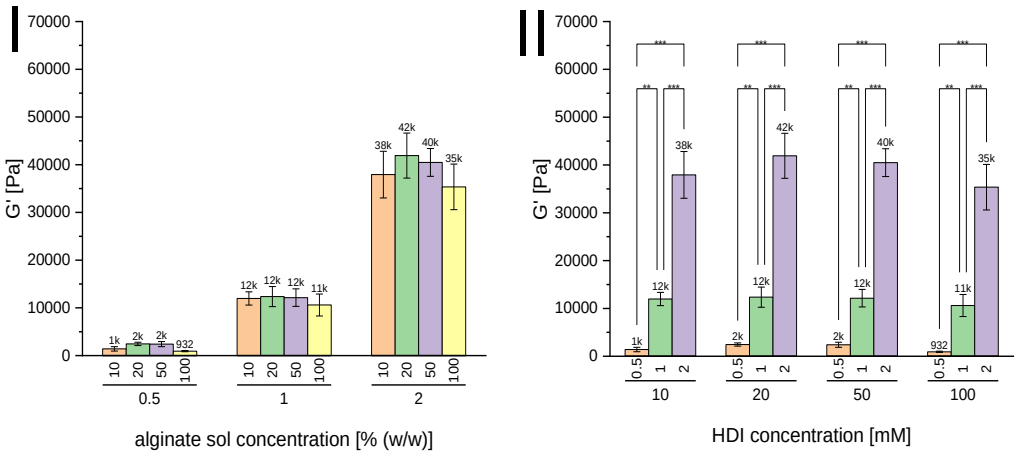

Figure 47: Two-way ANOVA with Bonferroni post-hoc testing (HDI concentration (I) or alginate sol concentration as the compared parameter (II)) of the storage modulus G' of 0.5 – 2.0% (w/w) food-grade alginate ACHs, which were cross-linked with 1.0 M Sr^{2+} and 10 – 100 mM HDI in water.

Just like the storage moduli, the respective phase shift δ values also demonstrated negligible variance as the cross-linker concentration was adjusted between 10 and 100 mM. Further, the angles between the recorded stress and strain curves on average decreased insignificantly as the alginate concentration was increased from 0.5 to 1.0% (w/w), but significantly rose in the 2.0% (w/w) samples in every of the four chemical cross-linker concentration categories compared to the specimens of lesser alginate content with one exception, as depicted in Figure 48.

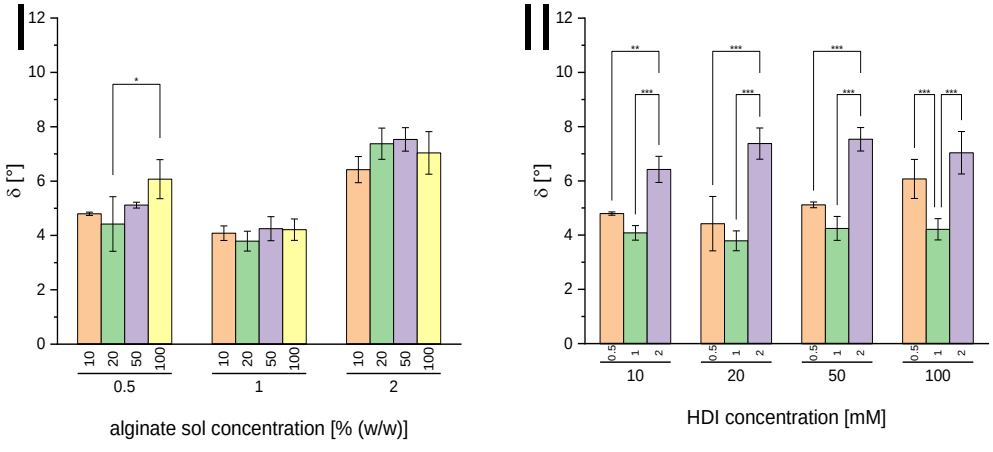

Figure 48: Two-way ANOVA with Bonferroni post-hoc testing (HDI concentration (I) or alginate sol concentration as the compared parameter (II)) of the phase shift angle δ of 0.5 – 2.0% (w/w) food-grade alginate ACHs, which were cross-linked with 1.0 M Sr^{2+} and 10 – 100 mM HDI in water.

As the concentration of the cross-linker HDI in the water-assisted cross-linking procedure did not influence the mechanical properties of the researched alginate scaffolds, the length of the aliphatic chain in the diisocyanate cross-linker was altered and ODI (C8) and DDI (C10) were deployed instead. Just like the variation in HDI concentration did not sway the material's storage moduli, the variation of the ODI or DDI concentration also did not have a significant influence in most instances either. Figure 49 further shows, that the same concentrations of different diisocyanate compounds did not yield hydrogels of significantly different storage moduli.

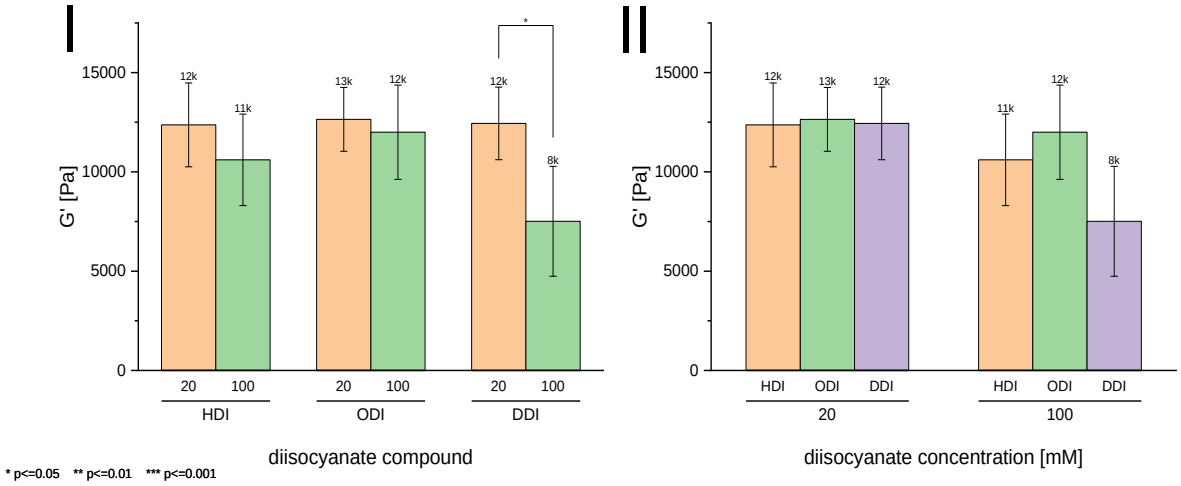

Figure 49: Two-way ANOVA with Bonferroni post-hoc testing (diisocyanate concentration (I) or cross-linker species as the compared parameter (II)) of the storage modulus G' of 1.0% (w/w) food-grade alginate ACHs, which were cross-linked with 1.0 M Sr^{2+} and 20 or 100 mM HDI, ODI, or DDI in water.

Besides the storage moduli, the phase shift δ values also demonstrated no significant changes as the concentration of the respective cross-linker was varied between 20 and 100 mM. However, in both concentration regimes, ODI cross-linked ACHs obtained significantly higher δ values than their HDI stabilized counterparts, as shown in Figure 50.

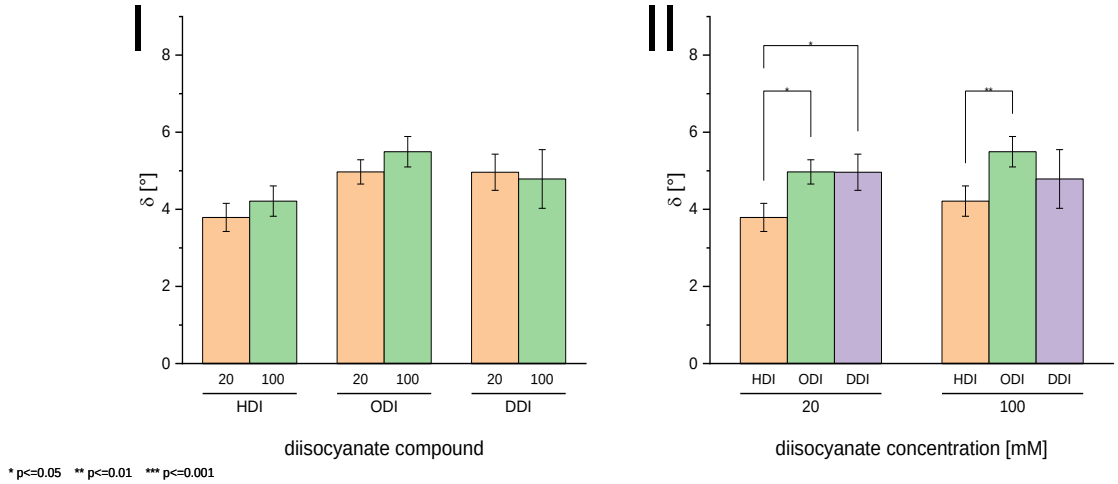

Figure 50: Two-way ANOVA with Bonferroni post-hoc testing (diisocyanate concentration (I) or cross-linker species as the compared parameter (II)) of phase shift δ values of 1.0% (w/w) food-grade alginate ACHs, which were cross-linked with 1.0 M Sr^{2+} and 20 or 100 mM HDI, ODI or DDI in water.

A change in the cross-linking procedure, in which the hydrogel bodies were not cross-linked in water, but in DMSO to form inter- and intramolecular urethane bonds at 125 °C without a polymerization of the diisocyanate compound, was conducted. This resulted in a vastly different relationship between chemical cross-linker and mechanical properties than in prior experiments. As demonstrated in Figure 51, a 100 mM concentration yielded very high storage moduli in oscillatory shearing rheometry of 92 kPa on average. To target the 1 to 10 kPa range, the concentration of the diisocyanate was lowered to as far as 5 mM. Between gels, that had been cross-linked with that concentration and 100 mM, the determined elastic moduli steadily increased with every increase in the diisocyanate concentration. Besides the 5 mM sample, the phase shift values were much higher at around 10 °, compared to the in-water cross-linked samples.

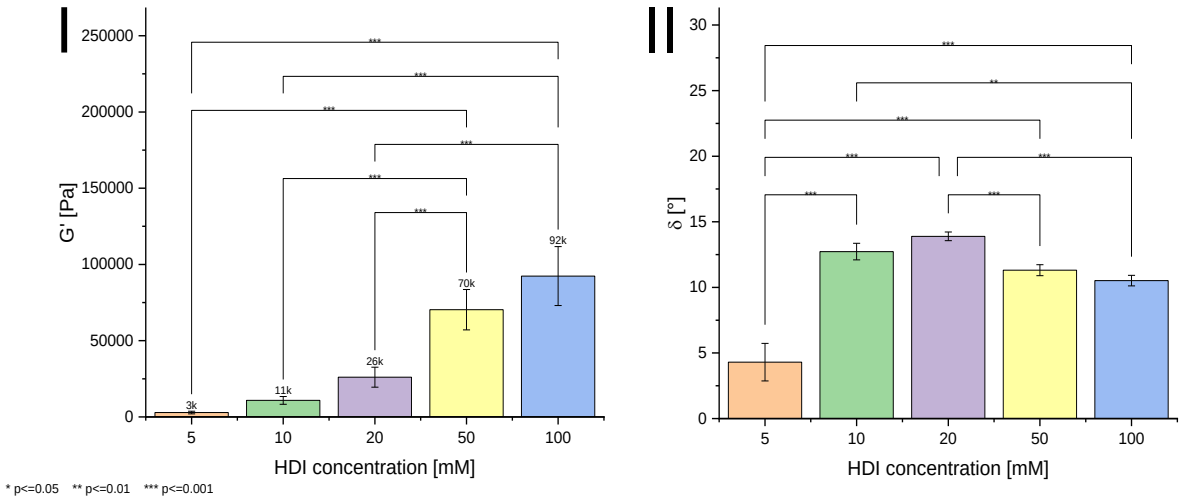

Figure 51: One-way ANOVA with Bonferroni post-hoc testing (HDI concentration as the compared parameter) of the storage modulus G'(I) and phase shift δ (II) of 1.0% (w/w) food-grade alginate ACHs, which were cross-linked with 1 M Sr^{2+} and 5 – 100 mM HDI in DMSO.

By tuning the length of the aliphatic backbone of the diisocyanate cross-linker in a water-free environment, a similar set of shearing mechanical properties could be determined, as showcased in Figure 52. Just like in the case of HDI cross-linking, ODI- and DDI-induced chemical stabilization also lead to higher storage moduli with an increase in the respective diisocyanate concentration in the DMSO cross-linker solution. Further, except when comparing 50 mM cross-linked gels, longer diisocyanate compounds also entailed an increase in the recorded storage modulus.

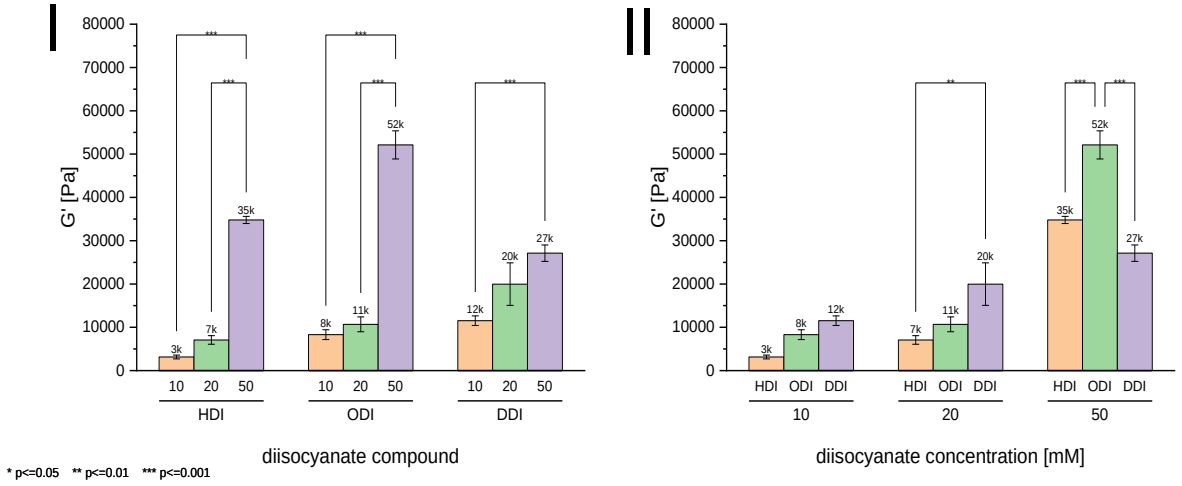

Figure 52: Two-way ANOVA with Bonferroni post-hoc testing (diisocyanate cross-linker concentration (I) or diisocyanate compound as the compared parameter (II)) of the storage modulus G' of 1.0% (w/w) alginate ACHs, which were cross-linked with 1 M Sr^{2+} and 10 – 50 mM HDI, ODI, or DDI in DMSO.

No significant difference with regard to the recorded phase shift δ values for gels, that were cross-linked with different concentrations of the same cross-linker type was observable, as demonstrated in Figure 53. However, for all cross-linker concentrations, which were utilized in water-free cross-linking, DDI-based scaffolds demonstrated the highest phase shift δ values followed by HDI and lastly ODI ones.

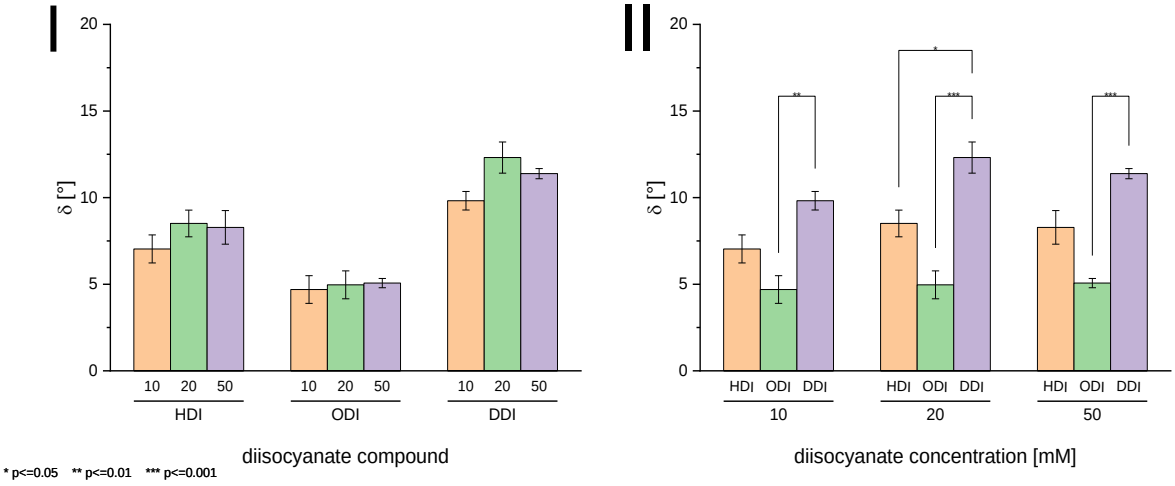

Figure 53: Two-way ANOVA with Bonferroni post-hoc testing (diisocyanate cross-linker concentration (I) or diisocyanate compound as the compared parameter (II)) of the phase shift δ values of 1.0% (w/w) alginate ACHs, which were cross-linked with 1 M Sr^{2+} and 10 – 50 mM HDI, ODI, or DDI in DMSO.

3.2.2 Mechanical Stability of Food- and Medical-Grade Alginate Hydrogels in Oscillatory Shearing Rheometry

As structural integrity plays a vital role in a biomaterial's utility in any tissue engineering application, the mechanical properties of alginate ACHs, which had been immersed in buffer solution for 7, 14, 28, 56, and 84 days in PBS were also determined oscillatory shearing rheometry. Gels, which originated from alginate sols of varying concentration and 1 M Sr^{2+} had been cross-linked with 100 mM HDI in water. After only three hours of PBS immersion, higher storage moduli were recorded for alginate ACHs of higher initial sol concentration. After one week of PBS immersion at 37 °C, all slice bodies maintained their integrity and the respective moduli did not demonstrate a significant change, as demonstrated in Figure 54. After the renewal of the PBS solution and one more week, after 14 days in total, the 0.5 and 0.75% (w/w) based sample disks partially disintegrated and no subsequent measurements could be performed in those instances. At this point, the 1.0% (w/w) sample was much lower in elastic modulus than after seven days, before it completely disintegrated as well. The 1.25 and the 1.5% (w/w) samples also yielded significantly lower storage moduli after 14 days. Their G' values remained in the 4 to 6 kPa range, while the 1.75 and 2.0% (w/w) samples registered a steady decline down to the same storage modulus level over an 8-week

timeframe. At twelve weeks into the stability experiment, no coherent sample of any alginate concentration could be examined as the sample disks would immediately tear upon contact. In section 3.2.1, it was shown, that no significant differences in phase shift values between samples of differing alginate concentration could be denoted. The same held true in this experiment over the timespan of three months.

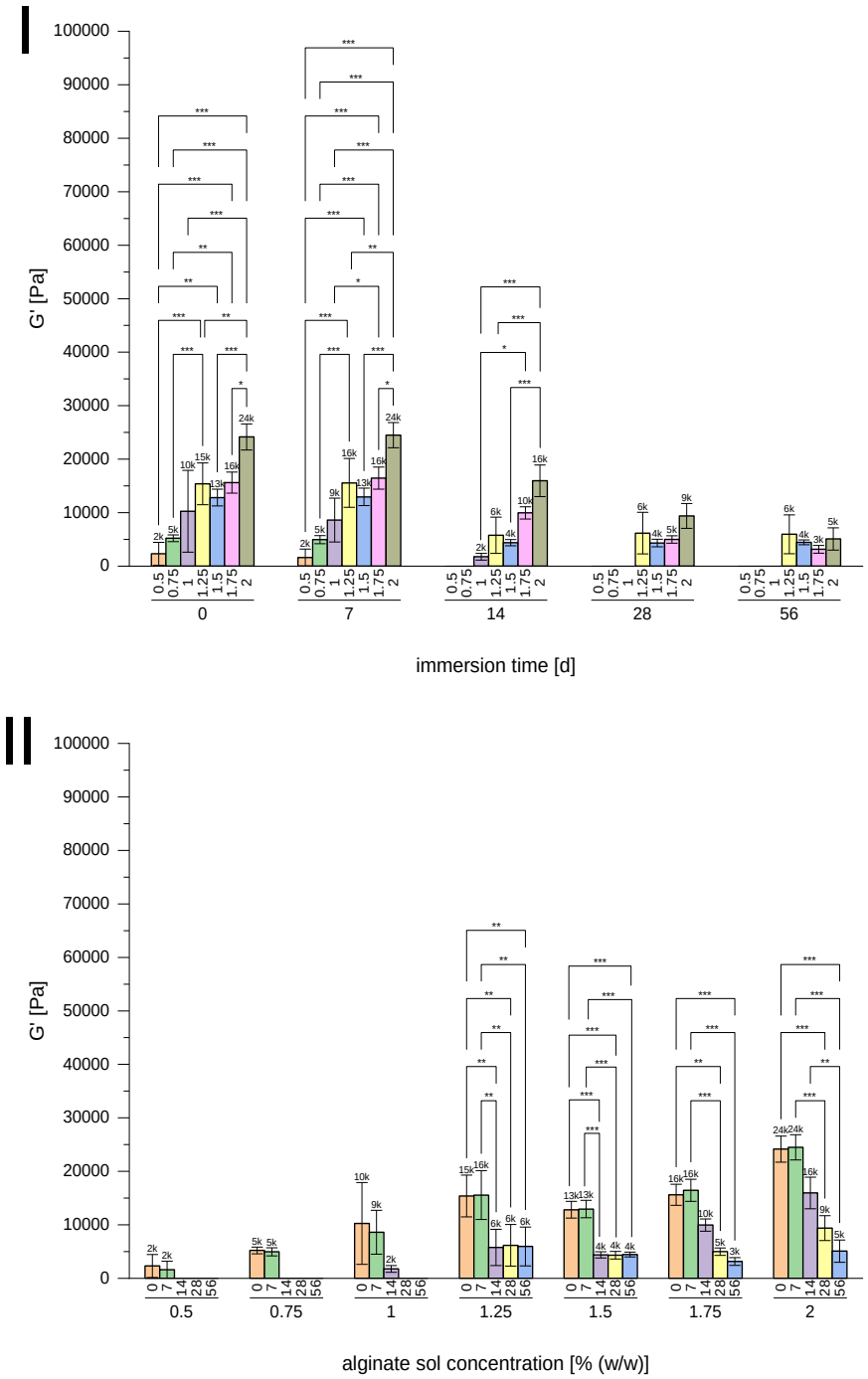

Figure 54: Two-way ANOVA with Bonferroni post-hoc testing (alginate sol concentration (I) or immersion time in PBS as the compared parameter (II)) of the storage modulus G' of 0.5 – 2.0% (w/w) food-grade alginate ACHs, which were cross-linked with 1.0 M Sr^{2+} and 100 mM HDI in water and were stored in renewed PBS solutions for twelve weeks.

By changing the density of an interpenetrating polymer network, which is not subject to ion-exchange reactions like the alginate polymer, one would assume, that this offers a pathway to alter the stability of the entire gel body in a buffer solution. As 100 mM in-water cross-linked 1.0% (w/w) food-grade alginate hydrogels were found to be only partially resilient in the buffered saline solution, 200 mM cross-linked ACHs were also examined in this instance. Although not significant, the 200 mM hydrogel specimen tended to be stiffer on average compared to its less cross-linked counterparts, as showcased in Figure 55. The alginate scaffolds, that had been cross-linked with 20 or 50 mM HDI maintained their mechanical integrity after seven days but completely disintegrated thereafter. The 100 mM samples performed slightly better in that regard, as they held up for up to 14 days as already highlighted above. Polymer gels, that were cross-linked with the highest HDI concentration, only disintegrated after 56 days or 8 weeks into the experiment with continuously declining storage moduli up to that point. No significant difference in the phase shift δ values with varying HDI concentration nor immersion time was determined in any instance.

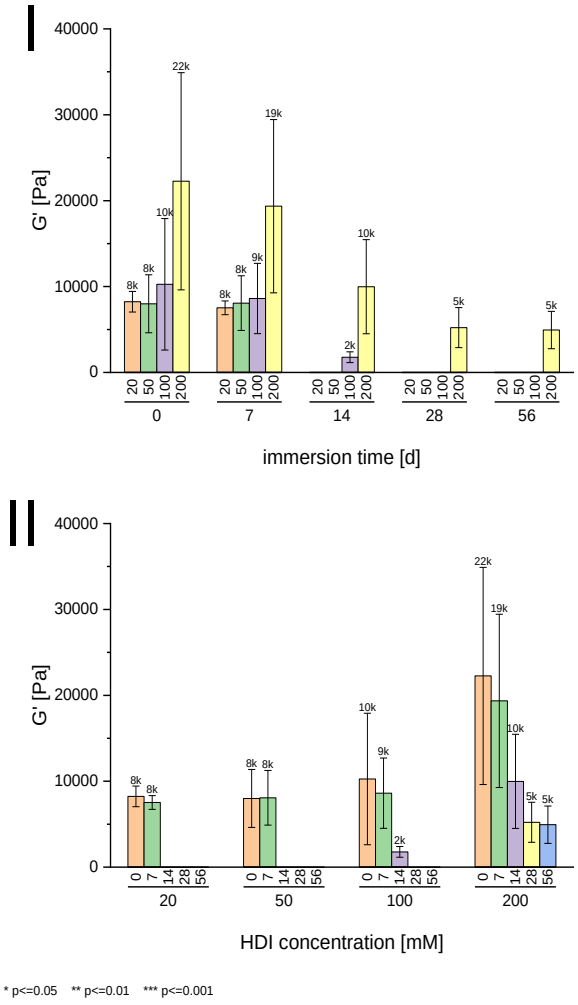

Figure 55: Two-way ANOVA with Bonferroni post-hoc testing (HDI cross-linker concentration (I) or immersion time in PBS as the compared parameter (II)) of storage moduli G' of 1.0% (w/w) food-grade alginate ACHs, which were cross-linked with 1.0 M Sr^{2+} and 20 – 200 mM HDI in water and were stored in renewed PBS solutions for twelve weeks.

In order to improve the resilience of alginate hydrogels in PBS, especially of the softer gel types, which are of a lower alginate concentration and had been cross-linked with lower amounts of HDI, the novel cross-linking procedure was utilized to cross-link gels in a water-free surrounding. As demonstrated by Figure 56 (I), 1.0% (w/w) alginate ACHs, which were cross-linked with 5 or 10 mM HDI in DMSO also failed to sustain their integrity beyond seven days of PBS immersion, just like the 20, 50, and for the most part, 100 mM in-water cross-linked samples, as shown before. However, as the alginate concentration was reduced to 0.5% (w/w), equal amounts of diisocyanate cross-linker sufficed to attain stability over the full 12-week long period of the experiment, whilst maintaining a constant level of mechanical stability according to the recorded storage moduli G', which is depicted in Figure 56 (II). Notably, an increase from 5 to 10 mM HDI did not alter the range of obtained storage moduli for 0.5% (w/w) food-grade hydrogels,

which contradicts the findings for 1.0% (w/w) hydrogels. Phase shift δ values also maintained a constant level of around 5 ° for all in-DMSO cross-linked 0.5% (w/w) food-grade samples over the whole 12-week timeframe, which was significantly lower than what was found for 1.0% (w/w) food-grade gels in the prior section.

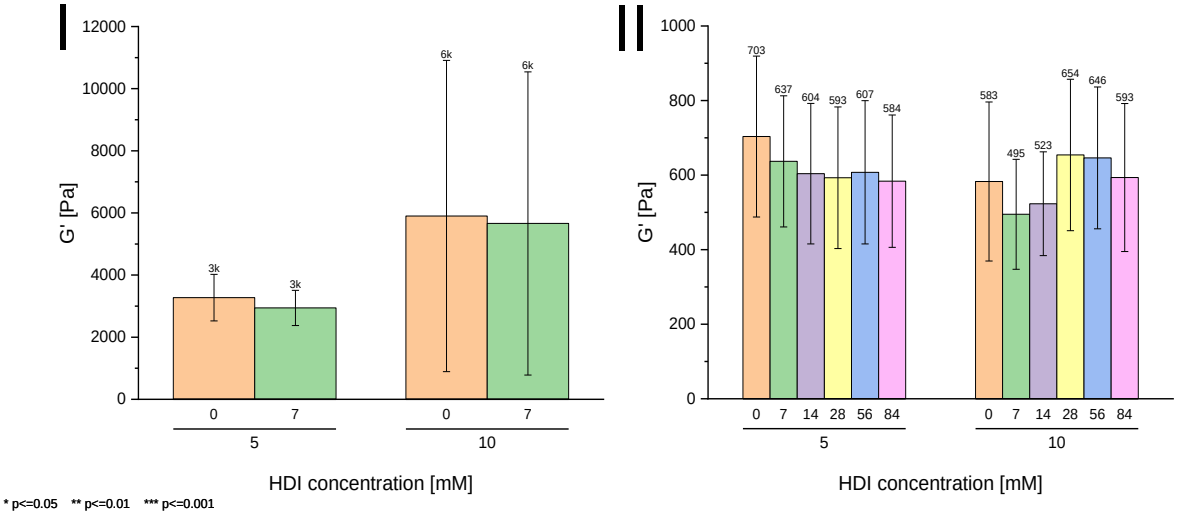

Figure 56: Two-way ANOVA with Bonferroni post-hoc testing (immersion time in PBS in days as the compared parameter) of storage moduli G' of 1.0% (w/w) (I) or 0.5% (w/w) (II) food-grade alginate ACHs, which were cross-linked with 1.0 M Sr^{2+} and 5 or 10 mM HDI in DMSO and were stored in renewed PBS solutions for twelve weeks.

Accordingly, the stability of medical-grade ACHs in the same environment, which ought to simulate a physiological setting, was also determined. As compared in Figure 57, a 0.5% (w/w) food-grade hydrogel (Protanal), which had been initially gelled with 1 M Sr^{2+} and chemically stabilized with 5 mM HDI in DMSO, and a 0.5% (w/w) medical-grade ACH (UP MVG 1003-03), which was formed with 1 M Ca^{2+} and cross-linked with an identical amount of HDI, yielded quite different elastic moduli consistently over the course of twelve weeks. However, in both instances, no significant decrease in mechanical stiffness could be determined. The stress-strain phase shifts were in the 4 to 6 ° range, with no significant variation between the food- and medical-grade counterparts.

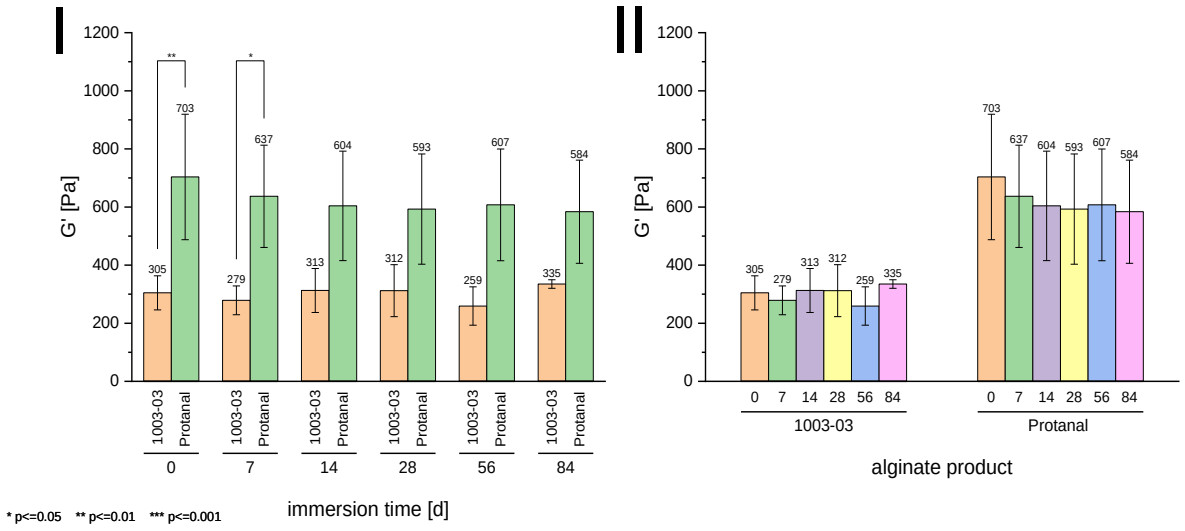

Figure 57: Two-way ANOVA with Bonferroni post-hoc testing (alginate product type (I) or immersion time in PBS in days as the compared parameter (II)) of storage moduli G' of 0.5% (w/w) alginate ACHs, which were cross-linked with 1.0 M Sr^{2+}(Protanal) or 1.0 M Ca^{2+}(UP-MVG 1003-03) and 5 mM HDI in DMSO and were stored in renewed PBS solutions for twelve weeks.

To attain medical-grade hydrogels of a higher elastic modulus in the 1 to 10 kPa range, alginate ACHs of a higher alginate content were cross-linked with higher amounts of HDI and underwent the same stability testing in PBS. PRONOVA UP-MVG 1003-03 and 1106-03 were deployed in 1.0 M Ca^{2+} and 1.0% (w/w) alginate hydrogels and cross-linked with 10 mM HDI in DMSO. As apparent in Figure 58, both types of medical-grade hydrogels were much more stable in the buffer solution than a similar 1.0 M Sr^{2+} and 1.0% (w/w) food-grade Protanal hydrogel, which had been chemically stabilized according to the same procedure. The food-grade hydrogel only maintained its integrity for seven days as was also demonstrated prior in Figure 56 (I), while both UP gels did not significantly decrease their mechanical rigidity during a 4-week period, after which the experiment was stopped, as no change in mechanical properties had occurred until that point in time. Overall, medical-grade ACHs exhibited lower overall storage moduli in the 2 to 3 kPa range and much less variability between sample disks of the same parameter group. No significant difference in storage moduli could be determined between groups or with time, at least as long as the food-grade hydrogel samples were still intact.

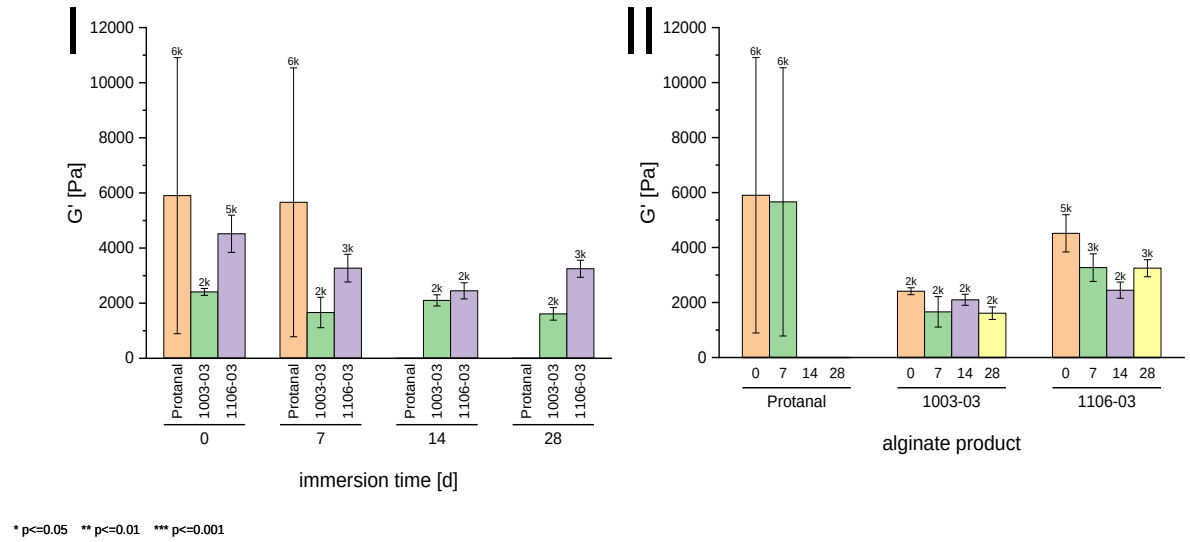

Figure 58: Two-way ANOVA with Bonferroni post-hoc testing (alginate product type (I) or immersion time in PBS as the compared parameter (II)) of storage moduli G' of 1.0% (w/w) alginate ACHs, which were cross-linked with 1.0 M Sr^{2+}(Protanal) or 1.0 M Ca^{2+}(UP-MVG 1003-03/1106-03) and 10 mM HDI in DMSO and were stored in renewed PBS solutions for four weeks.

Remarkably, the stress-strain phase shift values of both medical-grade hydrogel specimens were significantly higher than those of the food-grade sample of the same alginate and HDI concentration, as demonstrated in Figure 59. Furthermore, as time went on, the δ values significantly decreased in both types of medical-grade hydrogels during the four weeks.

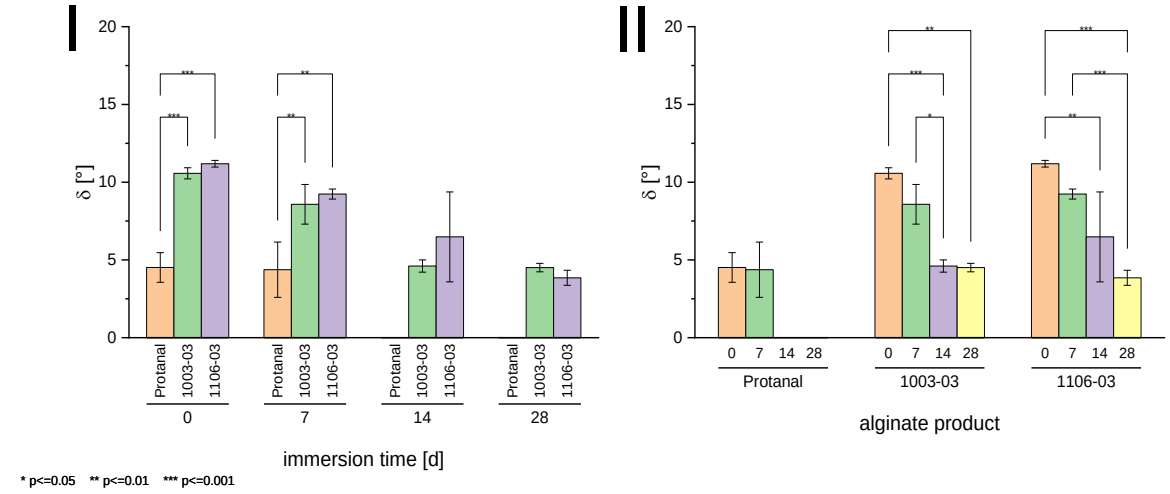

Figure 59: Two-way ANOVA with Bonferroni post-hoc testing (alginate product type (I) or immersion time in PBS as the compared parameter (II)) of phase shift δ angles of 1.0% (w/w) alginate ACHs, which were cross-linked with 1.0 M Sr^{2+}(Protanal) or 1.0 M Ca^{2+}(UP-MVG 1003-03/1106-03) and 10 mM HDI in DMSO and were stored in renewed PBS solutions for four weeks.

Higher HDI concentrations were deployed to attain even higher storage moduli. As shown in Figure 60, an increase of the diisocyanate compound to 20 and 50 mM HDI elevated the mean G' values to ~9,

respectively, 18 – 25 kPa, which in the latter case exceeded the upper targeted range, that had been set as the goal of this work. In accordance with the three samples 1 M Ca 5 mM HDI 0.5% UP-MVG 1003-03, 1 M Ca 10 mM HDI 1.0% UP-MVG 1003-03, and 1 M Ca 10 mM HDI 1.0% UP-MVG 1106-03, which were evaluated in Figure 57 and 58, the 1 M Ca 20 mM HDI 1.0% UP-MVG 1003-03 sample suffered no loss in mechanical integrity over the course of four weeks. Only in the stiffest medical-grade hydrogel class, which was cross-linked with 50 mM, a significant decrease in mechanical rigidity was recognizable with time.

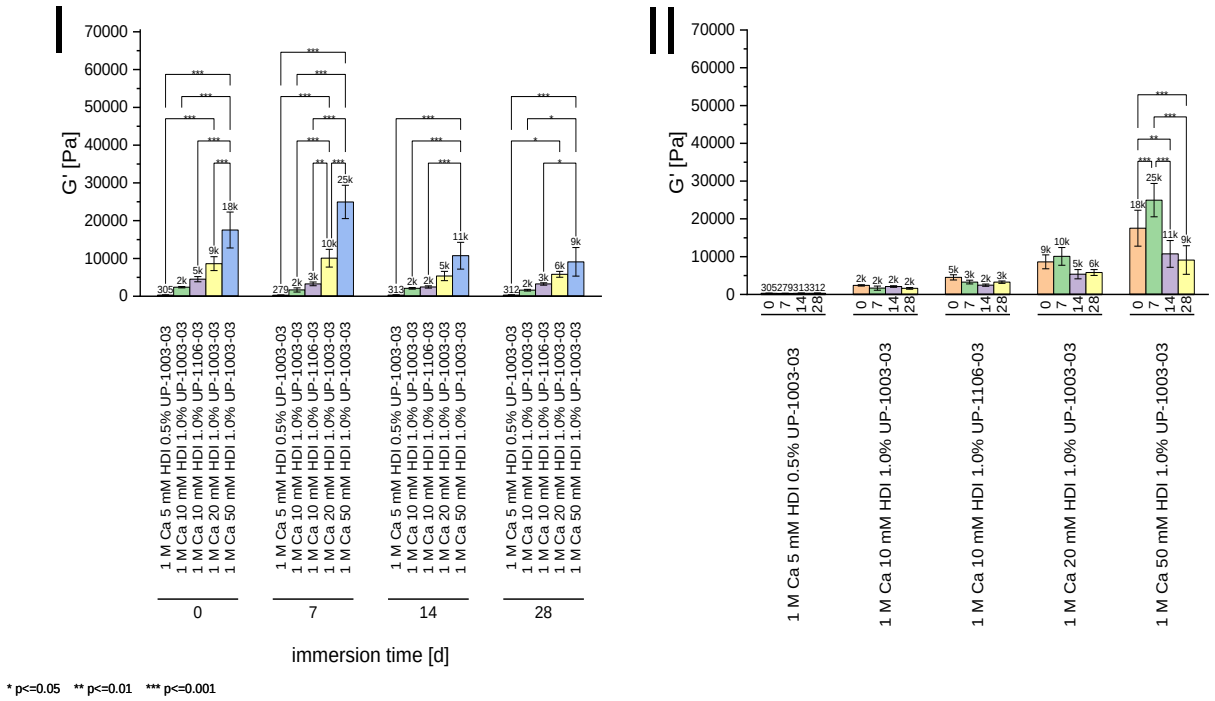

Figure 60: Two-way ANOVA with Bonferroni post-hoc testing (gel specimen (I) or immersion time in PBS as the compared parameter (II)) of storage moduli G' of 0.5 or 1.0% (w/w) medical medical-grade alginate ACHs (UP-MVG 1003-03/1106-03), which were cross-linked with 1.0 M $Ca^{2+}$and 5, 10, 20, or 50 mM HDI in DMSO and were stored in renewed PBS solutions for four weeks.

Just like the two 1.0% (w/w) medical-grade hydrogel versions (1003-03/1106-03), that were cross-linked with 10 mM, the 20 and 50 mM analogs also demonstrated a distinct decline in δ values as the PBS immersion experiment progressed over the weeks, as shown in Figure 61.

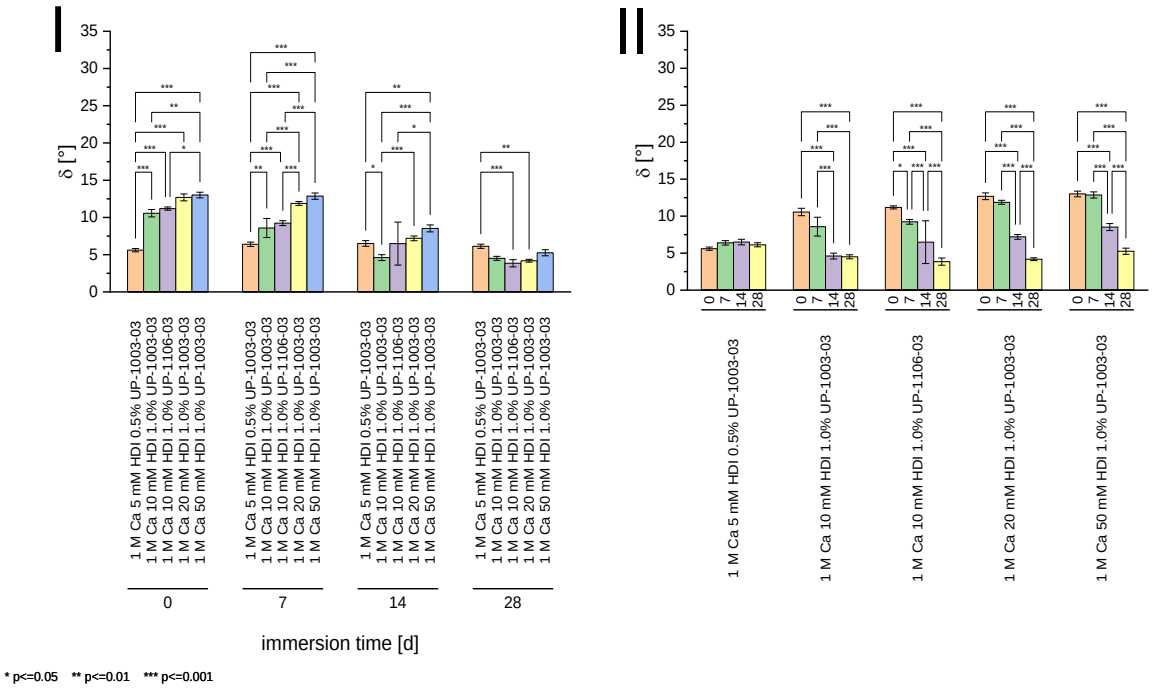

Figure 61: Two-way ANOVA with Bonferroni post-hoc testing (gel specimen (I) or immersion time in PBS as the compared parameter (II)) of phase shift δ values of 0.5 or 1.0% (w/w) medical medical-grade alginate ACHs (UP-MVG 1003-03/1106-03), which were cross-linked with 1.0 M $Ca^{2+}$and 5, 10, 20, or 50 mM HDI in DMSO and were stored in renewed PBS solutions for four weeks.

3.2.3 Microindentation with the Atomic Force Microscope of Food-Grade Alginate Anisotropic Capillary Hydrogels

To gain access to the microscopic mechanical properties of the alginate scaffolds, microindentation experiments were performed in a 16 × 16 grid in an area of 100 × 100 µm of each sample. The indentations were performed in two different extend and retract cycles to the surface, with the extend steps being performed at 1 and 5 µm/s. After being immersed in PBS for three hours prior to the AFM force-distance measurement, the 0.5% and 0.75% (w/w) food-grade hydrogel samples, that had been cross-linked with 100 mM HDI in water, were unstable due to excessive swelling and could not be handled with tweezers nor could they be attached to Petri dishes. Alginate scaffolds, which were obtained from 1.0 to 2.0% (w/w) alginate sols, were more stable and thus could be tested by indenting them from the top and parallel to the capillary structure. At the onset of the stability test, they demonstrated a significant increase in apparent elastic modulus E_{app} with an increase in alginate content, except for the 1.75% (w/w) sample. Samples, which were indented perpendicular and to the side of their capillary system demonstrated slightly higher elastic moduli, than those indented from the top, except in the case of the 1.5% (w/w) sample. With the 1.25%

(w/w) sample being the odd one out, the E_{app} values in this indentation direction also increased steadily as the respective alginate concentration in the gel body increased.

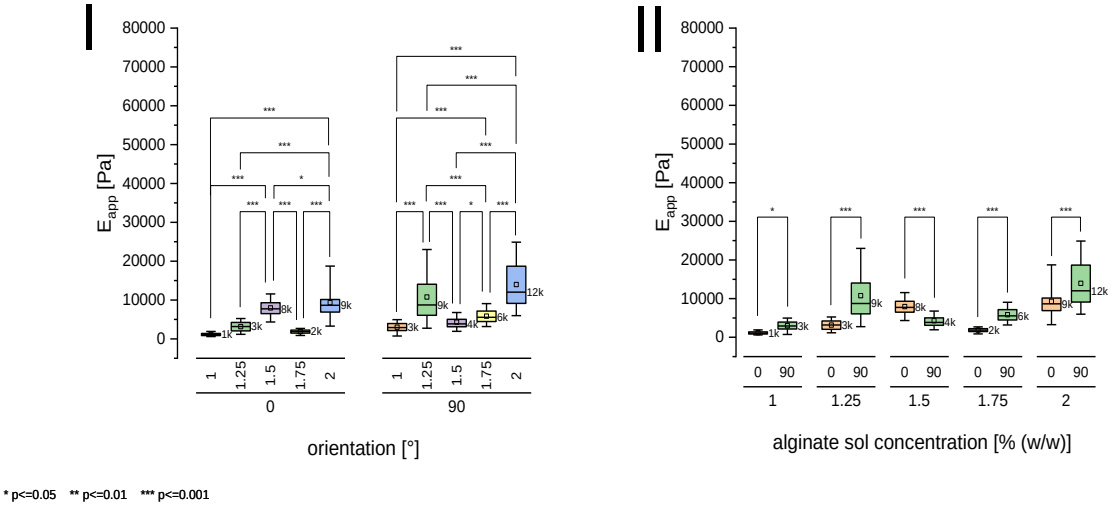

Figure 62: Two-way ANOVA with Bonferroni post-hoc testing (alginate sol concentration (I) or indentation orientation to the capillaries as the compared parameter (II)) of the apparent elastic modulus E_{app} of 1.0 – 2.0% (w/w) food-grade alginate ACHs, which were cross-linked with 1 M Sr^{2+} and 100 mM HDI in water.

1.0% (w/w) food-grade alginate ACHs, which had been cross-linked with 20, 50, 100, or 100 mM in water, demonstrated a lot of variability with regard to their stability in PBS. The 20 and 50 mM cross-linked specimens did not outlast a PBS immersion for three hours and are therefore not included in Figure 63. The 100 mM and 200 mM samples did not show a distinct difference in elastic modulus overall, as the 200 mM samples were of higher stiffness when indented parallel to the capillary structure, but softer in a perpendicular orientation than the ones cross-linked in the lower HDI concentration regime.

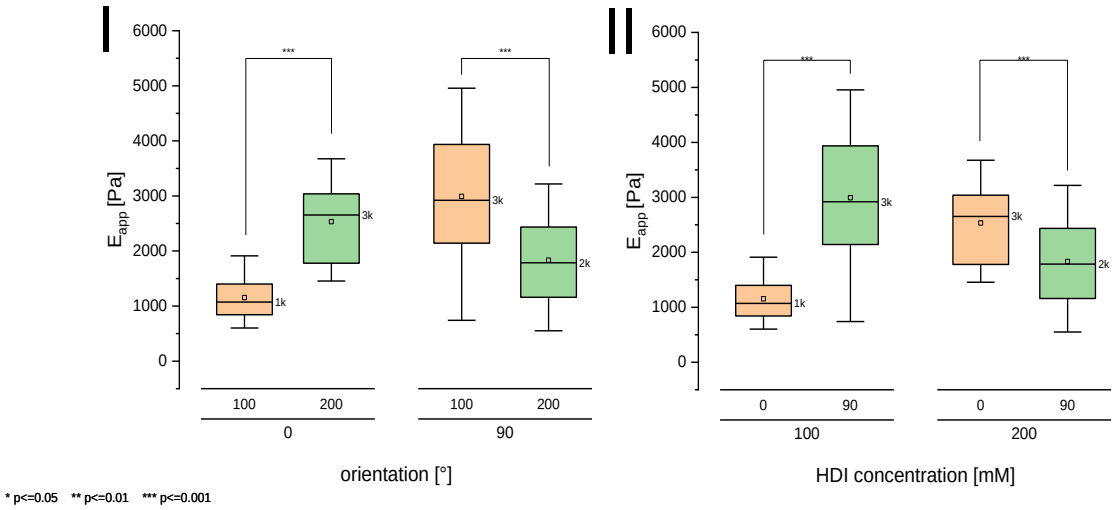

Figure 63: Two-way ANOVA with Bonferroni post-hoc testing (HDI cross-linker concentration (I) or indentation orientation to the capillaries as the compared parameter (II)) of the apparent elastic modulus E_{app} of 1.0% (w/w) food-grade alginate ACHs, which were cross-linked with 1 M Sr^{2+} and 100 or 200 mM HDI in water.

1.0% (w/w) food-grade hydrogels, which were cross-linked in a water-free environment and did not exhibit an interpenetrating network of polyurea, demonstrated a more distinct dependency between the amount of deployed HDI cross-linking agent and the elasticity of the resulting polymer network structure in indentation testing. Gel specimens, that were stabilized with a low concentration of 5 mM HDI, were not stable in PBS and disintegrated. As shown in Figure 64, ACHs, that had been cross-linked with HDI, starting out from 10 and ranging as high as 50 mM, demonstrated steadily increasing apparent elastic moduli, with no significant variation as the indentation orientation was changed. The only significantly different moduli between both tested angles of indentation were the 100 mM cross-linked samples, which also distinctly overshot the targeted elastic modulus target range. As the overall haptics of the gels were also rather plastic-like, further cross-linking procedures from a water-free environment only involved HDI concentrations as high as 50 mM, just like in the case of the rheometer samples from above.

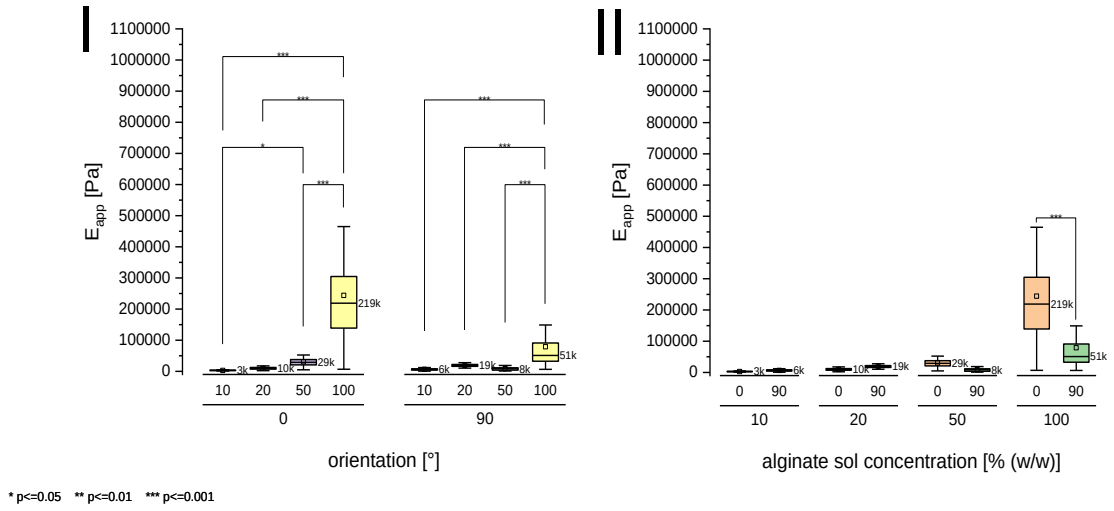

Figure 64: Two-way ANOVA with Bonferroni post-hoc testing (HDI cross-linker concentration (I) or indentation orientation to the capillaries as the compared parameter (II)) of the apparent elastic modulus E_{app} of 1.0% (w/w) food-grade alginate ACHs, which were cross-linked with 1 M Sr^{2+} and 10 – 100 mM HDI in DMSO.

As shown in Figure 65, food-grade alginate ACHs, which were formed from 0.5% (w/w) alginate sols and were subsequently cross-linked with HDI in DMSO, demonstrated lower apparent elastic moduli than identically cross-linked 1.0% (w/w) gels from before. Further, a significant increase in apparent elastic modulus was only present as the concentration of the diisocyanate was increased to 50 mM and the alginate scaffolds material was indented parallel to the capillary system.

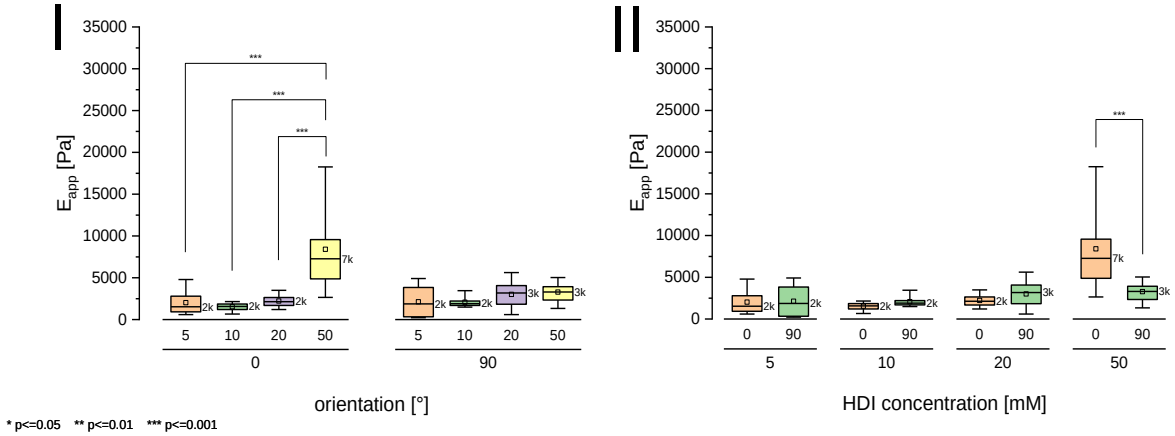

Figure 65: Two-way ANOVA with Bonferroni post-hoc testing (HDI cross-linker concentration (I) or indentation orientation to the capillaries as the compared parameter (II)) of the apparent elastic modulus E_{app} of 0.5% (w/w) food-grade alginate ACHs, which were cross-linked with 1 M Sr^{2+} and 5 – 50 mM HDI in DMSO.

3.2.4 Mechanical Stability of Food- and Medical-Grade Alginate Hydrogels in Microindentation Experiments

In accordance with the stability testing of alginate ACHs in oscillatory shearing rheometry, sample slices, whose mechanical properties would be examined in AFM microindentation experiments, were also immersed in PBS at 37 °C and measured after 7, 14, 28, 56, and 84 days of immersion. As mentioned prior, the 0.5 and 0.75% (w/w) samples, which had been stabilized with 100 mM HDI in water, did not even maintain their integrity for three hours in PBS. Thus no further investigation was possible in the timeframe of this experiment. Upon indentation parallel or in a 0 ° angle to the capillary orientation, the 1.0% (w/w) samples did not yield a significant variation in apparent elastic modulus beyond the ~1 kPa range for twelve weeks, as shown in Figure 66. In the same indentation orientation, no significant change in the modulus at the end of the 12-week timespan compared to the initial value was determined for the 1.25% (w/w) sample either, however, apparent moduli, which were recorded during that period demonstrated significant variability this time around. All other samples of higher alginate concentration underwent significant changes over the course of twelve weeks, with a steady decrease in E_{app} until the end of the 12-week test when the samples were indented parallel to the capillaries. The only exception here was the 1.75% (w/w) sample, which overall yielded very inconsistent results.

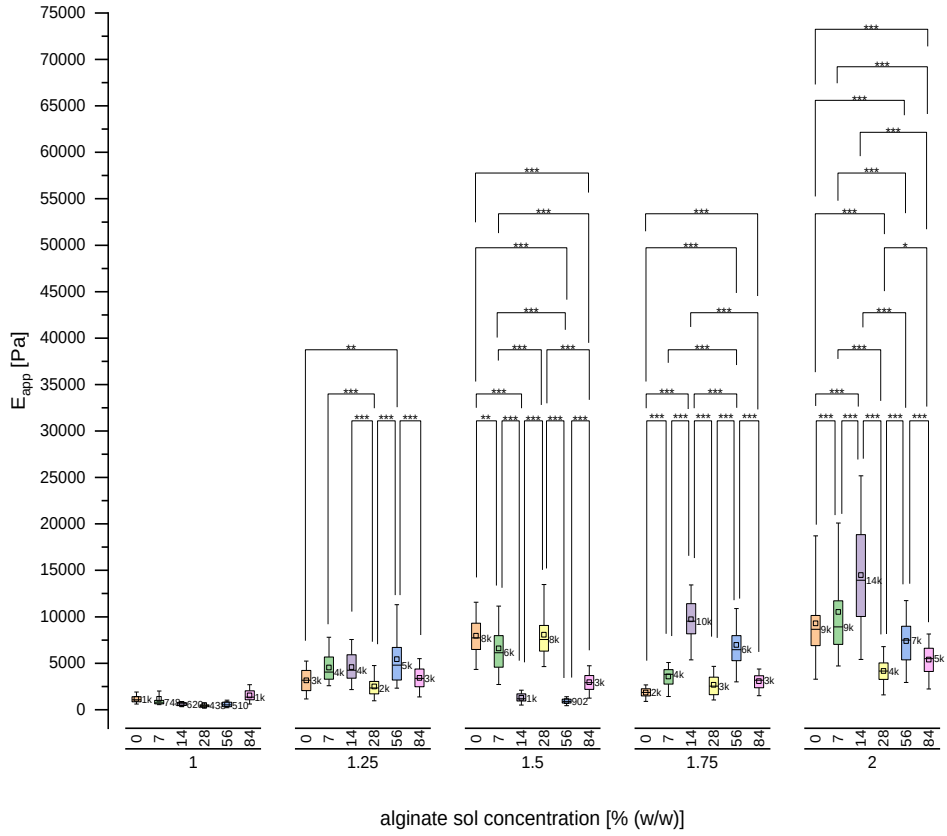

Figure 66: Two-way ANOVA with Bonferroni post-hoc testing (immersion time in PBS in days as the compared parameter) of the apparent elastic modulus E_{app} of 1.0 – 2.0% (w/w) alginate ACHs, which were cross-linked with 1 M Sr^{2+} and 100 mM HDI in water and were stored in renewed PBS solutions for twelve weeks; indentation of the samples parallel to the orientation of the capillary system.

When the capillary structures of all samples of varying alginate concentration were indented from the side or at a 90 ° angle, the apparent elastic moduli did not undergo any significant change over twelve weeks from start to finish. However, at interim times in between significant variability in apparent elastic moduli, as shown in Figure 67, was observable.

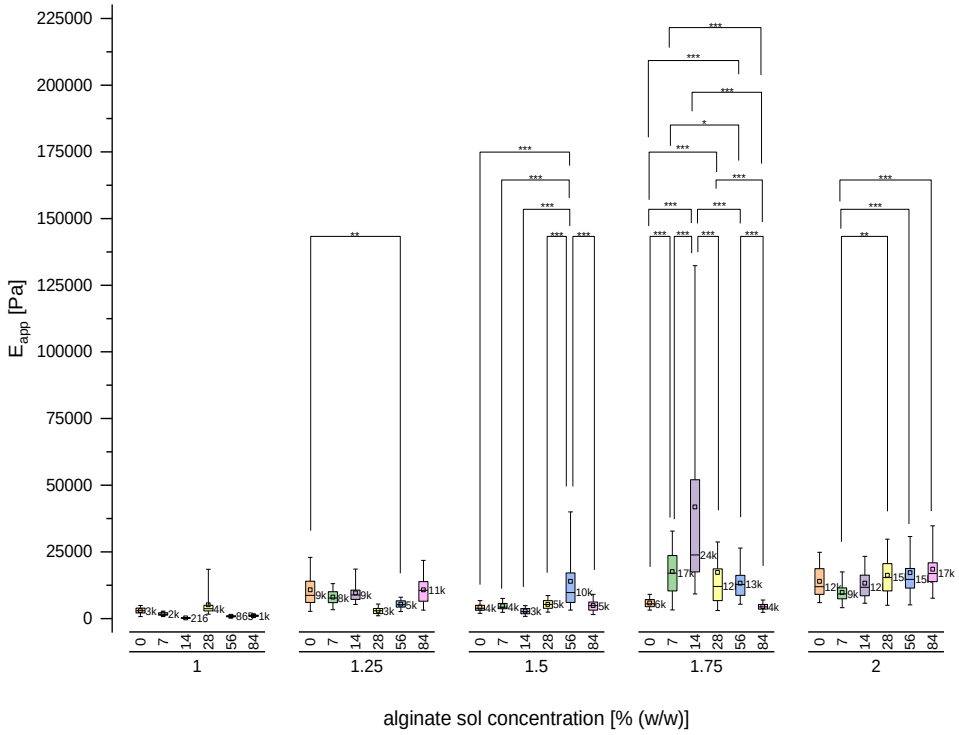

Figure 67: Two-way ANOVA with Bonferroni post-hoc testing (immersion time in PBS in days as the compared parameter) of the apparent elastic modulus E_{app} of 1.0 – 2.0% (w/w) alginate ACHs, which were cross-linked with 1 M Sr^{2+} and 100 mM HDI in water and were stored in renewed PBS solutions for twelve weeks; indentation of the samples perpendicular to the orientation of the capillary system.

After seven days, ACHs, which were cross-linked in water with 100 mM HDI, yielded apparent elastic moduli ranging from 1 to 9 kPa. The observed values of E_{app} tended to be higher for samples derived from a more concentrated alginate solution, with a few exceptions. When the side of the capillary structure was indented, similar moduli were obtained compared to capillary-parallel indentation. However, there were significant differences observed in three specific cases, as depicted in Figure 68.

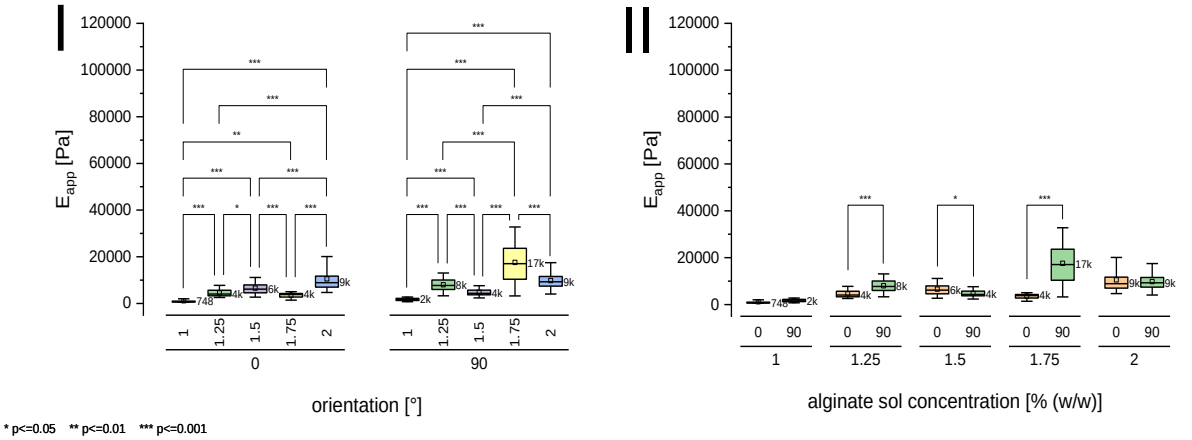

Figure 68: Two-way ANOVA with Bonferroni post-hoc testing (alginate sol concentration (I) or indentation orientation to the capillaries as the compared parameter (II)) of the apparent elastic modulus E_{app} of 1.0 – 2.0% (w/w) alginate ACHs, which were cross-linked with 1 M Sr^{2+} and 100 mM HDI in water, after seven days of immersion in PBS at 37 °C.

As illustrated in Figure 69, following a storage period of 14 days in buffer solution, the range of elastic moduli was slightly wider than after seven days, with once again higher E_{app} for alginate ACHs of higher alginate content with some exceptions. The samples appeared to be of significantly higher elasticity perpendicular to the capillary direction in some instances.

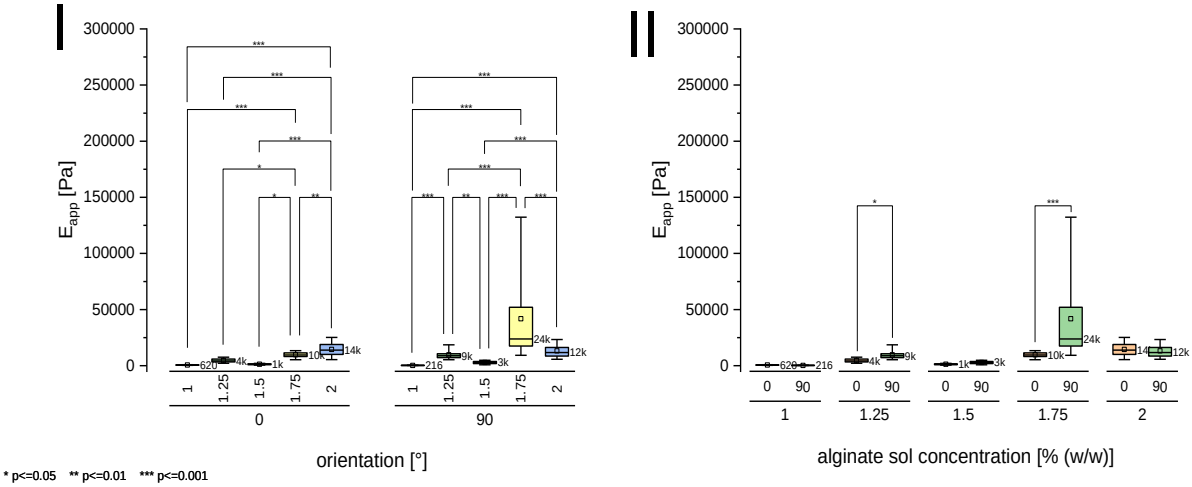

Figure 69: Two-way ANOVA with Bonferroni post-hoc testing (alginate sol concentration (I) or indentation orientation to the capillaries as the compared parameter (II)) of the apparent elastic modulus E_{app} of 1.0 – 2.0% (w/w) alginate ACHs, which were cross-linked with 1 M Sr^{2+} and 100 mM HDI in water, after 14 days of immersion in PBS at 37 °C.

As shown in Figure 70, 28 days after the PBS immersion commenced, the samples appeared to have become less stiff in indentation parallel to the capillaries than at the 14-day point in time, but perpendicular to it no significant change occurred in most cases. Overall the moduli for higher concentrated alginate ACHs were

approaching those of less concentrated specimens at this point. Once again, the only significant difference between indentation orientations was a stiffer matter perpendicular to the capillaries in some instances.

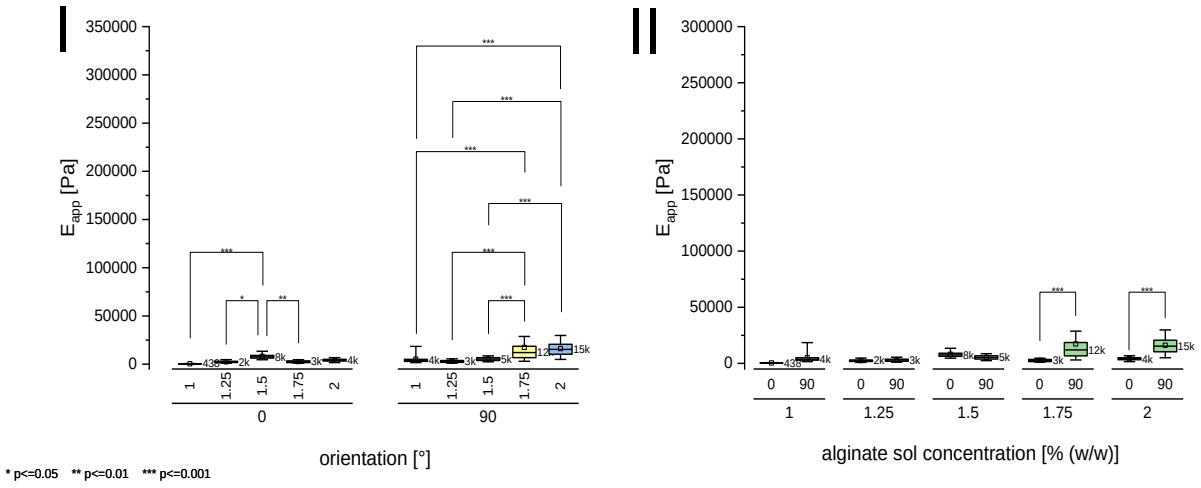

Figure 70: Two-way ANOVA with Bonferroni post-hoc testing (alginate sol concentration (I) or indentation orientation to the capillaries as the compared parameter (II)) of the apparent elastic modulus E_{app} of 1.0 – 2.0% (w/w) alginate ACHs, which were cross-linked with 1 M Sr^{2+} and 100 mM HDI in water, after 28 days of immersion in PBS at 37 °C.

After 56 days of PBS immersion, the three alginate hydrogels of the highest alginate concentration demonstrated significantly higher elastic moduli perpendicular to the capillaries than parallel to them, as demonstrated by Figure 71. Overall, the difference in outcome between hydrogels of varying alginate concentrations was more distinct than 28 days into the experiment.

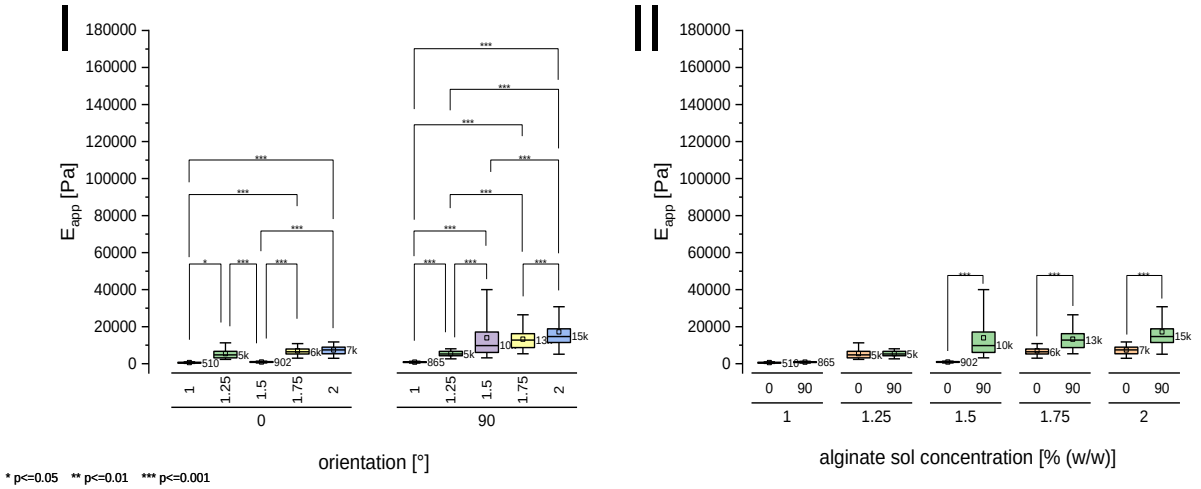

Figure 71: Two-way ANOVA with Bonferroni post-hoc testing (alginate sol concentration (I) or indentation orientation to the capillaries as the compared parameter (II)) of the apparent elastic modulus E_{app} of 1.0 – 2.0% (w/w) alginate ACHs, which were cross-linked with 1 M Sr^{2+} and 100 mM HDI in water, after 56 days of immersion in PBS at 37 °C.

And finally, after twelve weeks or 84 days of storage in the PBS buffer solution and renewal of the solution at every measurement increment, the elastic moduli parallel to the capillaries were lower than in prior weeks. The decrease was not as pronounced perpendicular to the capillary structures, which was apparent in significantly higher elastic moduli in that orientation in almost all instances, as can be seen in Figure 72.

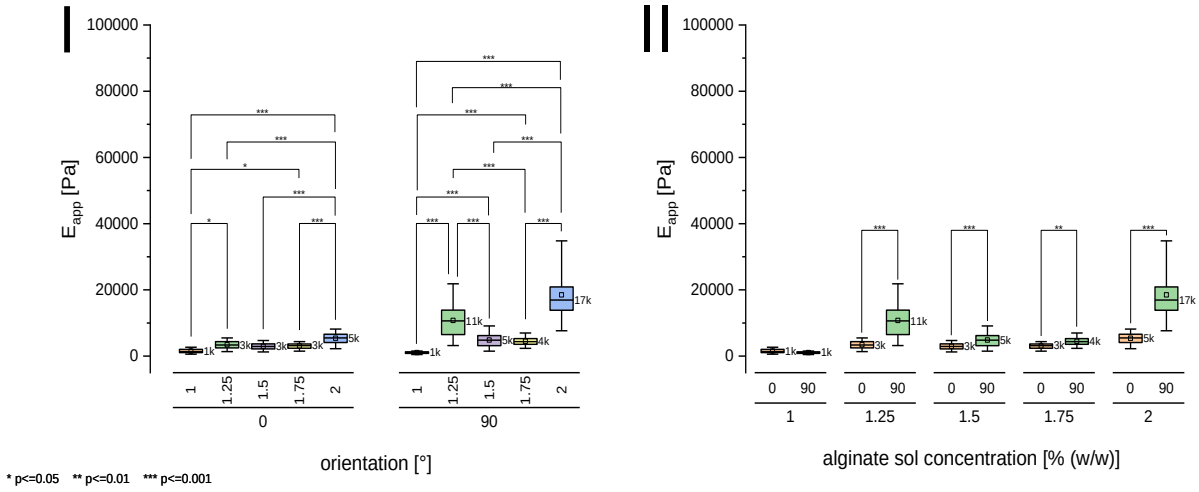

Figure 72: Two-way ANOVA with Bonferroni post-hoc testing (alginate sol concentration (I) or indentation orientation to the capillaries as the compared parameter (II)) of the apparent elastic modulus E_{app} of 1.0 – 2.0% (w/w) alginate ACHs, which were cross-linked with 1 M Sr^{2+} and 100 mM HDI in water, after 84 days of immersion in PBS at 37 °C.

Further, a 1.0% (w/w) food-grade alginate hydrogel, which was also cross-linked with 1 M Sr^{2+} and chemically with 10 mM HDI in a water-free environment, instead of with 100 mM HDI in water, was examined. As pointed out in Figure 73, indentation parallel to the capillaries yielded fairly consistent elastic moduli, with no significant decrease over the course of twelve weeks. With the exception of the 7-day sample, indentation perpendicular to the capillaries also yielded fairly consistent elastic moduli in the same timeframe. Just like in prior water-cross-linked samples, this iteration of food-grade hydrogels also appeared to be of significantly higher elastic modulus perpendicular to the capillary structure in some instances.

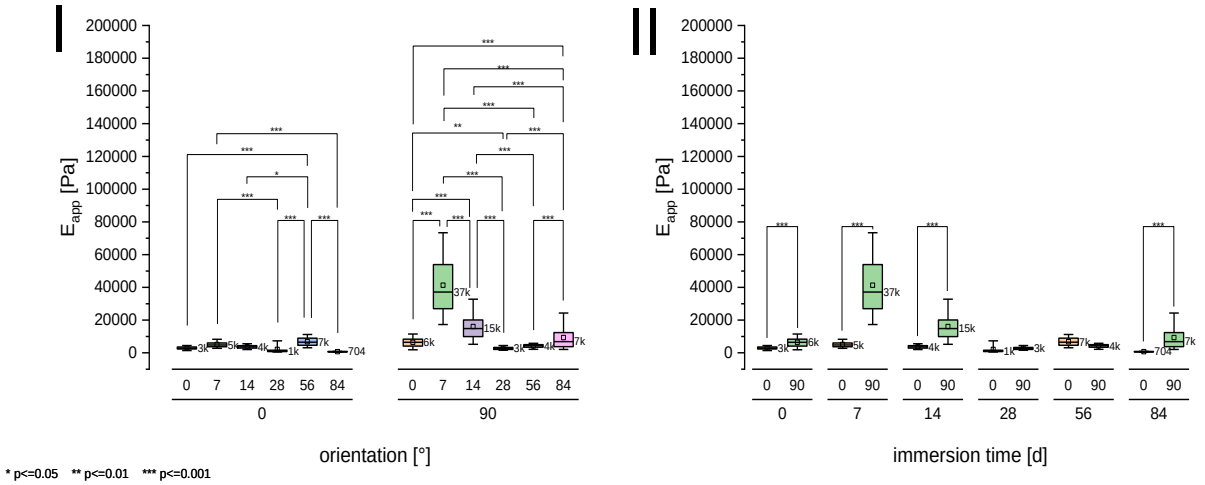

Figure 73: Two-way ANOVA with Bonferroni post-hoc testing (PBS immersion time (I) or orientation of indentation to the capillary system as the compared parameter (II)) of the apparent elastic modulus E_{app} of 1.0 % (w/w) alginate ACHs, which were cross-linked with 1 M Sr^{2+} and 10 mM HDI in DMSO.

As demonstrated in section 3.2.2, selected medical-grade alginate ACHs, that underwent oscillatory shearing rheometry demonstrated no significant decrease in mechanical properties over a 4-week period, except a 50 mM cross-linked sample, which was not tested in this instance. A similar outcome was obtained in indentation testing, as no significant decrease in elastic moduli was present in any of the Pronova UP MVG 1003-03 samples over the 4-week timeframe as shown in Figure 74. The stiffest hydrogel class even demonstrated a slight increase in apparent elastic moduli in indentation parallel and perpendicular to the capillaries over the course of four weeks.

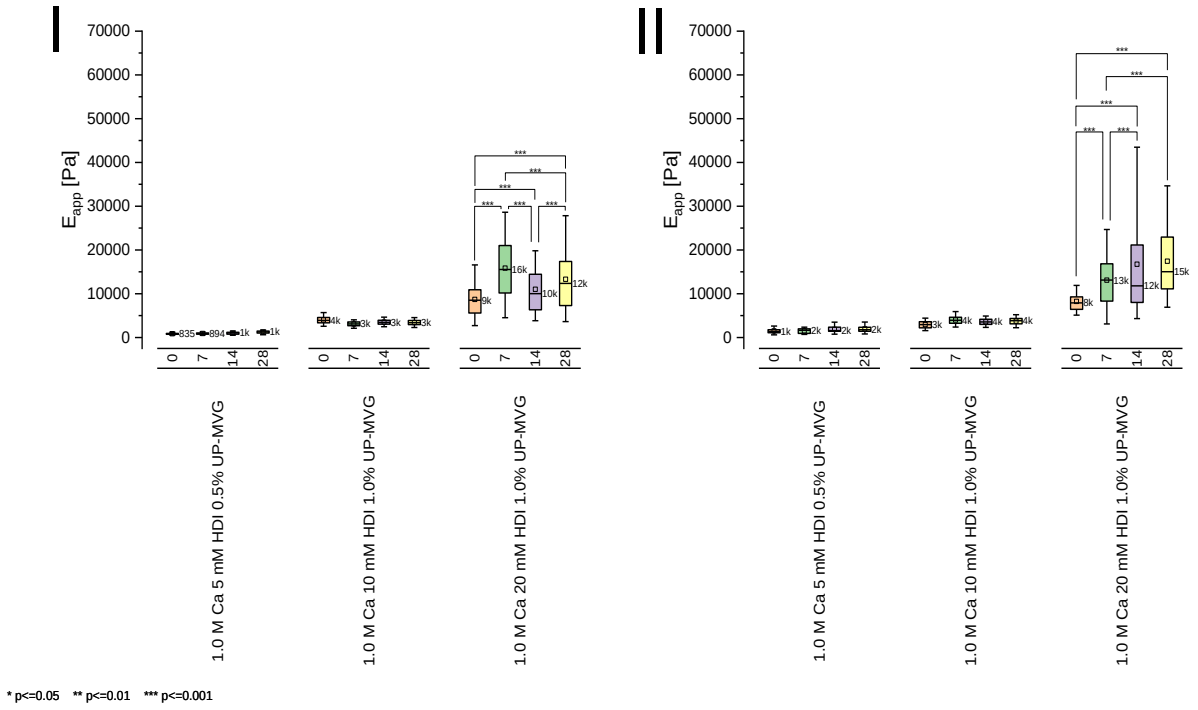

Figure 74: Two-way ANOVA with Bonferroni post-hoc testing (PBS immersion time in days as the compared parameter) of the apparent elastic modulus E_{app} of 1.0% (w/w) medical-grade alginate ACHs (UP MVG 1003-03), which were cross-linked with 1 M Ca^{2+} and 5, 10, or 20 mM HDI in DMSO and were stored in renewed PBS solutions for 28 days; indentation parallel to the capillaries (I) or perpendicular to them (II).

More specifically, the three different parameter setups yielded gels with significantly different apparent elastic moduli at the ~1 kPa, the 3 – 4 kPa level, and finally, the 8 – 9 kPa level after three hours or zero days of PBS immersion, as shown in Figure 75. The apparent moduli did not conclusively differ as the indentation orientation was changed.

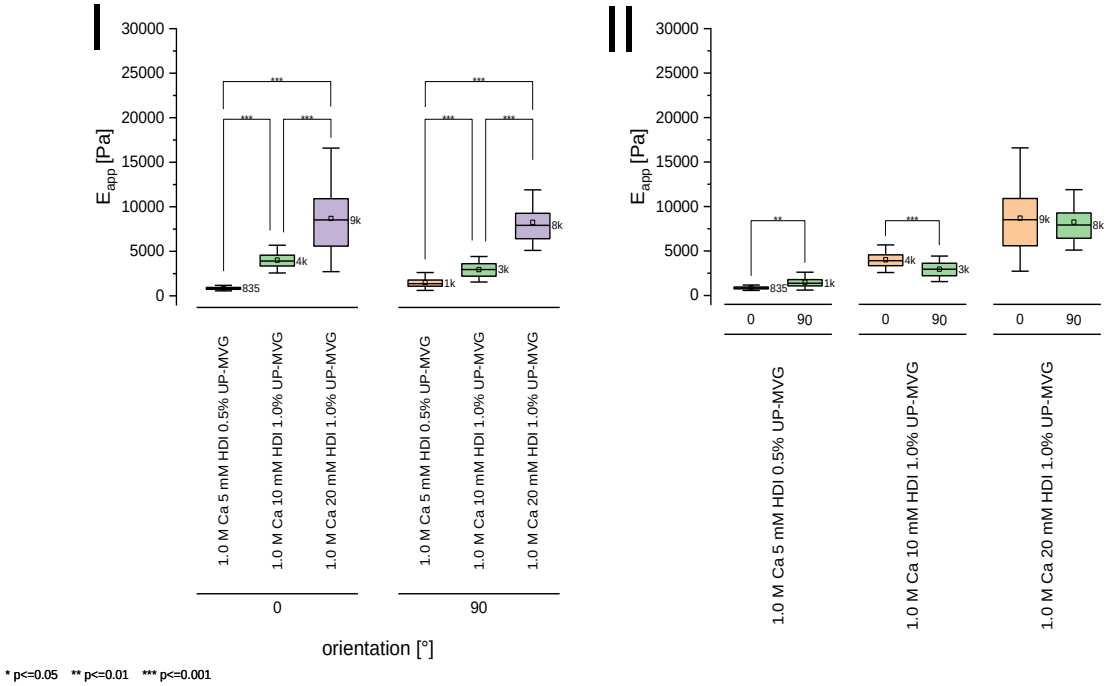

Figure 75: Two-way ANOVA with Bonferroni post-hoc testing (sample specimen (I) or indentation orientation to the capillaries as the compared parameter (II)) of the apparent elastic modulus E_{app} of 0.5 or 1.0% (w/w) medical-grade alginate ACHs (UP MVG 1003-03), which were cross-linked with 1 M Ca^{2+} and 5, 10, or 20 mM HDI in DMSO, after 0 days of immersion in PBS.

After 7, 14, and 28 days of PBS immersion, slightly different apparent elastic moduli were recorded for each medical-grade hydrogel class, however, the significant differences in E_{app} between all three sample groups persisted, with moduli ranging between 1 and 16 kPa, as demonstrated in Figure 76, 77, and 78. Overall, no distinct trend in E_{app} with regard to the indentation orientation was observable.

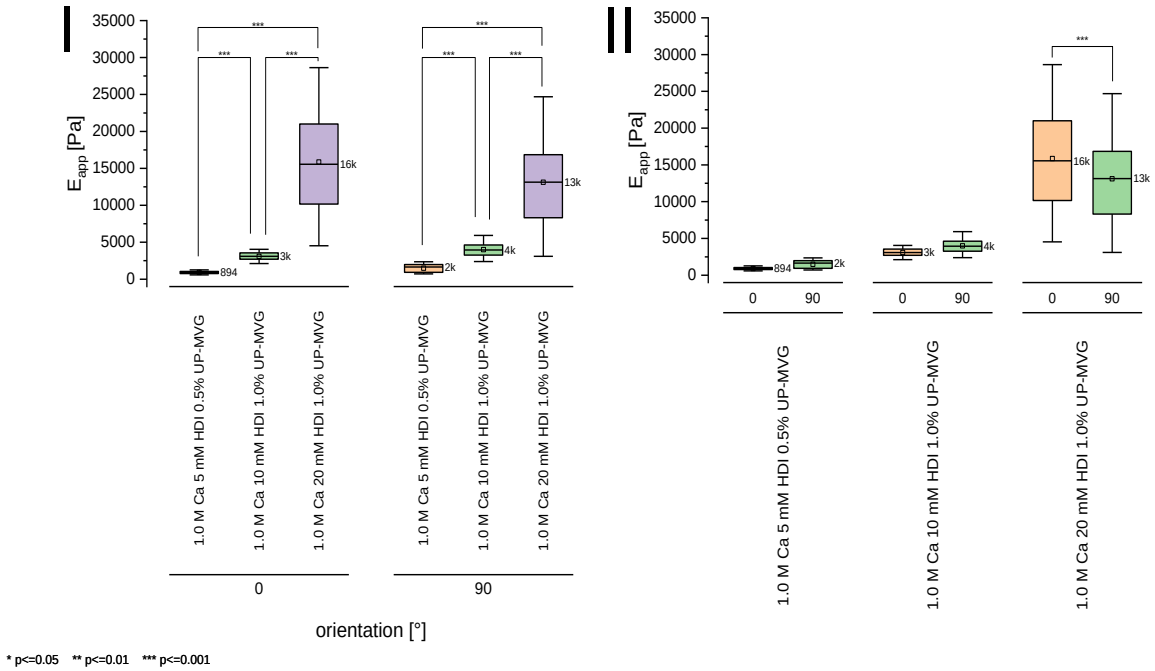

Figure 76: Two-way ANOVA with Bonferroni post-hoc testing (sample specimen (I) or indentation orientation to the capillaries as the compared parameter (II)) of the apparent elastic modulus E_{app} of 0.5 or 1.0% (w/w) medical-grade alginate ACHs (UP MVG 1003-03), which were cross-linked with 1 M Ca^{2+} and 5, 10, or 20 mM HDI in DMSO, after seven days of immersion in PBS.

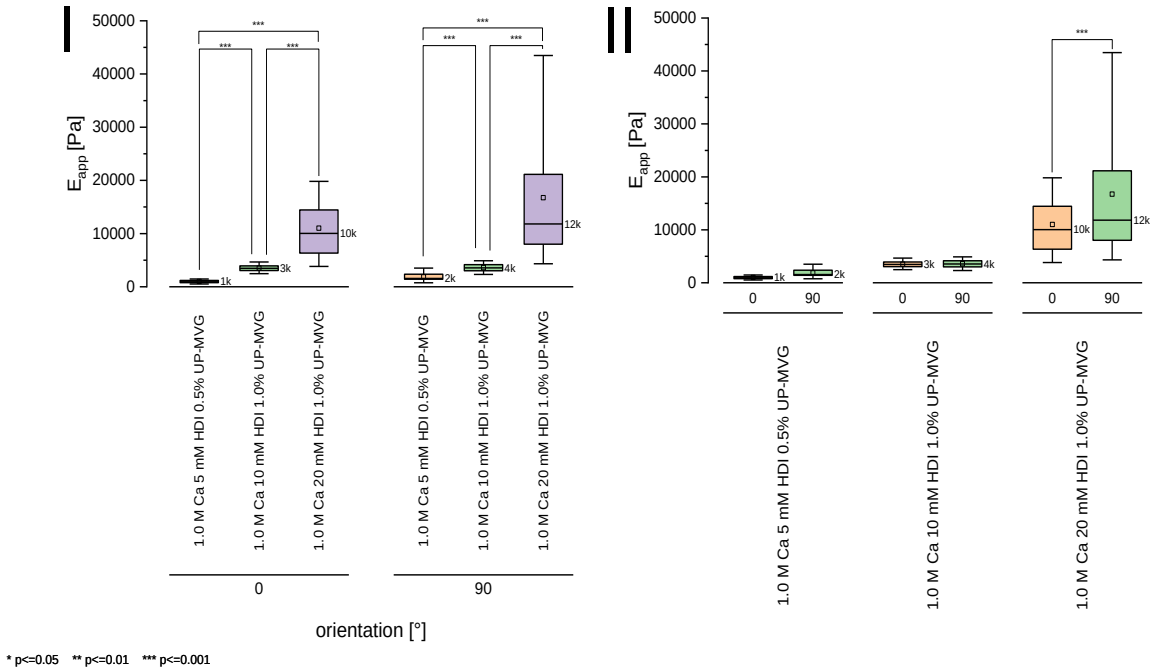

Figure 77: Two-way ANOVA with Bonferroni post-hoc testing (sample specimen (I) or indentation orientation to the capillaries as the compared parameter (II)) of the apparent elastic modulus E_{app} of 0.5 or 1.0% (w/w) medical-grade alginate ACHs (UP MVG 1003-03), which were cross-linked with 1 M Ca^{2+} and 5, 10, or 20 mM HDI in DMSO, after 14 days of immersion in PBS.

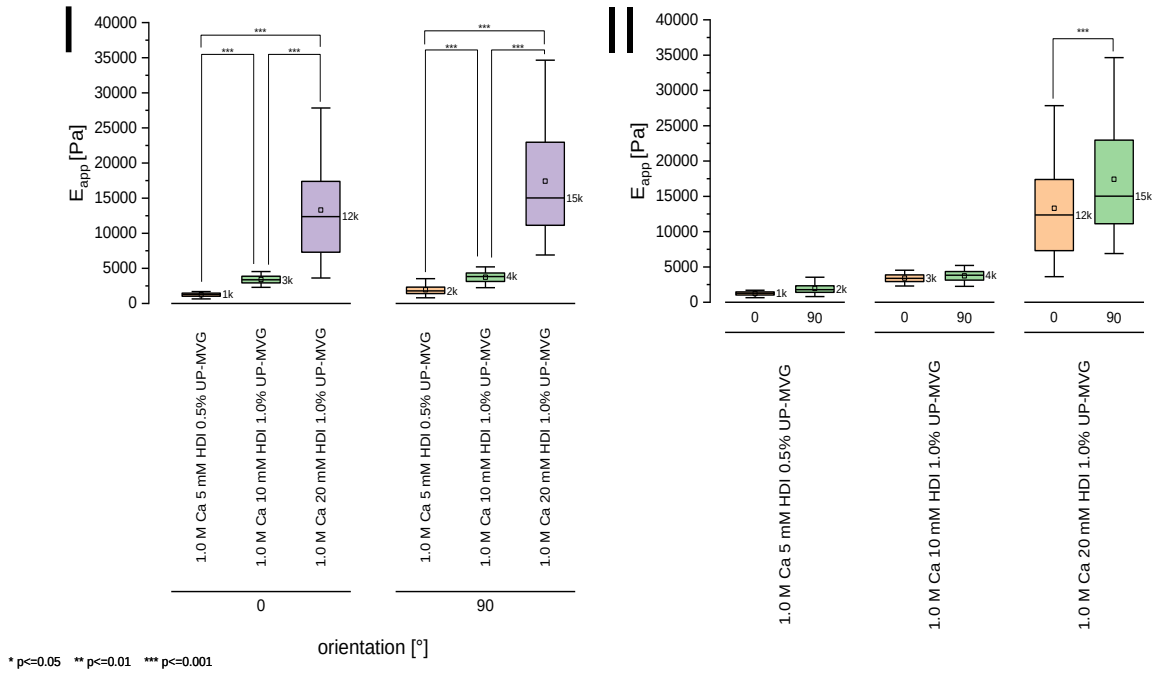

Figure 78: Two-way ANOVA with Bonferroni post-hoc testing (sample specimen (I) or indentation orientation to the capillaries as the compared parameter (II)) of the apparent elastic modulus E_{app} of 0.5 or 1.0% (w/w) medical-grade alginate ACHs (UP MVG 1003-03), which were cross-linked with 1 M Ca^{2+} and 5, 10, or 20 mM HDI in DMSO, after 28 days of immersion in PBS.

3.2.5 Stress Relaxation in Microindentation Experiments

During the extension phase of the microindentation experiments, the cantilever approach was performed with 1 µm/s or 5 µm/s on 1 M Ca 5 mM HDI 0.5% UP-MVG 1003-03, 1 M Ca 10 mM HDI 1.0% UP-MVG 1003-03, and 1 M Ca 20 mM HDI 1.0% UP-MVG 1003-03 samples. After the indentation was completed at the set indentation force threshold, a 4-second pause in a constant cantilever height ensued. The development of the indentation force was recorded over this timespan and a bi-exponential decay function was fitted to the data. According to the procedure described above in section 2.3.1, the ratio of the function variables A_2 and A_1 was determined and compared to the phase shift δ values of the rheometry experiment, as demonstrated for 1 µm/s indentation experiments (Figure 79 (I)) and 5 µm/s indentation experiments (Figure 79 (II)) of the pooled data of the three samples. A linear correlation between the phase shift δ and the A_2/A_1 values was mainly present when comparing the 1 µm/s results to the respective δ values with a Pearson's R-value of 0.36. The analogous measurements after the 5 µm/s approach correlated to the phase shift data with merely a Pearson's R of 0.12. Further, as the relaxation data of the three samples was pooled, an indentation with 5 µm/s yielded higher A_2/A_1 values than the lower indentation speed approaches, indicating a more distinct force relaxation in the pause segment of the experiment (Figure 79 (III)).

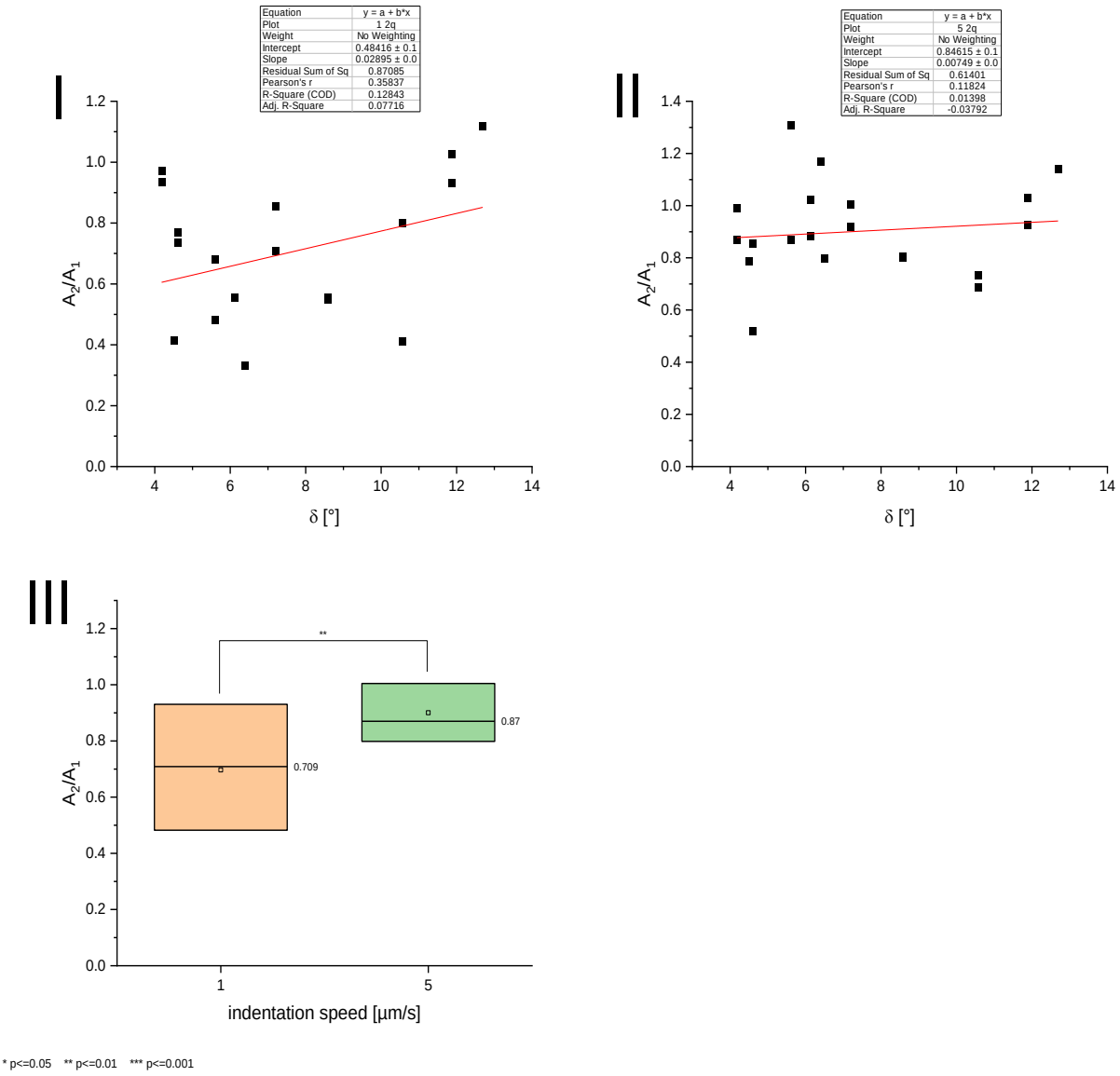

Figure 79: Ratio of the bi-exponential decay function variables A_2/A_1 compared to the phase shift δ values in 1 µm/s indentation experiments (I) and in 5 µm/s indentation experiments (II) of three different medical-grade alginate samples; one-way ANOVA of the ratio of the bi-exponential decay function variables A_2/A_1 (indentation speed as the compared parameter) (III).

3.3 Release of Sodium Alginate in Buffer Medium

The supernatant of gel slices, which underwent PBS immersion for up to twelve weeks and were measured in oscillatory shearing rheometry after 1, 2, 4, 8, and 12 weeks, was sampled after each rheometry measurement and renewed with 50 mL of fresh PBS buffer. Gel samples of different food-grade alginate concentrations (Figure 80 (I)), that were cross-linked with 1 M Sr^{2+} and 100 mM HDI in water, demonstrated a high retention of alginate, except in the case of the 0.75% (w/w)-based alginate gel group. Upon varying the amount of diisocyanate cross-linker, higher degrees of alginate retention were observable in gels, that were exposed to a higher concentration of HDI cross-linker. Food-grade hydrogels, which were

cross-linked with Sr^{2+} and only 20 or 50 mM HDI in water did not retain any alginate past the 14-day point (Figure 80 (II)). Food-grade alginate ACHs, which underwent cross-linking in a water-free environment demonstrated similar alginate retention levels at much lower diisocyanate concentrations (Figure 80 (III)). Remarkably, in this instance, a higher HDI concentration entailed a slightly lower amount of retained alginate in 0.5 and 1.0% (w/w) food-grade alginate gels. Lastly, the alginate retention of medical-grade alginate samples was researched. Just like in the 0.5% (w/w) food-grade alginate and 5 mM HDI setup, a complete retention of alginate was achieved in the medical-grade analog, but here with Ca^{2+} instead of Sr^{2+} as the cross-linking species in the physical cross-linking procedure. Higher medical-grade alginate concentrations combined with higher amounts of HDI cross-linker yielded gels, which released slightly more alginate. The medical-grade UP-MVG 1106-03 sample retained slightly more alginate than the 1003-03 sample of an otherwise identical composition (Figure 80 (IV)). The experiment was stopped after four weeks, as in no case any alginate release had occurred beyond the 2-week mark, and rheometry and microindentation testing also did not hint at any decay in mechanical properties after that point in time either.

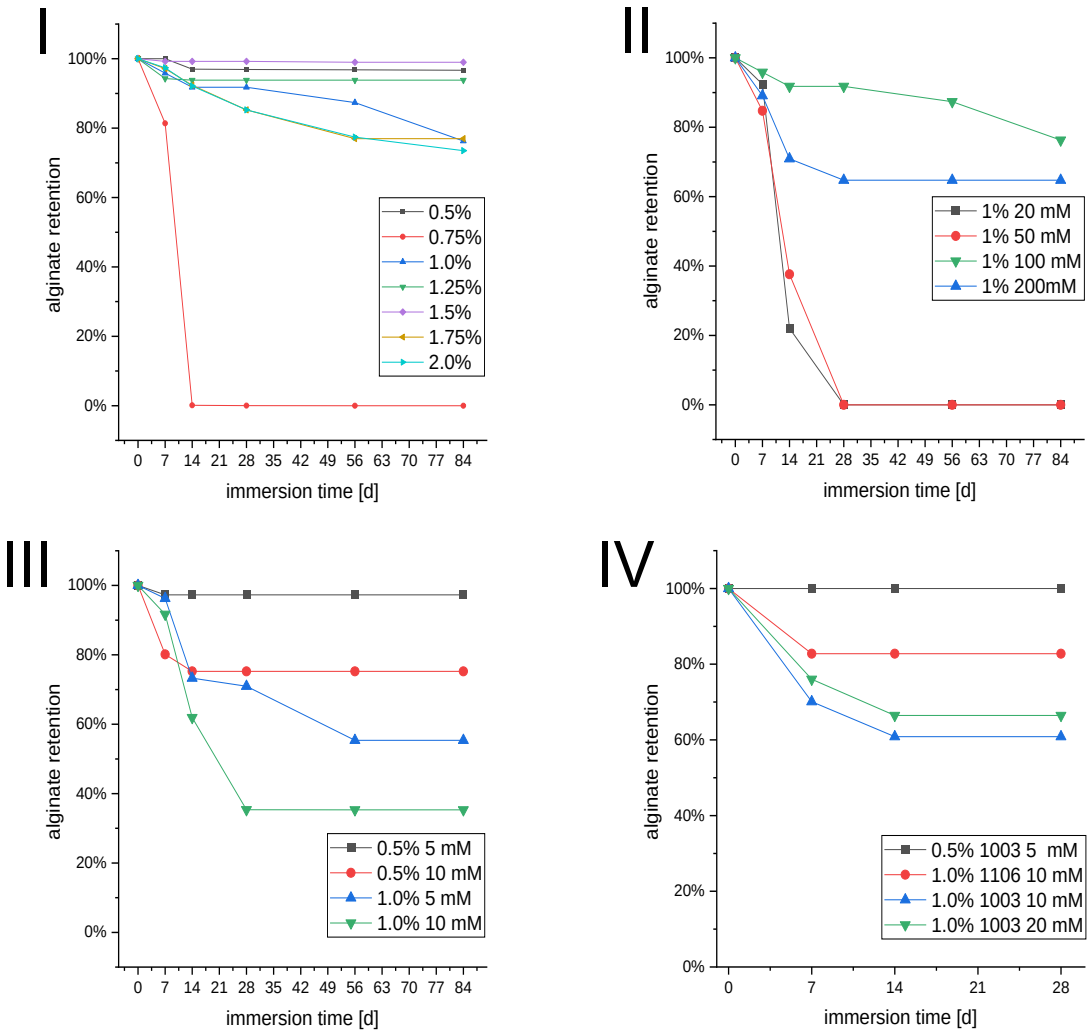

Figure 80: Relative amount of retained alginate after 7, 14, 28, 56, and 84 days of immersion in PBS buffer solution with a renewal of the solution after each determination point; alginate retention of hydrogels of various concentrations of food-grade alginate, which were cross-linked with 1 M Sr^{2+} and 100 mM HDI in water (I), alginate retention of 1.0% (w/w) food-grade hydrogels, which were cross-linked with 1 M Sr^{2+} and 20 – 100 mM HDI in water (II), alginate retention of 0.5 and 1.0% (w/w) food-grade hydrogels, which were cross-linked with 1 M Sr^{2+} and 5 or 10 mM HDI in DMSO (III), and alginate retention of 0.5 and 1.0% (w/w) medical-grade hydrogels (UP MVG 1003-03/1106-03), which were cross-linked with 1 M Ca^{2+} and 5 – 20 mM HDI in DMSO (IV).

3.4 Viscosity Average Molar Mass of Sodium Alginate Products

In order to gauge the average viscosity molar mass M, capillary viscosimetry and rheometry experiments were performed with two different sodium alginate products in 0.1 M NaCl. In all two tested instances, the reduced viscosity results between both testing methods roughly converged, yielding similar intrinsic viscosity outcomes. Overall, the food-grade alginate product Protanal (Figure 81 (II)) demonstrated a higher intrinsic viscosity than the medical-grade UP MVG 1003-03 product (Figure 81 (I)).

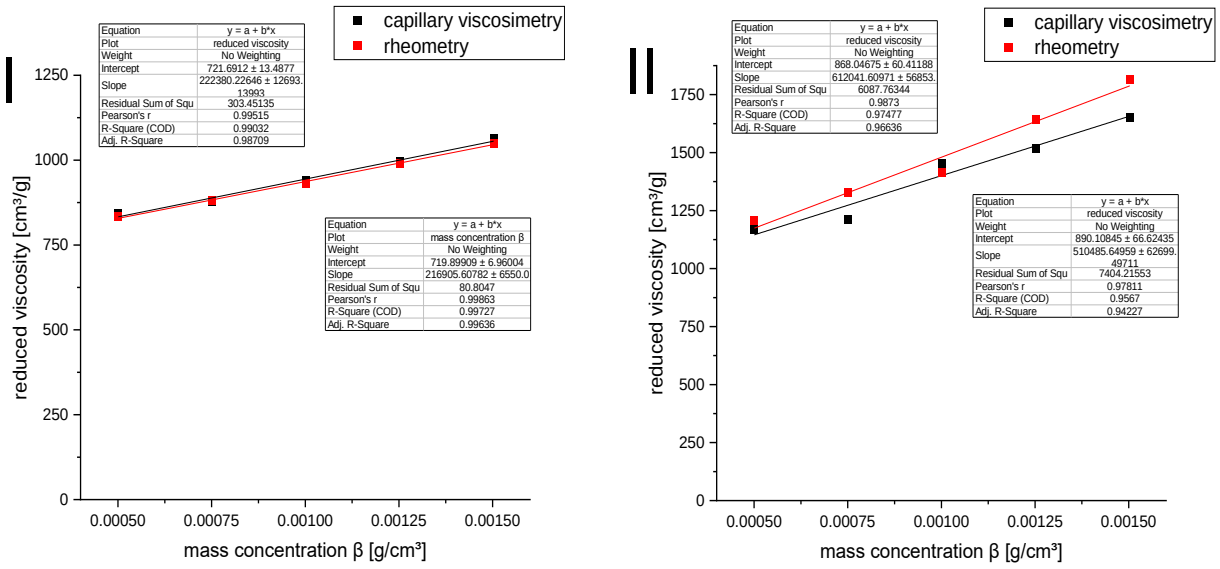

Figure 81: Reduced viscosity of Pronova UP MVG 1003-03 (I) and Protanal (II) for five different mass concentrations.

By deploying the Kuhn-Houwink-Sakurada relationship with the exemplary parameters $K_{[\eta]}$ = 0.000073 and α = 0.92 (alginate product from *Macrocystis pyrifera* in 0.1 M NaCl at 25 °C) one could obtain average viscosity molar masses for every alginate product, as shown in Table 7 [219].

Table 7: Intrinsic viscosities and exemplary average viscosity molar masses for two different kinds of alginate products in rheometry and capillary viscometry measurements.

alginate product	intrinsic viscosity [cm³/g] (rheometry)	intrinsic viscosity [cm³/g] (capillary viscosimetry)	M [kDa] (rheometry)	M [kDa] (capillary viscosimetry)
Pronova UP MVG 1003-03	720	722	268	269
Protanal	868	890	329	338

3.5 Swelling of Alginate Hydrogels in Buffer Solution

Food-grade alginate hydrogels were swollen in PBS overnight and their swelling ratio was determined after freeze-drying. Upon a variation of the alginate content in 100 mM HDI in-water cross-linked hydrogels, an increase in alginate concentration was accompanied by a successive reduction in swelling ratio, as showcased in Figure 82.

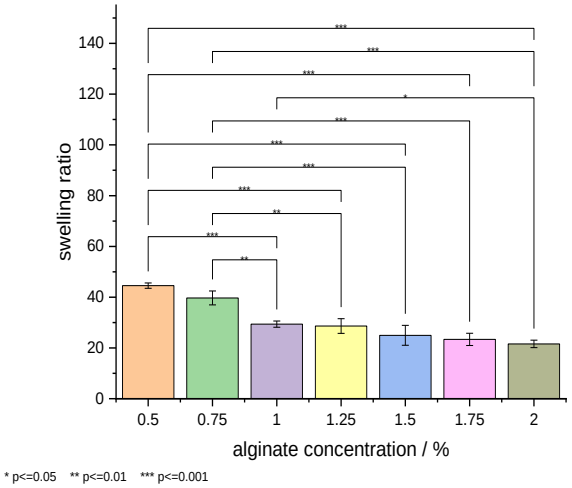

Figure 82: One-way ANOVA with Bonferroni post-hoc testing (alginate concentration as the compared parameter) of the swelling ratio of 0.5 – 2.0% (w/w) food-grade alginate ACHs, that were cross-linked with 1 M Sr^{2+} and 100 mM HDI in water.

After an initial increase in swelling ratio as the HDI concentration was increased from 20 to 50 mM, the swelling ratio continuously declined upon further increases in HDI of in-water cross-linked 1.0% (w/w) food-grade hydrogels, as apparent in Figure 83.

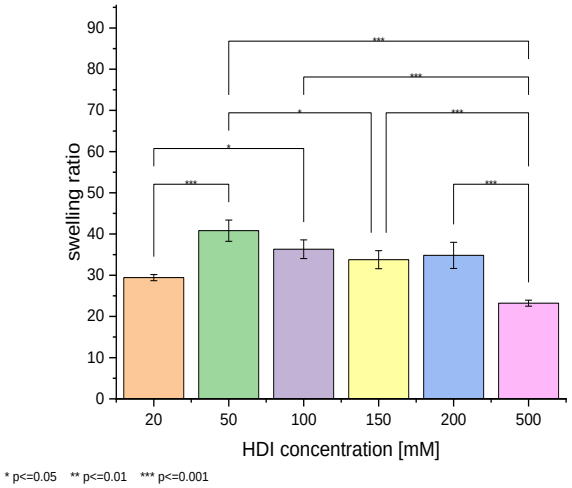

Figure 83: One-way ANOVA with Bonferroni post-hoc testing (HDI concentration as the compared parameter) of the swelling ratio of 1.0% (w/w) food-grade alginate ACHs, that were cross-linked with 1 M Sr^{2+} and 20 – 500 mM HDI in water.

In the water-free cross-linking environment, the variation of the diisocyanate concentration entailed significantly reduced swelling rations in the case of HDI cross-linking of 1.0% (w/w) food-grade hydrogels. No such clear case could be stated as ODI or DDI were deployed instead, as also demonstrated in Figure 84.

Remarkably, at any tested diisocyanate concentration, a lengthening of the aliphatic chain in the diisocyanate compound led to a decrease in the swelling ratio of the hydrogel specimen.

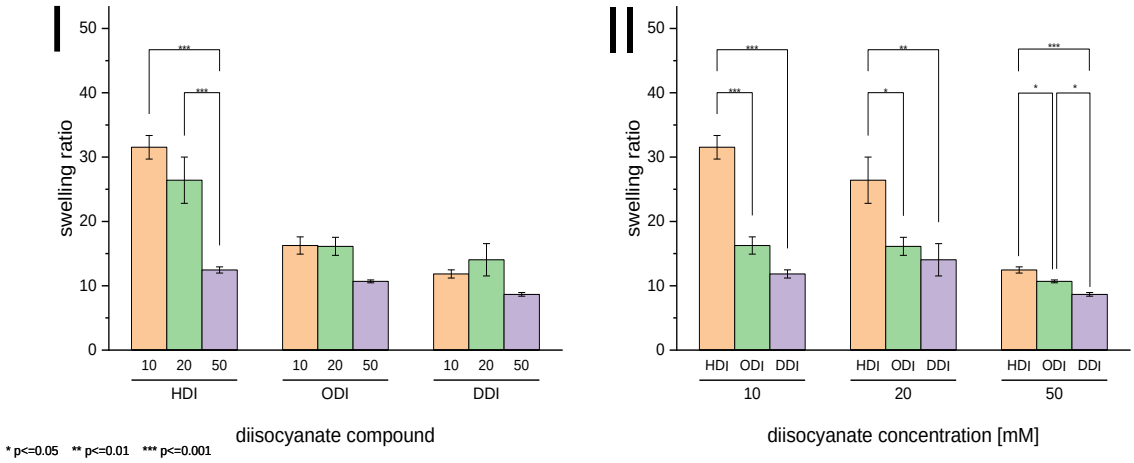

Figure 84: Two-way ANOVA with Bonferroni post-hoc testing (HDI concentration (I) or diisocyanate compound as the compared parameter (II)) of the swelling ratio of 1.0% (w/w) food-grade alginate ACHs, that were cross-linked with 1 M Sr^{2+} and 20 – 50 mM HDI, ODI, or DDI in DMSO.

A select group of 0.5 or 1.0% (w/w) medical-grade alginate hydrogels, which were cross-linked with 5 to 20 mM HDI in DMSO, were also tested in swelling experiments as shown in Figure 85. Notably, an increase in HDI also entailed a reduction in swelling ratio, as has already been stated for food-grade gels above. Further, a Sr^{2+}-based 0.5% (w/w) UP MVG 1003-03 hydrogel, that was cross-linked with 5 mM HDI, obtained a larger swelling ratio than an equivalent gel, that was cross-linked with 1 M Ca^{2+} instead.

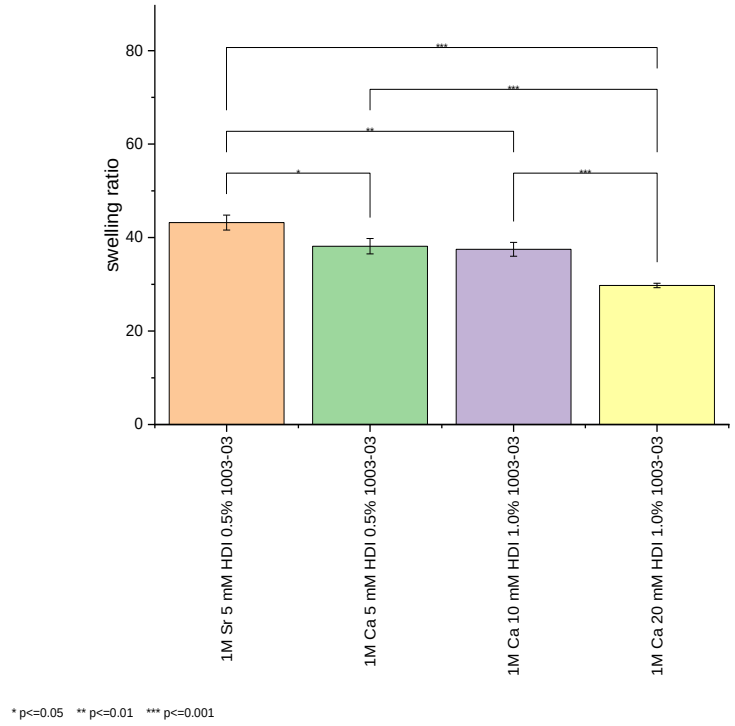

Figure 85: One-way ANOVA with Bonferroni post-hoc testing (sample specimen as the compared parameter) of the swelling ratio of 0.5 or 1.0% (w/w) medical-grade alginate ACHs, that were cross-linked with 1 M Sr^{2+} or 1 M Ca^{2+} and 5 – 20 mM HDI in DMSO.

4. Discussion

4.1 The Physical Cross-linking Procedure in the Formation of an Alginate Anisotropic Capillary Hydrogel

The ionotropic gelation process with different polyelectrolytes, which would yield unique anisotropic structures for different polymer and cation combinations, was first described by Thiele. Alginate and a variety of bivalent cations offer the formation of very ordered capillary structures [202]. In prior work, Sr^{2+} and Ca^{2+} were established as reliable gelation ions for the alginate products at hand in our group. Food-grade alginate ACHs, which were cross-linked with 1 M Sr^{2+} and later-on, chemically stabilized via a diisocyanate compound, demonstrated smaller median capillary diameter than ACHs, that were physically cross-linked with an equal concentration of Ca^{2+} (Sr^{2+}: 31 µm; Ca^{2+}: 80 µm). The resulting lower capillary density and porosity of Ca^{2+}-based ACHs could be detrimental to its proficiency as a permissive biomaterial in the SC. However, the 1 M Ca^{2+}-based ACHs achieved a formation of capillaries in the targeted 80 to 100 µm range, which is thought to facilitate the penetration of the host tissue. The fact, that smaller capillary-yielding alginate ACHs obtain a higher capillary density and a higher porosity has already been stated prior [220]. As mentioned in section 1.5, alginate ACHs had been more permissive for PNS axons as the diameter was increased up to 77 µm [212]. Thus, in order to elevate the diameter of capillaries in Sr^{2+}-based hydrogels, the reduction of the ion concentration was probed and successively larger median diameter values (0.125 M Sr^{2+}: 46 µm) were obtained for smaller deployed cation concentrations. Unfortunately, as the Sr^{2+} concentration was taken below 0.125 M, the completion of the gelling process was not attainable within 48 hours and a further increase in capillary diameter was hardly detectable. Hydrogels, which underwent ionotropic gelation with calcium concentrations below 1 M, yielded significantly too large capillary structures (0.25 M Ca^{2+}: 156 µm), which is known to negatively impact the degree of orientation of regenerating axons inside such a porous biomaterial [207].

Medical-grade hydrogels, which were cross-linked with very low concentrations of Sr^{2+}, only partially achieved high enough median capillary diameters (1003-03: 70 µm; 1106-03: 78 µm), but only with strontium concentrations as low as 0.025 M. At such low concentration regimes, the gelation process took up to three days until completion, and the capillary structure was less uniform than in gels, that had been cross-linked with 1 M Sr^{2+}. This may negatively impact the hydrogel's prowess as a structured biomaterial. Medical-grade 1 M Ca^{2+} cross-linked gels, which posed the majority of gels, that underwent *in-vitro* and *in-vivo* testing, obtained capillaries with median diameters between 74 and 108 µm. On the downside, the

increased capillary dimensions lead to a depressed capillary density and overall volume porosity compared to strontium-fabricated medical-grade hydrogels. In general, all types of hydrogel scaffolds, which possessed smaller capillary features would also display a higher density of capillaries per area and higher degrees of volume porosity. Further, when analyzing the development of capillary dimensions within the gel, one could see an increase in capillary diameter in sections of the gel body, which were further from the top of the gel, where the bodies were covered by the bivalent cationic solution in the ionotropic gelation process. Accordingly, both, capillary densities and porosities continuously declined from top to bottom of the respective gel body. This would occur regardless of the initially deployed cationic species concentration. As the advancing gelation front in the gel body progressed from top to bottom, the concentration of the cationic species was diminishing, hence, the successive increase in capillary diameter. This matches the findings with hydrogels, which were physically cross-linked with an overall lower cation concentration and yielded larger capillary structures in general as a consequence.

Upon a variation of the cation concentration, and thus, the capillary diameter, density, and volume porosity, no significant change in storage modulus G' or phase shift values in oscillatory shearing rheometry measurements could be determined in food-grade alginate hydrogels. Isotropic alginate hydrogels, which only underwent ionotropic cross-linking with calcium, had shown a strong dependence between storage modulus and calcium cross-linker concentration in prior research, where higher calcium cross-linker concentrations lead to a drastic increase in modulus [221]. This effect may be suppressed in our hydrogel samples due to the subsequent introduction of a chemical cross-linker and the replacement of the cations in the acidic washing process. Our prior research concluded, that a variation of the cross-linking cationic species (1 M Ba^{2+}, Sr^{2+}, Zn^{2+}or Ni^{2+}) in alginate ACHs would alter the size of the capillary structures, in which larger capillary structures would also demonstrate a higher degree of porosity and a lower mechanical rigidity in rheometry experiments [220]. This matches with findings of Shahriari et al., in which the elastic moduli of caprolactone biomaterials are also inversely correlated to their porosity [113]. This could not be confirmed for our alginate biomaterial, as the concentration of the cationic species did significantly affect the porosity of the scaffold, but not the storage moduli in rheometry.

4.2 The Alginate Product and its Concentration in the Alginate Biomaterial

Although significant differences in capillary diameters were determined in alginate ACHs, which originated from alginate sols of varying concentration and 1 M Sr^{2+} in a physical cross-linking process, all median capillary dimensions ranged closely between 31 to 49 µm. A steady decline in capillary density and volume

porosity of the hydrogels was observable with rising respective alginate concentrations. Because more alginate matter had to be housed in a certain volume of hydrogel scaffold, the thickness of the capillary walls was significantly increased and the porosity decreased as the respective alginate concentration was increased. As a porosity of 80% (v/v) was superior to 50% (v/v) in SCI-deployed biomaterials, a lower alginate concentration would be favorable in this context [98]. More precisely, porosities in the 70 to 75% (v/v) were shown to be a sweet spot in nerve conduit scaffolds, a level, which was not achieved in any alginate ACH in this work [101]. Food-grade gels, that had been cross-linked with 1M Sr^{2+} reached their highest porosity of 50% (v/v) as the concentration of the alginate sol was lowered to 0.5% (w/w). Slightly lower levels of up to 43% (v/v) volume porosity were recorded for 0.5% (w/w) medical-grade Sr^{2+}-based hydrogels. Overall, no distinct difference in capillary morphology between different batches of Sr^{2+}-based UP MVG alginate could be determined. Merely 20 to 31% (v/v) of volume porosity was determined in Ca^{2+} medical-grade hydrogels. SEM images of food- and medical-grade alginate hydrogels confirmed the findings from light-microscopic investigations, as the increase in porosity and capillary density in lesser concentrated alginate hydrogels was apparent by the thinner capillary walls and thus much denser porous structure. The capillary walls in 0.5% (w/w) food- and medical-grade ACHs were also much more fragile, rough, and deformed than those in their respective 1.0% (w/w) counterparts.

When tuning the diameter, porosity, and capillary density of the capillary system, one has to take into account the potential effects of the structural change on other properties, like the mechanical ones. Food-grade alginate ACHs, which originated from alginate sols of varying concentration and were cross-linked with 1 M Sr^{2+} and 100 mM HDI in water, demonstrated a successive increase of G' values from 1 to 32 kPa in rheometry experiments, as the alginate concentration was increased from 0.5% (w/w) to 2.0% (w/w). In our previous research on the mechanical properties of a similar alginate ACH from a different alginate product (Manugel DJX), 2.0% (w/w) hydrogels (1 M Sr^{2+}; 10 – 100 mM HDI as the cross-linker in water) occupied a similar storage modulus range as gels of an identical alginate concentration and cross-linking regime in this present work [220]. Analogous hydrogels in the same alginate concentration range, which were examined in AFM microindentation, were recorded with apparent elastic moduli E_{app} of 1 – 9 kPa (lowest to highest alginate concentration; indentation parallel to capillaries) and 3 – 12 kPa (lowest to highest alginate concentration; indentation perpendicular to capillaries) in this present work.

More to the point, as summarized in Table 8, disks of 0.5 and 0.75% (w/w) food-grade alginate ACHs (100 mM HDI in-water cross-linking), that underwent stability testing in a PBS medium for up to 12 weeks,

demonstrated merely one week of mechanical integrity up to a point, which allowed for a measurement in the rheometer. The 0.5% (w/w) samples consistently obtained a G' of 2 kPa and the 0.75% (w/w) ones a G' of 5 kPa for this one week in PBS. In those two cases, the PBS supernatant in the 0.5% (w/w) sample did not show a significant release of alginate subunits over the course of twelve weeks, but in the case of the 0.75% (w/w) sample, the entirety of the total amount of alginate in the sample disks was also dissolved after two weeks. The high retention in the case of the 0.5% (w/w) sample was most likely due to an imperfect sampling routine. The 0.5% (w/w) sample completely disintegrated into smaller pieces after the measurement interval at seven days and any not dissolved but merely fragmented alginate matter might not have been sampled correctly in the decanting process and was discarded in the renewal process of the buffer medium. Small slices of identical gel samples, which were intended for the examination in AFM microindentation experiments and were immersed in PBS over an identical timeframe, did not withstand the buffer solution at all, as they completely disintegrated within three hours before any measurement was possible.

1.0% (w/w) food-grade hydrogels performed only slightly better in retaining their mechanical properties in rheometry analysis, as the samples initially yielded a G' of 10 kPa and could be analyzed two weeks into the experiment with a final G' of 2 kPa before this sample class also disintegrated into smaller parts. On the contrary, only 24% (w/w) of the alginate dry weight was released over the whole 12-week timeframe, which was more than what was released from the 0.5% (w/w) sample, but significantly less, than from the 0.75% (w/w) sample. Once again, due to the complete disintegration of the sample 14 days into the experiment, the sampling might have also been subpar in that instance. In microindentation measurements, in which the 1.0% (w/w) samples were hard to handle with tweezers, the samples nonetheless yielded consistent mechanical integrity for twelve weeks, with E_{app} fluctuating between 0.4 – 1 kPa (indentation parallel to capillaries) and 0.2 – 4 kPa (indentation perpendicular to capillaries).

All higher alginate concentrations in ACHs, that were cross-linked with 100 mM HDI in water, provided hydrogel slices, that maintained their mechanical properties for eight weeks but were too fragile at week 12, which disallowed rheometry examination. Thus, in rheometry, the 1.25% (w/w) gels at first initially yielded a G' of 15 kPa, but eventually decayed to 6 kPa after eight weeks, while only 7% (w/w) of alginate was released from the gel bodies during the whole 12-week timeframe. Much lower and discontinuous moduli were recorded in microindentation experiments with E_{app} between 3 – 5 kPa (indentation parallel to capillaries) and 3 – 11 kPa (indentation perpendicular to capillaries) during the 12-week immersion period.

1.5% (w/w) ACHs hardly released any alginate to the PBS solution and their storage modulus decreased from 13 to 4 kPa during the 8-week period. Similarly, in microindentation experiments, the apparent elastic modulus decreased from 8 to 3 kPa (indentation parallel to capillaries) or remained rather constant in the 4 – 5 kPa (indentation perpendicular to capillaries) range during the 12-week period.

In 1.75% (w/w) alginate ACHs, G' values ranged between 16 kPa after 3 hours to 3 kPa after eight weeks, while the supernatant buffer solution diverted 23% (w/w) of the alginate matter from the samples after 12 weeks in PBS. For that sample, very inconsistent E_{app}, ranging from 10 to 3 kPa (indentation parallel to capillaries) and 24 to 4 kPa (indentation perpendicular to capillaries) were recorded over the whole 12-week timeframe.

In the highest tested alginate concentration, in 2.0% (w/w) samples, a G' decay from initially 24 to 5 kPa was present in eight weeks. About 26% (w/w) of the alginate was dissolved in the 8-week timeframe. In 2.0% (w/w) hydrogels (Sr^{2+}), that originated from a different alginate product (Manugel DJX), our previous research concluded that 100 mM HDI would suffice to retain almost 100% (w/w) of alginate mass over the course of twelve weeks [220]. In a PLGA biomaterial, that was used in a rodent SCI test, the material merely lost about 5% (w/w) of its initial mass after twelve weeks and only after 24 weeks a significant loss of biomaterial mass occurred alongside a loss of the anisotropic scaffold structure in a physiological surrounding [161]. The moduli in microindentation were also very inconsistent again, with values ranging from 5 kPa to 14 kPa (indentation parallel to capillaries) and 9 to 17 kPa (indentation perpendicular to capillaries) during the 12-week period.

Overall, in rheometry experiments, the storage moduli declined in every alginate concentration class over the course of eight weeks, with a more distinct decay in mechanical stability for higher concentrated, stiffer alginate hydrogels. Further, as indicated in Table 8, at any given interim, the hydrogel of the highest alginate concentration usually also yielded the stiffest hydrogels in rheometry and microindentation testing, with only a few exceptions. Almost without exception, the recorded apparent elastic moduli in microindentation testing were lower than the measured storage moduli in rheometry testing in this instance. Also, on overage, higher E_{app} values were recorded as the samples were indented perpendicular to the capillary systems compared to a capillary-parallel indentation. Contrary to the strongly declining G' values as the experiment progressed, the E_{app} values of these food-grade hydrogels did not demonstrate the same strong trend with time. The evolution of the mechanical properties in rheometry and microindentation testing did not match

the release behavior of the respective samples in buffer solution well, as a strong decay in moduli was not always accompanied by a significant degree of alginate release and vice versa. Thus, one can conclude, that a mechanical disintegration of the sample did not always go hand in hand with a dissolution of the alginate polymer.

Table 8: Measurement timeframe in weeks until no more sampling was possible due to sample integrity (Rheometry / AFM microindentation testing; in this case "12 w" indicates, that the samples did not disintegrate in the 12-week timeframe of the experiment) and point in time after which all alginate was released (Purpald assay; in this case "12 w" indicates, that not all alginate was released during the whole 12-week timeframe) from samples of different alginate concentration, that were cross-linked with 100 mM HDI in water; the corresponding range of measurement results for rheometry (G'), microindentation testing (E_{app} parallel (=) or E_{app} perpendicular to capillaries (⊥)), and amount of alginate released are given below.

	rheometry	AFM microindentation		alginate release
alginate concentration / % (w/w)		∥	⊥	
0.5	1 w	< 3 h	< 3 h	12 w
	2 kPa	-	-	-3%
0.75	1 w	< 3 h	< 3 h	2 w
	5 kPa	-	-	-100%
1	2 w	12 w	12 w	12 w
	2 – 10 kPa	0.4 – 1 kPa	0.2 – 4 kPa	-24%
1.25	8 w	12 w	12 w	12 w
	6 – 16 kPa	3 – 5 kPa	3 – 11 kPa	-7%
1.5	8 w	12 w	12 w	12 w
	4 – 13 kPa	1 – 8 kPa	4 – 10 kPa	-1%
1.75	8 w	12 w	12 w	12 w
	3 – 16 kPa	2 – 10 kPa	4 – 24 kPa	-23%
2	8 w	12 w	12 w	12 w
	5 – 24 kPa	4 – 14 kPa	9 – 17 kPa	-26%

Collagen hydrogels, that were deployed in canine SCI demonstrated similar moduli of elasticity in ultrasound elastography as food-grade alginate hydrogels in the 0.5 – 1.0% (w/w) range in our work, ranging from ~2 kPa in the case of 4.5 mg/mL gelled collagen to as much as 8 kPa for 7.5 mg/mL ones, thus also yielding stiffer scaffold structures as a higher polymer concentration was deployed in gelation [114]. Further, polyphenol biomaterials, that were tested in rodent SCI, yielded between 0.4 and 2 kPa in rheometry testing with higher storage moduli as the amount of monomer was increased, as has been elaborated on in section 1.2.5.2 [145].

The phase shift δ values in our work were significantly higher as the concentration of the alginate polymer in 10 – 100 mM HDI in-water cross-linked food-grade hydrogels was increased from 0.5 or 1.0 to 2.0% (w/w). Overall, the determined δ values (4 to 6 °) were larger than in our prior research with a different food-grade alginate product (Manugel DJX), where on average merely ~2.9 ° of phase shift was detected, which equated to a G'/G'' ratio of about 20 [220]. Thus, more viscoelastic hydrogel samples were obtained in our present work with the product Protanal.

As the alginate concentration in the food-grade ACH was incrementally raised from 0.5 to 2.0% (w/w), the swelling ratio successively decreased from roughly 40 to 20. In prior studies of our group, 2.0% (w/w) alginate ACHs from a different alginate product (Manugel DJX), that had also been cross-linked with 100 mM in water, yielded much lower swelling ratios from as low as ~7 (Sr^{2+} hydrogels) up to ~13 (Ni^{2+} hydrogels) [220]. Similar observations of lower swelling ratios with higher polymer concentrations were also reported for a polyphenol biomaterial, as discussed in section 1.2.5.2.

Although a different cation was utilized for physical cross-linking, one can clearly state, that 1 M Sr^{2+} cross-linked food-grade hydrogels clearly obtained higher storage moduli (584 – 703), than 1 M Ca^{2+} cross-linked 0.5% (w/w) medical-grade (1003-03) hydrogels (305 – 335 Pa), with 5 mM HDI in DMSO as the common chemical cross-linker in a 12-week PBS immersion experiment. This matches with findings in the viscosity measurements, which indicated, that the medical-grade (UP MVG 1003-03) alginate product merely possessed a viscosity average molar mass of 268 – 269 kDa, but the food-grade product reached 329 – 338 kDa. However, one has to note, that these values are subject to high uncertainty, as different alginate products from different algae genera have distinct $K_{[\eta]}$ and α parameters. Unfortunately, the algae subtype of the utilized alginate products in this work could not be further specified by the manufacturers due to proprietary information. The result, that a higher average molar mass of the alginate polymer was indicative of a stiffer gel body after gelling, matches with findings, that isotropic Sr^{2+} alginate gels with a polymer weight average molar mass of 70, respectively 257 kDa, yielded gels with a G' of 5.9, respectively 8.15 kPa [222]. However, when evaluating this relationship between polymer weight and the mechanical properties of the resulting gel matrix, one has to take into account the guluronic acid content of the alginate product. While all utilized alginate products contained ≥ 60% (w/w) of guluronic acid, the exact monomer composition was unknown. This may have unclear implications on the difference in mechanical properties between alginate product classes, as calcium alginate hydrogels of a higher guluronic acid content have been shown to elicit higher elastic moduli [223].

When comparing 1.0% (w/w) medical- and food-grade hydrogels, which were both cross-linked with 10 mM HDI in DMSO, the medical-grade specimens were much more stable, as no decay in G' nor E_{app} occurred at all over the course of four weeks. On the other hand, the food-grade samples disintegrated merely one week into the rheometry experiment. Both medical-grade 10 mM HDI cross-linked ACHs (1003-03/1106-03) obtained similar and constant storage moduli in the 4-week timeframe. The drastic difference between food- and medical-grade hydrogels (10 mM HDI in-DMSO cross-linking) was also apparent, as both medical-grade hydrogels (1003-03/1106-03) retained more than 60% (w/w) of the dry matter, while the food-grade samples retained less than 40% (w/w) over the timeframe of twelve weeks. For a general biomaterial, the real degradation monitoring *in-vivo*, would not only have to account for simple dissolution, as this work did, but also account for proteolytic degradation by enzymes, such as proteases, which are present in the SC ECM. However, this is neglectable in the case of alginate, as alginate lyases, which break down alginate via a β-elimination process, are not present in the human body but mainly in marine organisms, such as soil bacteria [224], [225].

4.3 The Chemical Cross-linking Methodology

As showcased in the prior section, 1 M Sr^{2+} and 0.5, 1.0, and 2.0% (w/w) food-grade alginate hydrogels, which had been cross-linked with HDI in water, demonstrated significantly different storage moduli upon a variation of the respective polymer concentration inside the scaffold matrix. However, the same samples did not show any significant variation in G' as the diisocyanate compound concentration was altered between 10 and 100 mM and ranged firmly around 1 – 2 kPa (0.5% (w/w) alginate ACH), 10 – 12 kPa (1.0% (w/w) alginate ACH), and 35 – 42 kPa (2.0% (w/w) alginate ACH). In this concentration range of HDI, the resulting interpenetrating network, which was formed in the aqueous environment, did not seem to affect the storage modulus nor the phase shift δ values of the scaffold in rheometry testing. Even higher diisocyanate concentrations than 100 mM, however, did affect the mechanical properties, as a 200 mM HDI cross-linked version of the 1.0% (w/w) alginate ACH demonstrated higher storage moduli (22 kPa), than 100 mM cross-linked ones (10 – 12 kPa).

Further, in 12-week stability testing, food-grade 1.0% (w/w) hydrogel specimens, that had undergone the 20 – 100 mM HDI in-water cross-linking procedure, not only were of roughly equal storage modulus but also demonstrated similar degradation behavior, as 14 days into the experiment, all samples either disintegrated completely or their modulus subsided dramatically (10 to 2 kPa) in the case of the 100 mM sample. On the other hand, the mechanical integrity of the 200 mM analogous sample disks was slightly

enhanced, as the storage moduli continuously decreased until eight weeks into the experiment (22 to 5 kPa) and only after that point in time the samples disintegrated. A similar picture was drawn by the alginate retention profile of these 1.0% (w/w) ACHs, which were cross-linked in water. The 20 and 50 mM samples did not retain any alginate mass beyond the 14-day mark, while the two higher diisocyanate concentrations were sufficient to ensure no release in excess of 35% (w/w) of the initial mass. This is in contrast to our prior research, in which 10 mM HDI sufficed to retain almost 100% (w/w) of the dry matter of a 2.0% (w/w) alginate gel (Manugel DJX). This was despite the fact, that rheometry samples in those prior experiments would show an almost total loss of elastic properties at seven days if the HDI concentration was below 100 mM. Hence, the present 1% (w/w) food-grade alginate gels (Protanal) were more susceptible to failure in alginate retention experiments but more resilient in rheometry examination, than the former 2.0% (w/w) samples (Manugel DJX) [220]. In the present indentation experiments, an increase in modulus with a rise of HDI from 100 to 200 mM could not be confirmed, as on the one hand, 200 mM cross-linked 1.0% (w/w) ACHs demonstrated a higher E_{app} than 100 mM HDI cross-linked ones when the indentation was parallel to the capillary orientation, but lower apparent elastic moduli as the indentation was performed in a perpendicular direction. 20 or 50 mM HDI in-water cross-linked 1.0% (w/w) food-grade hydrogels were not even able to withstand the buffer solution for three hours, which matched the fragile characteristics found in the alginate retention and rheometry experiments. On the flip side, 100 mM HDI cross-linked slices of alginate gels could be measured over the whole 12-week timeframe in microindentation testing, which was due to their smaller size, as the larger disks in rheometry testing were harder to handle and therefore, would tend to rip or disintegrate much easier in their very swollen state. Both, 20 and 100 mM HDI were sufficient to establish an interpenetrating network dense enough to reinforce 2.0% (w/w) hydrogel slices for twelve weeks in a buffer medium in prior research in a Sr^{2+}-based food-grade alginate ACH (Manugel DJX). However, in that instance, much higher E_{app} values were recorded, ranging as high as 250 kPa (100 mM HDI) [220]. Merely an E_{app} of 4 – 14 kPa (indentation parallel to capillaries) and 9 – 17 kPa (indentation perpendicular to capillaries) in 2.0% (w/w) food-grade gels (100 mM HDI in-water cross-linking) of the present work were recorded. Also, beyond 20 mM HDI, the swelling ratio continuously declined from 41 to 23, as 50 to 500 mM HDI in ascending increments were utilized in the cross-linking procedure in water in Sr^{2+}-based 1.0% (w/w) food-grade hydrogels. This matches with prior findings of our group, which also stated declining swelling ratios in Sr^{2+} food-grade 2.0% (w/w) alginate ACHs (Manugel DJX), but merely from ~16 to ~6 as the HDI concentration was increased from 10 to 100 mM [220]. Lower

equilibrium swelling ratios with increased amounts of chemical cross-linker were also found in poly(vinyl alcohol) hydrogels, that were cross-linked with glutaraldehyde and swollen in phosphate buffer or various salt solutions. Due to the fact, that as terminal groups underwent cross-linking reactions, the hydrogen bonding capabilities of the polymer diminished and thus also its swelling ability [226], [227]. A variation of the cross-linking species in water by utilizing ODI or DDI instead of HDI did not conclusively change G' nor the δ value. Just like HDI, the in-water ODI or DDI cross-linked scaffolds did not significantly change their mechanical properties in rheometry testing upon a variation of the respective diisocyanate concentration. Not only did alginate gels of lower alginate content (0.5 and 0.75% (w/w)), that had been cross-linked with 100 mM HDI in water, not obtain moduli as low as it was targeted in this work, but they also failed to maintain their mechanical integrity over the timespan of the stability testing in PBS. The same held true, as gels of a higher concentration (1.0% (w/w)), that were cross-linked with HDI concentration as low as 20 mM, were not only not softer with regard to their mechanical properties, but they also failed to adhere to their initial form over the 12-week experiment.

Evidently, to obtain stable hydrogels of much lower mechanical rigidity with moduli as low as 1 kPa, a novel cross-linking approach had to be used for our class of hydrogel samples. To do so preliminary experiments were performed with 1.0% (w/w) food-grade hydrogels, that were cross-linked with 100 mM HDI in DMSO at 125 °C. Ultimately, a very high storage modulus was obtained (92 kPa), however, HDI concentrations as low as 5 mM, yielded much softer samples in rheometry testing, with G' values as low as 3 kPa. In microindentation testing the range of moduli in median E_{app} values was even wider, ranging from 3 to 219 kPa (indentation parallel to capillaries) and 6 to 51 kPa (indentation perpendicular to capillaries) as the HDI concentration was successively raised from 10 to 100 mM. In other research, alginate hydrogels, that were chemically cross-linked with adipic dihydrazide demonstrated similar behavior in oscillatory shearing rheometry, as gels, that were cross-linked with 0.15 M of this bi-functional cross-linker obtained a significantly higher storage modulus (~40 kPa) than those, that were cross-linked with merely 0.05 M of it (~9 kPa) [221]. 5 mM HDI cross-linked 1.0% (w/w) samples, that had been prepared for indentation testing, disintegrated in 50 mL PBS within three hours, thus, no measurement was possible. Our 1.0% (w/w) hydrogels in question, whose moduli occupied the desired 1 to 10 kPa range, had been cross-linked with 5 or 10 mM HDI, which prove to be insufficient to chemically stabilize the scaffolds in the PBS medium beyond the one-week mark in rheometry testing. This partially matches with findings from indentation testing, in which 5 mM of HDI did not even suffice to stabilize the food-grade hydrogel for even three hours,

but 10 mM of HDI was enough to attain intact hydrogels for the entire 12-week experiment. Contrary to that, 0.5% (w/w) hydrogels, which were cross-linked with only 5 or 10 mM were stable in rheometry stability testing (~600 Pa) for twelve weeks. Unfortunately, no mechanical stability testing in microindentation experiments was done with 0.5% (w/w) gels in that case, however, in contrast to the 1.0% (w/w) samples, 5 mM sufficed to stabilize the 0.5% (w/w) scaffolds for at least three hours. In that instance, an elevation of HDI from 5 to 20 mM did not lead to a significant increase in E_{app} as the indentation was performed parallel to the capillaries (~2 kPa) or perpendicular to them (~2 – 3 kPa). An increase in HDI cross-linker to 50 mM yielded hydrogels of much higher stiffness as the indentation was performed parallel to the capillaries (~7 kPa), but not in the perpendicular orientation (~3 kPa). Overall, during the whole immersion period in PBS, the 0.5% (w/w) alginate samples (5/10 mM HDI) released significantly less alginate matter than the 1.0% (w/w) ones, however, none of the in-DMSO cross-linked specimens eventually released all of its alginate matter. In contrast to the hydrogels, that were cross-linked in water in the first place, some of these samples, which were treated with the diisocyanate compound in DMSO at 125 °C not only achieved very low elastic moduli but were also mechanically stable over a 12-week-period in PBS while doing so, which is favorable when a stable but soft biomaterial is of interest.

The same water-free cross-linking approach was also probed for ODI and DDI instead of HDI. 10, 20, or 50 mM of the respective diisocyanate was deployed on 1.0% (w/w) food-grade hydrogels. Just like in the HDI scenario, hydrogels, that were cross-linked with one of the other two diisocyanates, also demonstrated higher storage moduli, but not significantly changed phase shift values with an increase in cross-linker concentration. However, no clear difference in storage modulus could be established in hydrogels, that were cross-linked with differing diisocyanates of the same concentration. Notably, the phase shift values of HDI in-DMSO cross-linked samples were much higher (5 – 12.5 °) than they had been established in water-cross-linked ones in this present or prior research with 2.0% (w/w) hydrogels of a different alginate product (Manugel DJX) [220]. Thus, quite viscoelastic hydrogels with G'/G" ratios as low as 4.5 (compared to ~20 in the previous research) could be provided in our novel cross-linking approach. Apparently, the mere covalent cross-linking of adjacent monomers of the alginate backbone instead of the introduction of an interpenetrating polymer network permitted a higher degree of reorganization of the polymer matrix under stress, which resulted in a more viscoelastic response of the material.

A longer aliphatic chain in the diisocyanate compound, that was deployed in the water-free cross-linking process, clearly led to a smaller swelling ratio. The influence of the diisocyanate concentration was less clear,

however, higher ones tended to entail lower swelling ratios, as was also found in the water cross-linked approach and our prior studies [220]. The same was found, as the length of the alkyl chain of a diamine cross-linker, that cross-linked an activated ester sidechain in the synthesis of a poly(N-isopropyl acrylamide) gel was altered between two and twelve methylene units. Starting from an initial two methylene units, the swelling ratio in water declined from ~3.5 to ~2.3 for six to twelve methylene units in the diamine compound. Longer alkyl chains in the bifunctional cross-linking species rendered the resulting gel more hydrophobic and led to a decrease in swelling ratio. Further, the swelling ratio was drastically lowered from > 10 to almost 1, as the concentration of ethylenediamine (the shortest tested cross-linker) was raised from 20 to 80 mM in the gelation mixture [228]. Both of these two effects were observable in the swelling ratio of our ACHs, which had been cross-linking with rather hydrophobic diisocyanate species. Overall, the swelling ratios of food-grade gels, that had been cross-linked with 20 to 500 mM HDI in water, roughly matched those, that were obtained with only 10 mM of HDI in DMSO. Especially in the case of the shortest cross-linking compound HDI, higher concentrations of diisocyanate in the DMSO-based cross-linking process lead to significantly lower swelling ratios in hydrogels.

Due to the mentioned improvements in gel stability and mechanical properties variability, the more refined medical-grade hydrogels in our work were solely chemically cross-linked in DMSO at 125 °C. The softest hydrogel class, which was designed to occupy the 1 kPa modulus range, was constituted of a 1 M Ca^{2+} 0.5% (w/w) UP-MVG 1003-03 UP hydrogel, that had been chemically stabilized with 5 mM HDI in DMSO. This hydrogel class obtained consistently low G' of ~300 Pa and E_{app} of ~1 kPa during a 4-week PBS immersion. The next highest modulus class was obtained by raising the concentration of the medical-grade product to 1.0% (w/w) and the HDI cross-linker to 10 mM. To obtain such stiffness attributes and not elevate the alginate concentration past 0.5% (w/w) would have necessitated a much more drastic increase in the cross-linker HDI, which would be unfavorable due to potentially arising cytotoxic effects *in-vivo* [72]. This combination of alginate product and chemical cross-linker yielded hydrogels with storage moduli of 2 – 5 kPa (UP-MVG 1003-03/1106-03) and apparent elastic moduli of 3 – 4 kPa (1003-03) over the course of four weeks. A further increase of the HDI concentration to 20 mM yielded gels with G' of 5 – 9 kPa and E_{app} of 9 – 16 kPa. The two stiffer medical-grade hydrogels demonstrated a slight decrease in storage moduli over the 4-week period while completely maintaining their stiffness in microindentation testing, which is a clear indication, that, in those instances, the shearing history of the hydrogel disks might have affected the results going forward. Like their food-grade counterparts, medical-grade hydrogels, that were cross-linked

with higher concentrations of HDI, counterintuitively released more of their respective alginate matter to the surrounding PBS solution over the course of four weeks, but already reached a plateau after two weeks. Further, in both, food- and medical-grade ACHs, the combination of 0.5% (w/w) alginate and 5 mM HDI cross-linker resulted in gels, that released no alginate at all, thus posing an optimum alginate / HDI ratio with regards to inertness in buffer solution. At this point, one would have to monitor if the degradation rate of our biomaterial would be shown as too low *in-vivo*, as this could entail a higher risk of inflammation or compression of regenerating nerves in an SCI application [94]. Table 9 shows the storage and apparent elastic moduli, and the alginate release of the medical-grade UP MVG 1003-03 alginate samples, which all originated from 1.0 M Ca^{2+} and 5 – 20 mM HDI cross-linking in DMSO. The three different samples all differed significantly with regards to their moduli in both examination methodologies. Remarkably, contradicting the results that were obtained with food-grade alginate samples, that had been cross-linked with HDI in water (Table 8), these medical-grade in-DMSO cross-linked samples obtained higher moduli in microindentation than in rheometry testing. Further, no distinct difference in E_{app} between different indentation orientations was observable. None of the listed medical-grade samples underwent a decay of the storage nor the apparent elastic moduli, but significant differences in alginate release were observed during the first two of the four weeks.

Table 9: Measurement timeframe in weeks until no more sampling was possible due to sample integrity (Rheometry / AFM microindentation testing; in this case "4 w" indicates, that the medical-grade samples did not disintegrate in the 4-week timeframe of the experiment) and point in time after which all alginate was released (Purpald assay; in this case "4 w" indicates, that not all alginate was released during the whole 12-week timeframe) from medical-grade samples (UP MVG 1003-03) of varying alginate content, that were cross-linked with 5 – 20 mM HDI in DMSO; the corresponding range of measurement results for rheometry (G'), microindentation testing (E_{app} parallel to capillaries (=) or E_{app} perpendicular to capillaries (⊥)), and amount of alginate released are given below.

	rheometry	AFM microindentation		alginate release
medical-grade gel specimen		∥	⊥	
1 M Ca 5 mM HDI 0.5% UP-MVG	4w	4w	4w	4w
	0.3 kPa	1 kPa	1 - 2 kPa	0%
1 M Ca 10 mM HDI 1.0% UP-MVG	4w	4w	4w	4w
	2 kPa	3 - 4 kPa	3 - 4 kPa	-39%
1 M Ca 20 mM HDI 1.0% UP-MVG	4w	4w	4w	4w
	5- 9 kPa	9 - 16 kPa	8 - 15 kPa	-34%

The most stable calcium medical-grade gel in PBS, but also the softest of all medical-grade hydrogel samples also demonstrated the highest swelling ratio of 38, which was on par with the ratios obtained by food-grade hydrogels with the highest swelling ratio. Also, the swelling ratio in 1.0% (w/w) medical-grade hydrogels

lowered from 37 to 30 as the cross-linker in DMSO was raised from 10 to 20 mM HDI, which is consistent with the trend that was established in food-grade ACHs. As lower swelling ratios were favored in *in-vivo* applications (section 1.2.5), the higher swelling ratio of softer medical- and food-grade alginate ACHs in this work has to be considered as a potential detriment.

4.4 Stress-Relaxation in Microindentation Experiments

Although the correlation between phase shift δ values and the A_2/A_1 ratio was not good, higher A_2/A_1 tended to correlate with higher δ values in rheometry testing. This was expected, as materials, that are less elastic and more viscous in nature, undergo a more distinct force relaxation (Figure 10). As the force decay occurs faster in a rather viscous material (Figure 10 (III)) than in a rather elastic material (Figure 10 (II)), the time, after which a certain degree of force relaxation (e.g. 1/e) is reached, is shorter. Thus if one were to fit a faster decay to a bi-exponential fit, the term, whose relaxation time to obtain 1/e of the initial force is shorter, obtains a higher prefactor. Also, in rheometry testing, higher phase shift δ values indicate a more viscous behavior of a viscoelastic material, as the strain response to a stress-controlled setup is muted for a longer time and does not directly arise as soon the stress is applied, like in a perfect elastic solid. In this example, the prefactor A_2 would be higher if the shorter (0.1 s) decay function would predominantly contribute to the fit and A_1 would exhibit higher values if the longer (1 s) portion of the bi-exponential function would dominate. The three different medical-grade hydrogels obtained significantly decaying δ values as the rheometry measurements were performed over a 4-week timeframe. By the same token, the A_2/A_1 ratio also trended lower with immersion time, given the correlation to the phase shift values. More indicative of the ability of this method to identify viscoelastic behavior in indentation measurements, is the fact that when the stress relaxations after the 1 and 5 µm/s approaches were compared with each other, the data would indicate that the sample's response after a 5 µm/s indentation is distinctly more viscoelastic, as a higher A_2/A_1 ratio was determined. The elastic response of an ideal solid would not discriminate if the indentation was performed faster or slower and the same amount of force-build up would be the consequence eventually, as the force or stress buildup are solely dependent on the applied strain (Figure 9 (II); Eq. 2; Eq. 3). In a viscoelastic material however, the material creeps and relaxes stress as soon as stress, respectively strain, are applied to it (Figure 10; Figure 12). Thus, if the application of a strain to a viscoelastic material in a stress relaxation experiment occurs faster, the buildup of stress will be more pronounced, as there is less time for the sample to rearrange and thus relax some of the stress during the strain build-up. Hence, a more pronounced stress- or force relaxation and thus a higher A_2/A_1 ratio during the observed 4-second

timeframe would be recorded in the case of the pause segment, which ensued the faster 5 μm/s indentations of the samples. This was the case, as a statistically significant difference between both fit parameter ratios was present in the stress relaxation fit data after the two indentation speed indentations.

5. *In-Vivo* Experiments of Alginate Anisotropic Capillary Hydrogels

We manufactured four different medical-grade alginate ACHs, which were much softer than those of our previous work and are much more in line with the mechanical properties of the native SC, ranging from 1 to 20 kPa in storage modulus and apparent elastic modulus. Our colleagues at the Spinal Cord Injury Center of the Heidelberg University Hospital utilized Female Fischer-344 rats to conduct *in-vivo* experiments. An incomplete C5 injury was inflicted and patched with one of the three 1 M Ca^{2+} UP MVG 1003-03 ACH hydrogels (Table 9) of varying stiffness. Hereby, the variation of mechanical properties was obtained by varying the alginate concentration and the concentration of the cross-linker HDI in a water-free cross-linking procedure in DMSO. Before implantation, the gels were coated with a mixture of PLO and laminin. Four weeks post-implantation, histological examination of the injury site revealed, that the reaction of microglia and macrophages was much more pronounced in stiffer alginate ACH-treated specimens. Further, more host cells invaded the softer hydrogel samples and fewer CSPGs were secreted in the recovery process. The gels of lower modulus also allowed for the greatest degree of vascularization and axonal growth to occur inside the biomaterial. On the flip side, stiffer alginate ACHs provided a scaffold, that enhanced the uniformity of axonal regrowth, as they exhibited the most parallel growth inside their capillary lumen. As no combinatorial model, such as rostral or caudal cell or growth factor interventions were performed, no axonal re-entry into the host parenchyma was observed as expected.

6. Conclusion

The use of biomaterials in SCI treatments has the potential to revolutionize the way we treat and manage this debilitating condition. Biomaterials offer a range of benefits, including the ability to mimic the properties of natural tissue, which can minimize rejection and promote tissue healing. However, it is important, that the mechanical properties of these biomaterials are carefully monitored and tuned to ensure that they are appropriate for the intended application. One of the most important reasons for monitoring and tuning the mechanical properties of a biomaterial used in SCI is to minimize the risk of damage to the surrounding tissue. When a biomaterial is implanted in the body, it is subjected to various mechanical loads, such as compression, tension, and shear. If the mechanical properties of the biomaterial are significantly different from those of the host tissue, it can cause damage to the surrounding tissue and impede the healing process. Thus, if the elastic modulus of the biomaterial is much higher than that of the SC, it might not be able to conform to the natural shape of the SC. Similarly, if the compressive strength of the biomaterial is much lower than that of the SC, it will not be able to provide adequate support and may collapse under load, causing further damage to the cord.

Further, it is important to note that the mechanical properties of a biomaterial are not static, but can change over time. Factors such as the environment, temperature, and mechanical loads can all affect the mechanical properties of a biomaterial. Therefore, it is important to monitor and tune the mechanical properties of a biomaterial over time, to ensure that it continues to perform optimally. Future *in-vitro* and *in-vivo* SCI recovery models, that incorporate a biomaterial scaffold should provide sufficient information on its mechanical properties. This information is not available in most research and if it is, the measurement setups, measurement parameters, and data evaluation are hardly comparable, which does not provide a sound basis on which to evaluate and compare results. We outlined a procedure to fabricate anisotropic capillary alginate hydrogels, which can be tuned with regard to their capillary morphology, as well as to their mechanical properties in a replicable manner. Alginate anisotropic hydrogels with a high amount of guluronic acid content have been identified as a versatile biomaterial in tissue engineering and regenerative medicine, in particular also the guided regeneration of nerves in the central and peripheral nervous system. In our approach, the capillary dimensions of an alginate capillary hydrogel could be adjusted seamlessly from 20 to 100 µm, which in turn unequivocally affected the capillary density and porosity. Besides that, a continuous spectrum of mechanical properties in the form of storage modulus or apparent elastic modulus, ranging from as low as several hundred Pa up to over 100 kPa, could be established by varying key

parameters in our two-pronged physical and chemical cross-linking procedure. The insights gained from experiments with a food-grade alginate product were successfully applied to medical-grade hydrogels, which were tailored to meet very specific demands, which had been established before this work. Thus, a reduction of the modulus of elasticity in rheometry and microindentation from 15 to 45 kPa in our prior work to values, which are more in line with the native SC tissue, was successfully implemented in this present work. Further, the dimension of the capillary lumen of the alginate ACH was adjusted to meet requirements, that had been identified in *in-vivo* and *in-vitro* experiments beforehand. Our fine-tuned anisotropic alginate biomaterial has already been utilized in follow-up *in-vivo* experiments in the rodent SC. While a distinct influence of the mechanical properties on the outcome of the experiment is clearly observable, the majority of investigations are still ongoing.

Bibliography

[1] S. Rossignol, *Principles of Spinal Cord Injury Clinical Practice*. 2013.

[2] M. Ganau, R. Zewude, and M. G. Fehlings, "Functional Anatomy of the Spinal Cord," in *Degenerative Cervical Myelopathy and Radiculopathy*, Cham: Springer International Publishing, 2019, pp. 3–12.

[3] D. B. Choi, G. Nam, D. M. Groh, S. Syed, J. S. Fridley, and Z. L. Gokaslan, "Spinal Cord Anatomy," in *Spinal Cord Tumors*, K. I. Arnautović and Z. L. Gokaslan, Eds. Cham: Springer International Publishing, 2019, pp. 43–53.

[4] T. Popović, Dejan B.; Sinkjær, "Central nervous System Lesions Leading to Disability," *J. Autom. Control*, vol. 18, no. 2, pp. 11–23, 2008.

[5] J. T. Hughes, "The Edwin Smith Surgical Papyrus: an analysis of the first case reports of spinal cord injuries," *Spinal Cord*, vol. 26, no. 2, pp. 71–82, 1988.

[6] N. A. Silva, N. Sousa, R. L. Reis, and A. J. Salgado, "From basics to clinical: A comprehensive review on spinal cord injury," *Prog. Neurobiol.*, vol. 114, pp. 25–57, 2014.

[7] M. Adams and J. F. R. Cavanagh, "International Campaign for Cures of Spinal Cord Injury Paralysis (ICCP): another step forward for spinal cord injury research," *Spinal Cord*, vol. 42, no. 5, pp. 273–280, 2004.

[8] B. H. Dobkin and L. A. Havton, "Basic Advances and New Avenues in Therapy of Spinal Cord Injury," *Annu. Rev. Med.*, vol. 55, no. 1, pp. 255–282, 2004.

[9] National SCI Statistical Center, "Spinal Cord Injury (SCI) Facts and Figures at a Glance," *J. Spinal Cord Med.*, vol. 39, no. 2, pp. 243–244, 2016.

[10] A. Alizadeh, S. M. Dyck, and S. Karimi-Abdolrezaee, "Traumatic Spinal Cord Injury: An Overview of Pathophysiology, Models and Acute Injury Mechanisms," *Front. Neurol.*, vol. 10, pp. 1–25, 2019.

[11] J. W. Middleton, A. Dayton, J. Walsh, S. B. Rutkowski, G. Leong, and S. Duong, "Life expectancy after spinal cord injury: a 50-year study," *Spinal Cord*, vol. 50, no. 11, pp. 803–811, 2012.

[12] K. Haastert-Talini *et al.*, "Chitosan tubes of varying degrees of acetylation for bridging peripheral nerve defects," *Biomaterials*, vol. 34, no. 38, pp. 9886–9904, 2013.

[13] P. J. O'Connor, "Survival after spinal cord injury in Australia," *Arch. Phys. Med. Rehabil.*, vol. 86, no. 1, pp. 37–47, 2005.

[14] B. K. Kwon, C. G. Fisher, M. F. Dvorak, and W. Tetzlaff, "Strategies to Promote Neural Repair and Regeneration After Spinal Cord Injury," *Spine (Phila. Pa. 1976).*, vol. 30, no. 17 suppl., pp. 3–13, 2005.

[15] C. H. Tator, "Update on the Pathophysiology and Pathology of Acute Spinal Cord Injury," *Brain Pathol.*, vol. 5, no. 4, pp. 407–413, 1995.

[16] S. Woerly *et al.*, "Heterogeneous PHPMA hydrogels for tissue repair and axonal regeneration in the injured spinal cord," *J. Biomater. Sci. Polym. Ed.*, vol. 9, no. 7, pp. 681–711, 1998.

[17] L. Wolman, "The Disturbance of Circulation in Traumatic Paraplegia in Acute and Late Stages: A Pathological Study," pp. 213–226, 1964.

[18] L. D. Hachem, C. S. Ahuja, and M. G. Fehlings, "Assessment and management of acute spinal cord injury: From point of injury to rehabilitation," *J. Spinal Cord Med.*, vol. 40, no. 6, pp. 665–675, 2017.

[19] C. M. Dumont *et al.*, "Aligned hydrogel tubes guide regeneration following spinal cord injury," *Acta Biomater.*, vol. 86, pp. 312–322, 2019.

[20] R. E. von Leden, Y. J. Yauger, G. Khayrullina, and K. R. Byrnes, "Central Nervous System Injury and Nicotinamide Adenine Dinucleotide Phosphate Oxidase: Oxidative Stress and Therapeutic Targets," *J. Neurotrauma*, vol. 34, no. 4, pp. 755–764, 2017.

[21] N. B. Pivovarova and S. B. Andrews, "Calcium-dependent mitochondrial function and dysfunction in neurons," *FEBS J.*, vol. 277, no. 18, pp. 3622–3636, 2010.

[22] B. C. Walters *et al.*, "Guidelines for the management of acute cervical spine and spinal cord injuries: 2013 update," *Clin. Neurosurg.*, vol. 60, pp. 82–91, 2013.

[23] C. S. Ahuja *et al.*, "Traumatic spinal cord injury - Repair and regeneration," *Clin. Neurosurg.*, vol. 80, no. 3, pp. S22–S90, 2017.

[24] M. G. Fehlings *et al.*, "Early versus Delayed Decompression for Traumatic Cervical Spinal Cord Injury: Results of the Surgical Timing in Acute Spinal Cord Injury Study (STASCIS)," *PLoS One*, vol. 7, no. 2, pp. 1–8, 2012.

[25] M. Bracken, "A Randomized, Controlled Trial of Methylprednisolone or Naloxone in the Treatment of Acute Spinal Cord Injury," *N. Engl. J. Med.*, vol. 322, no. 20, pp. 1405–1411, 1990.

[26] M. N. Hadley, "Blood pressure management after acute spinal cord injury," *Neurosurgery*, vol. 50, no. 3 suppl., pp. 58–62, 2002.

[27] E. Mazzoni *et al.*, "Bioactive Materials for Soft Tissue Repair," *Front. Bioeng. Biotechnol.*, vol. 9, no. February, pp. 1–17, 2021.

[28] J. R. Wilson, D. W. Cadotte, and M. G. Fehlings, "Clinical predictors of neurological outcome, functional status, and survival after traumatic spinal cord injury: a systematic review.," *J. Neurosurg. Spine*, vol. 17, no. 1 suppl., pp. 11–26, 2012.

[29] D. M. Basso, M. S. Beattie, and J. C. Bresnahan, "A Sensitive and Reliable Locomotor Rating Scale for Open Field Testing in Rats," *J. Neurotrauma*, vol. 12, no. 1, pp. 1–21, 1995.

[30] Z. Cai *et al.*, "Photosensitive Hydrogel Creates Favorable Biologic Niches to Promote Spinal Cord Injury Repair," *Adv. Healthc. Mater.*, vol. 8, no. 13, pp. 1–10, 2019.

[31] A. P. Tran, P. M. Warren, and J. Silver, "The Biology of Regeneration Failure and Success After Spinal Cord Injury," *Physiol. Rev.*, vol. 98, no. 2, pp. 881–917, 2018.

[32] L. Huang *et al.*, "Glial Scar Formation Occurs in the Human Brain after Ischemic Stroke," *Int. J. Med. Sci.*, vol. 11, no. 4, pp. 344–348, 2014.

[33] J. M. Cregg, M. A. DePaul, A. R. Filous, B. T. Lang, A. Tran, and J. Silver, "Functional regeneration beyond the glial scar," *Exp. Neurol.*, vol. 253, pp. 197–207, 2014.

[34] C. M. Galtrey and J. W. Fawcett, "The role of chondroitin sulfate proteoglycans in regeneration and plasticity in the central nervous system," *Brain Res. Rev.*, vol. 54, no. 1, pp. 1–18, 2007.

[35] F. Matsui and A. Oohira, "Proteoglycans and injury of the central nervous system," *Congenit. Anom. (Kyoto).*, vol. 44, pp. 181–188, 2004.

[36] M. A. Anderson *et al.*, "Astrocyte scar formation aids central nervous system axon regeneration," *Nature*, vol. 532, no. 7598, pp. 195–200, 2016.

[37] J. Silver, "The glial scar is more than just astrocytes," *Exp. Neurol.*, vol. 286, pp. 147–149, 2016.

[38] J. Silver and J. H. Miller, "Regeneration beyond the glial scar," *Nat. Rev. Neurosci.*, vol. 5, no. 2, pp. 146–156, 2004.

[39] T. Führmann, P. N. Anandakumaran, and M. S. Shoichet, "Combinatorial Therapies After Spinal Cord Injury: How Can Biomaterials Help?," *Adv. Healthc. Mater.*, vol. 6, no. 10, pp. 1–21, 2017.

[40] D. Joung *et al.*, "3D Printed Stem-Cell Derived Neural Progenitors Generate Spinal Cord Scaffolds," *Adv. Funct. Mater.*, vol. 28, no. 39, pp. 1–10, 2018.

[41] A. M. Parr *et al.*, "Transplanted adult spinal cord–derived neural stem/progenitor cells promote early functional recovery after rat spinal cord injury," *Neuroscience*, vol. 155, no. 3, pp. 760–770, 2008.

[42] V. R. Dasari, "Mesenchymal stem cells in the treatment of spinal cord injuries: A review," *World J. Stem Cells*, vol. 6, no. 2, p. 120, 2014.

[43] R. Volkman and D. Offen, "Concise Review: Mesenchymal Stem Cells in Neurodegenerative Diseases," *Stem Cells*, vol. 35, no. 8, pp. 1867–1880, 2017.

[44] V. Neirinckx, D. Cantinieaux, C. Coste, B. Rogister, R. Franzen, and S. Wislet-Gendebien, "Concise Review: Spinal Cord Injuries: How Could Adult Mesenchymal and Neural Crest Stem Cells Take Up the Challenge?," *Stem Cells*, vol. 32, no. 4, pp. 829–843, 2014.

[45] C. Deister and C. E. Schmidt, "Optimizing neurotrophic factor combinations for neurite outgrowth," *J. Neural Eng.*, vol. 3, no. 2, pp. 172–179, 2006.

[46] N. I. Bamber, H. Li, X. Lu, M. Oudega, P. Aebischer, and X. M. Xu, "Neurotrophins BDNF and NT-3 promote axonal re-entry into the distal host spinal cord through Schwann cell-seeded mini-channels," *Eur. J. Neurosci.*, vol. 13, no. 2, pp. 257–268, 2001.

[47] S. Karamouzian, S. N. Nematollahi-Mahani, N. Nakhaee, and H. Eskandary, "Clinical safety and primary efficacy of bone marrow mesenchymal cell transplantation in subacute spinal cord injured patients," *Clin. Neurol. Neurosurg.*, vol. 114, no. 7, pp. 935–939, 2012.

[48] M. Sasaki *et al.*, "BDNF-Hypersecreting Human Mesenchymal Stem Cells Promote Functional Recovery, Axonal Sprouting, and Protection of Corticospinal Neurons after Spinal Cord Injury," *J. Neurosci.*, vol. 29, no. 47, pp. 14932–14941, 2009.

[49] L. Yao *et al.*, "Human umbilical cord blood stem cell transplantation for the treatment of chronic spinal cord injury," *Neural Regen. Res.*, vol. 8, no. 5, pp. 397–403, 2013.

[50] J. M. Ryan, F. P. Barry, J. M. Murphy, and B. P. Mahon, "Mesenchymal stem cells avoid allogeneic rejection," *J. Inflamm.*, vol. 2, no. 1, p. 8, 2005.

[51] E. Y. Kim, K. Lee, and M. K. Kim, "The potential of mesenchymal stem cells derived from amniotic membrane and amniotic fluid for neuronal regenerative therapy," *BMB Rep.*, vol. 47, no. 3, pp. 135–140, 2014.

[52] K. Menezes *et al.*, "Human Mesenchymal Cells from Adipose Tissue Deposit Laminin and Promote Regeneration of Injured Spinal Cord in Rats," *PLoS One*, vol. 9, no. 5, pp. 1–15, 2014.

[53] L. E. Kokai, K. Marra, and J. P. Rubin, "Adipose stem cells: biology and clinical applications for tissue repair and regeneration," *Transl. Res.*, vol. 163, no. 4, pp. 399–408, 2014.

[54] H. Iwai *et al.*, "Allogeneic Neural Stem/Progenitor Cells Derived From Embryonic Stem Cells Promote Functional Recovery After Transplantation Into Injured Spinal Cord of Nonhuman Primates," *Stem Cells Transl. Med.*, vol. 4, no. 7, pp. 708–719, 2015.

[55] R. P. Salewski, R. A. Mitchell, C. Shen, and M. G. Fehlings, "Transplantation of Neural Stem Cells Clonally Derived from Embryonic Stem Cells Promotes Recovery After Murine Spinal Cord Injury," *Stem Cells Dev.*, vol. 24, no. 1, pp. 36–50, 2015.

[56] M. Goulão and A. C. Lepore, "iPS Cell Transplantation for Traumatic Spinal Cord Injury," *Curr. Stem Cell Res. Ther.*, vol. 11, no. 4, pp. 321–328, 2016.

[57] C. A. Herberts, M. S. G. Kwa, and H. P. H. Hermsen, "Risk factors in the development of stem cell therapy," *J. Transl. Med.*, vol. 9, pp. 1–14, 2011.

[58] G. W. J. Hawryluk, A. Mothe, J. Wang, S. Wang, C. Tator, and M. G. Fehlings, "An In Vivo Characterization of Trophic Factor Production Following Neural Precursor Cell or Bone Marrow Stromal Cell Transplantation for Spinal Cord Injury," *Stem Cells Dev.*, vol. 21, no. 12, pp. 2222–2238, 2012.

[59] V. Moreno-Manzano *et al.*, "Activated Spinal Cord Ependymal Stem Cells Rescue Neurological Function," *Stem Cells*, vol. 27, no. 3, pp. 733–743, 2009.

[60] H. Yang, B. R. He, and D. J. Hao, "Biological Roles of Olfactory Ensheathing Cells in Facilitating Neural Regeneration: A Systematic Review," *Mol. Neurobiol.*, vol. 51, no. 1, pp. 168–179, 2015.

[61] A. Ramón-Cueto, M. I. Cordero, F. F. Santos-Benito, and J. Avila, "Functional recovery of paraplegic rats and motor axon regeneration in their spinal cords by olfactory ensheathing glia," *Neuron*, vol. 25, no. 2, pp. 425–435, 2000.

[62] R. Yao *et al.*, "Olfactory Ensheathing Cells for Spinal Cord Injury," *Cell Transplant.*, vol. 27, no. 6, pp. 879–889, 2018.

[63] M. Oudega *et al.*, "Axonal regeneration into Schwann cell grafts within resorbable poly(α-hydroxyacid) guidance channels in the adult rat spinal cord," *Biomaterials*, vol. 22, no. 10, pp. 1125–1136, 2001.

[64] M. B. Bunge, "Efficacy of Schwann cell transplantation for spinal cord repair is improved with combinatorial strategies," *J. Physiol.*, vol. 594, no. 13, pp. 3533–3538, 2016.

[65] X.-H. Zhou *et al.*, "Transplantation of Autologous Activated Schwann Cells in the Treatment of Spinal Cord Injury: Six Cases, more than Five Years of Follow-up," *Cell Transplant.*, vol. 21, pp. 39–47, 2012.

[66] S. Oraee-Yazdani *et al.*, "Co-transplantation of autologous bone marrow mesenchymal stem cells and Schwann cells through cerebral spinal fluid for the treatment of patients with chronic spinal cord injury: Safety and possible outcome," *Spinal Cord*, vol. 54, no. 2, pp. 102–109, 2016.

[67] I. Vismara, S. Papa, F. Rossi, G. Forloni, and P. Veglianese, "Current Options for Cell Therapy in Spinal Cord Injury," *Trends Mol. Med.*, vol. 23, no. 9, pp. 831–849, 2017.

[68] M. A. Anderson *et al.*, "Astrocyte scar formation AIDS central nervous system axon regeneration," *Nature*, vol. 532, no. 7598, pp. 195–200, 2016.

[69] M. V. Sofroniew, "Molecular dissection of reactive astrogliosis and glial scar formation," *Trends Neurosci.*, vol. 32, no. 12, pp. 638–647, 2009.

[70] J. M. Zuidema, G. P. Desmond, C. J. Rivet, K. R. Kearns, D. M. Thompson, and R. J. Gilbert, "Nebulized solvent ablation of aligned PLLA fibers for the study of neurite response to anisotropic-to-isotropic fiber/film transition (AFFT) boundaries in astrocyte-neuron co-cultures," *Biomaterials*, vol. 46, pp. 82–94, 2015.

[71] T. Schackel *et al.*, "Peptides and Astroglia Improve the Regenerative Capacity of Alginate Gels in the Injured Spinal Cord," *Tissue Eng. - Part A*, vol. 25, no. 7–8, pp. 522–537, 2019.

[72] X. Guan *et al.*, "Development of hydrogels for regenerative engineering," *Biotechnol. J.*, vol. 12, no. 5, pp. 1–19, 2017.

[73] M. Tsintou, K. Dalamagkas, and A. M. Seifalian, "Advances in regenerative therapies for spinal cord injury: A biomaterials approach," *Neural Regen. Res.*, vol. 10, no. 5, pp. 726–742, 2015.

[74] T. Mitra, G. Sailakshmi, A. Gnanamani, and A. B. Mandal, "Studies on Cross-linking of succinic acid with chitosan/collagen," *Mater. Res.*, vol. 16, no. 4, pp. 755–765, 2013.

[75] Š. Kubinová *et al.*, "SIKVAV-modified highly superporous PHEMA scaffolds with oriented pores for spinal cord injury repair," *J. Tissue Eng. Regen. Med.*, vol. 9, no. 11, pp. 1298–1309, 2015.

[76] S. Woerly, P. Petrov, E. Syková, T. Roitbak, Z. Simonová, and A. R. Harvey, "Neural Tissue Formation Within Porous Hydrogels Implanted in Brain and Spinal Cord Lesions: Ultrastructural, Immunohistochemical, and Diffusion Studies," *Tissue Eng.*, vol. 5, no. 5, pp. 467–488, 1999.

[77] H. Macková *et al.*, "RGDS- and SIKVAVS-Modified Superporous Poly(2-hydroxyethyl methacrylate) Scaffolds for Tissue Engineering Applications," *Macromol. Biosci.*, vol. 16, no. 11, pp. 1621–1631, 2016.

[78] J. M. Oliveira *et al.*, "Hydrogel-based scaffolds to support intrathecal stem cell transplantation as a gateway to the spinal cord: clinical needs, biomaterials, and imaging technologies," *npj Regen. Med.*, vol. 3, no. 1, pp. 1–9, 2018.

[79] B. Kaczmarek, K. Nadolna, and A. Owczarek, *The physical and chemical properties of hydrogels based on natural polymers*. Elsevier Inc., 2020.

[80] C. G. Williams, A. N. Malik, T. K. Kim, P. N. Manson, and J. H. Elisseeff, "Variable cytocompatibility of six cell lines with photoinitiators used for polymerizing hydrogels and cell encapsulation," *Biomaterials*, vol. 26, no. 11, pp. 1211–1218, 2005.

[81] E. M. Ahmed, "Hydrogel: Preparation, characterization, and applications: A review," *J. Adv. Res.*, vol. 6, no. 2, pp. 105–121, 2015.

[82] H. Ismail, M. Irani, and Z. Ahmad, "Starch-Based Hydrogels: Present Status and Applications," *Int. J. Polym. Mater. Polym. Biomater.*, vol. 62, pp. 411–420, 2013.

[83] S. Van Vlierberghe, P. Dubruel, and E. Schacht, "Biopolymer-based hydrogels as scaffolds for tissue engineering applications: A review," *Biomacromolecules*, vol. 12, no. 5, pp. 1387–1408, 2011.

[84] N. Ghane, M. H. Beigi, S. Labbaf, M. H. Nasr-Esfahani, and A. Kiani, "Design of hydrogel-based scaffolds for the treatment of spinal cord injuries," *J. Mater. Chem. B*, vol. 8, no. 47, pp. 10712–10738, 2020.

[85] T. Führmann, J. Obermeyer, C. H. Tator, and M. S. Shoichet, "Click-crosslinked injectable hyaluronic acid hydrogel is safe and biocompatible in the intrathecal space for ultimate use in regenerative strategies of the injured spinal cord," *Methods*, vol. 84, pp. 60–69, 2015.

[86] M. F. Akhtar, M. Hanif, and N. M. Ranjha, "Methods of synthesis of hydrogels … A review," *Saudi Pharm. J.*, vol. 24, no. 5, pp. 554–559, 2016.

[87] E. Aurand, J. Wagner, C. Lanning, and K. Bjugstad, "Building Biocompatible Hydrogels for Tissue Engineering of the Brain and Spinal Cord," *J. Funct. Biomater.*, vol. 3, no. 4, pp. 839–863, 2012.

[88] C. N. Bowman and C. J. Kloxin, "Toward an Enhanced Understanding and Implementation of Photopolymerization Reactions," *Am. Inst. Chem. Eng.*, vol. 54, no. 11, pp. 2775–2795, 2008.

[89] L. Dong and A. S. Hoffman, "A novel approach for preparation of pH-sensitive hydrogels for enteric drug delivery," *J. Control. Release*, vol. 15, no. 2, pp. 141–152, 1991.

[90] Q. Wen, A. Basu, P. A. Janmey, and A. G. Yodh, "Non-affine deformations in polymer hydrogels," *Soft Matter*, vol. 8, no. 31, pp. 8039–8049, 2012.

[91] A. Göpferich, "Mechanisms of polymer degradation and erosion," *Biomaterials*, vol. 17, no. 2, 1996.

[92] O. Wichterle and D. Lím, "Hydrophilic Gels for Biological Use," *Nature*, vol. 185, pp. 117–118, 1960.

[93] N. Peppas, P. Bures, W. Leobandung, and H. Ichikawa, "Hydrogels in pharmaceutical formulations," *Eur. J. Pharm. Biopharm.*, vol. 50, no. 1, pp. 27–46, 2000.

[94] K. S. Straley, C. W. P. Foo, and S. C. Heilshorn, "Biomaterial design strategies for the treatment of spinal cord injuries," *J. Neurotrauma*, vol. 27, no. 1, pp. 1–19, 2010.

[95] X. Yu, G. P. Dillon, and R. V. Bellamkonda, "A laminin and nerve growth factor-laden three-dimensional scaffold for enhanced neurite extension," *Tissue Eng.*, vol. 5, no. 4, pp. 291–304, 1999.

[96] R. Marchand, S. Woerly, L. Bertrand, and N. Valdes, "Evaluation of two cross-linked collagen gels implanted in the transected spinal cord," *Brain Res. Bull.*, vol. 30, no. 3–4, pp. 415–422, 1993.

[97] K. M. Pawelec, J. Koffler, D. Shahriari, A. Galvan, M. H. Tuszynski, and J. Sakamoto, "Microstructure and in vivo characterization of multi-channel nerve guidance scaffolds," *Biomed. Mater.*, vol. 13, no. 4, pp. 1–26, 2018.

[98] L. E. Kokai, Y. C. Lin, N. M. Oyster, and K. G. Marra, "Diffusion of soluble factors through degradable polymer nerve guides: Controlling manufacturing parameters," *Acta Biomater.*, vol. 5, no. 7, pp. 2540–2550, 2009.

[99] S. R. Peyton *et al.*, "Marrow-Derived Stem Cell Motility in 3D Synthetic Scaffold Is Governed by Geometry Along With Adhesivity and Stiffness," vol. 108, no. 5, pp. 1181–1193, 2011.

[100] Š. Kubinová *et al.*, "SIKVAV-modified highly superporous PHEMA scaffolds with oriented pores for spinal cord injury repair," *J. Tissue Eng. Regen. Med.*, vol. 9, no. 11, pp. 1298–1309, 2015.

[101] G. E. Rutkowski and C. A. Heath, "Development of a bioartificial nerve graft. II. Nerve regeneration in vitro," *Biotechnol. Prog.*, vol. 18, no. 2, pp. 373–379, 2002.

[102] R. M. Smeal, R. Rabbitt, R. Biran, and P. A. Tresco, "Substrate Curvature Influences the Direction of Nerve Outgrowth," *Ann. Biomed. Eng.*, vol. 33, no. 3, pp. 376–382, 2005.

[103] E. Fournier, C. Passirani, C. N. Montero-Menei, and J. P. Benoit, "Biocompatibility of implantable synthetic polymeric drug carriers: focus on brain biocompatibility," *Biomaterials*, vol. 24, no. 19, pp. 3311–3331, 2003.

[104] Y. D. Teng *et al.*, "Functional recovery following traumatic spinal cord injury mediated by a unique polymer scaffold seeded with neural stem cells," *Proc. Natl. Acad. Sci.*, vol. 99, no. 5, pp. 3024–3029, 2002.

[105] J. B. Shim, R. F. Ankeny, H. Kim, R. M. Nerem, and G. Khang, "A study of a three-dimensional PLGA sponge containing natural polymers co-cultured with endothelial and mesenchymal stem cells as a tissue engineering scaffold," *Biomed. Mater.*, vol. 9, no. 4, pp. 1–10, 2014.

[106] A. J. Engler, S. Sen, H. L. Sweeney, and D. E. Discher, "Matrix Elasticity Directs Stem Cell Lineage Specification," *Cell*, vol. 126, no. 4, pp. 677–689, 2006.

[107] N. D. Leipzig and M. S. Shoichet, "The effect of substrate stiffness on adult neural stem cell behavior," *Biomaterials*, vol. 30, no. 36, pp. 6867–6878, 2009.

[108] S. Musah, S. A. Morin, P. J. Wrighton, D. B. Zwick, S. Jin, and L. L. Kiessling, "Glycosaminoglycan-Binding Hydrogels Enable Mechanical Control of Human Pluripotent Stem Cell Self-Renewal," *ACS Nano*, vol. 6, no. 11, pp. 10168–10177, 2012.

[109] P. Moshayedi *et al.*, "The relationship between glial cell mechanosensitivity and foreign body reactions in the central nervous system," *Biomaterials*, vol. 35, no. 13, pp. 3919–3925, 2014.

[110] B. A. Aguado, W. Mulyasasmita, J. Su, K. J. Lampe, and S. C. Heilshorn, "Improving viability of stem cells during syringe needle flow through the design of hydrogel cell carriers," *Tissue Eng. - Part A*, vol. 18, no. 7–8, pp. 806–815, 2012.

[111] M. Gao *et al.*, "Templated agarose scaffolds for the support of motor axon regeneration into sites of complete spinal cord transection," *Biomaterials*, vol. 34, no. 5, pp. 1529–1536, 2013.

[112] S. Woerly, R. Marchand, and G. Lavallée, "Intracerebral implantation of synthetic polymer/biopolymer matrix: a new perspective for brain repair," *Biomaterials*, vol. 11, no. 2, pp. 97–107, 1990.

[113] D. Shahriari, J. Y. Koffler, M. H. Tuszynski, W. M. Campana, and J. S. Sakamoto, "Hierarchically Ordered Porous and High-Volume Polycaprolactone Microchannel Scaffolds Enhanced Axon Growth in Transected Spinal Cords," *Tissue Eng. - Part A*, vol. 23, no. 9–10, pp. 415–425, 2017.

[114] J. Prager *et al.*, "Stiffness-matched biomaterial implants for cell delivery: clinical, intraoperative ultrasound elastography provides a 'target' stiffness for hydrogel synthesis in spinal cord injury," *J. Tissue Eng.*, vol. 11, pp. 1–14, 2020.

[115] C. T. McKee, J. A. Last, P. Russell, and C. J. Murphy, "Indentation Versus Tensile Measurements of Young's Modulus for Soft Biological Tissues," *Tissue Eng. Part B Rev.*, vol. 17, no. 3, pp. 155–164, 2011.

[116] R. D. Bartlett, D. Choi, and J. B. Phillips, "Biomechanical properties of the spinal cord: Implications for tissue engineering and clinical translation," *Regen. Med.*, vol. 11, no. 7, pp. 659–673, 2016.

[117] S. Cheng, E. C. Clarke, and L. E. Bilston, "Rheological properties of the tissues of the central nervous system: A review," *Med. Eng. Phys.*, vol. 30, no. 10, pp. 1318–1337, 2008.

[118] D. E. Koser, E. Moeendarbary, J. Hanne, S. Kuerten, and K. Franze, "CNS cell distribution and axon orientation determine local spinal cord mechanical properties," *Biophys. J.*, vol. 108, no. 9, pp. 2137–2147, 2015.

[119] E. K. Walsh and A. Schettini, "Calculation of brain elastic parameters in vivo," *Am. J. Physiol. - Adv. Physiol. Educ.*, vol. 247, pp. 693–700, 1984.

[120] M. J. Paszek *et al.*, "Tensional homeostasis and the malignant phenotype," *Cancer Cell*, vol. 8, no. 3, pp. 241–254, 2005.

[121] K. Choi, J. L. Kuhn, M. J. Ciarelli, and S. A. Goldstein, "The elastic moduli of human subchondral, trabecular, and cortical bone tissue and the size-dependency of cortical bone modulus," *J. Biomech.*, vol. 23, no. 11, pp. 1103–1113, 1990.

[122] K. Ichihara, T. Taguchi, Y. Shimada, I. Sakuramoto, S. Kawano, and S. Kawai, "Gray Matter of the Bovine Cervical Spinal Cord is Mechanically More Rigid and Fragile than the White Matter," vol. 18, no. 3, pp. 361–367, 2001.

[123] H. Ozawa, T. Matsumoto, T. Ohashi, M. Sato, and S. Kokubun, "Comparison of spinal cord gray matter and white matter softness: Measurement by pipette aspiration method," *J. Neurosurg.*, vol. 95, no. 2 suppl., pp. 221–224, 2001.

[124] A. R. Tunturi, "Elasticity of the spinal cord, pia, and denticulate ligament in the dog," *J. Neurosurg.*, vol. 48, no. 6, pp. 975–979, 1978.

[125] L. E. Bilston and L. E. Thibault, "The mechanical properties of the human cervical spinal cord In Vitro," *Ann. Biomed. Eng.*, vol. 24, no. suppl. 1, pp. 67–74, 1995.

[126] T. K. Hung, G. L. Chang, H. S. Lin, F. R. Walter, and L. Bunegin, "Stress-strain relationship of the spinal cord of anesthetized cats," *J. Biomech.*, vol. 14, no. 4, pp. 269–276, 1981.

[127] G. L. Chang, T. K. Hung, and W. W. Feng, "An in-vivo measurement and analysis of viscoelastic properties of the spinal cord of cats," *J. Biomech. Eng.*, vol. 110, no. 2, pp. 115–122, 1988.

[128] E. Moeendarbary *et al.*, "The soft mechanical signature of glial scars in the central nervous system," *Nat. Commun.*, vol. 8, pp. 1–11, 2017.

[129] X. Yu and R. V Bellamkonda, "Dorsal root ganglia neurite extension is inhibited by mechanical and chondroitin sulfate-rich interfaces," *J. Neurosci. Res.*, vol. 66, no. 2, pp. 303–310, 2001.

[130] J. Pupkaite, J. Rosenquist, J. Hilborn, and A. Samanta, "Injectable Shape-Holding Collagen Hydrogel for Cell Encapsulation and Delivery Cross-linked Using Thiol-Michael Addition Click Reaction," *Biomacromolecules*, vol. 20, no. 9, pp. 3475–3484, 2019.

[131] F. Y. Hsieh, H. H. Lin, and S. hui Hsu, "3D bioprinting of neural stem cell-laden thermoresponsive biodegradable polyurethane hydrogel and potential in central nervous system repair," *Biomaterials*, vol. 71, pp. 48–57, 2015.

[132] M. K. Gordon and R. A. Hahn, "Collagens," *Cell Tissue Res.*, vol. 339, no. 1, pp. 247–257, 2010.

[133] S. W. P. Kemp, S. Syed, S. K. Walsh, D. W. Zochodne, and R. Midha, "Collagen nerve conduits promote enhanced axonal regeneration, Schwann cell Association, and neovascularization compared to silicone conduits," *Tissue Eng. - Part A*, vol. 15, no. 8, pp. 1975–1988, 2009.

[134] A. K. Lynn, I. V. Yannas, and W. Bonfield, "Antigenicity and immunogenicity of collagen," *J. Biomed. Mater. Res.*, vol. 71B, no. 2, pp. 343–354, 2004.

[135] C. Chen *et al.*, "Collagen/heparin sulfate scaffolds fabricated by a 3D bioprinter improved mechanical properties and neurological function after spinal cord injury in rats," *J. Biomed. Mater. Res. - Part A*, vol. 105, no. 5, pp. 1324–1332, 2017.

[136] J. Oudry, T. Lynch, J. Vappou, L. Sandrin, and V. Miette, "Comparison of four different techniques to evaluate the elastic properties of phantom in elastography: is there a gold standard?," *Phys. Med. Biol.*, vol. 59, no. 19, pp. 5775–5793, 2014.

[137] C. Shi, Y. Zhu, X. Ran, M. Wang, Y. Su, and T. Cheng, "Therapeutic Potential of Chitosan and Its Derivatives in Regenerative Medicine," *J. Surg. Res.*, vol. 133, no. 2, pp. 185–192, 2006.

[138] A. I. Cañas, J. P. Delgado, and C. Gartner, "Biocompatible scaffolds composed of chemically crosslinked chitosan and gelatin for tissue engineering," *J. Appl. Polym. Sci.*, vol. 133, no. 33, pp. 1–10, 2016.

[139] N. L. Francis *et al.*, "An ice-templated, linearly aligned chitosan-alginate scaffold for neural tissue engineering," *J. Biomed. Mater. Res. - Part A*, vol. 101, no. 12, pp. 3493–3503, 2013.

[140] Y. Sun *et al.*, "3D printing collagen/chitosan scaffold ameliorated axon regeneration and neurological recovery after spinal cord injury," *J. Biomed. Mater. Res. Part A*, vol. 107, no. 9, pp. 1898–1908, 2019.

[141] S. Yao *et al.*, "Hierarchically aligned fibrin nanofiber hydrogel accelerated axonal regrowth and locomotor function recovery in rat spinal cord injury," *Int. J. Nanomedicine*, vol. 13, pp. 2883–2895, 2018.

[142] S. Yao *et al.*, "Co-effects of matrix low elasticity and aligned topography on stem cell neurogenic differentiation and rapid neurite outgrowth," *Nanoscale*, vol. 8, no. 19, pp. 10252–10265, 2016.

[143] J. Du *et al.*, *Prompt peripheral nerve regeneration induced by a hierarchically aligned fibrin nanofiber hydrogel*, vol. 55. 2017.

[144] W. Bensaïd, J. T. Triffitt, C. Blanchat, K. Oudina, L. Sedel, and H. Petite, "A biodegradable fibrin scaffold for mesenchymal stem cell transplantation," *Biomaterials*, vol. 24, no. 14, pp. 2497–2502, 2003.

[145] L. Zhou *et al.*, "Soft Conducting Polymer Hydrogels Cross-Linked and Doped by Tannic Acid for Spinal Cord Injury Repair," *ACS Nano*, vol. 12, no. 11, pp. 10957–10967, 2018.

[146] N. Siddiqui, S. Asawa, B. Birru, R. Baadhe, and S. Rao, "PCL-Based Composite Scaffold Matrices for Tissue Engineering Applications," *Mol. Biotechnol.*, vol. 60, no. 7, pp. 506–532, 2018.

[147] M. Abedalwafa, F. Wang, L. Wang, and C. Li, "Biodegradable poly-epsilon-caprolactone (PCL) for tissue engineering applications: A review," *Rev. Adv. Mater. Sci.*, vol. 34, no. 2, pp. 123–140, 2013.

[148] M. Dadsetan, A. M. Knight, L. Lu, A. J. Windebank, and M. J. Yaszemski, "Stimulation of neurite outgrowth using positively charged hydrogels," *Biomaterials*, vol. 30, no. 23–24, pp. 3874–3881, 2009.

[149] B. K. Chen *et al.*, "Comparison of polymer scaffolds in rat spinal cord: A step toward quantitative assessment of combinatorial approaches to spinal cord repair," *Biomaterials*, vol. 32, no. 32, pp. 8077–8086, 2011.

[150] M. Dadsetan, J. P. Szatkowski, M. J. Yaszemski, and L. Lu, "Characterization of Photo-Cross-Linked Oligo[poly(ethylene glycol) fumarate] Hydrogels for Cartilage Tissue Engineering," *Biomacromolecules*, vol. 8, no. 5, pp. 1702–1709, 2007.

[151] P. D. Dalton, L. Flynn, and M. S. Shoichet, "Manufacture of poly(2-hydroxyethyl methacrylate-co-methyl methacrylate) hydrogel tubes for use as nerve guidance channels," *Biomaterials*, vol. 23, no. 18, pp. 3843–3851, 2002.

[152] J. S. Belkas, C. A. Munro, M. S. Shoichet, M. Johnston, and R. Midha, "Long-term in vivo biomechanical properties and biocompatibility of poly(2-hydroxyethyl methacrylate-co-methyl methacrylate) nerve conduits," *Biomaterials*, vol. 26, no. 14, pp. 1741–1749, 2005.

[153] Y. Katayama, R. Montenegro, T. Freier, R. Midha, J. S. Belkas, and M. S. Shoichet, "Coil-reinforced hydrogel tubes promote nerve regeneration equivalent to that of nerve autografts," *Biomaterials*, vol. 27, no. 3, pp. 505–518, 2006.

[154] E. C. Tsai, P. D. Dalton, M. S. Shoichet, and C. H. Tator, "Synthetic hydrogel guidance channels facilitate regeneration of adult rat brainstem motor axons after complete spinal cord transection," *J. Neurotrauma*, vol. 21, no. 6, pp. 789–804, 2004.

[155] E. C. Tsai, P. D. Dalton, M. S. Shoichet, and C. H. Tator, "Matrix inclusion within synthetic hydrogel guidance channels improves specific supraspinal and local axonal regeneration after complete spinal cord transection," *Biomaterials*, vol. 27, no. 3, pp. 519–533, 2006.

[156] A. Hejcl *et al.*, "Acute and delayed implantation of positively charged 2-hydroxyethyl methacrylate scaffolds in spinal cord injury in the rat: Laboratory investigation," *J. Neurosurg. Spine*, vol. 8, no. 1, pp. 67–73, 2008.

[157] A. Hejčl *et al.*, "Dynamics of tissue ingrowth in SIKVAV-modified highly superporous PHEMA scaffolds with oriented pores after bridging a spinal cord transection," *J. Mater. Sci. Mater. Med.*, vol. 29, no. 7, 2018.

[158] A. Bakshi, O. Fisher, T. Dagci, B. T. Himes, I. Fischer, and A. Lowman, "Mechanically engineered hydrogel scaffolds for axonal growth and angiogenesis after transplantation in spinal cord injury.," *J. Neurosurg. Spine*, vol. 1, no. 3, pp. 322–329, 2004.

[159] V. Pertici *et al.*, "The use of poly(N-[2-hydroxypropyl]- methacrylamide) hydrogel to repair a T10 spinal cord hemisection in rat: A behavioural, electrophysiological and anatomical examination," *ASN Neuro*, vol. 5, no. 2, pp. 149–166, 2013.

[160] J. a Friedman, A. J. Windebank, M. J. Moore, R. J. Spinner, B. L. Currier, and M. J. Yaszemski, "Biodegradable Polymer Grafts for Surgical Repair of the Injured Spinal Cord," *Spinal Cord*, vol. 51, no. 3, pp. 742–752, 2002.

[161] M. J. Moore *et al.*, "Multiple-channel scaffolds to promote spinal cord axon regeneration," *Biomaterials*, vol. 27, no. 3, pp. 419–429, 2006.

[162] E. Riande, R. Díaz-Calleja, M. G. Prolongo, R. M. Masegosa, and C. Salom, *Polymer Viscoelasticity*. 2000.

[163] N. W. Tschoegl, *The Phenomenological Theory of Linear Viscoelastic Behavior*. 1985.

[164] H. F. Brinson, "Polymer Engineering Science and Viscoelasticity: An Introduction," 2008.

[165] Y. Akagi, J. P. Gong, U. Chung, and T. Sakai, "Transition between Phantom and Affine Network Model Observed in Polymer Gels with Controlled Network Structure," *Macromolecules*, vol. 46, no. 3, pp. 1035–1040, 2013.

[166] L. R. G. Treloar, *The Physics of Rubber Elasticity*. 1975.

[167] D. E. Hanson, "The molecular kink paradigm for rubber elasticity: Numerical simulations of explicit polyisoprene networks at low to moderate tensile strains," *J. Chem. Phys.*, vol. 135, no. 5, pp. 1–7, 2011.

[168] P. A. Kelly, "5. Material Behaviour and Mechanics Modelling," in *Solid Mechanics Part I: An Introduction to Solid Mechanics*, 2015, pp. 113–142.

[169] P. A. Kelly, "10. Viscoelasticity," in *Solid Mechanics Part I: An Introduction to Solid Mechanics*, 2015, pp. 283–342.

[170] J. P. Lasalle, L. Sirovich, and F. John, *Lectures on Viscoelasticity Theory*. 1972.

[171] J. D. Ferry, *Viscoelastic properties of polymers*. 1980.

[172] E. Manias, "Oversimplified Viscoelasticity The Maxwell Model." https://zeus.plmsc.psu.edu/~manias/MatSE447/02_FluidModels.pdf

[173] D. Roylance, *Engineering Viscoelasticity*. 2001.

[174] E. A. López-Guerra and S. D. Solares, "Modeling viscoelasticity through spring–dashpot models in intermittent-contact atomic force microscopy," *Beilstein J. Nanotechnol.*, vol. 5, no. 1, pp. 2149–2163, 2014.

[175] M. Hess *et al.*, "Terminology of polymers containing ionizable or ionic groups and of polymers containing ions," *Pure Appl. Chem.*, vol. 78, no. 11, pp. 2067–2074, 2006.

[176] W.-M. Kulicke and C. Clasen, *Viscosimetry of polymers and polyelectrolytes*. 2004.

[177] D. Wang and T. P. Russell, "Advances in Atomic Force Microscopy for Probing Polymer Structure and Properties," *Macromolecules*, vol. 51, no. 1, pp. 3–24, 2018.

[178] G. Binning, C. F. Quate, and C. Gerber, "Atomic Force Microscope," *Phys. Rev. Lett.*, vol. 56, no. 9, 1986.

[179] S. Scheuring, T. Sapra, and D. J. Müller, *Handbook of Single-Molecule Biophysics*. New York, NY: Springer US, 2009.

[180] M. Radmacher, M. Fritz, C. M. Kacher, J. P. Cleveland, and P. K. Hansma, "Measuring the viscoelastic properties of human platelets with the atomic force microscope," *Biophys. J.*, vol. 70, no. 1, pp. 556–567, 1996.

[181] R. Garcia, "Nanomechanical mapping of soft materials with the atomic force microscope: methods, theory and applications," *Chem. Soc. Rev.*, vol. 49, pp. 5850–5884, 2020.

[182] H. J. Butt, B. Cappella, and M. Kappl, "Force measurements with the atomic force microscope: Technique, interpretation and applications," *Surf. Sci. Rep.*, vol. 59, no. 1–6, pp. 1–152, 2005.

[183] JPK Instruments Application Note, "Determining the elastic modulus of biological samples using atomic force microscopy."

[184] W. C. Oliver, F. R. Brotzen, and P. G. M., "On the generality of the relationship among contact stiffness, contact area, and elastic modulus during indentation," *J. Mater. Res.*, vol. 7, no. 3, pp. 613–617, 1992.

[185] H. Hertz, "Über die Berührung fester elastischer Körper," *J. für die reine und Angew. Math.*, vol. 92, pp. 156–171, 1881.

[186] D. L. Kaplan, *Biopolymers from Renewable Resources*. 1998.

[187] K. Draget, O. Smidsrød, and G. Skjåk-Bræk, "Alginates form algae," in *Polysaccharides and polyamides in the food iindustries: properties, production and patents*, 2005, pp. 1–30.

[188] A. Haug, H. S. Gewitz, W. Völker, C.-G. Hedén, B. Malmgren, and H. Palmstierna, "Ion Exchange Properties of Alginate Fractions," *Acta Chem. Scand.*, vol. 13, pp. 1250–1251, 1959.

[189] A. Haug, "The Affinity of Some Divalent Metals to Different Types of Alginates," *Acta Chem. Scand.*, vol. 15, no. 8, pp. 1794–1795, 1961.

[190] E. C. C. Stanford, "British Patent 142," 1881

[191] P. Gacesa, "Alginates," *Carbohydr. Polym.*, vol. 8, no. 3, pp. 161–182, 1988.

[192] Y. Atsuki, K., Tomoda, "Studies on seaweeds of Japan I. The chemical constituents of Laminara," *J. Soc. Chem. Ind. Japan*, vol. 29, pp. 509–517, 1926.

[193] L. Nelson, W. Cretcher, "The alginic acid from Macrocystis pyrifera," *J. Am. Chem. Soc.*, vol. 52, pp. 2130–2134, 1929.

[194] L. Nelson, W. Cretcher, "The properties of d-mannuronic acid and lactone," *J. Am. Chem. Soc.*, vol. 51, pp. 1914–1918, 1929.

[195] P. Bird, G., Haas, "On the constituent nature of the cell wall constituents of Laminara spp. Mannuronic acid," *Biochem. J.*, vol. 25, pp. 26–30, 1931.

[196] T. Miawa, "Alginic Acid," *J. Chem. Soc. Japan*, vol. 51, pp. 738–745, 1930.

[197] H. Fischer, F., Dörfel, "Die Polyuronsäuren der Braunalgen (Kohlenhydrate der Algen)," *Z. Physiol. Che.*, vol. 302, pp. 186–203, 1955.

[198] Haug A., "Fractionation of alginic acid," *Acta Chem. Scand.*, vol. 13, pp. 601–603, 1959.

[199] E. D. T. Atkins, W. Mackie, and E. E. Smolko, "Crystalline Structures of Alginic Acid," *Nat. Publ. Gr.*, vol. 225, pp. 626–628, 1970.

[200] O. Smidsrød and T. Painter, "Effect of periodate oxidation upon the stiffness of the alginate molecule in solution," *Carbohydr. Res.*, vol. 26, pp. 125–132, 1973.

[201] G. T. Grant, E. R. Morris, D. A. Rees, P. J. C. Smith, and D. Thom, "Biological interactions between polysaccharides and divalent cations: The egg-box model," *FEBS Lett.*, vol. 32, no. 1, pp. 195–198, 1973.

[202] H. Thiele and K. Hallich, "Kapillarstrukturen in ionotropen Gelen," *Kolloid-Zeitschrift*, vol. 151, no. 1, pp. 1–12, 1957.

[203] J. Thumbs and H. H. Kohler, "Capillaries in alginate gel as an example of dissipative structure formation," *Chem. Phys.*, vol. 208, no. 1, pp. 9–24, 1996.

[204] H. Treml, S. Woelki, and H. H. Kohler, "Theory of capillary formation in alginate gels," *Chem. Phys.*, vol. 293, no. 3, pp. 341–353, 2003.

[205] A. D. Augst, H. J. Kong, and D. J. Mooney, "Alginate hydrogels as biomaterials," *Macromol. Biosci.*, vol. 6, no. 8, pp. 623–633, 2006.

[206] J. Venkatesan *et al.*, "Seaweed polysaccharides and their potential biomedical applications," *Starch/Staerke*, vol. 67, no. 5–6, pp. 381–390, 2015.

[207] M. I. Günther, N. Weidner, R. Müller, and A. Blesch, "Cell-seeded alginate hydrogel scaffolds promote directed linear axonal regeneration in the injured rat spinal cord," *Acta Biomater.*, vol. 27, pp. 140–150, 2015.

[208] A. Blesch and M. H. Tuszynski, "Spinal cord injury: plasticity, regeneration and the challenge of translational drug development," *Trends Neurosci.*, vol. 32, no. 1, pp. 41–47, 2009.

[209] S. Liu *et al.*, "Regulated viral BDNF delivery in combination with Schwann cells promotes axonal regeneration through capillary alginate hydrogels after spinal cord injury," *Acta Biomater.*, vol. 60, pp. 167–180, 2017.

[210] M. A. LeRoux, F. Guilak, and L. A. Setton, "Compressive and shear properties of alginate gel: Effects of sodium ions and alginate concentration," *J. Biomed. Mater. Res.*, vol. 47, no. 1, pp. 46–53, 1999.

[211] P. Prang *et al.*, "The promotion of oriented axonal regrowth in the injured spinal cord by alginate-based anisotropic capillary hydrogels," *Biomaterials*, vol. 27, no. 19, pp. 3560–3569, 2006.

[212] K. Pawar *et al.*, "Increasing capillary diameter and the incorporation of gelatin enhance axon outgrowth in alginate-based anisotropic hydrogels," *Acta Biomater.*, vol. 7, no. 7, pp. 2826–2834, 2011.

[213] K. Pawar *et al.*, "Intrinsic and extrinsic determinants of central nervous system axon outgrowth into alginate-based anisotropic hydrogels," *Acta Biomater.*, vol. 27, pp. 131–139, 2015.

[214] P. Lu *et al.*, "Motor axonal regeneration after partial and complete spinal cord transection," *J. Neurosci.*, vol. 32, no. 24, pp. 8208–8218, 2012.

[215] K. Fouad, D. J. Bennett, R. Vavrek, and A. Blesch, "Long-Term Viral Brain-Derived Neurotrophic Factor Delivery Promotes Spasticity in Rats with a Cervical Spinal Cord Hemisection," *Front. Neurol.*, vol. 4, no. November, pp. 1–10, 2013.

[216] B. L. Strand *et al.*, "Poly-L-lysine induces fibrosis on alginate microcapsules via the induction of cytokines," *Cell Transplant.*, vol. 10, no. 3, pp. 263–275, 2001.

[217] N. Karak, *Vegetable oil-based polymers: Properties, processing and applications*. 2012.

[218] JPK Instruments, "NanoWizard Series User Manual," 2018.

[219] A. Martinsen, G. Skjåk-Bræk, O. Smidsrød, F. Zanetti, and S. Paoletti, "Comparison of different methods for determination of molecular weight and molecular weight distribution of alginates," *Carbohydr. Polym.*, vol. 15, no. 2, pp. 171–193, 1991.

[220] M. Nützl, M. Schrottenbaum, T. Müller, and R. Müller, "Mechanical properties and chemical stability of alginate-based anisotropic capillary hydrogels," *J. Mech. Behav. Biomed. Mater.*, vol. 134, pp. 1–11, 2022.

[221] H. J. Kong, E. Wong, and D. J. Mooney, "Independent Control of Rigidity and Toughness of Polymeric Hydrogels," *Macromolecules*, vol. 36, no. 12, pp. 4582–4588, 2003.

[222] B. E. Larsen, J. Bjørnstad, E. O. Pettersen, H. H. Tønnesen, and J. E. Melvik, "Rheological characterization of an injectable alginate gel system," *BMC Biotechnol.*, vol. 15, no. 1, pp. 1–12, 2015.

[223] O. Smidsrød, "Molecular Basis for some Physical Properties of Alginates in the Gel State," *Faraday Discuss. Chem. Soc.*, vol. 57, pp. 263–274, 1973.

[224] T. Freier, H. S. Koh, K. Kazazian, and M. S. Shoichet, "Controlling cell adhesion and degradation of chitosan films by N-acetylation," *Biomaterials*, vol. 26, no. 29, pp. 5872–5878, 2005.

[225] V. Guarino, T. Caputo, R. Altobelli, and L. Ambrosio, "Degradation properties and metabolic activity of alginate and chitosan polyelectrolytes for drug delivery and tissue engineering applications," *AIMS Mater. Sci.*, vol. 2, no. 4, pp. 497–502, 2015.

[226] S. Khan and N. M. Ranjha, "Effect of degree of cross-linking on swelling and on drug release of low viscous chitosan/poly(vinyl alcohol) hydrogels," *Polym. Bull.*, vol. 71, no. 8, pp. 2133–2158, 2014.

[227] H. Hosseinzadeh, "Synthesis and swelling properties of a poly(vinyl alcohol)-based superabsorbing hydrogel," *Curr. Chem. Lett.*, vol. 2, no. 3, pp. 153–158, 2013.

[228] S. Ida, A. Katsurada, M. Tsujio, M. Nakamura, and Y. Hirokawa, "Crosslinker-based regulation of swelling behavior of poly(N-isopropylacrylamide) gels in a post-polymerization crosslinking system," *Gels*, vol. 6, no. 1, 2020.

Appendix

Appendix A: Stress Relaxation in Maxwell Elements

The Maxwell element is deformed at t = 0, which strains the whole element by an absolute distance x_0. Immediately the series builds up the force F_0, which enacts on the spring element with the spring constant E and initially displaces it by an absolute distance x_s, which equals to x_0 at t = 0. As the viscous damper creeps, the spring deformation is relieved and the viscous damper of viscosity η gets strained by x_d in the timeframe t. Therefore, for the initial stress, or here, force, one can assume Eq. 30.

$$F = E\, x_s = \eta\, \frac{dx_d}{dt} \tag{30}$$

The total displacement x_0 is at all times the sum of the displacement of the two elements of the Maxwell element, yielding Eq. 31 and 32.

$$x_0 = x_s + x_d \tag{31}$$

$$x_s = x_0 - x_d \tag{32}$$

Consequently, one can rewrite and integrate Eq. 30 as Eq. 33, 34, and 35.

$$E(x_0 - x_d) = \eta \left(\frac{dx_d}{dt}\right) \tag{33}$$

$$\frac{E}{\eta}\, dt = \frac{dx_d}{(x_0 - x_d)} \tag{34}$$

$$\frac{E}{\eta}\, t = -\ln(x_0 - x_d) + C \tag{35}$$

With the initial damper strain $x_d = 0$ at t = 0, one obtains $C = \ln(x_0)$, which results in Eq. 36 and 37.

$$-\frac{E}{\eta}\, t = \ln \frac{(x_0 - x_d)}{x_0} \tag{36}$$

$$\frac{x_0 - x_d}{x_0} = e^{\left(-\frac{Et}{\eta}\right)} \tag{37}$$

By combining Eq. 30, Eq. 32, and Eq. 37, the force decay of the Maxwell element can be expressed as Eq. 38 [172].

$$F(t) = k\, x_0\, e^{-\frac{Et}{\eta}} \tag{38}$$

Thus, at the time λ, the force in the Maxwell element diminishes to $F(\lambda) = \frac{F_0}{e}$, with $\lambda = \frac{\eta}{E}$.

Appendix B: Calculation of Wiechert Model Force Relaxation Factors in Python

```
import os
import glob
import pandas as pd
import numpy as np
from scipy.optimize import curve_fit


def pathfind():

    txtfiles_list = glob.glob("*txt")
    cwd = os.getcwd()
    paths = list()

    for line in txtfiles_list:
      path = cwd + "\\" + line
      paths.append(path)
    return paths
paths=pathfind()

def pause1(paths):
  def main(paths):

    result_list = np.array([0,1,2,3,4,5,6,7,8])
    for item in paths:
      daten = item

      def data1(daten):

        df = pd.read_table(daten, names=["verticalTipPosition"], encoding="latin1")
        i = 0
        for row in df["verticalTipPosition"]:
          i = i + 1
          if row == "# segmentIndex: 1":
            break

         df_pause = df.iloc[i + 11: i + 4 * 2048]
        df_pause = df_pause["verticalTipPosition"].str.split(" ", 6, expand=True)

        del df_pause[0]
        del df_pause[2]
        del df_pause[3]
```

```
            del df_pause[4]
            del df_pause[5]

            return df_pause
        df_pause = data1(daten)

        def floatconvert(df_pause):
            df_alt = pd.DataFrame({1: [1, 2, 3], 6: [1 ,2, 3]}, index=[0, 1, 2])
            try:
                df_pause[6] = df_pause[6].astype(float)
                df_pause[1] = df_pause[1].astype(float)
                return df_pause
            except:
                return df_alt
        df_pause = floatconvert(df_pause)

        def curvefit(df_pause):

            def func(x, a0, a1, a2):
                return a0 + a1 * np.exp(-x / 1) + a2 * np.exp(-x / 0.1)

            popt, pcov = curve_fit(func, df_pause[6], df_pause[1], p0=None, sigma=None, absolute_sigma=False)
            a0, a1, a2 = popt

            df_pcov = pd.DataFrame(pcov)
            perr = np.sqrt(np.diag(pcov))
            df_perr = pd.DataFrame({"parameter": popt, "errorparameter": perr, "ratio": perr / popt}, index=["ao",
"a1", "a2"])
            return df_perr
        df_perr = curvefit(df_pause)


        df_perr_t = df_perr.T
        df_perr_tr = pd.DataFrame(df_perr_t.values.reshape(1, -1), columns=[0,1,2,3,4,5,6,7,8])
        npresultfit = np.array(df_perr_tr)
        result_list = np.vstack((result_list, npresultfit))

    return result_list

result = main(paths)
resultdf = pd.DataFrame(result)
resultdf = resultdf[(resultdf[[7,8]] > 0).all(1)]
resultdf = resultdf[(resultdf[[7,8]] < 0.1).all(1)]

resultdf.insert(3, "a2/a1", "")
resultdf[3] = resultdf[2]/resultdf[1]
total_rows = len(resultdf)
quartiles = np.percentile(resultdf[3], [25,50,75])
quartiles2 = np.append(quartiles, total_rows)
return quartiles2
```

```
quartiles1 = pause1(paths)
quartiles1df = pd.DataFrame(data = quartiles1, index = ["1. Q", "2. Q", "3. Q", "n"], columns = ["1 µm/s"])

def pause2(paths):
  def main(paths):

    result_list = np.array([0,1,2,3,4,5,6,7,8])
    for item in paths:
      daten = item

      def data1(daten):

        df = pd.read_table(daten, names=["verticalTipPosition"], encoding="latin1")
        i = 0
        for row in df["verticalTipPosition"]:
          i = i + 1
          if row == "# segmentIndex: 4":
            break

         df_pause = df.iloc[i + 11: i + 4 * 2048]
        df_pause = df_pause["verticalTipPosition"].str.split(" ", 6, expand=True)

        del df_pause[0]
        del df_pause[2]
        del df_pause[3]
        del df_pause[4]
        del df_pause[5]

        return df_pause
      df_pause = data1(daten)

      def floatconvert(df_pause):
        df_alt = pd.DataFrame({1: [1, 2, 3], 6: [1 ,2, 3]}, index=[0, 1, 2])
        try:
          df_pause[6] = df_pause[6].astype(float)
          df_pause[1] = df_pause[1].astype(float)
          return df_pause
        except:
          return df_alt
      df_pause = floatconvert(df_pause)

      def curvefit(df_pause):

        def func(x, a0, a1, a2):
          return a0 + a1 * np.exp(-x / 1) + a2 * np.exp(-x / 0.1)

        popt, pcov = curve_fit(func, df_pause[6], df_pause[1], p0=None, sigma=None, absolute_sigma=False)
        a0, a1, a2 = popt

        df_pcov = pd.DataFrame(pcov)
```

```
            perr = np.sqrt(np.diag(pcov))
            df_perr = pd.DataFrame({"parameter": popt, "errorparameter": perr, "ratio": perr / popt}, index=["ao",
"a1", "a2"])
            return df_perr
        df_perr = curvefit(df_pause)


        df_perr_t = df_perr.T
        df_perr_tr = pd.DataFrame(df_perr_t.values.reshape(1, -1), columns=[0,1,2,3,4,5,6,7,8])
        npresultfit = np.array(df_perr_tr)
        result_list = np.vstack((result_list, npresultfit))

    return result_list

  result = main(paths)
  resultdf = pd.DataFrame(result)
  resultdf = resultdf[(resultdf[[7,8]] > 0).all(1)]
  resultdf = resultdf[(resultdf[[7,8]] < 0.1).all(1)]

  resultdf.insert(3, "a2/a1", "")
  resultdf[3] = resultdf[2]/resultdf[1]
  total_rows = len(resultdf)
  quartiles = np.percentile(resultdf[3], [25,50,75])
  quartiles2 = np.append(quartiles, total_rows)
  return quartiles2
quartiles2 = pause2(paths)
quartiles2df = pd.DataFrame(data = quartiles2, index = ["1. Q", "2. Q", "3. Q", "n"], columns = ["5 µm/s"])

quartiles = quartiles1df.join(quartiles2df)
quartiles.to_csv("quartiles.csv", sep = ";")
```

Acronyms

ACH	anisotropic capillary hydrogel
AFM	atomic force microscope
ANOVA	analysis of variance
BBB	Basso, Beattie, and Bresnahan
BDNF	brain-derived neurotrophic factor
BM	biomaterial
C	cervical
CNS	central nervous system
CSPG	chondroitin sulfate proteoglycans
DDI	decamethylene diisocyanate
DMSO	dimethyl sulfoxide
ECM	extracellular matrix
EDMA	ethylene dimethacrylate
ESC	embryonic stem cell
GFAP	glial fibrillary acidic protein
HDI	hexamethylene diisocyanate
HEMA	2-hydroxyethyl methacrylate
MMA	methyl methacrylate
MSC	mesenchymal stem cell
NSC	neural stem cell
ODI	octamethylene diisocyanate
PBS	phosphate-buffered saline
PHEMA	poly(2-hydroxyethyl methacrylate)
PHEMA-MMA	poly(2-hydroxyethyl methacrylate-co-methyl methacrylate)
PHMPA	poly(N-(2-hydroxypropyl) methacrylamide)
PLGA	poly(D, L-lactic-co-glycolic acid)
PLO	poly-L-ornithine
PNS	peripheral nervous system
PU	polyurethane

p.a.	*pro analysi*
SC	spinal cord
SCI	spinal cord injury
SEM	scanning electron microscope
SLS	standard linear solid
T	thoracic

Acknowledgments

An dieser Stelle danke ich all jenen die mich bei dem Erstellen dieser Arbeit und in der Zeit am Lehrstuhl begleitet haben.

Dabei gilt mein besonderer Dank Apl. Prof. Dr. Rainer Müller, der mir das Thema und die Förderung des Projektes überlassen hat und mich bei allen experimentellen Arbeiten stets unterstützt hat und mir dabei aber die Freiheit, eigene Ideen und Ansätze umzusetzen, immer eingeräumt hat. Die Ziele dieser Arbeit konnten nur durch gemeinsame wissenschaftliche Diskussionen sukzessive abgearbeitet und umgesetzt werden.

Ebenfalls bedanke ich mich bei den Mitarbeitern des Querschnittzentrum der Klinik für Paraplegiologie des Universitätsklinikums Heidelberg, allen voran Dr. Thomas Schackel, Dr. Radhika Puttagunta und Yifeng Zheng, mit denen wir zusammen die Ziele dieser Arbeit in einiger Vorarbeit abstecken konnten und deren Expertise bei der Umsetzung von *in-vivo* Versuchen mit unseren Proben sehr geschätzt wurde.

Für die Unterstützung bei Laborarbeiten bedanke ich mich bei Bianca Gruber, Florian Wegner, Michelle Schmidbauer und Maximilian Kunstmann.

Ein besonderes Dankeschön auch an meine Bürokollegen Jonas, Pierre und Florian, die sowohl ein freundschaftliches Arbeitsklima geschaffen haben, als auch für außerfachliche Diskussionen immer zu begeistern waren.

Für die finanzielle Unterstützung des Projektes bedanke ich mich bei der Deutschen Forschungsgemeinschaft (MU 2787/3-3).

Eidesstattliche Erklärung

(1) Ich erkläre hiermit an Eides statt, dass ich die vorliegende Arbeit ohne unzulässige Hilfe Dritter und ohne Benutzung anderer als der angegebenen Hilfsmittel angefertigt habe; die aus anderen Quellen direkt oder indirekt übernommenen Daten und Konzepte sind unter Angabe des Literaturzitats gekennzeichnet.

(2) Bei der Auswahl und Auswertung folgenden Materials haben mir die nachstehend aufgeführten Personen in der jeweils beschriebenen Weise entgeltlich/unentgeltlich geholfen:

1. Bianca Gruber: Durchführung von Viskosimetriemessungen; Zulassungsarbeit
2. Maximilian Kunstmann: Herstellung von Alginat Hydrogelen, Rheometermessungen; Zulassungsarbeit

(3) Weitere Personen waren an der inhaltlich-materiellen Herstellung der vorliegenden Arbeit nicht beteiligt. Insbesondere habe ich hierfür nicht die entgeltliche Hilfe eines Promotionsberaters oder anderer Personen in Anspruch genommen. Niemand hat von mir weder unmittelbar noch mittelbar geldwerte Leistungen für Arbeiten erhalten, die im Zusammenhang mit dem Inhalt der vorgelegten Dissertation stehen.

(4) Die Arbeit wurde bisher weder im In- noch im Ausland in gleicher oder ähnlicher Form einer anderen Prüfungsbehörde vorgelegt.

Regensburg, Mai 2023 _____

Maximilian Nützl